

Copyright

by

Cherelle Jalisa Thomas

2018

**The Dissertation Committee for Cherrelle Jalisa Thomas Certifies that this is the approved version of the following dissertation:**

**Surface Functionalization of CuInSe<sub>2</sub> and CsPbI<sub>3</sub> Nanocrystals:  
Conversion Yields, Exciton Kinetics, and Thermal Stability**

**Committee:**

Brian A. Korgel, Supervisor

Delia Milliron

John G. Ekerdt

Simon M. Humphrey

Guihua Yu

**Surface Functionalization of CuInSe<sub>2</sub> and CsPbI<sub>3</sub> Nanocrystals:  
Conversion Yields, Exciton Kinetics, and Thermal Stability**

**by**

**Cherrelle Jalisa Thomas**

**Dissertation**

Presented to the Faculty of the Graduate School of

The University of Texas at Austin

in Partial Fulfillment

of the Requirements

for the Degree of

**Doctor of Philosophy**

**The University of Texas at Austin**

**December 2018**

## **Dedication**

*“The ultimate test of man’s conscience may be his willingness to sacrifice something today for future generations whose words of thanks will not be heard.”*

*~ Gaylord Nelson*

This dissertation is dedicated to my parents and grandparents who sacrificed their dreams to come to America and give their children a better life. Your sacrifices were not in vain!



## Acknowledgements

First and foremost, I would like to thank God for guiding my footsteps along this tumultuous but needed journey. I was forced out of my comfort zone and pushed into my purpose. There were times where this path was difficult, but I thank God for keeping me focus. Secondly, I want to thank Dr. Korgel for affording me the opportunity to travel, live, and research abroad. Furthermore, I want to thank Dr. Korgel for supporting my ideas and encouraging me to apply to graduate school. His guidance has allowed me to navigate through graduate school and strengthening my voice. Apart from research, he has introduced me to many cultures and experiences that I probably wouldn't have experienced on my own; to include dinner on tatami mats and his tatemaie approach to life. I would also like to thank the members of my committee: Dr. Milliron, Dr. Ekerdt, Dr. Humphrey, and Dr. Yu. I want to thank Dr. Humphrey for helping me to understand inorganic chemistry. His impromptu meetings were extremely helpful and I learned a lot. I want to thank Luisa Gil-Fandino for accompanying us on the Japan trip and introducing me to the world of textiles.

I would like to thank all members of the Korgel lab, old and new generations. Specifically, I want to thank Dr. Vahid Akhavan, Dr. Brian Goodfellow, Dr. Matthew Panthani, Dr. Chet Steinhagen, Dr. Timothy Bogart, Dr. Jackson Stolle, Dr. Taylor Harvey, Dr. Christian Bosoy, Dr. Xiaotang Lu, Dr. Yixuan Yu, Dr. Doug Pernik, and Dr. Philip Liu for mentoring me as an undergraduate student, answering any questions that I may have regardless of their distance, helping me start my project, allowing me to pitch ideas, and teaching me laboratory skills and techniques aside from literature. I want to thank my lab cohorts whom matriculated at the same time as me: Emily Adkins, Adrien Guillaussier, Vikas Reddy Voggu, and Dorothy Silbaugh. Over the years we have supported each other

through graduate school and I am blessed to call these amazing people friends. Thank you to the younger generations of graduate students: Hyun Gyung Kim, Taizhi Jiang, Tim Siegler, Dan Houck, Tushti Shah, Yangning Zhang, Michael Abney, William Sullivan, Wen Liu, and Jungchul Noh for being great and talented labmates. Specifically, Yangning who worked closely with me on the perovskite project, Tushti whom I bounced ideas off and talked about books and podcasts for hours.

I would also like to thank my undergraduate researchers Soa-Jin Sher, Adi Shetkar, and Demi Arellano. You all taught me a lot about planning experiments, effective communication, and time management. I would like to thank my collaborators Raymond Lewandowski and John Topping for allowing me the opportunity to research and fabricate microgroove photovoltaic devices. That experience was invaluable to my graduate career. Furthermore, I would like to thank Dr. Leonard Francis at the international Iberian Nanotechnology laboratory (INL) for allowing me to conduct research in his lab. Additionally, I would like to thank Detlef Smilgies and Richard Schaller for assisting me with in-situ measurements at CHESS and Argonne respectively. A special thanks to all of the managers who taught me how to use the precious laboratory characterization equipment: Dwight Romanovicz, Vincent Lynch, Hugo Celio, Karalee Jarvis, Raluca Gearba, Angela Spangenberg, and Damon Smith. I am extremely blessed to have Kate Baird and Jon Peck as the graduate coordinator and administrative assistant; their conversation and knowledge on university policies will always stick with me.

While I was in graduate school, my friends and families endure it with me. I am forever grateful for you all. I want to thank Bianca Williams, Kevin Vasquez, Kayla Henderson, and Jamie Barber for being amazing people to confide get lunch with when I needed a break. I want to give a special shout out to Bianca for being my roommate for two years and dealing with my crazy schedule and impromptu concerts. I would like to

thank Adrien, Kevin, and Emily for performing karaoke with me after those rough weeks. I want to thank Vikas for introducing me to Indian cuisine. I would like to thank Ms. Tibbs for instilling in me that women can do well in math and science and not expecting anything less from me. I would like to thank Mrs. Wilkerson for introducing me to college and giving me the skills to do well. Many thanks to Miesha and Ken Aubrey for being very supportive of me through this time. Many thanks to James Alexander for the encouraging and thought provoking conversations. Furthermore, I would like to thank my best friends Symone Alexander and Adesua Ojeifoh; y'all have truly kept me sane and grounded throughout these years. I am truly blessed to be surrounded by ambitious, courageous, and intelligent women. Y'all are the true definition of a support system! Thank you to my siblings for being so understanding and encouraging. Thank you to Verlyn and Everton Thomas my parents for being supportive and trying to understand my research. Additionally, thank you for giving me the opportunity that wasn't afforded to you. Last but not least, many thanks to Kenneth Davis for putting up with my schedule and taking the time to understand the graduate school life.

## **Abstract**

### **Surface Functionalization of CuInSe<sub>2</sub> and CsPbI<sub>3</sub> Nanocrystals: Conversion Yields, Exciton Kinetics, and Thermal Stability**

Cherrelle Jalisa Thomas, Ph.D

The University of Texas at Austin, 2018

Supervisor: Brian A. Korgel

Solar power is a viable solution to the reduction of global dependence on non-renewable resources. Currently, silicon photovoltaic (PV) devices dominate the market. These devices are not only expensive to manufacture but also have a lengthy production process and they emit significant amounts of CO<sub>2</sub> into the atmosphere. Nanocrystal PVs have the potential to significantly lower manufacturing cost while maintaining high efficiencies. However, challenges with nanocrystal's surface chemistry have impacted their performance. This dissertation examines the surface functionalization effects for copper indium diselenide (CIS) and cesium lead iodide (CsPbI<sub>3</sub>) nanocrystals. Specifically, the effects of surface ligands on conversion yields, exciton kinetics, superlattice formation and thermal stability were explored. Using the hot injection synthetic method, nanocrystals were functionalized with organic ligands. The nanocrystals were characterized using various techniques, such as transmission electron microscopy, transient absorption spectroscopy, and small and wide-angle X-ray scattering. It was found that nanocrystals with less surface vacancies demonstrated the

highest PV device performances. Additionally, longer lifetimes were discovered for nanocrystals with phosphinic acid ligands. These results are important prerequisites to the fabrication of low cost nanocrystal PV devices. By determining how the ligands affect the optical and electronic properties, the desired characteristics can be engineered and formed into nanoinks that can be deposited onto substrates under ambient conditions; opposed to the traditionally high energy processing.

## Table of Contents

List of Tables .....	xv
List of Figures .....	xvi
Chapter 1: Introduction .....	1
1.1: Introduction to Renewable Energy .....	1
1.2 Photovoltaic Fundamentals .....	2
1.2.2: P-N junction .....	4
1.2.3: Multiexciton Generation .....	5
1.2.4: Photovoltaic Device Testing .....	7
1.3: Types of Solar Cells .....	8
1.3.1: Silicon PV Devices .....	8
1.3.2: Second Generation Solar Cells (Thin Films) .....	11
1.3.3: Solution Processed Solar Cells .....	12
1.4: nanocrystal self-Assemblies .....	15
1.5: $\text{CuIn}_{1-x}\text{Ga}_x\text{Se}_2$ Nanocrystal solar cells .....	15
1.6: Cesium Lead Halide Nanocrystal solar cells .....	16
1.7: Conclusions and Dissertation Overview .....	17
1.8: References .....	18
Chapter 2: Synthesis and Characterization of $\text{Cu}(\text{In}_x\text{Ga}_{1-x})\text{Se}_2$ Nanocrystals .....	31
2.1: Introduction .....	31
2.2: $\text{CuIn}_{1-x}\text{Ga}_x\text{Se}_2$ Nanocrystal Synthesis .....	32
2.2.1: materials .....	32
2.2.2: $\text{CuIn}_{1-x}\text{Ga}_x\text{Se}_2$ one-pot synthesis .....	33

2.2.3: CuIn <sub>1-x</sub> Ga <sub>x</sub> Se <sub>2</sub> hot injection synthesis.....	33
2.2.3.1: Metals hot injection .....	33
2.2.3.2: DPP:Se injection .....	34
2.2.3.3: TOP:Se injection.....	34
2.2.4: CuInSe <sub>2</sub> one-pot Synthesis .....	35
2.2.4.1: CuInSe <sub>2</sub> one-pot Synthesis_NaBH <sub>4</sub> .....	35
2.2.5: CuInSe <sub>2</sub> Hot Injection Synthesis .....	35
2.2.5.1: Metals injection.....	35
2.2.5.2: DPP:Se injection .....	36
2.2.5.3: TBP:Se injection .....	36
2.2.5.4: TOP:Se injection.....	37
2.2.6: Isolation of CuIn <sub>1-x</sub> Ga <sub>x</sub> Se <sub>2</sub> Nanocrystals .....	37
2.2.7: Characterization of CuIn <sub>1-x</sub> Ga <sub>x</sub> Se <sub>2</sub> Nanocrystals.....	38
2.3: Results and discussion .....	38
2.3.1: CuIn <sub>1-x</sub> Ga <sub>x</sub> Se <sub>2</sub> Nanocrystals.....	38
2.3.2: CuInSe <sub>2</sub> Nanocrystals .....	40
2.4.: Conclusions.....	48
2.6: References.....	49
Chapter 3: Chemical Mechanisms of Copper Indium Diselenide Nanocrystal Synthesis Studied by <sup>31</sup> P Nuclear Magnetic Resonance Spectroscopy .....	54
3.1 Introduction.....	54
3.2: Experimental Details and Characterization .....	56
3.2.1: Experimental Details .....	56
3.2.2: Materials Characterization.....	59

3.3: Results and discussions.....	60
3.3.1: Method I_DPP .....	61
3.3.3: Method III_hybrid .....	68
3.3.4: Cu and In Study .....	71
3.3.5: Bond cleavage experiments .....	73
3.3.6:Nanocrystal PV Device Performance .....	75
3.3.7: Mechanism.....	78
3.4: Conclusions.....	82
3.5: References.....	82
Chapter 4: Synthesis and Characterization of Perovskite Nanocrystals .....	90
4.1: Introduction.....	90
4.2: Perovskite Nanocrystal Synthesis.....	92
4.2.1: Materials .....	92
4.2.2: Formation of the Cs-oleate and FA-oleate Reactants .....	92
4.2.3: CsPbX <sub>3</sub> nanocrystal synthesis.....	93
4.2.4: CsFAPbX <sub>3</sub> (X = I or Br) nanocrystal synthesis.....	93
4.2.5: FAPbI <sub>3</sub> nanocrystal synthesis .....	94
4.2.6: CsFAMAPbX <sub>3</sub> (X = I or Br) Nanocrystal Synthesis .....	94
4.2.7: Isolation of Nanocrystal.....	95
4.2.8: Characterization of Perovskite Nanocrystals.....	96
4.3: Results and conclusion .....	97
4.3.1: CsPbX <sub>3</sub> nanocrystals.....	97
4.3.2: Doping organic perovskite nanocrystals using Cs.....	103



4.4: Conclusions.....	107
4.5: References.....	108
Chapter 5: Thermal stability of Perovskite nanocrystals .....	114
5.1: Introduction.....	114
5.2: Experimental details and Characterization Methods .....	116
5.2.1: Materials and Experimental Details.....	116
5.2.1: Materials Characterization.....	118
5.3: Results and Discussion .....	118
5.4: Conclusions.....	128
5.5: References.....	129
Chapter 6: High-Energy Carrier Dynamics of CsPbI <sub>3</sub> Perovskite Nanocrystals .....	134
6.1: Introduction.....	134
6.2: Experimental Details and Characterization Methods .....	136
6.2.1: Experimental Details .....	136
6.2.2: Materials Characterization.....	137
6.3: Results and Discussion .....	138
6.4: Conclusions.....	151
6.5: References.....	152
Chapter 7: Conclusions and Future Directions .....	158
7.1: Conclusions.....	158
7.1.1: CuIn <sub>1-x</sub> Ga <sub>x</sub> Se <sub>2</sub> nanocrystal Synthesis.....	159
7.1.2: CuInSe <sub>2</sub> <sup>31</sup> P Nuclear Magnetic Resonance .....	159
7.1.3: Perovskite Nanocrystals.....	160

7.1.4: Thermal stability of Perovskite nanocrystals.....	160
7.1.5: High Energy Carrier Dynamics of CsPbI <sub>3</sub> Perovskite Nanocrystals.....	161
7.2: Future Directions .....	162
7.2.1: Understanding the CuIn <sub>1-x</sub> Ga <sub>x</sub> Se <sub>2</sub> Nanocrystals Surface Chemistry	162
7.2.2: Lead – Free Perovskite Nanocrystals .....	163
7.2.2: Flexible Perovskite Nanocrystal Photovoltaic Devices.....	166
7.3: References.....	166
<b>APPENDIX (OR APPENDICES).....</b>	<b>170</b>
Appendix A.....	170
A.1 Supporting Figures.....	170
Appendix B .....	174
B.1: Supporting Data .....	174
Appendix C.....	181
C.1: Supporting Data .....	181
References.....	188
Vita.....	206

## List of Tables

Table 3.1: Chemical shifts observed in $^{31}\text{P}$ NMR and the corresponding chemical species. ....	63
Table C1: Absorption cross section, $\sigma$ , with respect to pump wavelength for each nanocrystal dispersion. $\sigma$ was determined by fitting the data with a Poisson distribution (Chapter 6, eq 1), where QY is the carrier multiplication quantum yield and $\sigma_x$ is the absorption cross section at the respective pump wavelength ( $X = 400 \text{ nm}, 310 \text{ nm}, 290 \text{ nm}, \text{ or } 245 \text{ nm}$ ). 187	187
Table C2: Carrier multiplication efficiency with respect to pump wavelength for each nanocrystal dispersion. CM efficiency was determined by dividing the higher energy pump QYs with the QY at 400 nm, subtract 1 from that value and multiply by 100 for each dispersion. ....	187

## List of Figures

Figure 1.1: An illustration of the typical solar cell construction. ....	3
Figure 1.2: Diagram of the photovoltaic effect. When a photon of light is absorbed by the semiconducting absorbing layer of the solar panel, an electron is excited from the valence band to the conduction band leaving a hole behind. <sup>20</sup> .....	3
Figure 1.3: P-n junction energy level schematic. Upon absorption of a photon, an electron – is excited from the valence band to the conduction band leaving behind a hole +. Due to the electric field the electrons and holes are shuttled away from each other. <sup>23</sup> .....	5
Figure 1.4: A diagram of the Shockley-Queisser limit. Based off of theoretical calculations a single junction material with a band gap of 1.4 could have an efficiency of 34%. Adapted from reference [36] <sup>36</sup> , copyright 1961 American Institute of Physics. ....	6
Figure 1.5: An illustration of the carrier multiplication (CM) process. Photons with energy greater than or equal to twice the band gap is absorbed and creates a hot electron and hole (in red). As the electron relaxes to the bottom of the conduction band, the energy lost is used to excite a new exciton pair. The second exciton pair is short lived and recombines with the hole via auger recombination. ....	7
Figure 1.6: CO <sub>2</sub> emissions from photovoltaic devices life cycle. Negative values are attributed to the recycling of material for future production. Adapted from reference [46] <sup>46</sup> , Copyright 2013 Elsevier Ltd.....	10
Figure 1.7: manufacturing process for silicon based photovoltaic devices. Adapted from reference [47] <sup>47</sup> , copyright 2012 Elsevier Ltd.....	11

Figure 1.8: Best research-Cell Efficiencies over the past 40 years. Reprint from reference<sup>86</sup> .....14

Figure 2.1: TEM images of CIGS nanocrystals synthesized via one pot (A&D) and hot injection (B, C, E, & F) methods. A) One pot synthetic method of CIGS where X= 0.70. B) Metals (Cuacac, Inacac<sub>3</sub>, and Gaacac<sub>3</sub>) hot injection synthetic method of CIGS nanocrystals where X = 0.70. C) DPP hot injection synthetic method of CIGS nanocrystals where X = 0.70. D) One pot synthetic method of CIGS where X= 0.70. E) Metals (Cuacac, Inacac<sub>3</sub>, and Gaacac<sub>3</sub>) hot injection synthetic method of CIGS nanocrystals where X = 0.70. F) TOP hot injection synthetic method of CIGS where X = 0.70. ....39

Figure 2.2: XRD spectra of CIGS nanocrystals synthesized using one pot and hot injection techniques (metals and DPP. The peaks are referenced to the CIGS chalcopyrite crystal pattern of PDF#00-035-1102, CuSe PDF#01-071-0044, and In<sub>2</sub>Se<sub>3</sub>PDF#01-071-0447. ....40

Figure 2.3: TEM images of CIS nanocrystals synthesized via one pot (A&F) and hot injection (B, C, D, E) methods. A) One pot synthetic method of CIS. B) Metals (Cu(acac)<sub>2</sub> and In(acac)<sub>3</sub>) hot injection synthetic method of CIS nanocrystals. C) DPP hot injection synthetic method of CIS nanocrystals. D) TBP hot injection synthetic method of CIS. E) TOP hot injection synthetic method of CIS nanocrystals. F) NaBH<sub>4</sub> one pot synthetic method of CIS.....42

Figure 2.4: XRD spectra of CIS nanocrystals synthesized using one pot, NaBH<sub>4</sub>, and hot injection techniques (metals, DPP TBP, and TOP). The peaks are referenced to the CIS cubic crystal pattern of PDF#01-079-1809.....43

Figure 2.5: TEM images of CIS nanocrystals synthesized using the hot injection method, DPP (A, C, E, G, and I) and TBP (B, D, F, H, and J), with different solvents. A) DPP method using octadecanol as a solvent. B) TBP method using octadecanol as a solvent. C) DPP method using octadecylamine as the solvent. D) TBP method using octadecylamine as the solvent. E) DPP method using octadecene as the solvent. F) TBP method using octadecene as the solvent. G) DPP method using 1-dodecanol as the solvent. H) TBP method using 1-dodecanol as the solvent. I) DPP method using dodecanethiol as the solvent. J) TBP method using dodecanethiol as the solvent.....44

Figure 2.6: XRD spectra of CIS nanocrystals synthesized using hot injection techniques of DPP and TBP using other solvents besides oleylamine. The peaks are referenced to the CIS cubic crystal pattern of PDF#01-079-1809. ....45

Figure 2.7: High resolution TEM EDS elemental mapping images of CIS nanocrystals synthesized via the metals hot injection method. Some of the particles demonstrated an even distribution of Cu and In within the nanocrystals. ....46

Figure 2.8: High resolution TEM EDS elemental mapping images of CIS nanocrystals synthesized via the metals hot injection method. Some of the nanoparticles show Cu deficiencies along the edge of the nanocrystals. ....47

Figure 2.9: High resolution TEM EDS elemental mapping images of CIS nanocrystals synthesized via the metals hot injection method. Some of the nanoparticles showed oxygen rich surface which may be due to exposure of ambient conditions or surface treatments of the nanocrystals. ....48

Figure 3.1: General schematic of Methods I, II, and III, shown in A, B, and C respectively. The reactions begin by degassing the reaction flask at 110°C at ~ 150 mTorr for 1 hr. Then under N<sub>2</sub> gas the flask temperature is raised to 240°C. Upon reaching 180°C the Se reactant is injected into the flask. Once the flask has reached the reaction temperature of 240°C, it is held at this temperature for 10 minutes. The reaction flask is cooled by removing the heating mantle. After isolation of CuInSe<sub>2</sub> nanocrystals via centrifugation, the percent yield was determined to be 80%, 5%, and 47% for methods I, II, and III respectively. ....61

Figure 3.2: Room temperature <sup>31</sup>P-NMR spectra of reaction products obtained by combining CuCl, InCl<sub>3</sub> in OLA with DPP=Se and heating to 150°C for various times indicated on the left of each spectra in CDCl<sub>3</sub>. (A) Method I reaction (using 1 mL of a 1M DPP=Se solution (1 mmol Se and 5.75 mmol DPP) DPP=Se/(Cu + In) of 1:1) upon addition of the metal precursors DPP=Se peak vanishes and tetraphenylbiphosphine (TPBP) peak appears. (B) Method I with an increase in the DPP=Se/(Cu + In) molar ratio of 5.75:1 the binding of the metals to the DPP=Se (δ = 7ppm) produces an observable peak at δ = 22ppm (red box) and tetraphenylbiphosphine (TPBP) peak reappears (green box) as in A. There is no change in the spectra after 40 min. ....64

Figure 3.3: Room temperature  $^{31}\text{P}$ -NMR spectra of reaction products obtained by combining  $\text{CuCl}$ ,  $\text{InCl}_3$  in OLA with TBP=Se and heating to  $150^\circ\text{C}$  for various times indicated on the left of each spectra in  $\text{CDCl}_3$ . (A) Method II reaction (using 1 mL of a 1M TBP=Se solution (1 mmol Se and 4.05 mmol TBP) TBP=Se/(Cu + In) of 1:1) The TBP=Se complex remained throughout the 60 minutes. (B) A magnified spectra of Method II with an increase in the TBP=Se/(Cu + In) molar ratio of 4.05:1 .The TBP=Se complex shows small chemical shifting over the duration of the reaction. The inset shows that there was no excess TBP in the reaction. ....67

Figure 3.4: A Room temperature  $^{31}\text{P}$ -NMR spectra of reaction products obtained by combining  $\text{CuCl}$ ,  $\text{InCl}_3$ , DPP in OLA with TBP=Se and heating to  $150^\circ\text{C}$  for various times indicated on the left of each spectra in  $\text{CDCl}_3$ . (A) Method III reaction (using 1 mL of a 1M TBP=Se solution (1 mmol Se and 4.05 mmol TBP) TBP=Se/(Cu + In) of 1:1). Throughout the duration of the reaction there was no significant increase observed in the TBP peak (-32.5 ppm). The inset shows the emergence of the TPBP peak which is observed in method I. (B) Method III with an increase in the TBP=Se/(Cu + In) molar ratio of 4.05:1. Over the course of the reaction the TPBP peak (-15 ppm) was observed. This observation insinuates a phosphine switch between the tertiary TBP and the secondary DPP. C&D) Magnified  $^{31}\text{P}$ -NMR spectra of B. ....70



Figure 3.5: $^{31}\text{P}$ -NMR spectra in $\text{CDCl}_3$ of DPP=Se with (A) Cu and (B) In precursors bonded to the phosphine chalcogenide. Slight chemical shifting is observed upon the addition of the metal precursor. The additional peak that is observed around $\delta = -40\text{ppm}$ is from DPP-CuCl. It is to note that the peaks are not completely aligned due to environmental differences between the samples. ....	72
Figure 3.6: $^{31}\text{P}$ -NMR spectra in $\text{CDCl}_3$ of TBP=Se with (A) Cu and (B) In precursors bonded to the phosphine chalcogenide molecule. Slight chemical shifting is observed, but no additional peaks are observed upon the metal addition. ....	73
Figure 3.7: TGA data for DPP=Se (A, C, and E) and TBP=Se (B, D, and F) copper precursor heating experiments. (A ) DPP=Se and CuCl (B) TBP=Se and CuCl (C) DPP and CuCl (D) TBP and CuCl (E) DPP=Se and Cu:OLA (F) TBP=Se and Cu:OLA. The black curve reflects TBP=Se and the red curve DPP=Se for each spectrum respectively. ....	75
Figure 3.8. Current-voltage curves for $\text{CuInSe}_2$ nanocrystal photovoltaic devices employing (A) $\text{CuInSe}_2$ nanocrystals from Method II (B) $\text{CuInSe}_2$ nanocrystals from Method I (C) $\text{CuInSe}_2$ nanocrystals from Method III. The above current-voltage curves are shown with illumination $100\text{ mW/cm}^2$ , AM 1.5. ....	77

Figure 3.9: (**scheme 1**) Proposed mechanism for CuInSe<sub>2</sub> nanocrystal formation using Method I (A) and Method II (B). (I) shows the formation of the phosphine chalcogenide molecule. (II) Depicts the injection of the phosphine chalcogenide molecule into OLA. (III) The formation of the intermediate complex. (IV) Bond cleavage between the phosphine and Se to form CuInSe<sub>2</sub> nanocrystals. ....80

Figure 3.10: (**scheme 2**) Break down on step (IV) in figure 3.9 for Method I (A) and Method II (B). (A) I. A nucleophilic attack on the phosphorous atom with excess DPP on the intermediate complex yielding CuInSe<sub>2</sub> nanocrystals and tetraphenylbiphosphine TPBP (seen in Figure 3.2) II. Nucleophilic attack OLA on the intermediate complex yielding CuInSe<sub>2</sub> nanocrystals and DPP-OLA. (B) Nucleophilic attack on the intermediate complex with 2 OLA molecules yielding in CuInSe<sub>2</sub> and TBP as products. However, the production of TBP isn't shown in Figure 3.3 insinuating that the excess TBP are in low concentrations.....81

Figure 4.1: Perovskite crystal structure where the purple circles denotes the A sites, gray sphere denotes the B sites, and the green spheres denotes the X sites. Adapted from reference (7), copyrighted 2013 Elsevier B.V.....91

Figure 4.2.: TEM, high resolution TEM, and SEM images of CsPbBr<sub>3</sub>, CsPbI<sub>3</sub> synthesized with oleic acid (OA), and CsPbI<sub>3</sub> synthesized with diisooctylphosphinic acid (DOPA). (A) CsPbBr<sub>3</sub> nanocrystals with an average side length of (B) CsPbI<sub>3</sub> nanocrystals, synthesized with OA, with an average side length of  $8.6 \pm 1.5$  nm (OA). (C) CsPbI<sub>3</sub> nanocrystals, synthesized with DOPA, with an average side length of  $17.5 \pm 2.8$  nm (PA). (D-F) High resolution TEM images of CB, OA, and PA nanocrystals respectively. (G-I) SEM images of order arrays of CB, OA, and PA nanocrystals respectively.....98

Figure 4.3: CsPbI<sub>3</sub> and CsPbBr<sub>3</sub> nanocrystals absorbance spectra (A) and PL spectra (B). The inset illustrates the magnified absorbance spectra between 600 nm and 800 nm. Room temperature absorbance and PL spectra of CsPbBr<sub>3</sub> and CsPbI<sub>3</sub> nanocrystals dispersed in hexane. OA (black curve), PAB (red curve), and CB (blue curve). The samples were observed using a 400 nm excitation wavelength. ....99

Figure 4.4: CsPbI<sub>3</sub> nanocrystals absorbance and PL spectra for varying concentration of Cs-oleate (A-B), 0.019M (red line), 0.029M (blue line), 0.059M (black line), and 0.1M (green line). CsPbBr<sub>3</sub> nanocrystals absorbance and PL spectra for varying concentration of Cs-oleate (C-D). The spectra were collected from nanocrystal dispersion in anhydrous hexane at room temperature. The samples were observed using a 400 nm excitation wavelength. ....100

Figure 4.5: Room temperature solution based time-resolved PL of CsPbBr <sub>3</sub> and CsPbI <sub>3</sub> nanocrystals using a 402 nm laser. The spectra was fitted to a 2-exponential fitting (red curve). t denotes the average decay time ( $\tau$ ). (A) CsPbI <sub>3</sub> nanocrystals synthesized with DOPA (PA). (B) CsPbI <sub>3</sub> nanocrystals synthesized with oleic acid (OA). (C) CsPbBr <sub>3</sub> nanocrystals (CB).....	101
Figure 4.6: Room temperature XRD spectra of CsPbBr <sub>3</sub> nanocrystals. The reference pattern $\alpha$ -Cubic (PDF#01-076-8588) and $\gamma$ -orthorhombic (PDF) .....	102
Figure 4.7: Room temperature XRD spectra of CsPbI <sub>3</sub> nanocrystals, OA (black curve) and PA (red curve).The reference pattern $\alpha$ -Cubic (PDF#01-076-8588) and $\gamma$ -orthorhombic (black orthorhombic crystal structure) (Henry Snaith's paper) .....	103
Figure 4.8.: TEM images of (A) CsFAPbI <sub>3</sub> nanocrystals (B) FAPbI <sub>3</sub> nanocrystals. (C) CsFAMAPbI <sub>3</sub> nanocrystals (D) CsFAMAPb(BrI) <sub>3</sub> .....	105
Figure 4.9: Room Temperature absorbance spectra (A) and PL spectra (B). The inset illustrates the magnified absorbance spectra between 650 nm and 800 nm. FAPbI <sub>3</sub> (black line), CsFAPbI <sub>3</sub> (red line), CsFAMAPbI <sub>3</sub> (blue line), and CsFAMAPb(BrI) <sub>3</sub> (green line) were dispersed in anhydrous hexane and excited using a 450 nm wavelength. ....	106
Figure 4.10: Room temperature XRD spectra of FAPbI <sub>3</sub> , CSMAFAPbI <sub>3</sub> , and CsFAPbI <sub>3</sub> nanocrystals. The black pattern is the FAPbI <sub>3</sub> simulation for the cubic (a = 6.3641 Å) crystal structure. The CsFAPbI <sub>3</sub> .....	107

Figure 5.1: CsPbI<sub>3</sub> nanocrystals TEM images (A and B) along with ordered assemblies SEM images (C and D). (A) CsPbI<sub>3</sub> nanocrystals synthesized with oleic acid (OA) with an average side length of  $8.6 \pm 1.5$  nm. (B) CsPbI<sub>3</sub> nanocrystals synthesized with diisooctylphosphinic acid (PA) with an average side length of  $17.5 \pm 2.8$  nm. (C) Ordered assemblies of CsPbI<sub>3</sub> OA nanocrystals slow evaporated on Si wafer. (D) Ordered assemblies of CsPbI<sub>3</sub> PA nanocrystals evaporated on Si wafers. ....120

Figure 5.2: GISAXS (A and B) and GIWAXS (C and D) of order assemblies of CsPbI<sub>3</sub> nanocrystals. (A) GISAXS pattern of CsPbI<sub>3</sub> OA nanocrystals with a simple cubic structure  $a_{SL} = 12$  nm with the (001)<sub>SL</sub> planes parallel to the Si substrates. (B) GISAXS pattern of CsPbI<sub>3</sub> PA nanocrystals. (C) GIWAXS pattern of CsPbI<sub>3</sub> OA nanocrystals exhibiting  $\gamma$ -orthorhombic crystal structure with the (002)<sub>NC</sub> planes parallel to the Si substrate. The circle, triangle, pentagon, and four point star represents the  $[-130]_{BD}$ ,  $[-110]_{BD}$ ,  $[100]_{BD}$ , and  $[-120]_{BD}$  beam directions. (D) GIWAXS pattern of CsPbI<sub>3</sub> PA nanocrystals displaying  $\gamma$ -orthorhombic crystal structure with the (002)<sub>NC</sub> and (110)<sub>NC</sub> orientations parallel to the Si substrates. The heart, pentagon, four-point star, circle, and star represents the  $[-110]_{BD}$ ,  $[-111]_{BD}$ ,  $[-221]_{BD}$ ,  $[-33-1]_{BD}$ ,  $[-22-3]_{BD}$  beam directions for the (110)<sub>NC</sub> orientation parallel to the Si substrate. The triangle represents the  $[-210]_{BD}$  beam direction from the (002)<sub>NC</sub> parallel orientation. ....122

Figure 5.3: GIWAXS patterns of CsPbI<sub>3</sub> OA nanocrystals exhibiting  $\gamma$ -orthorhombic crystal structure with the (002)<sub>NC</sub> planes parallel to the Si substrate heated from room temperature (RT) to 300°C. The circle, triangle, pentagon, and four point star represents the [-130]<sub>BD</sub>, [-110]<sub>BD</sub>, [100]<sub>BD</sub>, and [-120]<sub>BD</sub> beam directions. (A) RT, (B) 50°C (C) 100°C (D) 150°C (E) 200°C and (F) 300°C .....124

Figure 5.4: GISAXS patterns of CsPbI<sub>3</sub> OA nanocrystals with a simple cubic structure  $a_{SL} = 12$  nm with the (001)<sub>SL</sub> parallel orientation heated from room temperature (RT) to 300°C. (A) RT, (B) 50°C (C) 100°C (D) 150°C (E) 200°C and (F) 300°C .....125

Figure 5.5: GIWAXS patterns of CsPbI<sub>3</sub> PA nanocrystals exhibiting  $\gamma$ -orthorhombic crystal structure with the (110)<sub>NC</sub> and the (002)<sub>NC</sub> planes parallel to the Si substrate heated from room temperature (RT) to 300°C. The heart, pentagon, four-point star, circle, and star represents the [-110]<sub>BD</sub>, [-111]<sub>BD</sub>, [-221]<sub>BD</sub>, [-33-1]<sub>BD</sub>, [-22-3]<sub>BD</sub> beam directions for the (110)<sub>NC</sub> orientation and the triangle represents the [-210]<sub>BD</sub> beam direction from the (002)<sub>NC</sub> orientation. (A) RT, (B) 50°C (C) 100°C (D) 150°C (E) 200°C and (F) 300°C .....127

Figure 5.6: GISAXS patterns of CsPbI<sub>3</sub> PA nanocrystals with weak ordering heated from room temperature (RT) to 300°C. (A) RT, (B) 50°C (C) 100°C (D) 150°C (E) 200°C and (F) 300°C .....128

Figure 6.1: CsPbI<sub>3</sub> nanocrystals size histograms and TEM images (A-C) along with high resolution TEM images (D-E) and XRD spectra (E). (A) CsPbI<sub>3</sub> nanocrystals, synthesized with OA, with an average side length of  $8.6 \pm 1.5$  nm (OA). (B) CsPbI<sub>3</sub> nanocrystals, synthesized with DOPA, with an average side length of  $17.5 \pm 2.8$  nm (PAB). (C) CsPbI<sub>3</sub> nanocrystals, synthesized with DOPA, with an average side length of  $10.5 \pm 2.6$  nm (PAQ). (D-E) high resolution images of OA and PAB nanocrystals respectively. (F) Room temperature XRD spectra of CsPbI<sub>3</sub> nanocrystals, OA (black curve), PAB (red curve), and PAQ (blue curve). The reference pattern  $\alpha$ -Cubic (PDF#01-076-8588) and  $\gamma$ -orthorhombic (reference 31) .....140

Figure 6.2: CsPbI<sub>3</sub> nanocrystals absorbance spectra (A) and PL spectra (B). The inset illustrates the magnified absorbance spectra between 600 nm and 800 nm. Room temperature absorbance and PL spectra of CsPbI<sub>3</sub> nanocrystals dispersed in hexane. OA (black curve), PAB (red curve), and PAQ (blue curve). The samples were observed using a 400 nm excitation wavelength. The samples exhibited PL quantum yields of 30%, 7%, and 20% respectively. ....141

Figure 6.3: Delay time dependent transient absorption spectra of (A) OA ( $\langle N \rangle = 0.12$ ) nanocrystals (B) PAQ ( $\langle N \rangle = 0.11$ ) nanocrystals (C) PAB ( $\langle N \rangle = 0.40$ ) nanocrystals measured using a pump wavelength of 400 nm. ....143

Figure 6.4: Fluent dependent transient absorption kinetics of (A) OA nanocrystals (B) PAB nanocrystals (c) PAQ nanocrystals measured using a pump wavelength of 400 nm. All kinetics are observed at the absorption bleach peak 656 nm, 682 nm, and 658 nm. All spectra are normalized to 1 at long delay times (~ 2 ns), where only single excitons are present. ....145

Figure 6.5: Biexciton Auger lifetime spectra at a pump wavelength of 400 nm (A) OA nanocrystals (from figure 4  $\langle N \rangle = 0.24 - \langle N \rangle = 0.04$ ), (B) PAB nanocrystals (from figure 4  $\langle N \rangle = 0.79 - \langle N \rangle = 0.13$ ), and (C) PAQ nanocrystals (from figure 4  $\langle N \rangle = 0.21 - \langle N \rangle = 0.03$ ). The low fluence TA kinetics were subtracted from the high fluence TA kinetics. The kinetics are fitted to a single exponential decay (red lines). ....147

Figure 6.6: Rpop spectra, ratio of short and long time TA signals as a function of pump fluence (A) OA nanocrystals, (B) PAQ nanocrystals, and (C) PAB nanocrystals at 400 nm (black squares), 310 nm (red circles), 290 nm (blue triangles), and 245 nm (green upside down triangles) pump wavelengths. All data is fitted with a Poisson distribution (eq 1), where QY is the carrier multiplication quantum yield and  $\sigma_x$  is the absorption cross section at the respective pump wavelength ( $X = 400$  nm, 310 nm, 290 nm, or 245 nm). ....149

Figure 6.7: UV-vis absorbance spectra of the three capping ligands, OA (black squares), OLA (red circles), and DOPA (blue triangles), used in the CsPbI<sub>3</sub> nanocrystal synthesis. The vertical lines correspond to the pump wavelengths (400 nm, 310 nm, 290 nm, and 245 nm) used for TAS measurements.....151

Figure 7.1: SEM images of bulk CsGeI<sub>3</sub> crystals. ....164



Figure 7.2: X-ray diffraction pattern for CsGeI <sub>3</sub> bulk crystals. The bulk crystals show a rhombohedral crystal structure. The peaks labeled $\square$ denotes the CsI peaks. ....	164
Figure 7.3: SEM (A) and TEM (B) images of CsGeI <sub>3</sub> crystals after attempting to passivate with organic ligands. The cubic crystals shown in A were white and indicative of CsI. ....	165
Figure 7.4: High resolution TEM EDS image of CsGeI <sub>3</sub> crystals after attempts of passivation with organic ligands. The crystals are mainly composed of Cs and I. ....	165
Figure 7.5: This is a typical setup for the perovskite CsPbI <sub>3</sub> nanocrystal photovoltaic devices. Photons are shone through the glass and are absorbed by the CsPbI <sub>3</sub> layer to make exciton pairs. ....	166
Figure A.1: A&D show TEM Images of the nanocrystal product after washing for the TBP and DPP respectively. B&E illustrates the size distributions between the two syntheses. C shows the XRD patterns for the TBP & DPP systems. Both systems exhibit the chalcopyrite crystal structure (PDF# 01-079-1809). ....	170
Figure A.2: Shows the secondary phosphines in Method II. The red spectra is TBP as received, the green spectra is TBP=Se, and the blue is 0 min. ....	171
Figure A.3: DPP and OLA <sup>31</sup> P NMR study .....	171
Figure A.4: TBP and OLA <sup>31</sup> P NMR study .....	172
Figure A.5: DPP Selenium precursor study using <sup>1</sup> H NMR.....	172
Figure A.6: TBP selenium complex and OLA study via <sup>1</sup> H NMR.....	173

Figure B.1: A and B are SEM images of ordered assemblies of CsPbI<sub>3</sub> nanocrystals, synthesized with diisooctylphosphinic acid (PA) with an average side length of  $17.5 \pm 2.8$  nm, evaporated on a Si wafer. ....174

Figure B.2: A and B are SEM images of ordered assemblies of CsPbI<sub>3</sub> nanocrystals, synthesized with diisooctylphosphinic acid (PA) with an average side length of  $17.5 \pm 2.8$  nm, evaporated on a Si wafer. The nanocrystal concentration was increased 10x the original amount. The scale bar is 100 nm in length .....175

Figure B.3: After heating experiments GIWAXS images of (A) OA nanocrystals and (B) PA nanocrystals dispersed in anhydrous hexane and dried on a Si wafer. ....176

Figure B.4: GISAXS patterns of CsPbI<sub>3</sub> OA nanocrystals with weak ordering heated from room temperature (RT) to 300°C. (A) RT, (B) 50°C (C) 100°C (D) 150°C (E) 200°C and (F) 300°C Nanocrystals were dispersed in anhydrous chloroform before drying onto a Si wafer. ....177

Figure B.5: GIWAXS patterns of CsPbI<sub>3</sub> OA nanocrystals exhibiting  $\gamma$ -orthorhombic crystal structure with the (110)<sub>NC</sub> and the (002)<sub>NC</sub> planes parallel to the Si substrate heated from room temperature (RT) to 300°C. The heart, pentagon, four-point star, circle, and star represents the [-110]<sub>BD</sub>, [-111]<sub>BD</sub>, [-221]<sub>BD</sub>, [-33-1]<sub>BD</sub>, [-22-3]<sub>BD</sub> beam directions for the (110)<sub>NC</sub> orientation and the triangle represents the [-210]<sub>BD</sub> beam direction from the (002)<sub>NC</sub> orientation. (A) RT, (B) 50°C (C) 100°C (D) 150°C (E) 200°C and (F) 300°C Nanocrystals were dispersed in anhydrous chloroform before drying onto a Si wafer. ....178

Figure B.6: GISAXS patterns of CsPbI<sub>3</sub> PA nanocrystals with weak ordering heated from room temperature (RT) to 300°C. (A) RT, (B) 50°C (C) 100°C (D) 150°C (E) 200°C and (F) 300°C Nanocrystals were dispersed in anhydrous chloroform before drying onto a Si wafer. ....179

Figure B.7: GIWAXS patterns of CsPbI<sub>3</sub> PA nanocrystals exhibiting  $\gamma$ -orthorhombic crystal structure with the (110)<sub>NC</sub> and the (002)<sub>NC</sub> planes parallel to the Si substrate heated from room temperature (RT) to 300°C. The heart, pentagon, four-point star, circle, and star represents the [-110]<sub>BD</sub>, [-111]<sub>BD</sub>, [-221]<sub>BD</sub>, [-33-1]<sub>BD</sub>, [-22-3]<sub>BD</sub> beam directions for the (110)<sub>NC</sub> orientation and the triangle represents the [-210]<sub>BD</sub> beam direction from the (002)<sub>NC</sub> orientation. (A) RT, (B) 50°C (C) 100°C (D) 150°C (E) 200°C and (F) 300°C Nanocrystals were dispersed in anhydrous chloroform before drying onto a Si wafer. ....180

Figure C1: Histograms for CsPbI<sub>3</sub> nanocrystal dispersions for (A) OA, (B) PAQ, (C) PAB respectively. ....181

Figure C2: Fluent dependent transient absorption kinetics of (A) OA nanocrystals (B) PAQ nanocrystals (c) PAB nanocrystals measured using a pump wavelength of 310 nm. All kinetics are observed at the absorption bleach peak 656 nm, 658 nm, and 682 nm respectively. All spectra are normalized to 1 at long delay times (~ 2 ns), where only single excitons are present. The green spectra denotes the single-exciton curve found in figure 6.4. ....182

Figure C3: Fluent dependent transient absorption kinetics of (A) OA nanocrystals (B) PAQ nanocrystals (c) PAB nanocrystals measured using a pump wavelength of 290 nm. All kinetics are observed at the absorption bleach peak 656 nm, 658 nm, and 682 nm respectively. All spectra are normalized to 1 at long delay times (~ 2 ns), where only single excitons are present. The green spectra denotes the single-exciton curve found in figure 6.4. ....183

Figure C4: Fluent dependent transient absorption kinetics of (A) OA nanocrystals (B) PAQ nanocrystals (c) PAB nanocrystals measured using a pump wavelength of 245 nm. All kinetics are observed at the absorption bleach peak 656 nm, 658 nm, and 682 nm respectively. All spectra are normalized to 1 at long delay times (~ 2 ns), where only single excitons are present. The green spectra denotes the single-exciton curve found in figure 6.4. ....184

Figure C5: Auger lifetimes plotted with respect to nanocrystal volumes at a pump wavelength of 400 nm. The error bars corresponds to the standard deviations from the nanocrystal sizes and auger lifetimes for each sample. ....185

Figure C6: Transient absorption spectra of (A) OA nanocrystals (B) PAQ nanocrystals (C) PAB nanocrystals with varying  $\langle N \rangle$ , measured using a pump wavelength of 400 nm at a delay time of 2.5 ps .....186

# Chapter 1: Introduction

## 1.1: INTRODUCTION TO RENEWABLE ENERGY

15 TW of energy is consumed by the world yearly and of that 85 percent is produced from non-renewable resources such as coal and oil.<sup>1</sup> The future sources of energy will rely less on fossil fuels and more on renewable resources.<sup>2</sup> There are several renewable resources such as hydroelectric, wind, geothermal, biopower and solar.<sup>3,4,5,6</sup> Radiating 127,000 TW of energy to the earth yearly<sup>6-8</sup>, the inexhaustible energy from the sun has the ability to mitigate the use of non-renewable resources and potentially supply the world's energy need. There are two classifications of solar technologies capable of capturing the energy by utilizing passive solar and active solar technologies<sup>7,9</sup>. Passive solar technologies are those who captured the thermal and light energies without converting it into any other form of energy, to include direct, isolated, and indirect solar gain; such as solar energy collection and storage. Conversely, active solar technologies capture solar energy and convert it to heat and electric power via electrical and mechanical apparatuses. For the purpose of this dissertation, we will focus on the active solar technology of the solar cell.

Through solar cells also known as photovoltaic (PV) devices, we have the ability to capture this energy and convert it into electricity which grants economic, social, and environmental benefits. Even though the cost of solar panels have been significantly reduced over the years, the majority of the cost still comes from manufacturing and installing the panels<sup>10-14</sup>. By significantly reducing the panels cost, more photovoltaic

devices will be able to be employed in society. In this chapter, we will explore the device physics, types of solar cells, and the materials that we discuss in future chapters.

## **1.2 PHOTOVOLTAIC FUNDAMENTALS**

Solar panels convert sun light into electricity, however, there are scientific phenomenon that allow this to occur. In this section, the fundamental processes of these devices will be introduced.

During the 19<sup>th</sup> century, the photovoltaic effect was founded by the French scientist Alexandre-Edmond Becquerel<sup>15,16</sup>. The photovoltaic effect allows for the production of voltage or electric current in materials when exposed to light giving rise to the alternative name of the solar panel, photovoltaic devices. Using Becquerel's findings, scientists and engineers have created the solar cell also known as the photovoltaic (PV) device. The sun emits sunlight or light known to researchers as photons. These photons carry various wavelengths of electromagnetic radiation with the majority of the photons possessing wavelengths in the visible region (390 nm- 700 nm corresponding to energies of 1.8eV to 3.2eV) of the solar spectrum.<sup>17,18</sup> This brings us to the most important criteria for a PV device, the ability to absorb photons.

Typically, PV devices are composed of many layers as shown in figure 1.1. The absorber layer has the task of absorbing photons from the sun. Typically, this layer is composed of one or more semiconductor(s). Using the PV effect (Figure 1.2), photons greater than or equal to the band gap (the distance between the valance and conduction bands) are absorbed. This absorption promotes the formation of an exciton, an electron

from the valence band is excited to the conduction band leaving behind an electron hole also known as a hole (a positive charge); thus generating majority and minority carriers<sup>18,19</sup>. The generation of carriers provides the means for the photovoltaic devices to produce electricity. Given the photon energies shone on the earth, semiconductor materials with band gap energies less than 3.2eV will be the most ideal to serve as the absorber layer.

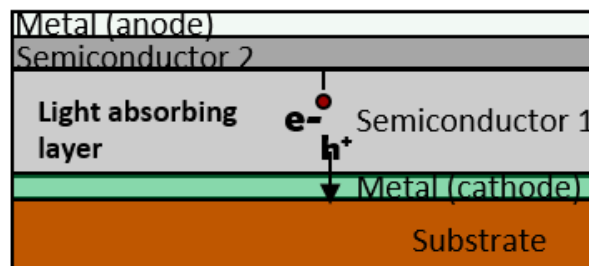


Figure 1.1: An illustration of the typical solar cell construction.

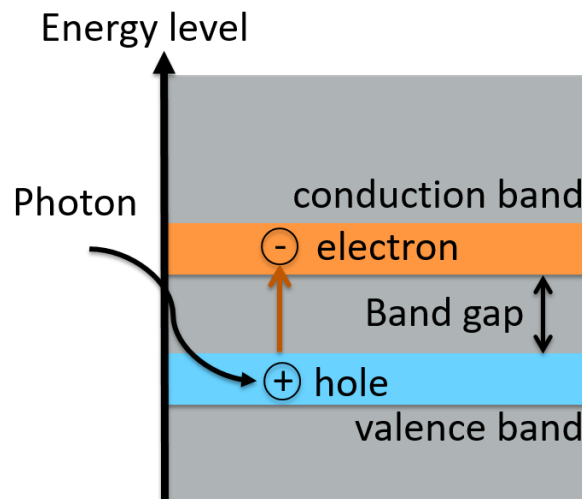


Figure 1.2: Diagram of the photovoltaic effect. When a photon of light is absorbed by the semiconducting absorbing layer of the solar panel, an electron is excited from the valence band to the conduction band leaving a hole behind.<sup>20</sup>

### **1.2.2: P-N junction**

Upon the photon(s) absorption, excitons are formed. However, the separation between the electron and hole is only short lived before they recombine a process called recombination<sup>21,22</sup>. Recombination occurs when an electron stabilizes in the valence band. In other words, the electron releases energy in the form of a photon and drops down from the conduction band to the valence band where it recombines with a hole. The recombination of the electron and hole will produce no current and will cause the photovoltaic devices to perform poorly.<sup>18</sup>

In order to avert recombination, p-n junctions (Figure 1.3) are used to collect the carriers<sup>18,21</sup>. When a n-type semiconductor material and a p-type semiconductor material are joined together, a p-n junction is formed. When these two layers come into contact with one another, a depletion region is formed at the junction. In the depletion region, free electrons and holes will attract each other and recombine. The recombination of the free electrons and holes will form an electric field that forces the carriers to separate and produce a photocurrent. This separation prevents the recombination of the electron and hole at the depletion region. Furthermore, when a photon with energy greater than or equal to the band gap is absorbed by either or both semiconductor materials creating an exciton, the electric field aids in the separation of the electron and hole creating a flow of current. PV devices are comprised of two electrical contacts (one on the p-type side and the other on the n-type) that enclose the semiconductor absorbing layer(s) and are there to collect the electrons or holes. In order to allow the semiconducting layer(s) to absorb



photons, one of the electrical contacts must be transparent. As a result, conducting oxides are used such as zinc oxide (ZnO) and indium tin oxide (ITO).

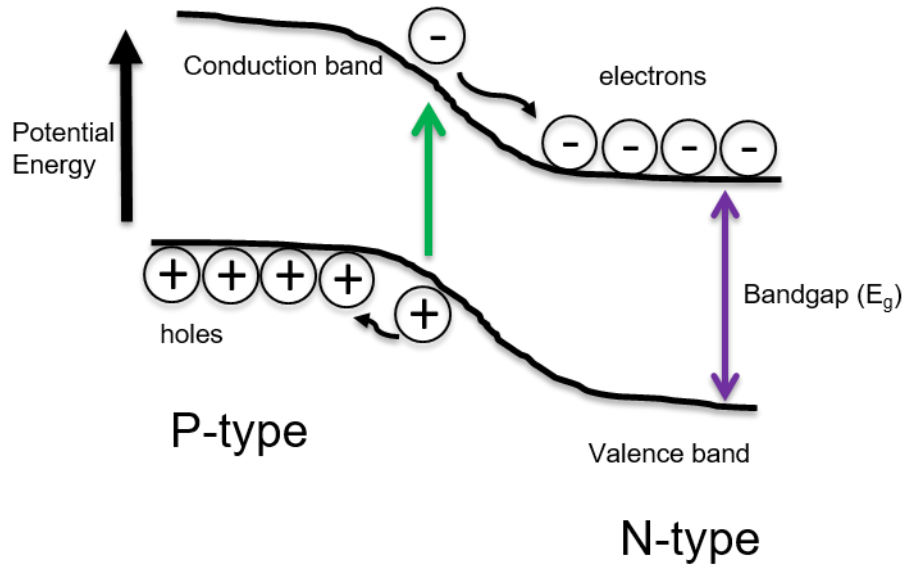


Figure 1.3: P-n junction energy level schematic. Upon absorption of a photon, an electron  $\ominus$  is excited from the valence band to the conduction band leaving behind a hole  $\oplus$ . Due to the electric field the electrons and holes are shuttled away from each other.<sup>23</sup>

### 1.2.3: Multiexciton Generation

When choosing a semiconducting material to act as the absorbing layer, we must consider the band gap of the material and how it relates to the Shockley-Queisser limit. The Shockley-Queisser limit<sup>24</sup> (Figure 1.4) refers to a single p-n junction maximum theoretical efficiency based on theoretical calculations. According to the calculations, the highest efficiency obtainable is about 34% employing the use of a material with a band gap of about 1.4 eV. The efficiency cap at 34% is due to the fact that photons with energy less than the band gap cannot be absorbed by the semiconducting layer and photons with

energies greater than the band gap, release the excess energy as heat. Moreover, when these high energy photons are absorbed they create hot carriers (electrons and holes) which are short lived and quickly recombine in the valance band. This process is known as the thermalization<sup>25-27</sup>.

There are several ways to surpass the Shockley-Queisser limit. One method is to construct multijunction solar cells, which have multiple absorbing layers with a range of band gaps which allows for a wider range of photon absorption<sup>28-31</sup>. Another method is through multiexciton generation (MEG) also known as carrier multiplication (CM)<sup>32-35</sup>, shown in Figure 1.5. Through this method, photons with energies at least twice the band gap have the ability to create more than one exciton pair. Through MEG, the theoretical limit of percent conversion can be increased to 43%.

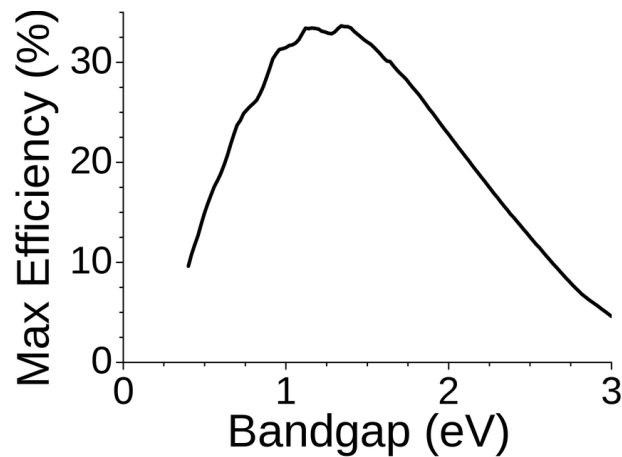


Figure 1.4: A diagram of the Shockley-Queisser limit. Based off of theoretical calculations a single junction material with a band gap of 1.4 could have an efficiency of 34%. Adapted from reference [36]<sup>36</sup>, copyright 1961 American Institute of Physics.

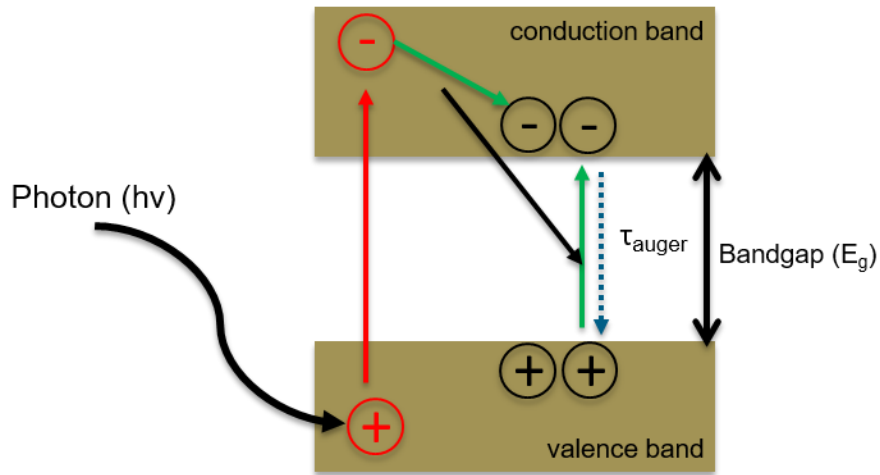


Figure 1.5: An illustration of the carrier multiplication (CM) process. Photons with energy greater than or equal to twice the band gap is absorbed and creates a hot electron and hole (in red). As the electron relaxes to the bottom of the conduction band, the energy lost is used to excite a new exciton pair. The second exciton pair is short lived and recombines with the hole via auger recombination.

#### 1.2.4: Photovoltaic Device Testing

The efficiency of the PV device is a universal parameter used to evaluate the overall performance of the device. The power conversion efficiency, PCE ( $\eta$ ), is measured using an Air Mass 1.5 solar simulator, with 1 sun intensity. The PCE is the ratio of the maximum power outputted by the device and the total power inputted to the device. In the equation below,  $P_{\text{max}}$  is equivalent to the open circuit voltage ( $V_{\text{oc}}$ ) multiplied by the short circuit current ( $J_{\text{sc}}$ ) and the fill factor (FF).  $P_{\text{in}}$  is equal to the power released from the solar simulator where ( $P_{\text{in}} = 100 \text{ mW/cm}^2$ ). The  $V_{\text{oc}}$  is the voltage difference of

electrical potential between two terminals of a device when disconnected from any circuit. The  $J_{sc}$  is the current flowing in the circuit when no opposing voltage is applied. The FF determines the quality of the photovoltaic devices, which typically ranges from 50% to 82% percent, it is the  $P_{max}/(V_{oc} * J_{sc})$ .

$$\eta = \frac{P_{max}}{P_{in}} = \frac{V_{oc} * J_{sc} * FF}{P_{in}}$$

External quantum efficiency (EQE) and internal quantum efficiency (IQE) are also common parameters used to determine the quality of a device. The ratio of the number of carriers collected by the solar cell to the number of photons being radiated on the device at a given energy, also known as the EQE. The IQE is the fraction of absorbed photons that are being converted to carriers in the device, also at a specific wavelength. It is possible for the EQE and IQE to reach values above 100% (due to CM); however, the PCE has limitations depending on the band gap of the material.

### **1.3: TYPES OF SOLAR CELLS**

Several areas of photovoltaic devices are currently being researched, including hybrid, solution processed, and thin film devices, with aims of improving efficiencies and manufacturing techniques.<sup>37,38</sup> For the purpose of this dissertation we will focus solely on single p-n junction PV devices.

#### **1.3.1: Silicon PV Devices**

Both single and multi-crystalline silicon photovoltaics currently dominate the photovoltaic market, making up approximately 90% of the solar market.<sup>39,40,41</sup> The

first solar panels were fabricated by Bell Labs using silicon p-n junctions<sup>42</sup>. Silicon is an abundant raw material, however, silicon photovoltaics are expensive to produce and emit significant amounts of CO<sub>2</sub> into the atmosphere.<sup>43, 44,45</sup> According to Figure 1.6, the fabrication stage of device manufacturing produces the highest CO<sub>2</sub> emission when compared to the other stages. The flow chart shown below (Figure 1.7) demonstrates the manufacturing process for silicon photovoltaics. Not only is this process costly due to the indirect nature of Si's bandgap, which requires thick absorbing layer(s) needed for optimal efficiencies, it is also time consuming and emits significant amounts of CO<sub>2</sub> into the atmosphere. Due to the need for thicker layers, Si solar panels are rigid and bulky. As a result, a new class of photovoltaics was created, known as the second generation.

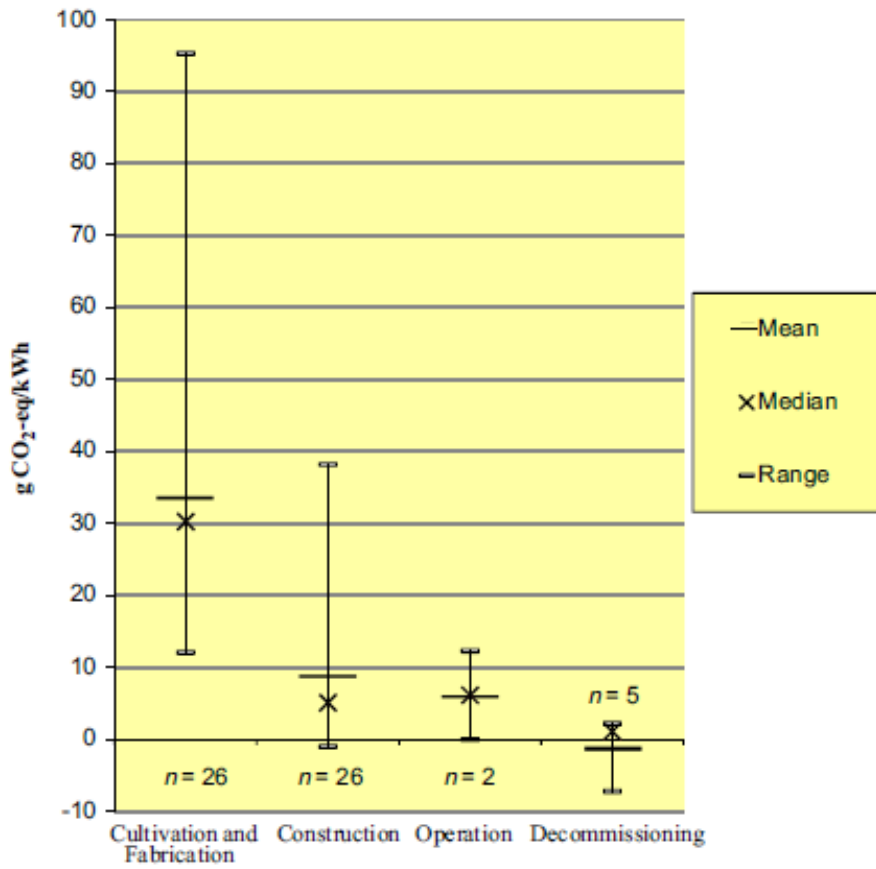


Figure 1.6: CO<sub>2</sub> emissions from photovoltaic devices life cycle. Negative values are attributed to the recycling of material for future production. Adapted from reference [46]<sup>46</sup>, Copyright 2013 Elsevier Ltd.

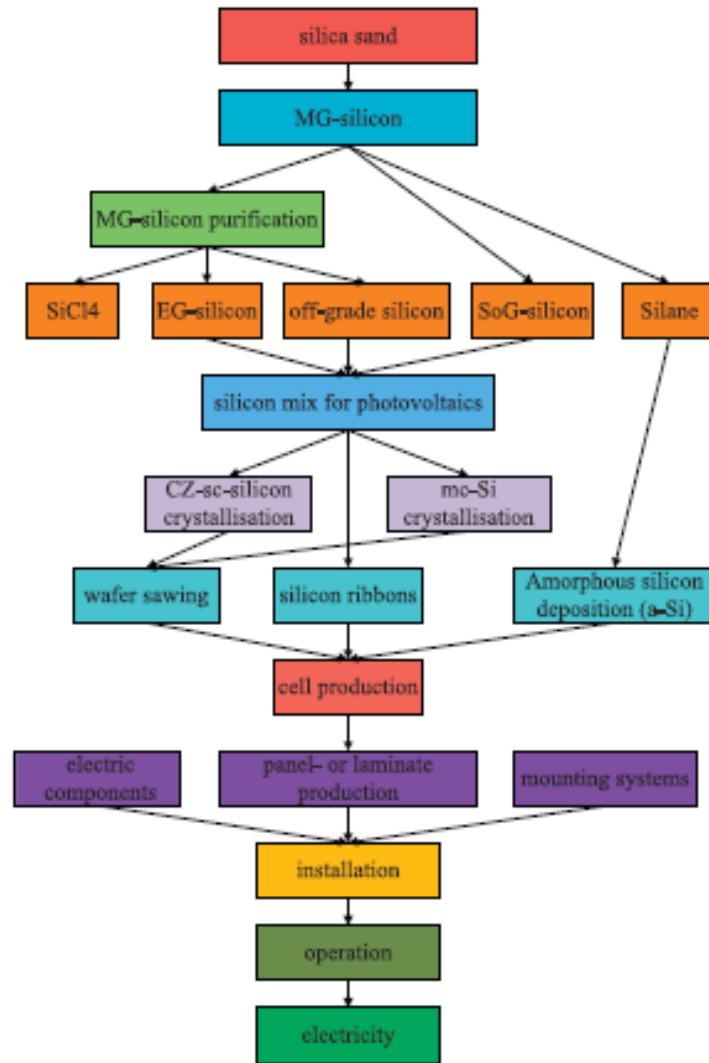


Figure 1.7: manufacturing process for silicon based photovoltaic devices. Adapted from reference [47]<sup>47</sup>, copyright 2012 Elsevier Ltd.

### 1.3.2: Second Generation Solar Cells (Thin Films)

Copper indium gallium diselenide (CIGS), cadmium telluride (CdTe), and amorphous silicon photovoltaic devices are a few modules that were fabricated from this generation.<sup>48-51</sup> Even though, the manufacturing cost of these devices have decreased significantly due to their direct band gaps and thinner absorber layers, their efficiencies

are not comparable to those of silicon. Solar power costs rely not only on the manufacturing and installation costs but also the efficiency. Therefore, the manufacturing of the second generation photovoltaic modules is still costly; due to the use of high temperatures and low vacuums for layer deposition, as well as low efficiencies. Gallium Arsenide, GaAs, thin film devices are an exception<sup>52</sup>. GaAs thin film devices have efficiencies comparable to silicon but require energy intensive fabrication methods, making them expensive to manufacture. As a result, solution based materials that don't require high temperatures, low vacuums, or harsh chemicals are being sought after.<sup>53, 54</sup>

### **1.3.3: Solution Processed Solar Cells**

By reducing the need for low vacuuming and high temperature manufacturing, solution processed solar cells have gained the interest of many researchers. There are several different types of solution processed cells, to include dye sensitized, organic, nanocrystal/quantum dots, and perovskite<sup>53,55-66</sup>. Dye sensitized solar cells are very attractive due to inexpensive materials used during fabrication. However, the liquid electrolyte used for hole transport hinders the ability to fabricate flexible devices. Conversely, organic solar cells have the ability to create flexible cells but the electron accepting fullerene is expensive<sup>55,65</sup>. Both systems suffer from photochemical instability. Over the past several years, perovskite solar cells have gained the interest of researchers due to their defect tolerant nature, ease of manufacturing, and high photon absorption. Currently, these devices show comparable efficiencies to the thin film solar cells at 21%. However, these systems suffer from moisture and performance instability.<sup>67</sup>



Depositing semiconductor materials via nanocrystal or quantum dot inks is a viable option for low-cost PV devices. Nanocrystals have the ability to tune the band gap of the materials, by altering the size via quantum confinement or composition of the nanocrystals. Conventionally, nanocrystals are composed of an inorganic core passivated or capped with organic ligands such as oleylamine. The organic ligands on the nanocrystals allow them to be colloiddally stable in numerous solvents.<sup>53,64,68</sup> These inks can deposit the semiconductor nanocrystals on a variety of substrates, such as plastics<sup>69,70</sup> and bacterial cellulose nanofibers<sup>71</sup>, using several different techniques that include spray coating, spin coating, and doctor blading. In addition, the nanocrystals/quantum dots have the ability to undergo CM as mentioned earlier.

The inorganic nanocrystal inks can be engineered to be air and thermally stable, and have high carrier mobility in the film.<sup>64,68</sup> These inks can be synthesized from a variety of materials; which expands the materials that can be used for PV device fabrication. Currently, several different materials are being studied, such as cadmium telluride (CdTe)<sup>53,72</sup>, lead sulfide (PbS)<sup>63,73,74</sup>, copper indium diselenide (CuInSe<sub>2</sub>)<sup>75-77</sup>, and cesium lead iodide (CsPbI<sub>3</sub>)<sup>78,79</sup> Figure 1.8. Another challenge for these devices is surface chemistry.

Despite all of the advantages described above, there are drawbacks. Nanocrystal surface chemistry is one of the problems with nanocrystal PVs. As mentioned above nanocrystals are capped with organic ligands that protects the nanocrystals from oxidation while allowing the nanocrystal to be colloidal stable in solution. However, the organic ligands hinders charge transport of the electrons.<sup>80-82</sup> Additionally, if the

nanocrystal isn't completely passivated with the protective ligand, surface traps can occur which inhibits extraction of the electrons. By exchanging the long organic ligands for shorter or inorganic ones, researchers have been able to improve device performances. However, achieving complete exchange is challenging and device efficiencies increases were small. Another method is to completely remove the ligands from the surface of the nanocrystals. One method is to heat the deposited nanocrystals under inert conditions at 550°C in a tube furnace (a process called sintering) or the nanocrystalline films are heated using a pulse forge also known as photonic curing.<sup>83,84</sup> Sintering has shown to increase the efficiencies of the solar cells, but defeats the purpose of using low cost materials due to intensive heating steps. The pulse forge uses less energy, but leaves behind a carbon shell impeding electron flow.<sup>85</sup>

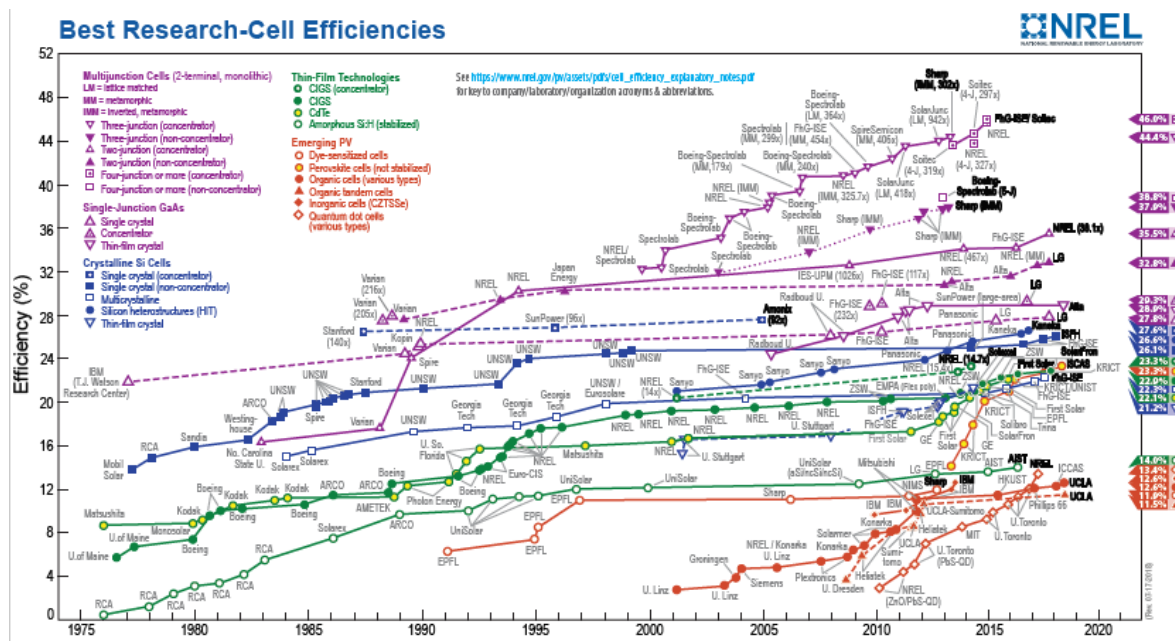


Figure 1.8: Best research-Cell Efficiencies over the past 40 years. Reprint from reference<sup>86</sup>

#### **1.4: NANOCRYSTAL SELF-ASSEMBLIES**

There are several materials that self-assemble into ordered structures, such as, DNA, opals, block copolymer, and nanocrystals. Self-assembly in nanocrystals is also known as superlattices, are order array of nanocrystals with well-defined symmetry and structures.<sup>87,87,88</sup> The formation of superlattices has been shown to increase the conductivity of the films due to interparticle coupling.<sup>89-92</sup> Superlattices have been formed using several different types of nanocrystals such as PbSe, PbS, and CdSe and shapes such as spheres and cubes.<sup>88</sup> There are several ways to form superlattices to include Langmuir Blodgettry (LB) and slow solvent evaporation.<sup>93,94</sup> The LB method is typically used to form controllable monolayers (1 ordered layer). Conversely, the slow solvent evaporation method allows nanocrystals dispersions to slowly evaporate from a vial. Leaving behind an ordered multilayer of nanocrystals. In this dissertation we will focus on the superlattice formation of cubic structures via slow solvent evaporation.

Self-assembled cubic structures has been very popular amongst researchers due to the strong electronic coupling, which have been shown to be three times larger than spheres when oriented face-to-face.<sup>95</sup> Various cubic nanoparticles have been researched for superlattice formation, including PbTe, Fe<sub>x</sub>O<sub>y</sub>, Pt, In<sub>2</sub>O<sub>3</sub>, and PbSe.<sup>88,95</sup> Cubic shaped nanocrystals have been shown to exhibit an array of superstructures; ranging from simple cubic to tetragonal and even rhombohedral structures.

#### **1.5: CuIn<sub>1-x</sub>Ga<sub>x</sub>Se<sub>2</sub> NANOCRYSTAL SOLAR CELLS**

CuIn<sub>1-x</sub>Ga<sub>x</sub>Se<sub>2</sub> is a promising absorber material for photovoltaic devices due to their high absorption coefficient and stability upon long term-term excitation.<sup>96,97</sup> Given the advantages of nanocrystal solution processed photovoltaic devices discussed earlier, it make sense to explore the synthesis of CuIn<sub>1-x</sub>Ga<sub>x</sub>Se<sub>2</sub> nanocrystal materials. There has

been a lot of research on the construction of  $\text{CuIn}_{1-x}\text{Ga}_x\text{Se}_2$  nanocrystal photovoltaic devices. Currently, these devices have reached percent conversion efficiencies of 7.1% when using high temperature processing, which is still well below the efficiency for the thin film materials which are 20.3%.<sup>98,99</sup> These nanocrystals have shown to exhibit CM behavior, but this hasn't helped in the improvement of the photovoltaic devices.<sup>84</sup> As a result, we must understand the surface chemistry and the synthesis of the nanocrystals themselves. In this dissertation, we focus on the synthesis of  $\text{CuIn}_{1-x}\text{Ga}_x\text{Se}_2$  nanocrystals and how the organic ligands effect the formation of  $\text{CuInSe}_2$  nanocrystals for photovoltaic purposes. By gaining a better understanding of the nanocrystals surface chemistry, we can engineer the nanocrystals to transport charge carriers more effectively which will increase photovoltaic performances.

## **1.6: CESIUM LEAD HALIDE NANOCRYSTAL SOLAR CELLS**

Metal lead halide perovskite (MLHP) nanocrystals are also promising materials for photovoltaics due to their tunable band gap, high quantum yields, and tolerance to surface defects<sup>100</sup>. Currently, MLHP nanocrystal devices hold the record performance for nanocrystal PV devices with efficiencies of 13.4%<sup>79</sup>. However, as mentioned above, these materials suffer from air and moisture instability and toxicity issues. One way to alleviate this issue is to exchange the weakly bound ligands to those that are more strongly bound<sup>62,101</sup>. In this dissertation, we focus on how the capping ligands effect the nanocrystal morphology, optical properties, exciton kinetics, thermal stability, and the self-assembly of the nanocrystals. Developing more stable nanocrystals will allow for the versatility of the nanoinks and increased device efficiencies.

## 1.7: CONCLUSIONS AND DISSERTATION OVERVIEW

Photovoltaic devices are a viable solution to reduce the global dependence on non-renewable resources. However, the cost to harvest this energy is still rather expensive. By using nanocrystals, we have the ability to lower the cost of manufacturing while maintaining the device performance. By understanding the surface chemistry of the nanocrystals, we will have the ability to continually improve the photovoltaic devices. Currently, several nanocrystal systems are used in photovoltaic devices. In this dissertation we will focus on the  $\text{Cu}(\text{In}_{1-x}\text{Ga}_x)\text{Se}_2$  and  $\text{CsPbI}_3$  nanocrystal systems.

The synthesis of  $\text{CuInSe}_2$  and  $\text{Cu}(\text{In}_{1-x}\text{Ga}_x)\text{Se}_2$  nanocrystal and their characterization by Transmission electron microscopy and X-ray diffraction are discussed in Chapter 2.  $^{31}\text{P}$  nuclear magnetic resonance of  $\text{CuInSe}_2$  nanocrystal synthesis using secondary and tertiary phosphines is discussed in Chapter 3. The synthesis of  $\text{CsPbX}_3$ ,  $\text{FAPbI}_3$ , and mixed cation and halide perovskite nanocrystals are discussed in Chapter 4. The thermal stability of the perovskite superlattice characterized by GISAXS and GIWAXS is discussed in Chapter 5. Exciton kinetics of  $\text{CsPbI}_3$  nanocrystals via transient absorption spectroscopy (TAS) is discussed in Chapter 6. Lastly, a summary of the work presented in this dissertation and future research directions are discussed in Chapter 7.

## 1.8: REFERENCES

1. Boundless. World Energy Use. *Boundless* (2015).
2. Alternative Energy - Wind, Solar, Hydro and other alt energy sources for home power. Available at: <http://www.altenergy.org/>. (Accessed: 11th August 2015)
3. de Vries, B. J. M., van Vuuren, D. P. & Hoogwijk, M. M. Renewable energy sources: Their global potential for the first-half of the 21st century at a global level: An integrated approach. *Energy Policy* **35**, 2590–2610 (2007).
4. Köberle, A. C., Gernaat, D. E. H. J. & van Vuuren, D. P. Assessing current and future techno-economic potential of concentrated solar power and photovoltaic electricity generation. *Energy* doi:10.1016/j.energy.2015.05.145
5. Lewis, N. S. & Nocera, D. G. Powering the planet: Chemical challenges in solar energy utilization. *Proc. Natl. Acad. Sci.* **103**, 15729–15735 (2006).
6. WEO. Available at: <http://www.iea.org/weo/>. (Accessed: 13th September 2018)
7. Kabir, E., Kumar, P., Kumar, S., Adelodun, A. A. & Kim, K.-H. Solar energy: Potential and future prospects. *Renew. Sustain. Energy Rev.* **82**, 894–900 (2018).
8. Besarati, S. M., Padilla, R. V., Goswami, D. Y. & Stefanakos, E. The potential of harnessing solar radiation in Iran: Generating solar maps and viability study of PV power plants. *Renew. Energy* **53**, 193–199 (2013).
9. Research on heat transfer performance of passive solar collector-storage wall system with phase change materials - ScienceDirect. Available at: <https://www.sciencedirect.com/science/article/pii/S037877881630202X>. (Accessed: 13th September 2018)

10. Residential Solar Panels Cost Analysis: Full Breakdown. *Solar Action Alliance*
11. Solar Energy vs Fossil Fuels: How Do They Compare? | EnergySage. *Solar News* (2017).
12. Nižetić, S., Giama, E. & Papadopoulos, A. M. Comprehensive analysis and general economic-environmental evaluation of cooling techniques for photovoltaic panels, Part II: Active cooling techniques. *Energy Convers. Manag.* **155**, 301–323 (2018).
13. Palm, J. Household installation of solar panels – Motives and barriers in a 10-year perspective. *Energy Policy* **113**, 1–8 (2018).
14. Solar Energy Industries Association; NAICS: 813910. EC & M: Electrical Construction and Maintenance; Overland Park. Informa (2018)
15. Williams, R. Becquerel Photovoltaic Effect in Binary Compounds. *The Journal of Chemical Physics*: Vol 32, No 5. 1505 (2004)
16. Rappaport, P. The photovoltaic effect and its utilization. *Sol. Energy* **3**, 8–18 (1959).
17. Solar Spectrum. Available at:  
<http://www.greenrhinoenergy.com/solar/radiation/characteristics.php>. (Accessed: 13th September 2018)
18. Solar Energy | PVEducation. Available at:  
<http://www.pveducation.org/pvcdrom/introduction/solar-energy>. (Accessed: 11th August 2015)

19. How Do Solar Panels Work? | Photovoltaic Cells. Available at: <https://www.livescience.com/41995-how-do-solar-panels-work.html>. (Accessed: 13th September 2018)
20. Principles of Photovoltaics, Photovoltaic Materials | Solar Energy. Available at: [http://www.greenrhinoenergy.com/solar/technologies/pv\\_cells.php](http://www.greenrhinoenergy.com/solar/technologies/pv_cells.php). (Accessed: 11th August 2015)
21. Nelson, J. *The Physics of Solar Cells*. (World Scientific Publishing Company, 2003).
22. Smith, M., Chen, G. D., Li, J. Z., Lin, J. Y., & Jiang, H. X. Excitonic recombination in GaN grown by molecular beam epitaxy: *Applied Physics Letters*: Vol 67, No 23, 3387 (1998).
23. Slide Show. Available at: [http://education.mrsec.wisc.edu/SlideShow/slides/pn\\_junction/pn\\_junction\\_solar.html](http://education.mrsec.wisc.edu/SlideShow/slides/pn_junction/pn_junction_solar.html). (Accessed: 11th August 2015)
24. Shockley, W. & Queisser, H. J. Detailed Balance Limit of Efficiency of p-n Junction Solar Cells. *J. Appl. Phys.* **32**, 510–519 (1961).
25. Iotti, R. C. & Rossi, F. Carrier thermalization versus phonon-assisted relaxation in quantum-cascade lasers: A Monte Carlo approach. *Appl. Phys. Lett.* **78**, 2902–2904 (2001).
26. Snoke, D. W., Braun, D., & Cardona, M. Carrier thermalization in Cu<sub>2</sub>O: Phonon emission by excitons. *Phys. Rev. B* **44**, 2991 (1991)



27. Efros, A. L., Kharchenko, V. A. & Rosen, M. Breaking the phonon bottleneck in nanometer quantum dots: Role of Auger-like processes. *Solid State Commun.* **93**, 281–284 (1995).
28. Dimroth, F. & Kurtz, S. High-Efficiency Multijunction Solar Cells. *MRS Bull.* **32**, 230–235 (2007).
29. King, R. R., Law, D. C., Edmondson, K. M., Fetzer, C. M., Kinsey, G. S., Yoon, H., Sherif, A., & Karam, N. H. 40% efficient metamorphic GaInP/GaInAs/Ge multijunction solar cells: Applied Physics Letters: Vol 90, No 18.183516 (2007).
30. Freundlich, A., & Alemu, A. Multi quantum well multijunction solar cell for space applications. *physica status solidi (c) - Wiley Online Library.* Vol 2, 8, 2978 - 2981 (2005).
31. Cotal, H., Fetzer, C., Boisvert, J., Kinsey, G., King, R., Herbert, P., Yoon, H., & Karam, N. III–V multijunction solar cells for concentrating photovoltaics - Energy & Environmental Science (RSC Publishing) Vol 2, 174 - 192 (2009).
32. Beard, M. C. & Ellingson, R. J. Multiple exciton generation in semiconductor nanocrystals: Toward efficient solar energy conversion. *Laser Photonics Rev.* **2**, 377–399 (2008).
33. Beard, M. C., Midgett, A. G., Hanna, M. C., Luther, J. M., Hughes, B. K., & Nozik, A. J. Comparing Multiple Exciton Generation in Quantum Dots To Impact Ionization in Bulk Semiconductors: Implications for Enhancement of Solar Energy Conversion. *Nano Lett.* **10**, 3019–3027 (2010).

34. Beard, M. C., Knutsen, K. P., Yu, P., Luther, J. M., Song, Q., Metzger, W. K., Ellingson, R. J., & Nozik, A. J. Multiple Exciton Generation in Colloidal Silicon Nanocrystals. *Nano Lett.* **7**, 2506–2512 (2007).
35. Beard, M. C., Midgett, A. G., Law, M., Semonin, O. E., Ellingson, R. J., & Nozik, A. J. Variations in the Quantum Efficiency of Multiple Exciton Generation for a Series of Chemically Treated PbSe Nanocrystal Films. *Nano Lett.* **9**, 836–845 (2009).
36. Shockley–Queisser limit. *Wikipedia, the free encyclopedia* (2015).
37. Miles, R. W., Zoppi, G. & Forbes, I. Inorganic photovoltaic cells. *Mater. Today* **10**, 20–27 (2007).
38. Parida, B., Iniyar, S. & Goic, R. A review of solar photovoltaic technologies. *Renew. Sustain. Energy Rev.* **15**, 1625–1636 (2011).
39. Mashreki, T. I.A., & Afzaal, M. Nanocrystalline Materials for Hybrid Photovoltaic Devices. *Advanced Materials Research*, Vol. 1116, 45-50 (2015).
40. Lee, Y., Park, C., Balaji, N., Lee, Y.-J. & Dao, V. A. High-efficiency Silicon Solar Cells: A Review. *Isr. J. Chem.* **55**, 1050–1063 (2015).
41. Solar Markets Around The World. Available at:  
[http://solarcellcentral.com/markets\\_page.html](http://solarcellcentral.com/markets_page.html). (Accessed: 12th August 2015)
42. Chapin, D. M., Fuller, C. S. & Pearson, G. L. A New Silicon p-n Junction Photocell for Converting Solar Radiation into Electrical Power. *J. Appl. Phys.* **25**, 676–677 (1954).
43. Brophy, V. & Lewis, J. O. *A Green Vitruvius: Principles and Practice of Sustainable Architectural Design*. (Routledge, 2012).

44. Saga, T. Advances in crystalline silicon solar cell technology for industrial mass production. *NPG Asia Mater.* **2**, 96–102 (2010).
45. Günes, S., Abdel-Mottaleb, M. S. A., Hoppe, H. & Ayuk Mbi Egbe, D. Solar Cells: From Sunlight into Electricity. *Int. J. Photoenergy* **2015**, e173963 (2015).
46. Nugent, D. & Sovacool, B. K. Assessing the lifecycle greenhouse gas emissions from solar PV and wind energy: A critical meta-survey. *Energy Policy* **65**, 229–244 (2014).
47. Peng, J., Lu, L. & Yang, H. Review on life cycle assessment of energy payback and greenhouse gas emission of solar photovoltaic systems. *Renew. Sustain. Energy Rev.* **19**, 255–274 (2013).
48. Green, M. A. Recent developments in photovoltaics. *Sol. Energy* **76**, 3–8 (2004).
49. Chu, T. L. & Chu, S. S. Thin film II–VI photovoltaics. *Solid-State Electron.* **38**, 533–549 (1995).
50. Green, M. A. Thin-film solar cells: review of materials, technologies and commercial status. *J. Mater. Sci. Mater. Electron.* **18**, 15–19 (2007).
51. Green, M. A. Crystalline and thin-film silicon solar cells: state of the art and future potential. *Sol. Energy* **74**, 181–192 (2003).
52. Mattos, L. S., Scully, S. R., Syfu, M., Olson, E., Yang, L., Ling, C., Kayes, B. M., & He, G. New module efficiency record: 23.5% under 1-sun illumination using thin-film single-junction GaAs solar cells. in *2012 38th IEEE Photovoltaic Specialists Conference* 003187–003190 (2012). doi:10.1109/PVSC.2012.6318255

53. Kamat, P. V. Quantum Dot Solar Cells. Semiconductor Nanocrystals as Light Harvesters. *J. Phys. Chem. C* **112**, 18737–18753 (2008).
54. Graetzel, M., Janssen, R. A. J., Mitzi, D. B. & Sargent, E. H. Materials interface engineering for solution-processed photovoltaics. *Nature* **488**, 304–312 (2012).
55. Sugathan, V., John, E. & Sudhakar, K. Recent improvements in dye sensitized solar cells: A review. *Renew. Sustain. Energy Rev.* **52**, 54–64 (2015).
56. Shalini, S., Balasundaraprabhu, R., Kumar, T. S., Prabavathy, N., Senthilarasu, S., & Prasanna, S. Status and outlook of sensitizers/dyes used in dye sensitized solar cells (DSSC): a review. *Int. J. Energy Res.* **40**, 1303–1320 (2016).
57. Gong, J., Liang, J., & Sumathy, K. Review on dye-sensitized solar cells (DSSCs): Fundamental concepts and novel materials. *Renewable and Sustainable Energy Reviews* **16**, 5848 - 5860 (2012).
58. Chamberlain, G. A. Organic solar cells: A review. *Sol. Cells* **8**, 47–83 (1983).
59. Wöhrle, D. & Meissner, D. Organic Solar Cells. *Adv. Mater.* **3**, 129–138 (1991).
60. Pivrikas, A., Sariciftci, N. S., Juška, G. & Österbacka, R. A review of charge transport and recombination in polymer/fullerene organic solar cells. *Prog. Photovolt. Res. Appl.* **15**, 677–696 (2007).
61. Sargent, E. H. Colloidal quantum dot solar cells. *Nat. Photonics* **6**, 133–135 (2012).
62. Akkerman, Q. A., Rainò, G., Kovalenko, M. V. & Manna, L. Genesis, challenges and opportunities for colloidal lead halide perovskite nanocrystals. *Nat. Mater.* **17**, 394–405 (2018).

63. Luther, J. M., Law, M., Beard, M. C., Song, Q., Reese, M. O., Ellingson, R. J., & Nozik, A. J. Schottky Solar Cells Based on Colloidal Nanocrystal Films. *Nano Lett.* **8**, 3488–3492 (2008).
64. Hillhouse, H. W. & Beard, M. C. Solar cells from colloidal nanocrystals: Fundamentals, materials, devices, and economics. *Curr. Opin. Colloid Interface Sci.* **14**, 245–259 (2009).
65. Hagfeldt, A., Boschloo, G., Sun, L., Kloo, L. & Pettersson, H. Dye-Sensitized Solar Cells. *Chem. Rev.* **110**, 6595–6663 (2010).
66. O'Regan, B. & Grätzel, M. A low-cost, high-efficiency solar cell based on dye-sensitized colloidal TiO<sub>2</sub> films. *Nature* **353**, 737–740 (1991).
67. Asghar, M. I., Zhang, J., Wang, H. & Lund, P. D. Device stability of perovskite solar cells – A review. *Renew. Sustain. Energy Rev.* **77**, 131–146 (2017).
68. Aldakov, D., Lefrançois, A. & Reiss, P. Ternary and quaternary metal chalcogenide nanocrystals: synthesis, properties and applications. *J. Mater. Chem. C* **1**, 3756–3776 (2013).
69. Reinhard, P., Chirilă, A., Blösch, P., Pianezzi, F., Nishiwaki, S., Buecheler, S., & Tiwari, A. N. Review of Progress Toward 20% Efficiency Flexible CIGS Solar Cells and Manufacturing Issues of Solar Modules. *IEEE J. Photovolt.* **3**, 572–580 (2013).
70. Pernik, D. R., Gutierrez, M., Thomas, C., Voggu, V. R., Yu, Y., Embden, J. v., Topping, A. J., Jasieniak, J. J., Vanden Bout, D. A., Lewandowski, R., & Korgel, B. A. Plastic Microgroove Solar Cells Using CuInSe<sub>2</sub> Nanocrystals. *ACS Energy Lett.* **1**, 1021–1027 (2016).

71. Voggu, V. R., Sham, J., Pfeffer, S., Pate, J., Phillip, L., Harvey, T. B., Brown, R. M., & Korgel, B. A. Flexible CuInSe<sub>2</sub> Nanocrystal Solar Cells on Paper. *ACS Energy Lett.* **2**, 574–581 (2017).
72. Bang, J. H. & Kamat, P. V. Quantum Dot Sensitized Solar Cells. A Tale of Two Semiconductor Nanocrystals: CdSe and CdTe. *ACS Nano* **3**, 1467–1476 (2009).
73. Szendrei, K., Gomulya, W., Yarema, M., Heiss, W. & Loi, M. A. PbS nanocrystal solar cells with high efficiency and fill factor. *Appl. Phys. Lett.* **97**, 203501 (2010).
74. Piliago, C., Protesescu, L., Bisri, S. Z., Kovalenko, M. V. & Loi, M. A. 5.2% efficient PbS nanocrystal Schottky solar cells. *Energy Environ. Sci.* **6**, 3054–3059 (2013).
75. Akhavan, V. A., Panthani, M. G., Goodfellow, B. W., Reid, D. K. & Korgel, B. A. Thickness-limited performance of CuInSe<sub>2</sub> nanocrystal photovoltaic devices. *Opt. Express* **18**, A411 (2010).
76. Akhavan, V. A., Goodfellow, B. W., Panthani, M. G., Reid, D. K., Hellebusch, D. J., Adachi, T., & Korgel, B. A. Spray-deposited CuInSe<sub>2</sub> nanocrystal photovoltaics. *Energy Environ. Sci.* **3**, 1600 (2010).
77. Panthani, M. G., Stolle, C. J., Reid, D. K., Rhee, D. J., Harvey, T. B., Akhavan, V. A., Yu, Y., & Korgel, B. A. CuInSe<sub>2</sub> Quantum Dot Solar Cells with High Open-Circuit Voltage. *J. Phys. Chem. Lett.* **4**, 2030–2034 (2013).
78. Swarnkar, A., Marshall, A. R., Sanhira, E. M., Chernomordik, B. D., Moore, D. T., Christians, J. A., Chakrabarti, T., & Luther, J. M. Quantum dot-induced phase stabilization of  $\alpha$ -CsPbI<sub>3</sub> perovskite for high-efficiency photovoltaics. *Science* **354**, 92–95 (2016).

79. Sanehira, E. M., Marshall, A. R., Christians, J. A., Harvey, S. P., Ciesielski, P. N., Wheeler, L. M., Schulz, P., Lin, L. Y., Beard, M. C., & Luther, J. M. Enhanced mobility CsPbI<sub>3</sub> quantum dot arrays for record-efficiency, high-voltage photovoltaic cells. *Sci. Adv.* **3**, eaao4204 (2017).
80. Kim, B.-S., Hong, J., Hou, B., Cho, Y., Sohn, J. In., Cha, S.N. & Kim, J. M. Inorganic-ligand exchanging time effect in PbS quantum dot solar cell. *Appl. Phys. Lett.* **109**, 063901 (2016).
81. Owen, J. S., Park, J., Trudeau, P.-E. & Alivisatos, A. P. Reaction Chemistry and Ligand Exchange at Cadmium–Selenide Nanocrystal Surfaces. *J. Am. Chem. Soc.* **130**, 12279–12281 (2008).
82. Stolle, C. J., Panthani, M. G., Harvey, T. B., Akhavan, V. A. & Korgel, B. A. Comparison of the Photovoltaic Response of Oleylamine and Inorganic Ligand-Capped CuInSe<sub>2</sub> Nanocrystals. *ACS Appl. Mater. Interfaces* **4**, 2757–2761 (2012).
83. Bucherl, C. N., Oleson, K. R. & Hillhouse, H. W. Thin film solar cells from sintered nanocrystals. *Curr. Opin. Chem. Eng.* **2**, 168–177 (2013).
84. Stolle, C. J., Harvey, T. B., Pernik, D. B., Hibbert, J. I., Du, J., Rhee, D. J., Akhavan, V. A., Schaller, R., D., & Korgel, B. A. Multiexciton Solar Cells of CuInSe<sub>2</sub> Nanocrystals. *J. Phys. Chem. Lett.* **5**, 304–309 (2014).
85. Stolle, C. J., Harvey, T. B. & Korgel, B. A. Photonic curing of ligand-capped CuInSe<sub>2</sub> nanocrystal films in *2014 IEEE 40th Photovoltaic Specialist Conference (PVSC)* 0270–0274 (2014). doi:10.1109/PVSC.2014.6924897

86. efficiency\_chart.jpg (4190×2456). Available at:  
[http://www.nrel.gov/ncpv/images/efficiency\\_chart.jpg](http://www.nrel.gov/ncpv/images/efficiency_chart.jpg). (Accessed: 12th August 2015)
87. Mallory, S. A., Valeriani, C. & Cacciuto, A. An Active Approach to Colloidal Self-Assembly. *Annu. Rev. Phys. Chem.* **69**, 59–79 (2018).
88. Boles, M. A., Engel, M. & Talapin, D. V. Self-Assembly of Colloidal Nanocrystals: From Intricate Structures to Functional Materials. *Chem. Rev.* **116**, 11220–11289 (2016).
89. Liljeroth, P., Overgaag, K., Urbieto, A., Grandidier, B., Hickey, S. G., & Vanmaekelbergh, D. Variable Orbital Coupling in a Two-Dimensional Quantum-Dot Solid Probed on a Local Scale. *Phys. Rev. Lett.* **97**, 096803 (2006).
90. Hanrath, T. Colloidal nanocrystal quantum dot assemblies as artificial solids. *J. Vac. Sci. Technol. A* **30**, 030802 (2012).
91. Whitham, K., Yang, J., Savitzky, B. H., Kourkoutis, L. F., Wise, F., & Hanrath, T. Charge transport and localization in atomically coherent quantum dot solids. *Nat. Mater. Lond.* **15**, 557–563 (2016).
92. Shabaev, A., Efros, A. L. & Efros, A. L. Dark and Photo-Conductivity in Ordered Array of Nanocrystals. *Nano Lett.* **13**, 5454–5461 (2013).
93. Zasadzinski, J. A., Viswanathan, R., Madsen, L., Garnæs, J. & Schwartz, D. K. Langmuir-Blodgett films. *Science* **263**, 1726–1733 (1994).
94. Peterson, I. R. & Girling, I. R. Langmuir-Blodgett films. *Sci. Prog. 1933-* **69**, 533–550 (1985).



95. Lu, W., Fang, J., Stokes, K. L. & Lin, J. Shape Evolution and Self Assembly of Monodisperse PbTe Nanocrystals. *J. Am. Chem. Soc.* **126**, 11798–11799 (2004).
96. Akhavan, V. A., Goodfellow, B. W., Panthani, M. G., Steinhagen, C., Harvey, T. B., Stolle, C. J., & Korgel, B. A. Colloidal CIGS and CZTS nanocrystals: A precursor route to printed photovoltaics. *J. Solid State Chem.* **189**, 2–12 (2012).
97. Panthani, M. G., Akhavan, V., Goodfellow, B., Schmidtke, J. P., Dunn, L., Dodabalapur, A., Barbara, P. F., & Korgel, B. A. Synthesis of CuInS<sub>2</sub>, CuInSe<sub>2</sub>, and Cu(In<sub>x</sub>Ga<sub>1-x</sub>)Se<sub>2</sub> (CIGS) Nanocrystal “Inks” for Printable Photovoltaics. *J. Am. Chem. Soc.* **130**, 16770–16777 (2008).
98. Harvey, T. B., Mori, I., Stolle, C. J., Bogart, T. D., Ostrowski, D., P., Glaz, M. S., Du, J., Pernik, D. R., Akhavan, V. A., Kesrounai, H., Vanden Bout, D. A., & Korgel, B. A. Copper Indium Gallium Selenide (CIGS) Photovoltaic Devices Made Using Multistep Selenization of Nanocrystal Films. *ACS Appl. Mater. Interfaces* **5**, 9134–9140 (2013).
99. Jackson, P., Hariskos, D., Lotter, E., Paetel, S., Wuerz, R., Menner, R., Wischmann, W., & Powalla, M. New world record efficiency for Cu(In,Ga)Se<sub>2</sub> thin-film solar cells beyond 20%. *Prog. Photovolt. Res. Appl.* **19**, 894–897 (2011).
100. Protesescu, L., Yakunin, S., Bodnarchuk, M. I., Krieg, F., Caputo, R., Hendon, C. H., Yang, R. X., Walsh, A., & Kovalenko, M. V. Nanocrystals of cesium lead halide perovskites (CsPbX<sub>3</sub>, X=Cl, Br, and I): novel optoelectronic materials showing bright emission with wide color gamut. *Nano Lett.* **15**, 3692–3696 (2015).
101. Krieg, F., Ochsenbein, S. T., Yakunin, S., Brinck, S. t., Aellen, P., Süess, A., Clerc, B., Guggisberg, D., Nazarenko, O., Shynkarenko, Y., Kumar, S., Shih, C.-J.,

Infante, I., & Kovalenko, M. V. Colloidal CsPbX<sub>3</sub> (X = Cl, Br, I) Nanocrystals 2.0: Zwitterionic Capping Ligands for Improved Durability and Stability. *ACS Energy Lett.* **3**, 641–646 (2018).

## Chapter 2: Synthesis and Characterization of $\text{Cu}(\text{In}_x\text{Ga}_{1-x})\text{Se}_2$ Nanocrystals

### 2.1: INTRODUCTION

Thin film copper indium gallium selenide photovoltaic devices have reached efficiencies of over 20%.<sup>1</sup> Conventionally, copper indium gallium selenide  $\text{Cu}(\text{In}_{1-x}\text{Ga}_x)\text{Se}_2$  films are created via co-evaporation of each element and then heated in a Se vapor.<sup>2,3</sup> In addition to this process being time intensive and expensive, there are difficulties in controlling the composition of the film due to material loss during the co-evaporation process. One way to mitigate these effects is to use nanocrystals. Nanocrystals can be used for a variety of applications such as light emitting diodes, transistors, photo detectors, targeted cell delivery, and photovoltaic (PV) devices.<sup>4</sup> Specifically, groups II-VI, IV-VI, and I-III-VI<sub>2</sub> such as CdSe, PbS, and  $\text{Cu}(\text{In}_{1-x}\text{Ga}_x)\text{Se}_2$  nanocrystals have been extensively studied and used for PV device fabrication.<sup>5,6</sup> In this chapter, we will focus on the group I-III-VI<sub>2</sub>  $\text{Cu}(\text{In}_{1-x}\text{Ga}_x)\text{Se}_2$  (CIGS) nanocrystals.

CIGS nanocrystals are very promising to serve as the absorber layer for nanocrystal PV devices.<sup>7,8</sup> Their band gap can be tuned to between 1.01 eV and 1.7 eV by changing the composition of Ga in the nanocrystals, where a band gap of 1.01 eV has no Ga and 1.7 eV has no In. Secondly, the CIGS nanocrystals have a high absorption coefficient which will allow them to absorb many photons which will be beneficial for exciton formation. Additionally, CIGS is stable upon long-term excitations this means that the devices can be used over and over, which is advantageous to consumers; and the elements are less toxic than other absorber materials like PbSe and CdSe.

Nanocrystals morphology (shape), size, crystal structure, stability, and optical and electronic properties depend on the reactants, temperature and synthetic route used.<sup>9</sup> There are several synthetic routes to fabricate CIGS nanocrystals.<sup>7,8,10-31</sup> In this chapter,

I will focus on the one-pot and hot-injection synthesis methods. In the one-pot method, all of the reactants, the metal salts and the chalcogenide (Se), are added into a reaction flask and heated at the reaction temperature. This method allows for the synthesis to be scaled up for larger amounts of products to be formed. Chloride and acetate metal salts along with elemental Se are the typical reactants for this synthesis mechanism. These reactions typically suffer from low reaction yields due to simultaneous nucleation and growth processes and less control than the hot-injection methods.<sup>32</sup>

The hot-injection method<sup>32</sup> allows for the formation of monodisperse nanocrystals by allowing the metal salts and the Se reactants to form separate nuclei while either the metal solution or Se solution is injected into the hot solution of the other. In contrast to the one-pot method, this process allows for the nucleation process to occur rapidly and transition into the growth stage faster. Usually, the metals are coordinated in oleylamine or octadecene. On the other hand, Se is usually coordinated to a phosphine or amine. This allows for faster reaction times. The hot-injection method allows for narrow size distribution, control of particle size, and higher product yields due to instantaneous nucleation but the synthesis has difficulty in being scaled up due to mixing.

## **2.2: $\text{CuIn}_{1-x}\text{Ga}_x\text{Se}_2$ NANOCRYSTAL SYNTHESIS**

### **2.2.1: materials**

Copper (I) chloride ( $\text{CuCl}$ , 97%), gallium (III) chloride ( $\text{GaCl}_3$ , ~99.99%), and indium (III) chloride ( $\text{InCl}_3$ , 98%) were obtained from 5N+ copper(I) chloride beads ( $\text{CuCl}$ , 99%), selenium powder (99%), copper (II) acetylacetonate ( $\text{Cu}(\text{acac})_2$ , 97%), gallium (III) acetylacetonate ( $\text{Ga}(\text{acac})_3$ , 99.99%), indium (III) acetylacetonate ( $\text{In}(\text{acac})_3$ , 99.9%), diphenylphosphine (DPP, 98%), tri-*n*-butylphosphine (TBP, 90%), trioctylphosphine (TOP, 97%), sodium borohydride ( $\text{NaBH}_4$ , ~98.0%), octylamine (99%), octadecylamine

(~99.0%), hexadecylamine (98%), and oleylamine (OLA, 70%) were obtained from Sigma-Aldrich company. Indium (III) chloride ( $\text{InCl}_3$ , 99%) was obtained from Strem Chemicals. Ethanol (99.5%) and toluene (99%) were obtained from Fischer scientific. All chemicals were used without further purification.

### **2.2.2: $\text{CuIn}_{1-x}\text{Ga}_x\text{Se}_2$ one-pot synthesis**

20 mL of degassed OLA was charged into a three neck flask along with 0.396 g  $\text{CuCl}$ , 0.619 g of  $\text{InCl}_3$ , 0.211 g of  $\text{GaCl}_3$ , and 0.632 g of Se in a nitrogen filled glovebox. The solution is degassed at  $110^\circ\text{C}$  for 1 hr at  $\sim 150$  mTorr to remove any residual water. After degassing, the reaction temperature is raised to  $260^\circ\text{C}$  under a blanket of  $\text{N}_2$  and held for 1-3 hours. After reacting, the heating mantle is removed and the reaction flask is allowed to cool to  $50^\circ\text{C}$  before isolating the particles via centrifugation.

### **2.2.3: $\text{CuIn}_{1-x}\text{Ga}_x\text{Se}_2$ hot injection synthesis**

#### **2.2.3.1: *Metals hot injection***

0.316 g of Se and 25 mL of OLA are charged into a 25-mL three neck round bottom flask and degassed at  $110^\circ\text{C}$  for 30 minutes at  $\sim 150$  mTor. 0.330 g of  $\text{In}(\text{acac})_3$ , 0.440 g of  $\text{Ga}(\text{acac})_3$ , and 0.524 g of  $\text{Cu}(\text{acac})_2$  along with 25 mL of OLA were charged into a separate 25-mL three neck round bottom flask and heated at  $80^\circ\text{C}$  for 1 hr at  $\sim 150$  mTorr. After 30 minutes under a blanket of  $\text{N}_2$  gas, the reaction temperature was increased from  $110^\circ\text{C}$  to  $250^\circ\text{C}$  and held for 1 hr. The metal solution was cooled down to room temperature and injected into the Se solution. The reaction flask was allowed to cool for 15 minutes before increasing the temperature back to  $250^\circ\text{C}$  and holding for 1 hr and 30 minutes under a blanket of  $\text{N}_2$ . The solution was cooled to  $50^\circ\text{C}$ , by removing the heating before isolation

of the nanoparticles via centrifugation. When injecting the metal, be careful not to let in any air or Cu will oxidize to the more favorable  $2^+$  state.

#### ***2.2.3.2: DPP:Se injection***

0.198 g of CuCl, 0.1326 g of InCl<sub>3</sub> and 0.2464 g of GaCl<sub>3</sub> was added to a 50-mL three neck round bottom flask along with 20 mL of OLA under inert conditions. The reaction flask was degassed at 110°C for 1 hr at ~150 mTorr. In a nitrogen filled glovebox, a solution of DPP, Se, and OLA was formed in a vile, with 0.316 g of Se, 2 mL of OLA, and 2 mL of DPP. The solution was allowed to stir on the stir on the stirring plate for 1 hour. After the metal solution was degassed for 1 hr, the reaction solution was heated to 240°C. Upon reaching 180°C, the Se solution was swiftly removed from the glovebox and injected through the septum into the flask. The reaction was allowed to reach 240°C and held for 1 hr and 15 minutes under a blanket of N<sub>2</sub> gas. After the reaction was done, the heating mantle was removed and the reaction was slowly cooled to room temperature, before isolating the particles via centrifugation.

#### ***2.2.3.3: TOP:Se injection***

0.198 g of CuCl, 0.1326 g of InCl<sub>3</sub> and 0.2464 g of GaCl<sub>3</sub> was added to a 50-mL three neck round bottom flask along with 20 mL of OLA in the glovebox. The reaction flask was degassed at 110°C for 1 hr at ~150 mTorr. In a nitrogen filled glovebox, a solution of TOP, Se, and OLA was formed in a vile, with 0.316 g of Se, 14 mL of OLA, and 6 mL of TOP. The solution was allowed to stir on the stirring plate in the glovebox for 1 hour. After the metal solution was degassed for 1 hr, the reaction solution was heated to 240°C. Upon reaching 180°C, the Se solution was swiftly removed from the glovebox and injected through the septum into the flask. The reaction was allowed to reach 240°C and

held for 1 hr and 15 minutes under a blanket of N<sub>2</sub> gas. After the reaction was done, the heating mantle was removed and the reaction was slowly cooled to room temperature, before isolating the particles via centrifugation.

#### **2.2.4: CuInSe<sub>2</sub> one-pot Synthesis**

20 mL of degassed OLA was charged into a three neck flask along with 0.396 g CuCl, 0.884 g of InCl<sub>3</sub>, and 0.632 g of Se in a nitrogen filled glovebox. The solution is degassed at 110°C for 1 hr at ~150 mTorr to remove any residual water and oxygen. After degassing, the reaction temperature is raised to 260°C under a blanket of N<sub>2</sub> and held for 1-3 hours. After reacting, the heating mantle is removed and the reaction flask is allowed to cool to 50°C before isolating the particles via centrifugation.

##### **2.2.4.1: CuInSe<sub>2</sub> one-pot Synthesis\_NaBH<sub>4</sub>**

50 mL of degassed OLA was charged into a three neck flask along with 0.495 g CuCl, 1.11 g of InCl<sub>3</sub>, 0.79 g of Se, and 0.326 g of NaBH<sub>4</sub> in a nitrogen filled glovebox. The solution is degassed at 110°C for 1 hr at ~150 mTorr to remove any residual water and oxygen. After degassing, the reaction temperature is raised to 250°C under a blanket of N<sub>2</sub> and held for 90 minutes. After reacting, the heating mantle is removed and the reaction flask is allowed to cool to 50°C before isolating the particles via centrifugation.

#### **2.2.5: CuInSe<sub>2</sub> Hot Injection Synthesis**

##### **2.2.5.1: *Metals injection***

0.316 g of Se and 25 mL of OLA are charged into a 25-mL three neck round bottom flask and degassed at 110°C for 30 minutes at ~150mTor. 0.824 g of In(acac)<sub>3</sub> and 0.524 g of Cu(acac)<sub>2</sub> along with 25 mL of OLA were charged into a separate 25-mL three neck

round bottom flask and heated at 80°C for 1 hr at ~150 mTorr. After 30 minutes under a blanket of N<sub>2</sub> gas, the reaction temperature was increased from 110°C to 250°C and held for 1 hr. The metal solution was cooled down to room temperature and injected into the Se solution. The reaction flask was allowed to cool for 15 minutes, before increasing the temperature back to 250°C and holding for 1 hr and 30 minutes under a blanket of N<sub>2</sub>. The solution was cooled to 50°C by removing the heating before isolation of the nanoparticles via centrifugation. When injecting the metal, be careful not to let in any air, or Cu will oxidize to the more favorable 2<sup>+</sup> state.

#### ***2.2.5.2: DPP:Se injection***

20 mL of degassed OLA, 0.495 g of CuCl, and 1.11 g of InCl<sub>3</sub> were added to a three neck round bottom flask in the glove box, degassed at 110°C at ~150 mTorr for 1 h. Under a blanket of dry N<sub>2</sub> gas, the flask temperature was raised to 240°C. Upon reaching 180°C, 10 mL of a 1.0 M of DPP:Se solution was swiftly removed from the glove box and injected through a rubber septum into the reaction flask. The introduction of the Se reagent produced a black solution. The reaction flask temperature was then raised to a final temperature of 240°C and maintained at this temperature for 10 mins to 1 hr and 15 minutes, prior to cooling, until room temperature.

#### ***2.2.5.3: TBP:Se injection***

50 mL of degassed oleylamine, 0.495 g of CuCl, and 1.11 g of InCl<sub>3</sub> were added to a three neck round bottom flask in the glove box, degassed at 110°C at ~150 mTorr for 1 h. Under a blanket of dry N<sub>2</sub> gas, the flask temperature was raised to 240°C. Upon reaching 180°C, 10 mL of a 1.0 M of TBP:Se solution was swiftly removed from the glove box and



injected through a rubber septum into the reaction flask. The introduction of the Se reagent gradually produced a black solution. The reaction flask temperature was then raised to a final temperature of 240°C and maintained at this temperature for 10 mins to 1 hr and 15 minutes, prior to cooling, until room temperature.

#### ***2.2.5.4: TOP:Se injection***

0.198 g of CuCl, 0.442 g of InCl<sub>3</sub> was added to a 50-mL three neck round bottom flask along with 20 mL of OLA in the glovebox. The reaction flask was degassed at 110°C for 1 hr at ~150 mTorr. In a nitrogen filled glovebox, a solution of TOP, Se, and OLA was formed in a vile, with 0.316 g of Se, 14 mL of OLA, and 6 mL of TOP. The solution was allowed to stir on the stirring plate in the glovebox for 1 hour. After the metal solution was degassed for 1 hr, the reaction solution was heated to 240°C. Upon reaching 180°C, the Se solution was swiftly removed from the glovebox and injected through the septum into the flask. The reaction was allowed to reach 240°C and held for 1 hr and 15 minutes under a blanket of N<sub>2</sub> gas. After the reaction was done, the heating mantle was removed and the reaction was slowly cooled to room temperature before isolating the particles via centrifugation.

#### **2.2.6: Isolation of CuIn<sub>1-x</sub>Ga<sub>x</sub>Se<sub>2</sub> Nanocrystals**

After cooling the reaction products, the nanocrystals were purified by dividing the reaction flask solution equally between two centrifuge tubes (for larger reactions, the solutions were split into several centrifuge tubes) and added 15 mL of ethanol to each tube. CuIn<sub>1-x</sub>Ga<sub>x</sub>Se<sub>2</sub> nanocrystals were thus precipitated by centrifugation at 4500 rpm for 5 minutes, the supernatant was discarded and the precipitate was dispersed in 10 mL of toluene. This dispersion was centrifuged at 5000 rpm for five minutes to remove poorly

capped particles from the dispersion. The supernatant was kept, while the precipitant was discarded and washed once more in ethanol and toluene and spun at 8000 rpm for 5 minutes. The final solution was concentrated using a rotary evaporator and dispersed in anhydrous toluene and stored in a N<sub>2</sub> filled glovebox.

### **2.2.7: Characterization of CuIn<sub>1-x</sub>Ga<sub>x</sub>Se<sub>2</sub> Nanocrystals**

CuIn<sub>1-x</sub>Ga<sub>x</sub>Se<sub>2</sub> nanocrystals were characterized using transmission electron microscopy (TEM), X-ray diffraction (XRD), and scanning electron microscopy (SEM). TEM was conducted using a JEOL 2010F TEM. The FEI Tecnai G2 TEM and JEOL 2010F TEM were operated at 200 kV. A Rigaku R-axis Spider diffractometer was used to perform powder XRD. The diffractometer was operated at 40 kV and 40 mV under a Cu K $\alpha$  radiation ( $\lambda = 1.5418 \text{ \AA}$ ) rotated at  $5^\circ \text{ sec}^{-1}$  for 10 min. 2DP and JADE were used to process the data and background subtraction. TEM and SEM samples were prepared by drop casting sample dispersions onto a mesh nickel carbon-coated grid, supplied by Electron Microscopy Sciences (Cat#: CF150-Ni), or p-doped Si wafers. XRD samples were prepared by drying nanocrystal dispersions, and adhering them to a nylon loop using mineral oil.

## **2.3: RESULTS AND DISCUSSION**

### **2.3.1: CuIn<sub>1-x</sub>Ga<sub>x</sub>Se<sub>2</sub> Nanocrystals**

Using one pot and hot injection techniques described in section 2.2.2 and 2.2.3, CIGS nanocrystals were synthesized using  $x = 0.70$ , isolated (section 2.2.5), and characterized (2.2.6). Figure 2.1 shows the TEM images of CIGS nanocrystals synthesized using different techniques. It is clear that the different techniques affects the morphology and size of the nanocrystals. The one pot and metals hot injection methods produce

nanocrystals that have similar morphologies and average diameter sizes of,  $21.7 \pm 9.6$  nm and  $15.1 \pm 8$  nm, respectively. Conversely, the nanocrystals synthesized with DPP exhibited various morphologies with an average diameter size of  $17.4 \pm 8.5$  nm. When TOP is used the resulting product is globs of materials that are hard to isolate from the un-reacted reactants. From XRD, the isolated nanocrystals are shown to have a tetragonal crystal structure. However, the isolated CIGS nanocrystals synthesized with DPP showed additional peaks, which may be due to the formation of by products such as  $\text{In}_2\text{Se}_3$ .

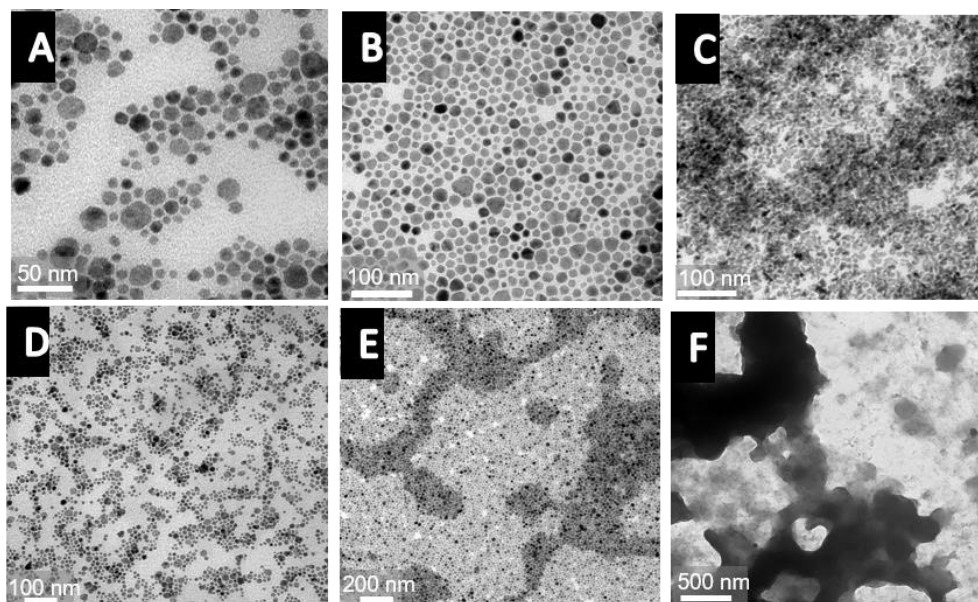


Figure 2.1: TEM images of CIGS nanocrystals synthesized via one pot (A&D) and hot injection (B, C, E, & F) methods. A) One pot synthetic method of CIGS where  $X = 0.70$ . B) Metals ( $\text{Cuacac}$ ,  $\text{Inacac}_3$ , and  $\text{Gaacac}_3$ ) hot injection synthetic method of CIGS nanocrystals where  $X = 0.70$ . C) DPP hot injection synthetic method of CIGS nanocrystals where  $X = 0.70$ . D) One pot synthetic method of CIGS where  $X = 0.70$ . E) Metals ( $\text{Cuacac}$ ,  $\text{Inacac}_3$ , and  $\text{Gaacac}_3$ ) hot injection synthetic method of CIGS nanocrystals where  $X = 0.70$ . F) TOP hot injection synthetic method of CIGS where  $X = 0.70$ .

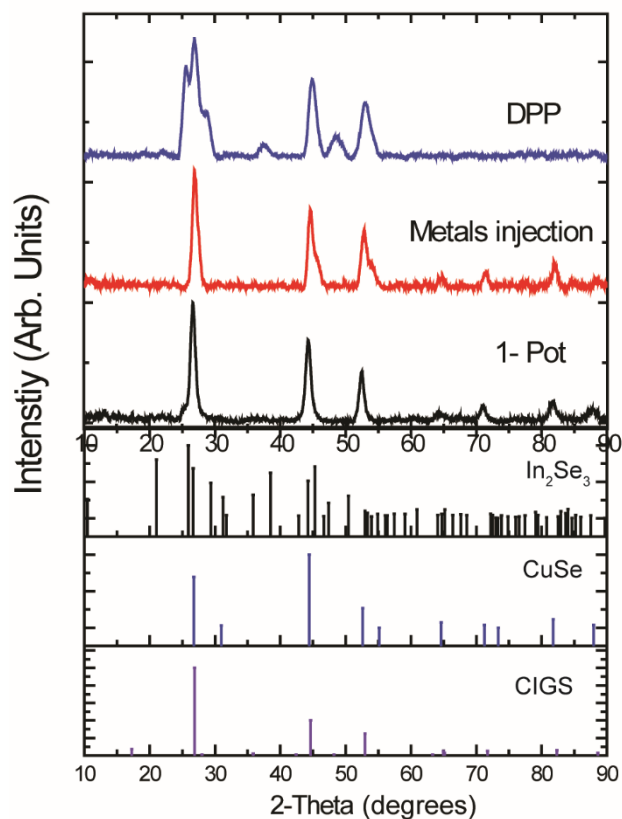


Figure 2.2: XRD spectra of CIGS nanocrystals synthesized using one pot and hot injection techniques (metals and DPP). The peaks are referenced to the CIGS chalcopyrite crystal pattern of PDF#00-035-1102, CuSe PDF#01-071-0044, and  $\text{In}_2\text{Se}_3$  PDF#01-071-0447.

### 2.3.2: $\text{CuInSe}_2$ Nanocrystals

CIS nanocrystals were synthesized, isolated, and characterized using similar methods as in the CIGS synthesis (section 2.2). TEM images of CIS nanocrystals are shown in Figure 2.3. CIS nanocrystals synthesized using the one pot and the  $\text{NaBH}_4$  methods exhibited an average diameters of  $11.8 \pm 3.9$  nm and  $9.7 \pm 3.0$  nm respectively. When the method was changed to the hot injection, the morphologies transitioned from spherical to triangular and multi morphologies. The average diameters for the metals ( $\text{CuCl}$  and  $\text{InCl}_3$ ), DPP, TBP, and TOP injections were  $12.3 \pm 7.54$  nm,  $12.5 \pm 5.4$  nm,  $10.8 \pm 3.8$  nm, and

12.5 ± 6.6 nm respectively. Conversely, to CIGS the TOP hot injection CIS method produced crystalline nanocrystals that can be seen in TEM and XRD (figure 2.3 and 2.4). Unlike CIGS nanocrystals, the synthetic method didn't affect the nanocrystals crystal structure, as shown in Figure 2.4. The nanocrystals exhibited a cubic crystal structure.

In all of the synthetic methods mention thus far, oleylamine has been used as the reaction solvent and nanocrystal capping ligands. However, these ligands have been known to be electrically insulating and hinder device performance<sup>27</sup>. As a result, other organic solvents and capping ligands are explored here. TEM images for CIS nanocrystals are shown for nanocrystals synthesized using octadecanol, octadecylamine, octadecene, 1-dodecanol, and dodecanethiol using the hot-injection technique in figure 2.5. Shorter chained organic solvents were used but didn't produce colloiddally stable materials. Nanocrystals synthesized using alcohols (octadecanol & 1-dodecanol) and octadecene were either hundred(s) of nanometers in length or produced very low reaction conversion yields. The nanocrystals synthesized using dodecanethiol produce smaller nanocrystals ~ 3 nm – 8 nm in diameter. Using octadecylamine as a solvent resulted in nanocrystals with similar morphologies as the other nanocrystals synthesized with the hot injection method using oleylamine as a solvent. Figure 2.6 shows the XRD spectra for the thiol and alcohol samples. Both hot injections using TBP resulted in the formation of the cubic phase of CIS. However, when using DPP the alcohol sample showed a strong peaks, alluding to In<sub>2</sub>Se<sub>3</sub> by product formation.

In high resolution TEM energy dispersive spectroscopy (EDS) elemental analysis was conducted on the materials. Through EDS, some of the nanocrystals were found to have a uniform distribution of metals (Cu and In) throughout the nanocrystal, Figure 2.7. However, there were some of the nanocrystals that exhibited Cu poor surfaces Figure 2.8

or oxygen rich surfaces Figure 2.9. This may be one explanation for low device performances.

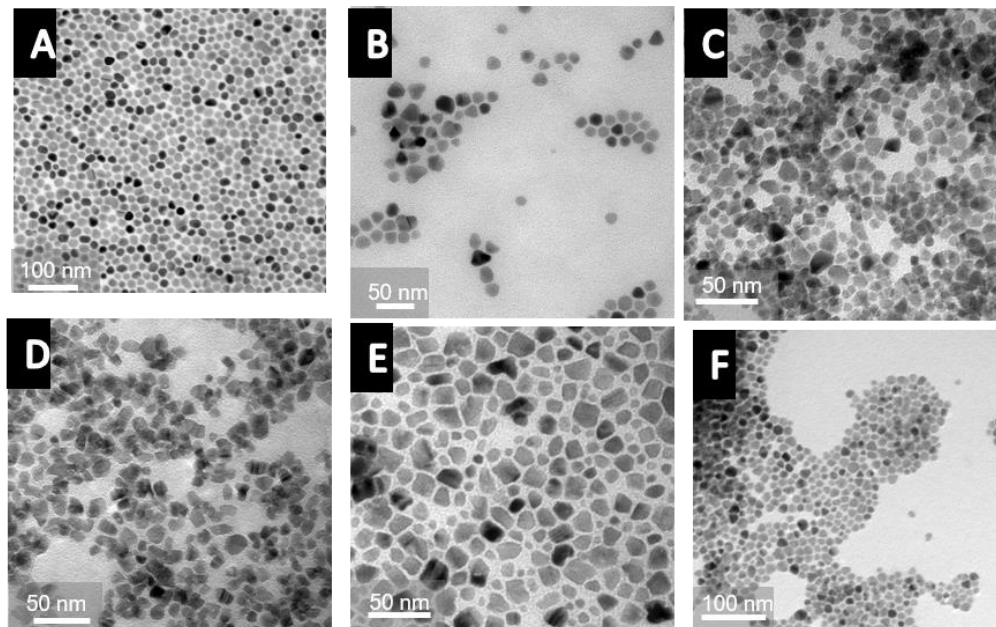


Figure 2.3: TEM images of CIS nanocrystals synthesized via one pot (A&F) and hot injection (B, C, D, E) methods. A) One pot synthetic method of CIS. B) Metals ( $\text{Cu}(\text{acac})_2$  and  $\text{In}(\text{acac})_3$ ) hot injection synthetic method of CIS nanocrystals. C) DPP hot injection synthetic method of CIS nanocrystals. D) TBP hot injection synthetic method of CIS. E) TOP hot injection synthetic method of CIS nanocrystals. F)  $\text{NaBH}_4$  one pot synthetic method of CIS.

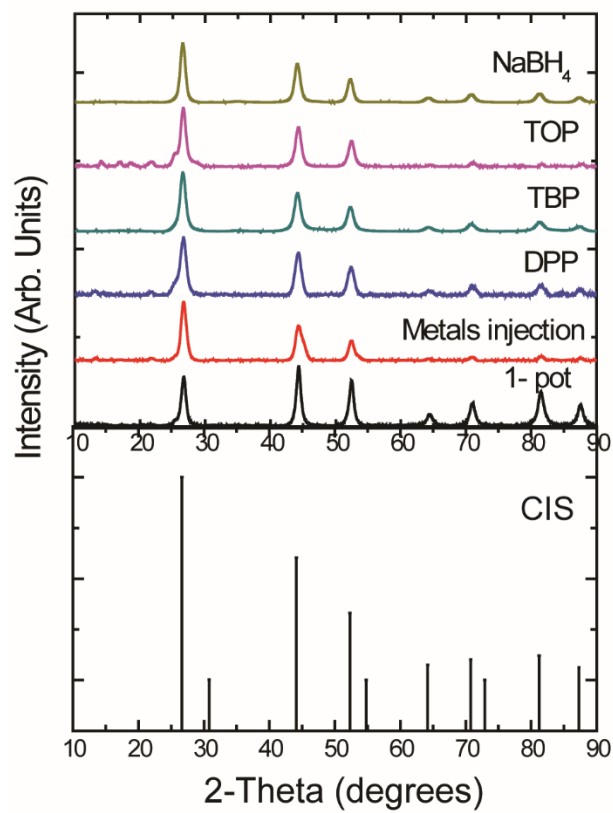


Figure 2.4: XRD spectra of CIS nanocrystals synthesized using one pot, NaBH<sub>4</sub>, and hot injection techniques (metals, DPP TBP, and TOP). The peaks are referenced to the CIS cubic crystal pattern of PDF#01-079-1809.

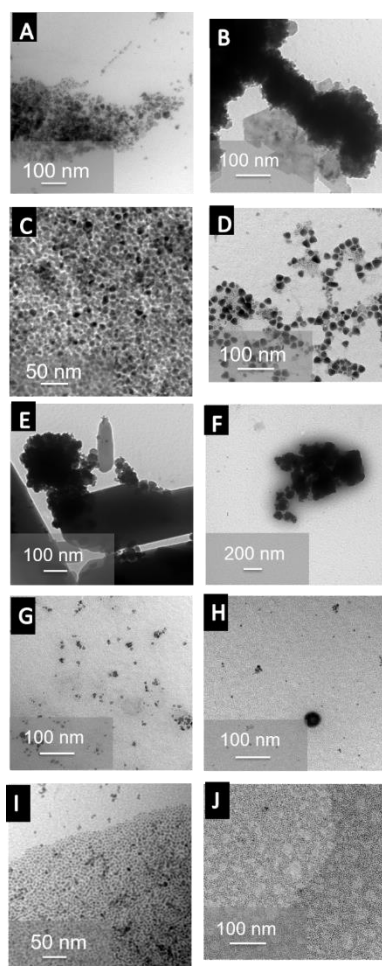


Figure 2.5: TEM images of CIS nanocrystals synthesized using the hot injection method, DPP (A, C, E, G, and I) and TBP (B, D, F, H, and J), with different solvents. A) DPP method using octadecanol as a solvent. B) TBP method using octadecanol as a solvent. C) DPP method using octadecylamine as the solvent. D) TBP method using octadecylamine as the solvent. E) DPP method using octadecene as the solvent. F) TBP method using octadecene as the solvent. G) DPP method using 1-dodecanol as the solvent. H) TBP method using 1-dodecanol as the solvent. I) DPP method using dodecanethiol as the solvent. J) TBP method using dodecanethiol as the solvent.



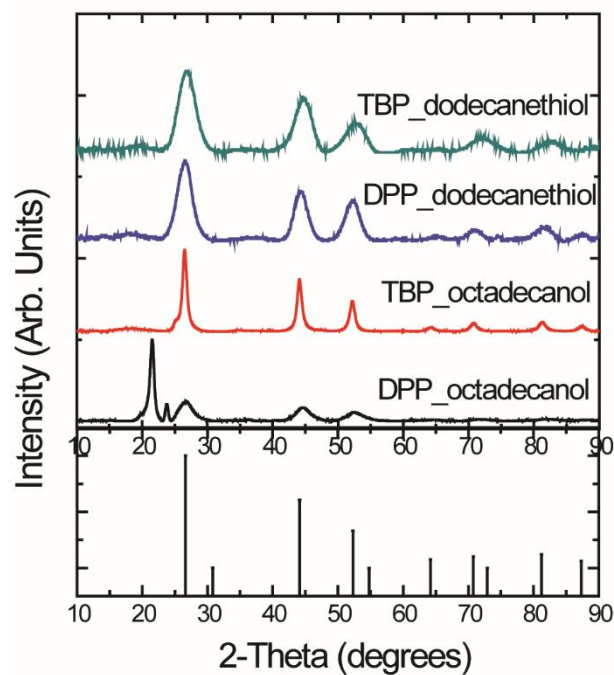


Figure 2.6: XRD spectra of CIS nanocrystals synthesized using hot injection techniques of DPP and TBP using other solvents besides oleylamine. The peaks are referenced to the CIS cubic crystal pattern of PDF#01-079-1809.

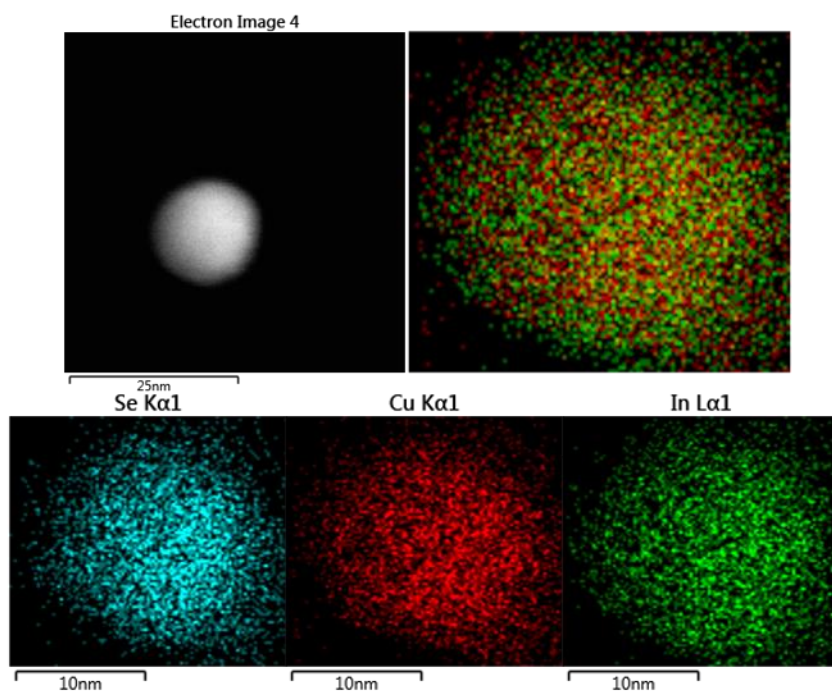


Figure 2.7: High resolution TEM EDS elemental mapping images of CIS nanocrystals synthesized via the metals hot injection method. Some of the particles demonstrated an even distribution of Cu and In within the nanocrystals.

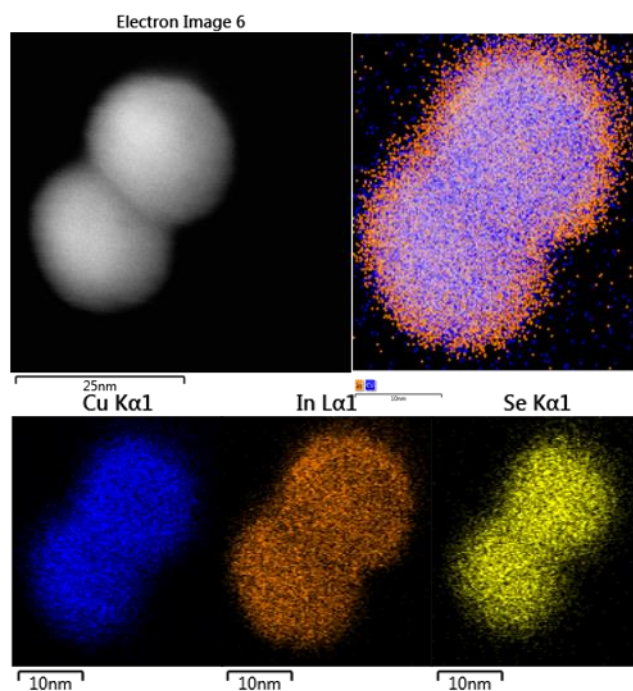


Figure 2.8: High resolution TEM EDS elemental mapping images of CIS nanocrystals synthesized via the metals hot injection method. Some of the nanoparticles show Cu deficiencies along the edge of the nanocrystals.

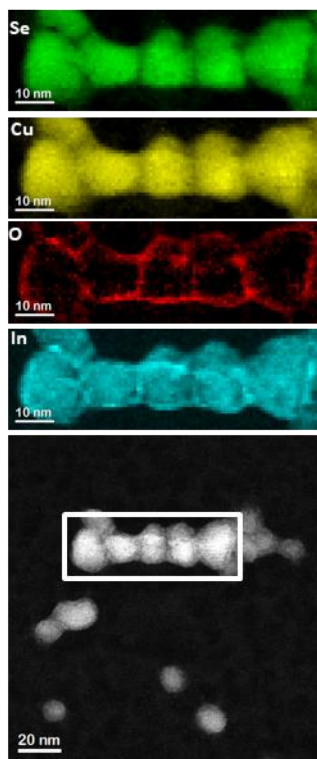


Figure 2.9: High resolution TEM EDS elemental mapping images of CIS nanocrystals synthesized via the metals hot injection method. Some of the nanoparticles showed oxygen rich surface which may be due to exposure of ambient conditions or surface treatments of the nanocrystals.

#### 2.4.: CONCLUSIONS

$\text{Cu}(\text{In}_{1-x}\text{Ga}_x)\text{Se}_2$  nanocrystals can be used for various applications to include targeted drug delivery, photo detectors, and photovoltaics. There are several methods that can be employed to synthesize these nanocrystals with different morphologies. CIGS and CIS nanocrystals were synthesized using two different general techniques one pot and hot injection methods. The hot injection method allows for the metals and chalcogenide reactants to form separate nuclei before reacting with each other and forming monomers. Alterations to the injection materials and solvents shows differences in nanocrystal morphology, average diameters and crystal structures.

## 2.6: REFERENCES

1. Jackson, P., Hariskos, D., Lotter, E., Paetel, S., Wuerz, R., Menner, R., Wischmann, W., & Powalla, M. New world record efficiency for Cu(In,Ga)Se<sub>2</sub> thin-film solar cells beyond 20%. *Prog. Photovolt. Res. Appl.* **19**, 894–897 (2011).
2. Acciarri, M., Le Donne, A., Marchionna, S., Meschia, M., Parravicini, J., Gasparotto, A., & Binetti, S. CIGS thin films grown by hybrid sputtering-evaporation method: Properties and PV performance. *Sol. Energy* (2018).  
doi:10.1016/j.solener.2018.02.024
3. Lindahl, J., Zimmermann, U., Szaniawski, P., Törndahl, T., Hultqvist, A., Salomé, P., Platzer-Björkman, C., & Edoff, M. Inline Cu(In,Ga)Se<sub>2</sub> Co-evaporation for High-Efficiency Solar Cells and Modules. *IEEE J. Photovolt.* **3**, 1100–1105 (2013).
4. Talapin, D. V., Lee, J.-S., Kovalenko, M. V. & Shevchenko, E. V. Prospects of Colloidal Nanocrystals for Electronic and Optoelectronic Applications. *Chem. Rev.* **110**, 389–458 (2010).
5. Sargent, E. H. Colloidal quantum dot solar cells. *Nat. Photonics* **6**, 133–135 (2012).
6. Kamat, P. V. Quantum Dot Solar Cells. Semiconductor Nanocrystals as Light Harvesters. *J. Phys. Chem. C* **112**, 18737–18753 (2008).
7. Dilena, E., Xie, Y., Vrescia, R., Prato, M., Maserati, L., Krahne, R., Paoletta, A., Bertoni, G., Povia, M., Moreels, I., & Manna, L. CuIn<sub>x</sub>Ga<sub>1-x</sub>S<sub>2</sub> Nanocrystals with Tunable Composition and Band Gap Synthesized via a Phosphine-Free and Scalable Procedure. *Chem. Mater.* **25**, 3180–3187 (2013).

8. Panthani, M. G., Akhavan, V., Goodfellow, B., Schmidtke, J. P., Dunn, L., Dodabalapur, A., Barbara, P. F., & Korgel, B. A. Synthesis of CuInS<sub>2</sub>, CuInSe<sub>2</sub>, and Cu(In<sub>x</sub>Ga<sub>1-x</sub>)Se<sub>2</sub> (CIGS) Nanocrystal ‘Inks’ for Printable Photovoltaics. *J. Am. Chem. Soc.* **130**, 16770–16777 (2008).
9. Yin, Y. & Alivisatos, A. P. Colloidal nanocrystal synthesis and the organic-inorganic interface. *Nat. Lond.* **437**, 664–70 (2005).
10. Akhavan, V. A., Goodfellow, B. W., Panthani, M. G., Steinhagen, C., Harvey, T. B., Stolle, C. J., & Korgel, B. A. Colloidal CIGS and CZTS nanocrystals: A precursor route to printed photovoltaics. *J. Solid State Chem.* **189**, 2–12 (2012).
11. Akhavan, V. A., Panthani, M. G., Goodfellow, B. W., Reid, D. K. & Korgel, B. A. Thickness-limited performance of CuInSe<sub>2</sub> nanocrystal photovoltaic devices. *Opt. Express* **18**, A411 (2010).
12. Akhavan, V. A., Goodfellow, B. W., Panthani, M. G., Reid, D. K., Hellebusch, D. J., Adachi, T., & Korgel, B. A. Spray-deposited CuInSe<sub>2</sub> nanocrystal photovoltaics. *Energy Environ. Sci.* **3**, 1600 (2010).
13. Castro, S. L., Bailey, S. G., Raffaele, R. P., Banger, K. K. & Hepp, A. F. Nanocrystalline Chalcopyrite Materials (CuInS<sub>2</sub> and CuInSe<sub>2</sub>) via Low-Temperature Pyrolysis of Molecular Single-Source Precursors. *Chem. Mater.* **15**, 3142–3147 (2003).
14. Chen, H., Yu, S.-M., Shin, D.-W. & Yoo, J.-B. Solvothermal Synthesis and Characterization of Chalcopyrite CuInSe<sub>2</sub> Nanoparticles. *Nanoscale Res. Lett.* **5**, 217–223 (2009).

15. Chiang, M.-Y., Chang, S.-H., Chen, C.-Y., Yuan, F.-W. & Tuan, H.-Y. Quaternary  $\text{CuIn}(\text{S}_{1-x}\text{Se}_x)_2$  Nanocrystals: Facile Heating-Up Synthesis, Band Gap Tuning, and Gram-Scale Production. *J. Phys. Chem. C* **115**, 1592–1599 (2011).
16. Chun, Y.-G., Kim, K.-H. & Yoon, K.-H. Synthesis of  $\text{CuInGaSe}_2$  nanoparticles by solvothermal route. *Thin Solid Films* **480–481**, 46–49 (2005).
17. Exstrom, C. L., Darveau, S. A., Martineq-Skinner, A. L., Ingersoll, M., Olejnicek, J., Mirasano, A., Haussler, A. T., Huguenin-Love, J., Kamler, C., Diaz, M., Ianno, N. J., & Soukup, R. J. Reaction pathway insights into the solvothermal preparation of  $\text{CuIn}_{1-x}\text{Ga}_x\text{Se}_2$  nanocrystalline materials. in *33rd IEEE Photovoltaic Specialists Conference, 2008. PVSC '08* 1–6 (2008). doi:10.1109/PVSC.2008.4922729
18. Grisar, H., Palchik, O., Gedanken, A., Palchik, V., Slifkin, M. A., & Weiss, A. M. Microwave-Assisted Polyol Synthesis of  $\text{CuInTe}_2$  and  $\text{CuInSe}_2$  Nanoparticles. *Inorg. Chem.* **42**, 7148–7155 (2003).
19. Li, B., Xie, Y., Huang, J. & Qian, Y. Synthesis by a Solvothermal Route and Characterization of  $\text{CuInSe}_2$  Nanowhiskers and Nanoparticles. *Adv. Mater.* **11**, 1456–1459 (1999).
20. Lee, H., Jeong, D.-s., Mun, T., Pejjai, B., Minnam Reddy, V. R., Anderson, T. J., & Park, C. Formation and characterization of  $\text{CuInSe}_2$  thin films from binary  $\text{CuSe}$  and  $\text{In}_2\text{Se}_3$  nanocrystal-ink spray. *Korean J. Chem. Eng.* **33**, 2486–2491 (2016).
21. Kar, M., Agrawal, R. & Hillhouse, H. W. Formation pathway of  $\text{CuInSe}_2$  nanocrystals for solar cells. *J. Am. Chem. Soc.* **133**, 17239–17247 (2011).

22. Jiang, C., Lee, J.-S. & Talapin, D. V. Soluble Precursors for  $\text{CuInSe}_2$ ,  $\text{CuIn}_{1-x}\text{Ga}_x\text{Se}_2$ , and  $\text{Cu}_2\text{ZnSn}(\text{S},\text{Se})_4$  Based on Colloidal Nanocrystals and Molecular Metal Chalcogenide Surface Ligands. *J. Am. Chem. Soc.* **134**, 5010–5013 (2012).
23. Guo, Q., Kim, S. J., Kar, M., Shafarman, W. N., Bikkire, R. W., Stach, E. A., Agrawal, R., & Hillhouse, H. W. Development of  $\text{CuInSe}_2$  Nanocrystal and Nanoring Inks for Low-Cost Solar Cells. *Nano Lett.* **8**, 2982–2987 (2008).
24. Guo, Q., Ford, G. M., Hillhouse, H. W. & Agrawal, R. Sulfide Nanocrystal Inks for Dense  $\text{Cu}(\text{In}_{1-x}\text{Ga}_x)(\text{S}_{1-y}\text{Se}_y)_2$  Absorber Films and Their Photovoltaic Performance. *Nano Lett.* **9**, 3060–3065 (2009).
25. Gu, S.-I., Shin, H.-S., Yeo, D.-H., Hong, Y.-W. & Nahm, S. Synthesis of the single phase CIGS particle by solvothermal method for solar cell application. *Curr. Appl. Phys.* **11**, S99–S102 (2011).
26. Grisar, H., Palchik, O., Gedanken, A., Palchik, V., Slifkin, M., & Weiss A. M. Microwave-Assisted Polyol Synthesis of  $\text{CuInTe}_2$  and  $\text{CuInSe}_2$  Nanoparticles. *Inorg. Chem.* **42**, 7148–7155 (2003).
27. Stolle, C. J., Panthani, M. G., Harvey, T. B., Akhavan, V. A. & Korgel, B. A. Comparison of the Photovoltaic Response of Oleylamine and Inorganic Ligand-Capped  $\text{CuInSe}_2$  Nanocrystals. *ACS Appl. Mater. Interfaces* **4**, 2757–2761 (2012).
28. Stolle, C. J., Harvey, T. B., Pernik, D. R., Hibbert, J. I., Du, J., Rhee, D. J., Akhavan, V. A., Schaller, R. D., & Korgel, B. A. Multiexciton Solar Cells of  $\text{CuInSe}_2$  Nanocrystals. *J. Phys. Chem. Lett.* **5**, 304–309 (2014).



29. Harvey, T. B., Mori, I., Stolle, C. J., Bogart, T. D., Ostrowski, D. P., Glaz, M. S., Du, J., Pernik, D. R., Akhavan, V. A., Kesrounai, H., Vanden Bout, D. A., & Korgel, B. A. Copper Indium Gallium Selenide (CIGS) Photovoltaic Devices Made Using Multistep Selenization of Nanocrystal Films. *ACS Appl. Mater. Interfaces* **5**, 9134–9140 (2013).
30. Panthani, M. G., Stolle, C. J., Reid, D. K., Rhee, D. J., Harvey, T. B., Akhavan, V. A., Yu, Y., & Korgel, B. A. CuInSe<sub>2</sub> Quantum Dot Solar Cells with High Open-Circuit Voltage. *J. Phys. Chem. Lett.* **4**, 2030–2034 (2013).
31. Akhavan, V. A., Harvey, T. B., Stolle, C. J., Ostrowski, D. P., Glaz, M. S., Goodfellow, B. W., Panthani, M. G., Reid, D. K., Vanden Bout, D. A., Korgel, B. A. Influence of Composition on the Performance of Sintered Cu(In,Ga)Se<sub>2</sub> Nanocrystal Thin-Film Photovoltaic Devices. *ChemSusChem* **6**, 481–486 (2013).
32. Kwon, S. G. & Hyeon, T. Formation Mechanisms of Uniform Nanocrystals via Hot-Injection and Heat-Up Methods. *Small* **7**, 2685–2702 (2011).

## Chapter 3: Chemical Mechanisms of Copper Indium Diselenide Nanocrystal Synthesis Studied by $^{31}\text{P}$ Nuclear Magnetic Resonance Spectroscopy\*

### 3.1 INTRODUCTION

Group I-III-VI<sub>2</sub> colloidal nanocrystals such as CuInSe<sub>2</sub> and CuIn<sub>x</sub>Ga<sub>1-x</sub>Se<sub>2</sub> have been examined for a variety of applications including photovoltaics, photodetectors and electronics.<sup>1,2</sup> Considerable effort has been given to the use of semiconductor nanocrystals for photovoltaic devices to potentially reduce the high cost associated with traditional photovoltaic fabrication methods.<sup>3,4</sup> Among the ternary and quaternary chalcogenide semiconductor nanocrystals, Cu(In<sub>1-x</sub>Ga<sub>x</sub>)Se<sub>2</sub> (CIGS) stands out as an excellent absorber layer for nanocrystal photovoltaic device fabrication.<sup>5</sup> CIGS displays a high absorption coefficient that has a tunable direct band gap that is directly controllable by the proportion of Ga incorporated and is stable upon long term-term excitation.

A number of different synthetic routes to obtain CIGS and related materials (*e.g.*, Cu(In<sub>1-x</sub>Ga<sub>x</sub>)S<sub>2</sub> and Cu<sub>2</sub>ZnSnS<sub>4</sub>) have been reported in the literature,<sup>2,6-10</sup> including one-pot<sup>5,11-16</sup> and hot precursor injection<sup>16-27</sup> methods. The one-pot synthetic method provides the ability to react metal salts with chalcogenide reactants for a scalable synthesis. However, depending on the reaction time, temperature, and reagents, different crystal structures and morphology may also be observed. This phenomenon was also observed in

---

\*The work contained in this chapter is the subject of a scholarly article that is currently in preparation. Authors on this work include Cherrelle J. Thomas, Vikas Voggu, Simon Humphrey, and Brian A. Korgel. Cherrelle Thomas was responsible for planning the research, and synthesis of nanocrystals and, analyzing the data, researching and writing the completed document. Vikas fabricated and tested the PV devices. Simon aided in the determination of the synthetic pathway.

the hot injection method. For example, Guo *et al.*<sup>17</sup> prepared CuInSe<sub>2</sub> nanocrystals by hot injection of elemental Se suspended in oleylamine into a solution of copper (I) chloride (CuCl) and indium trichloride (InCl<sub>3</sub>) in oleylamine. They observed that injection of the suspension of elemental Se in oleylamine at 285°C resulted in sphalerite CuInSe<sub>2</sub> nanocrystals; in comparison, injection of the Se suspension at 130°C accompanied by a slow temperature ramp to 285°C produced chalcopyrite CuInSe<sub>2</sub> nanocrystals. Additionally, hexagonal rings were fabricated by changing the selenium reactant to trioctylphosphine selenide (TOP=Se) and forming TOP metal (CuCl and InCl<sub>3</sub>) solutions.<sup>17</sup> In addition to morphology and crystal structure changes, Stolle *et al.*<sup>27</sup> observed multiexciton generation (MEG) in CuInSe<sub>2</sub> nanocrystals synthesized by hot injection of DPP=Se into a solution of CuCl, InCl<sub>3</sub>, and oleylamine, which is a potential way to increase PV device efficiencies and to exceed the so-called Shockley-Queisser limit.

There have been several studies to understand the reaction pathway of CIGS nanoparticle formation.<sup>28-31</sup> By adapting the synthetic method of Guo,<sup>17</sup> Kar *et al.*<sup>29</sup> observed the formation of intermediate Cu<sub>2-x</sub>Se and In<sub>2</sub>Se<sub>3</sub> phases before the eventual formation of CuInSe<sub>2</sub>.<sup>29</sup> Meanwhile, Ahmadi *et al.*<sup>28</sup> observed a similar reaction pathway for CuIn<sub>1-x</sub>Ga<sub>x</sub>Se<sub>2</sub> formation by X-ray diffraction (XRD) and transmission electron microscopy (TEM).<sup>26</sup> In 2011, Zhong *et al.*<sup>30</sup> found that CuInSe<sub>2</sub> can be produced through the formation of metal sulfide intermediate complex reacted with TBP=Se or TOP=Se.<sup>30</sup> Throughout the literature, phosphine selenides (*i.e.* TOP=Se) seem to favor the chalcopyrite crystal structure.<sup>2</sup> Although these previous studies provide insight into the formation of CIGS, few studies have been performed to study the use of phosphine

chalcogenides in the CIGS system, nor to fully assess how the use of these phosphine selenides might affect PV device performance. Panthani *et al.* showed the fabrication of CuInSe<sub>2</sub> using secondary and tertiary phosphine selenides (DPP=Se and TBP=Se respectively): DPP=Se increased the reaction yield and enabled lower reaction temperatures and the production of smaller diameter nanocrystals.<sup>18</sup>

Here, we investigate the role of two different Se reactants for CuInSe<sub>2</sub> nanocrystals, DPP=Se (Method I) and TBP=Se (Method II), which gives significantly different conversion yields. Reactions with DPP=Se result in high yields (*ca.* 80%), whereas TBP=Se leads to low yields (*ca.* 5%). Mechanistic insights were obtained using <sup>31</sup>P-NMR spectroscopy and thermogravimetric analysis. PV devices fabricated with nanocrystals from Method II demonstrated higher efficiencies >1% than those fabricated using Method I experienced efficiencies <1%. Moreover, a third synthetic method was used to increase the yield of Method II through the addition of DPP. We found that the addition of 1.5 mL of DPP to Method II gave reaction yields of ~47% and a PV device performance >1%. A probable reaction mechanism is proposed based on the <sup>31</sup>P-NMR data.

## **3.2: EXPERIMENTAL DETAILS AND CHARACTERIZATION**

### **3.2.1: Experimental Details**

**Materials:** Nitric acid 70%, copper(I) chloride beads (CuCl, 99%), selenium powder (99%), diphenylphosphine (DPP, 98%), tri-*n*-butylphosphine (TBP, 90%), and oleylamine (OLA, 70%) were obtained from Sigma-Aldrich company. Indium(III) chloride (InCl<sub>3</sub>, 99%) was obtained from Strem Chemicals and *d*<sub>3</sub>-chloroform (CDCl<sub>3</sub>) was

obtained from Cambridge Isotope Laboratories. Ethanol and toluene (99%) were obtained from Fischer scientific. All chemicals were used without further purification.

**Stock solutions:** Oleylamine was degassed in a three neck round bottom flask by heating to 110°C at ~150 mTorr overnight. 1.0 M stock solutions of DPP=Se and TBP=Se were produced by dissolving appropriate mass of selenium shot directly in appropriate amounts of DPP or TBP. All stock solutions were stored under air-free conditions.

**Nanocrystal synthesis.** 50 mL of degassed oleylamine, 0.495g (5 mmol) of CuCl, and 1.11g (5 mmol) of InCl<sub>3</sub> were added to a three neck round bottom flask in the glove box, degassed at 110°C at ~150 mTorr for 1 h. Under a blanket of dry N<sub>2</sub> gas, the flask temperature was raised to 240°C. Upon reaching 180°C, 10 mL of the 1.0 M of DPP=Se (Method I) or TBP=Se (Method II) stock solution was swiftly removed from the glove box and injected through a rubber septum into the reaction flask. The introduction of the Se reagent produced a black solution; when the TBP=Se reagent was used, the transition to a black solution occurred over several minutes. The reaction flask temperature was then raised to a final temperature of 240°C and maintained at this temperature for 10 min, prior to cooling, until room temperature.

A similar synthesis (Method III) was carried out, in which 50 mL of degassed oleylamine, 0.495g (5 mmol) of CuCl, 1.11g (5 mmol) of InCl<sub>3</sub>, and 1.5 mL (8.6 mmol) DPP were added to a three neck round bottom flask inside a glove box, and then degassed at 110°C at ~150 mTorr for 1 h. The introduction of the phosphine reagent produced a black solution. Under N<sub>2</sub>, the flask temperature was raised to 240°C; upon reaching 180°C, 10 mL of the 1 M of TBP=Se stock solution was swiftly injected into the reaction flask.

The reaction flask temperature was stabilized at 240°C for 10 minutes, the heat was removed and the reaction flask was slowly cooled.

After cooling the reaction product to 50°C, the nanocrystals were purified by dividing the sample equally between two centrifuge tubes and adding 15 mL of ethanol to each tube. CuInSe<sub>2</sub> nanocrystals were thus precipitated by centrifugation, 4500 rpm for 5 minutes, the supernatant was discarded and the precipitate was dispersed in 10 mL of toluene. This nanocrystal dispersion was subjected to repeated centrifugation to remove poorly-capped nanocrystals. This supernatant was kept and washed once more in ethanol and toluene. The final solution was concentrated using a rotary evaporator. Typical conversion yields for Methods I, II, and III are: 80, 5, and 47% respectively. TEM images and XRD data of the nanocrystals are shown in Appendix A.

**Nanocrystal synthesis for multinuclear NMR studies.** A modified version of our nanocrystal syntheses (shown in Fig 3.1), was employed to produce NMR samples. 5 mmol of CuCl and 5 mmol of InCl<sub>3</sub> were added to degassed oleylamine (50 mL) and further degassed at 110°C at ~150 mTorr for 2 hr to produce a 0.2 M stock solution. The solution was cooled and stored in the glove box. Aliquots (5 mL; 0.2 M) of the stock solution and the phosphine chalcogenide reagent (DPP=Se or TBP=Se, 1 mL; 1.0 M) were added to a vial, for a total of 5 vials, in the glove box. DPP was added to the vials for analysis of Method III. The vials were heated using an oil bath to 150°C. Each vial was heated for different lengths of time: 0, the first sign of a color change from yellow to black, 20, 40 and 60 min. The color change occurred after 1, 18 and 5 min for Methods I, II, and III,

respectively. 0.5 mL of each crude solution was added to 0.5 mL of CDCl<sub>3</sub> and loaded into an 8 inch NMR tube under N<sub>2</sub> gas.

### **3.2.2: Materials Characterization**

Nuclear magnetic resonance (NMR) spectroscopy was performed using an automatically tunable probe (suitable for analysis of <sup>1</sup>H, <sup>13</sup>C, <sup>31</sup>P and <sup>19</sup>F nuclei) on a Varian DirectDrive 400 (400 MHz) NMR spectrometer. The VNMRJ 2.3C software package was used to conduct the experiments. 0.5 mL of each crude solution was added to 0.5 mL of CDCl<sub>3</sub> and loaded into an 8 inch NMR tube under N<sub>2</sub> gas. For each <sup>31</sup>P-NMR spectrum acquisition, 128 scans with a relaxation delay and pulse angle of 1 sec and 45° respectively were collected with <sup>1</sup>H decoupling. For each <sup>1</sup>H spectrum, 8 scans were collected with a relaxation delay and pulse angle of 1 sec and 45°, respectively. All NMR spectra were analyzed via MestReNova. All spectra were acquired at room temperature.

Nanocrystals were imaged by transmission electron microscopy (TEM) using a FEI Tecnai G2 Spirit BioTwin TEM or a JEOL 2010F TEM. The FEI Tecnai G2 TEM and JEOL 2010F TEM were operated at 80 kV and 200 kV, respectively. Samples were prepared for imaging by drop-casting onto mesh nickel carbon-coated grids, supplied by Electron Microscopy Sciences ( Cat#: CF150-Ni).

A Rigaku R-axis Spider diffractometer was used to perform powder X-Ray diffraction analysis (PXRD). The nanocrystal dispersions were dried and adhered to a nylon loop using mineral oil. The diffractometer was operated at 40 kV and 40 mV under

a Cu-K $\alpha$  radiation ( $\lambda = 1.5418 \text{ \AA}$ ) at a rate of  $5^\circ 2\theta \text{ sec}^{-1}$ . 2DP and JADE were used to process the data and perform amorphous background subtractions.

Thermogravimetric analysis (TGA) was performed using a Mettler Thermogravimetric Analyzer, Model TGA/DSC 1. TGA experiments were conducted under N<sub>2</sub> flow at a heating rate of  $10^\circ\text{C min}^{-1}$  from  $30^\circ\text{C}$  to  $500^\circ\text{C}$ .

### **3.3: RESULTS AND DISCUSSIONS**

Our CuInSe<sub>2</sub> (CISe) nanocrystal synthesis methods have been previously reported<sup>4,12,32</sup> and is in section 3.2. Briefly, phosphine chalcogenide (either DPP=Se or TBP=Se) was injected into the reaction flask containing CuCl, InCl<sub>3</sub>, and Oleylamine (OLA) at  $180^\circ\text{C}$ . The temperature is raised to the reaction temperature of  $240^\circ\text{C}$  and held there for 10 minutes. After cooling, CISe nanocrystals are isolated via centrifugation. Due to the pyrophoric nature of the phosphines, our general synthesis was modified to a suitable method (Section 3.2).



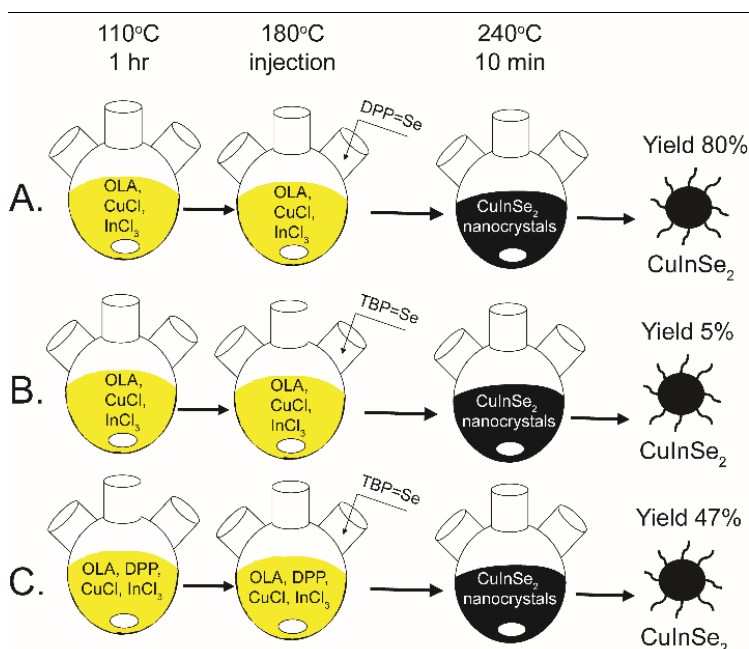
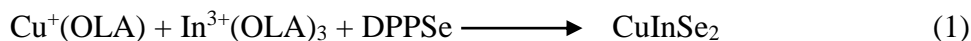


Figure 3.1: General schematic of Methods I, II, and III, shown in A, B, and C respectively. The reactions begin by degassing the reaction flask at 110°C at ~ 150 mTorr for 1 hr. Then under N<sub>2</sub> gas the flask temperature is raised to 240°C. Upon reaching 180°C the Se reactant is injected into the flask. Once the flask has reached the reaction temperature of 240°C, it is held at this temperature for 10 minutes. The reaction flask is cooled by removing the heating mantle. After isolation of CuInSe<sub>2</sub> nanocrystals via centrifugation, the percent yield was determined to be 80%, 5%, and 47% for methods I, II, and III respectively.

### 3.3.1: Method I\_DPP

Figure 3.2A shows <sup>31</sup>P-NMR spectra of reactant solutions containing 0.5 mmol each of CuCl and InCl<sub>3</sub> in 5 mL OLA with using 1 mL of a 1M DPP=Se solution (1 mmol Se and 5.75 mmol DPP) that have been heated to 150°C:



The reaction mixture changes color from yellow to red then to the final hue of black after only ~1 min of heating, indicating a transition from unreacted reactants to reactive species and nanocrystals. Even before heating, the DPP=Se peak ( $\delta = 7$  ppm) vanishes after adding the Cu and In reactants and a new peak appears at ( $\delta = -15$  ppm) corresponding to tetraphenylbiphosphine (TPBP). The appearance of TPBP indicates the formation of a reactive phosphine chalcogenide species, which is discussed later in the paper. Due to the fast kinetics of the reaction, we conducted the same experiment with a higher mole ratio of DPP=Se to metal reactants from 1:1 to 5.75:1 to observe the chemical compounds more closely; by injecting 1 mL of a 5.75M DPP=Se solution. Figure 3.2B shows  $^{31}\text{P}$ -NMR spectra for the prewashed, before nanocrystal isolation, reaction solution for method 1 with a 5.75:1 DPP=Se to metal reactants. The DPP=Se peak ( $\delta = 7$  ppm) shifts to ( $\delta = 22$  ppm). This down field shift may be due to the formation of the reactive phosphine and the formation of the metal(s) amine phosphine selenide active complex transition state that is not observable with excess DPP, due to the fact that large phosphine chalcogenide concentrations  $>5:1$  gives rise to additional  $^{31}\text{P}$  chemical shifts that are not observed otherwise<sup>33</sup>. Furthermore, the shifting and peak decrease and increase for unbound DPP is due to metals binding and formation and capping of nanocrystals.

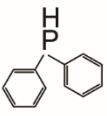
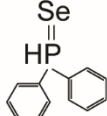
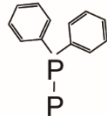
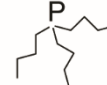
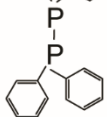
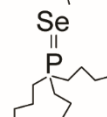
	ppm		ppm
	(DPP) -40.2		(DPPSe) 7.36
	(TPBP) -15.17		(TBP) -30.96
			(TBPSe) 36.35

Table 3.1: Chemical shifts observed in  $^{31}\text{P}$  NMR and the corresponding chemical species.

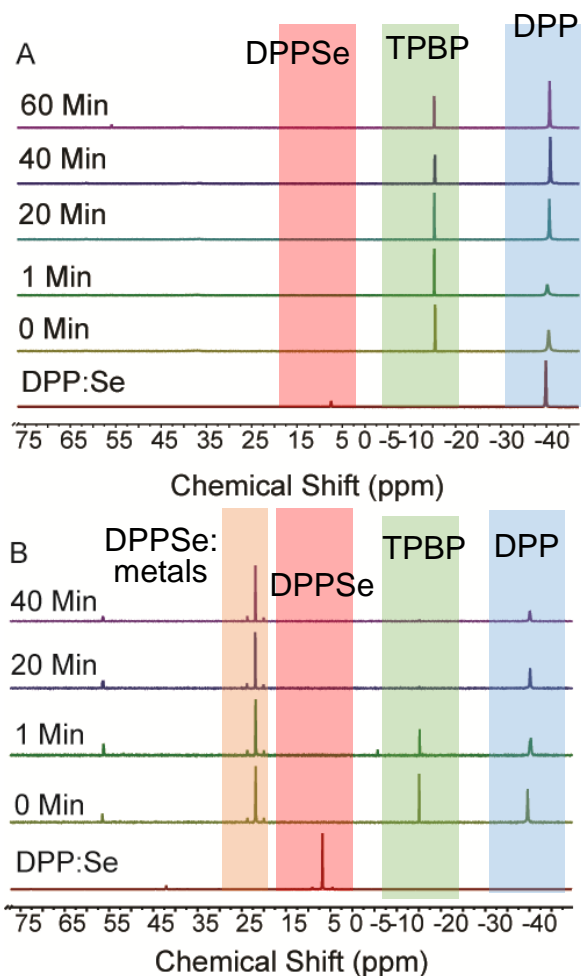


Figure 3.2: Room temperature  $^{31}\text{P}$ -NMR spectra of reaction products obtained by combining  $\text{CuCl}$ ,  $\text{InCl}_3$  in OLA with  $\text{DPP}=\text{Se}$  and heating to  $150^\circ\text{C}$  for various times indicated on the left of each spectra in  $\text{CDCl}_3$ . (A) Method I reaction (using 1 mL of a 1M  $\text{DPP}=\text{Se}$  solution (1 mmol Se and 5.75 mmol DPP)  $\text{DPP}=\text{Se}/(\text{Cu} + \text{In})$  of 1:1) upon addition of the metal precursors  $\text{DPP}=\text{Se}$  peak vanishes and tetraphenylbiphosphine (TPBP) peak appears. (B) Method I with an increase in the  $\text{DPP}=\text{Se}/(\text{Cu} + \text{In})$  molar ratio of 5.75:1 the binding of the metals to the  $\text{DPP}=\text{Se}$  ( $\delta = 7\text{ppm}$ ) produces an observable peak at  $\delta = 22\text{ppm}$  (red box) and tetraphenylbiphosphine (TPBP) peak reappears (green box) as in A. There is no change in the spectra after 40 min.

### 3.3.2: Method II\_TBP

Figure 3.3A illustrates the  $^{31}\text{P}$ -NMR of reactant solutions of 0.5 mmol each of  $\text{CuCl}$  and  $\text{InCl}_3$  in 5 mL OLA with 1 mL of a 1M TBP=Se solution (1 mmol Se and 4.05 mmol TBP) heated to  $150^\circ\text{C}$ :



These solutions change color much more gradually than the solutions with DPP=Se, turning from yellow to light brown to black after 18 min at  $150^\circ\text{C}$ . The reaction solutions transitioned, indicating the formation of nanoparticles. Unlike the reactions with DPP=Se (Method I), which produce viscous solutions as a result of higher conversion yields  $\sim 80\%$ , the solutions from Method II are less viscous consistent with low yields of  $\sim 5\%$ . As shown in figure 3.3A, the TBP=Se peak ( $\delta = 37$  ppm) remains relatively unchanged throughout the heating process, indicating that TBP forms a relatively unreactive complex with Se. To ensure that particle formation was hindered, we performed the same experiment but increased the ratio of TBP=Se to metals from 1:1 to 4.05:1, by injecting 1 mL of a 4.05M TBP=Se solution, figure 3.3B.

There is a slight upfield shift of the TBP=Se peak from 36.5 ppm to 36 ppm in the NMR spectra, indicating that the metals coordinate with the phosphine chalcogenide complex. In the CdSe system, Garcia-Rodriguez, R. *et al* observed a single chemical shift during room temperature experiments; however, upon cooling the sample, two distinct peaks were observed, a TOP=Se shift and a TOP=Se coordinating to Cd.<sup>34</sup> This makes us believe that a similar phenomenon may be occurring in our system, further analysis needs to be conducted.

Moreover, the secondary phosphine impurities in TBP allows for particle formation in both systems (with and without free TBP); which is supported by literature and shown in the Appendix A.<sup>33,35-37</sup> As seen in Method I, peak shifting and intensity changes are observed due to phosphine metal binding and particle formation and capping.

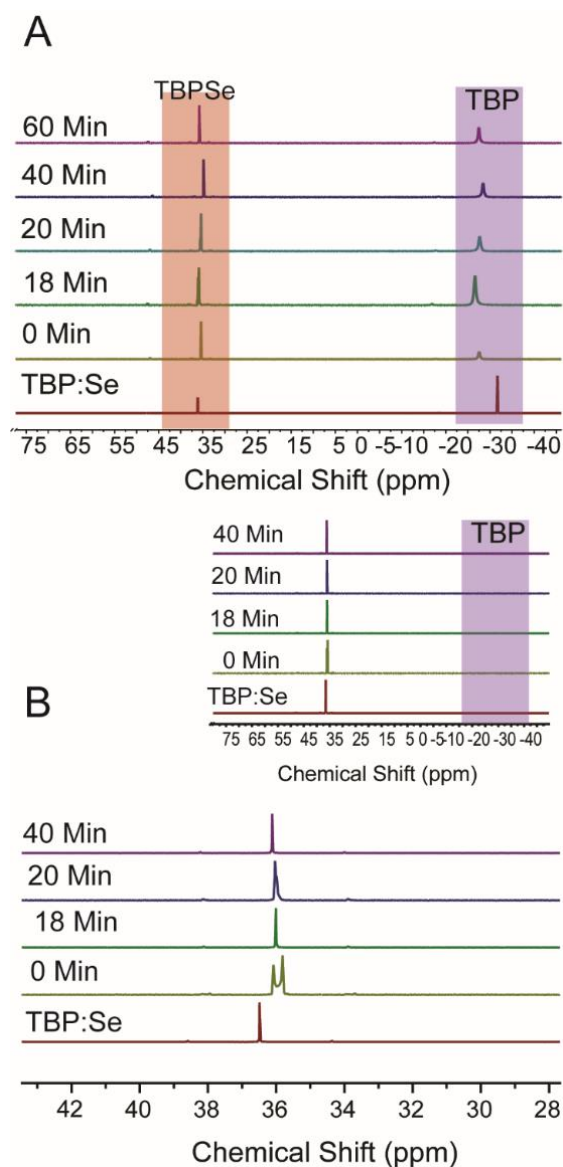
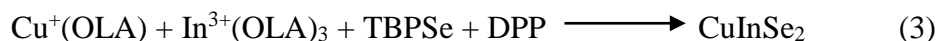


Figure 3.3: Room temperature  $^{31}\text{P}$ -NMR spectra of reaction products obtained by combining  $\text{CuCl}$ ,  $\text{InCl}_3$  in OLA with  $\text{TBP}=\text{Se}$  and heating to  $150^\circ\text{C}$  for various times indicated on the left of each spectra in  $\text{CDCl}_3$ . (A) Method II reaction (using 1 mL of a 1M  $\text{TBP}=\text{Se}$  solution (1 mmol Se and 4.05 mmol TBP)  $\text{TBP}=\text{Se}/(\text{Cu} + \text{In})$  of 1:1) The  $\text{TBP}=\text{Se}$  complex remained throughout the 60 minutes. (B) A magnified spectra of Method II with an increase in the  $\text{TBP}=\text{Se}/(\text{Cu} + \text{In})$  molar ratio of 4.05:1. The  $\text{TBP}=\text{Se}$  complex shows small chemical shifting over the duration of the reaction. The inset shows that there was no excess TBP in the reaction.

### 3.3.3: Method III\_hybrid

Method III involved the addition of 0.5 mmol each of CuCl and InCl<sub>3</sub> to 5 mL OLA with 1 mL of a 1M TBP=Se solution (1 mmol Se and 4.05 mmol TBP) and 0.3 mL DPP were heated at 150°C (Figure 3.4a):



Secondary phosphines are known to increase the yield of nanocrystal reactions that utilize tertiary phosphines in a number of systems, such as PbSe and CdSe.<sup>33</sup> DPP was added to the reaction to increase the yield of CuInSe<sub>2</sub> nanocrystals. Employing <sup>31</sup>P-NMR spectroscopy, we examined method III over the course of 60 min. Figure 3.4, shows that after 5 minutes of exposure to the oil bath, a color change from yellow to black. As shown in Figure 3.4A, a tetraphenylbiphosphine (TPBP) peak appears ( $\delta = -15$  ppm) immediately after mixing the reactants at room temperature (0 min) prior to heating.

The appearance of the TPBP chemical shift suggests that the reaction undergoes a similar reaction pathway as Method I; which has also been noted in literature for second and tertiary phosphine systems. Additionally, over the course of the reaction, a significant increase in the TBP peak is not observed; therefore, we hypothesize that the free TBP and the TBP released from the TBP=Se complex binds to the nanocrystal itself. In order to determine if a phosphine switch was occurring between TBP and DPP we ran Method III without excess TBP. In Figure 3.4B, a DPP=Se chemical shift was not observed; however, the TPBP peak was observed. This observation is indicative of the formation of the more



reactive phosphine chalcogenide reactant observed in Method I; therefore, suggesting a phosphine switch from TBP to DPP.

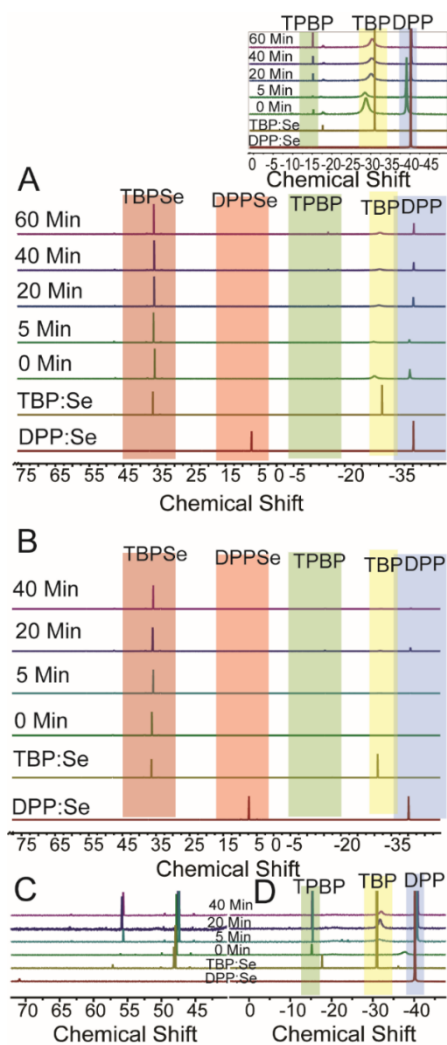


Figure 3.4: A Room temperature  $^{31}\text{P}$ -NMR spectra of reaction products obtained by combining  $\text{CuCl}$ ,  $\text{InCl}_3$ , DPP in OLA with TBP=Se and heating to  $150^\circ\text{C}$  for various times indicated on the left of each spectra in  $\text{CDCl}_3$ . (A) Method III reaction (using 1 mL of a 1M TBP=Se solution (1 mmol Se and 4.05 mmol TBP) TBP=Se/(Cu + In) of 1:1). Throughout the duration of the reaction there was no significant increase observed in the TBP peak (-32.5 ppm). The inset shows the emergence of the TPBP peak which is observed in method I. (B) Method III with an increase in the TBP=Se/(Cu + In) molar ratio of 4.05:1. Over the course of the reaction the TPBP peak (-15 ppm) was observed. This observation insinuates a phosphine switch between the tertiary TBP and the secondary DPP. C&D) Magnified  $^{31}\text{P}$ -NMR spectra of B.

### 3.3.4: Cu and In Study

By individually studying each metal (Cu and In) in the system and the interaction between DPP and TBP; we found that the Cu reagent reacts readily with both phosphines opposed to In. CuCl reacts with TBP=Se at room temperature, resulting in a color change from yellow to black; possibly indicating the formation of CuSe. Since DPP=Se is a solid at room temperature, the solution was heated during the addition of CuCl. The solution also experienced a color transformation yellow to red. This phenomenon was not observed when InCl<sub>3</sub> was added to DPP=Se, which makes us believe that the CuCl binding to the phosphine chalcogenide may actually be the intermediate for particle formation.

In addition to color change, chemical shifting was also observed in <sup>31</sup>P-NMR. (Figures 3.5 and 3.6) When using DPP=Se (Figure 3.5), we observed a chemical shift of the DPP=Se peak ( $\delta = 6.8$  ppm) to  $\delta = 7.2$  ppm upon the addition of CuCl to 1 mL of 5.75M of DPP=Se. Additionally, a broad peak emerges at  $\delta = -32.4$  ppm, which is due to the Cu binding to the phosphines. Furthermore, the DPP=Se peak vanishes upon the introduction of Cu:amine, (0.5 mmol of CuCl degassed in 5 mL of oleylamine at 110°C for 2 hours at 200 mTorr), with 1 mL of 5.75M of DPP=Se; however, the chemical shifts of -13.6 ppm and -33.8 ppm are observed which are also observed in Method I. This instigates the notion that the amine exchanged metal precursor may actually play a role in the kinetics and pathway of the reactions and that CuSe may be forming. Additionally, the peaks are broader and noisy due to the formation of nanocrystals<sup>38</sup>.

Moreover, when TBP=Se is used (figure 3.6) we observe slight chemical shifting of the TBP=Se peak from 36.5 ppm to 37 ppm and 37.1 ppm with the addition of CuCl and

Cu:amine. Slight peak shifting is observed with addition of the copper reactants, indicating binding to TBP=Se complex. Peak broadening is observed with the addition of Cu:amine to the phosphine chalcogenide, which may be attributed to the coordination of Cu to TBP=Se and the possibility of CuSe formation. However, the spectra isn't as nosy as the one in the DPP=Se discussed above, which may be due to the low yield of CuSe formation.

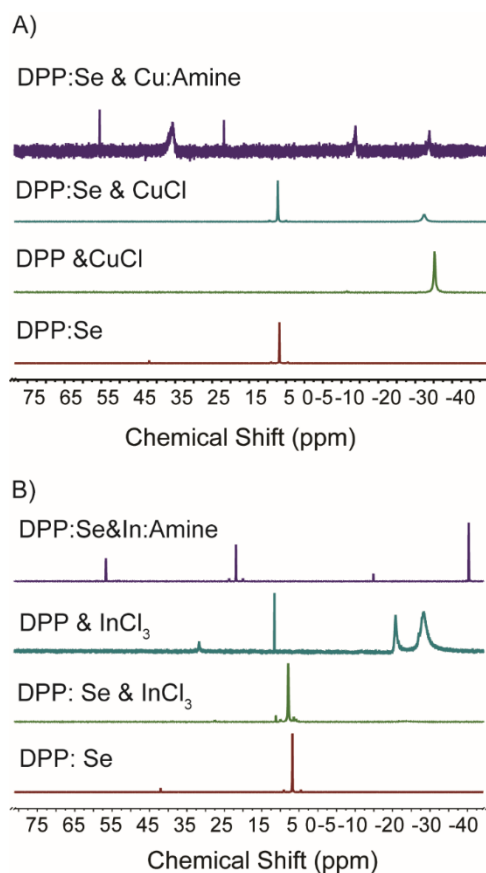


Figure 3.5: <sup>31</sup>P-NMR spectra in CDCl<sub>3</sub> of DPP=Se with (A) Cu and (B) In precursors bonded to the phosphine chalcogenide. Slight chemical shifting is observed upon the addition of the metal precursor. The additional peak that is observed around  $\delta = -40$  ppm is from DPP-CuCl. It is to note that the peaks are not completely aligned due to environmental differences between the samples.

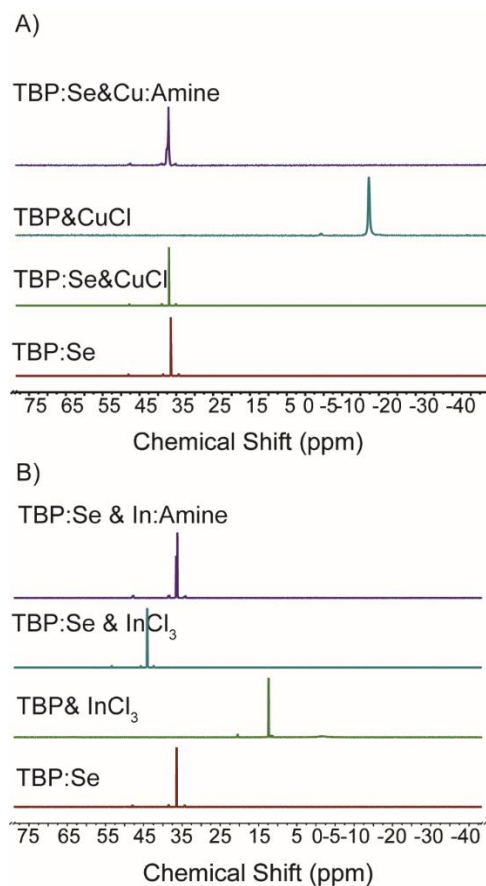


Figure 3.6:  $^{31}\text{P}$ -NMR spectra in  $\text{CDCl}_3$  of TBP=Se with (A) Cu and (B) In precursors bonded to the phosphine chalcogenide molecule. Slight chemical shifting is observed, but no additional peaks are observed upon the metal addition.

### 3.3.5: Bond cleavage experiments

In Figure 3.7, bond cleavage energy between the phosphine chalcogenide compounds, (TBP=Se and DPP=Se) and the Cu precursors (CuCl and Cu:OLA), were investigated using TGA. As shown in Figure 3.7A and 3.7B, weight loss occurs above 300°C for the TBP=Se-CuCl species and at around 200°C for DPP=Se-CuCl. This indicates that a reaction temperature of 240°C is not high enough for TBP to cleave from

the selenium copper complex, which may be the leading reason for low yield formation (Figure 3.7B). Higher reaction temperatures of 375°C were studied for Method II, but the resulting nanocrystals were not dispersible in toluene. Additionally, the DPP=Se-CuCl species exhibits two plateaus in the TGA data at around 200°C and ~400°C, indicating that there are two distinct chemical species. This is consistent with the <sup>31</sup>P-NMR data shown in Figure 3.5. Figure 3.7C shows that the DPP-CuCl species requires a higher temperature than the TBP-CuCl (Figure 3.7D) system in order for the phosphine metal bond to cleave. As a result, we believe that the first plateau at 200°C is due to DPP=Se-CuCl species which supports the higher yield for the DPP system. Even though DPP-CuCl demonstrates a need for higher temperatures, the formation of this compound is not significant to impede high conversion yields in Method I. Figure 3.7E and 3.7F shows that when the Cu:OLA precursor is used similar temperatures are needed to cleave the bond for both phosphine chalcogenide reactants. Thus suggesting that the amines allows the reaction mechanism for both systems to be similar.

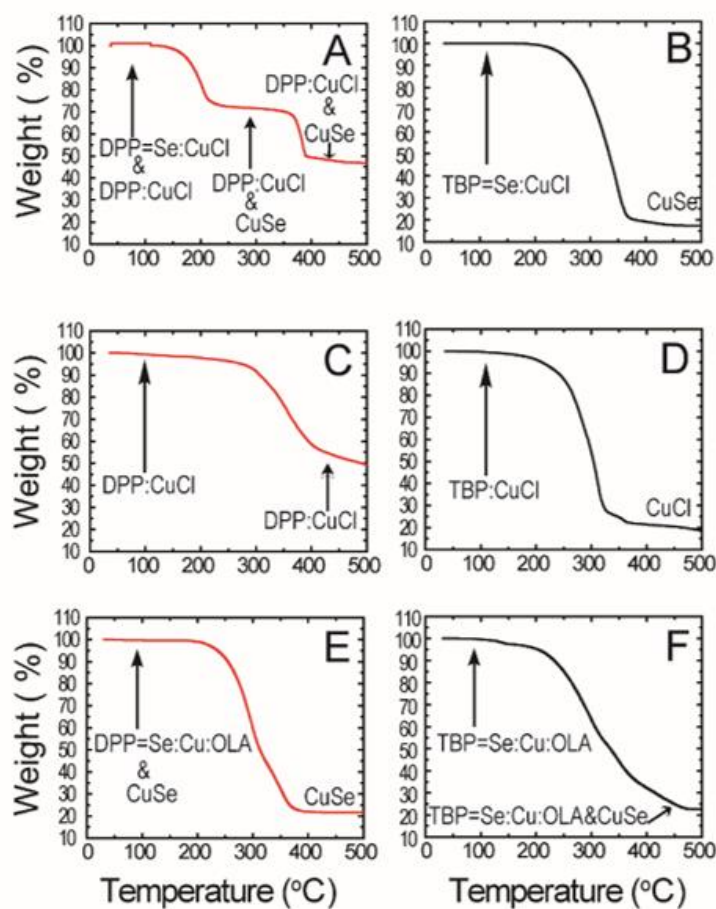


Figure 3.7: TGA data for DPP=Se (A, C, and E) and TBP=Se (B, D, and F) copper precursor heating experiments. (A ) DPP=Se and CuCl (B) TBP=Se and CuCl (C) DPP and CuCl (D) TBP and CuCl (E) DPP=Se and Cu:OLA (F) TBP=Se and Cu:OLA. The black curve reflects TBP=Se and the red curve DPP=Se for each spectrum respectively.

### 3.3.6: Nanocrystal PV Device Performance

PV devices were fabricated using the CuInSe<sub>2</sub> nanocrystals from each method as the active absorber layer. Our photovoltaic device structure has been previously described, but is briefly stated here. 60 nm of gold is thermally evaporated onto cleaned soda lime glass, CuInSe<sub>2</sub> is spray coated on to the substrate. Top contact layers are added to the

substrates, including cadmium sulfide (CdS), zinc oxide (ZnO), and indium tin oxide (ITO) ((In<sub>2</sub>O<sub>3</sub>):(SnO<sub>2</sub>)), via chemical bath deposition and sputtering, respectively. The device efficiency will be analyzed through photo response by utilizing an AM1.5 solar simulator. It is to note that all devices were tested without sintering.

The data in Figure 3.8 PV devices made using CuInSe<sub>2</sub> nanocrystals produced by the three different methods. PV devices made with CuInSe<sub>2</sub> nanocrystals produced by Method II have the highest efficiency. This may be due to the different surface passivation between the synthetic methods. Additionally, employing 8.6 mmol of DPP in Method III to increase product yield, does not affect the performance of the photovoltaic devices. This data supported with the <sup>31</sup>P-NMR data in Figure 3.4 insinuates that the TBP may assist in more effective surface passivation of the CuInSe<sub>2</sub> than with DPP.



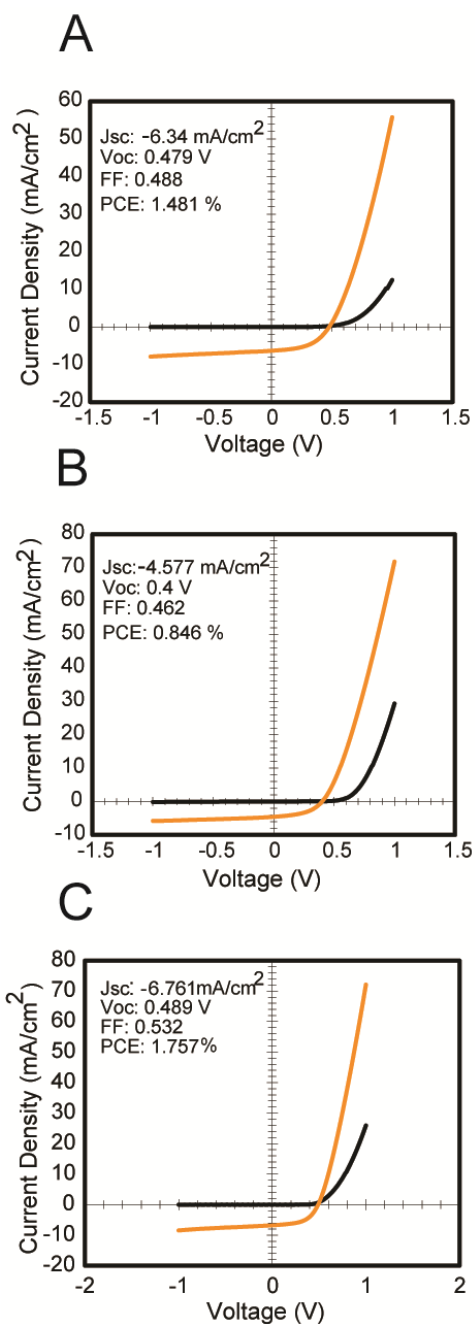


Figure 3.8. Current-voltage curves for  $\text{CuInSe}_2$  nanocrystal photovoltaic devices employing (A)  $\text{CuInSe}_2$  nanocrystals from Method II (B)  $\text{CuInSe}_2$  nanocrystals from Method I (C)  $\text{CuInSe}_2$  nanocrystals from Method III. The above current-voltage curves are shown with illumination  $100 \text{ mW}/\text{cm}^2$ , AM 1.5.

### 3.3.7: Mechanism

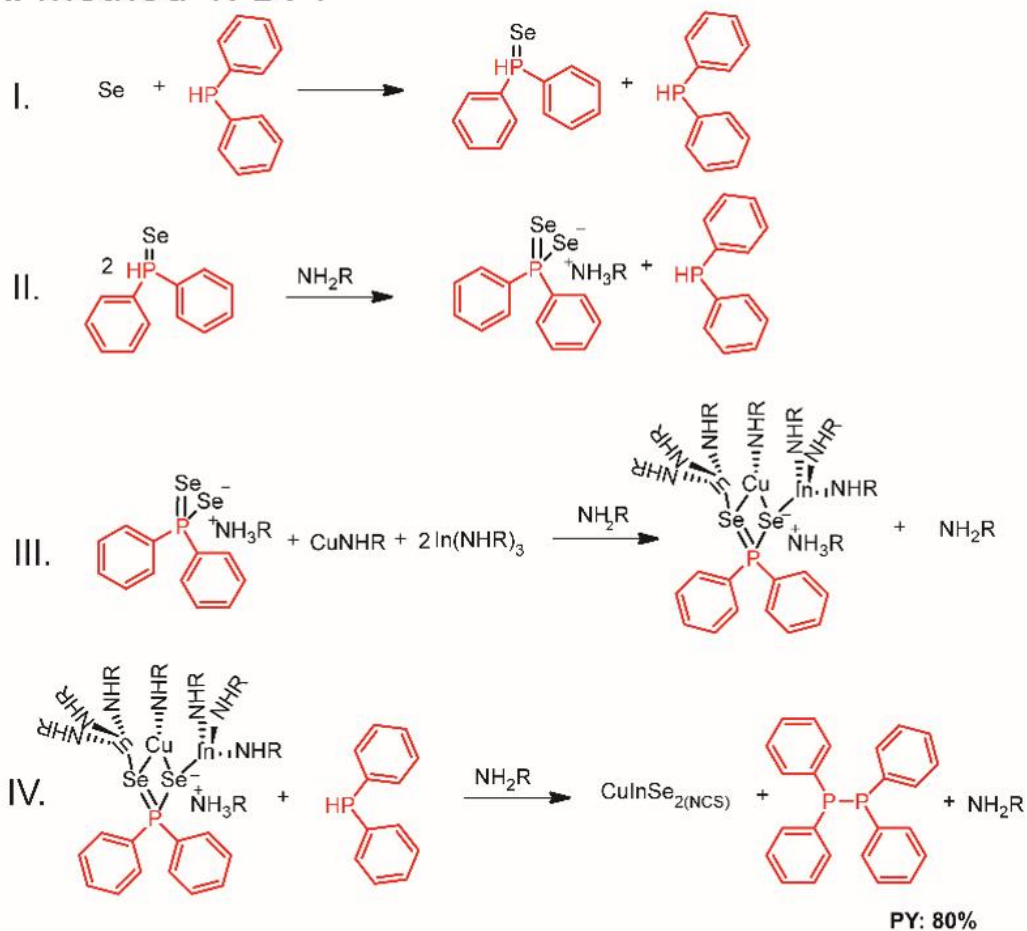
Figures 3.9 and 3.10 show schemes 1 and 2 show the proposed mechanism based on the  $^{31}\text{P}$ -NMR data shown above; figures 3.2 & 3.3. Phosphine selenides are formed that provide a more reactive Se reagent in the proper oxidation state  $\text{Se}^{2-}$  than the elemental Se. In Method II and III, the phosphine selenide reagent, shown in the first line of scheme 2, has one Se atom bonded to phosphorous; however, in Method I the phosphine selenide reactant contains two Se atoms once exposed to oleylamine. This phenomenon has also been observed in literature, which shows that the addition of oleylamine allows for the formation of the phosphine selenide, shown in scheme 1.<sup>39</sup> Shown in Appendix A, employing  $^{31}\text{P}$ -NMR we found that there were two phosphine selenide species upon the addition of oleylamine, the first shift at  $\delta = 7\text{ppm}$  and  $\delta = 22\text{ppm}$ . Due to the excess oleylamine used in the reaction (15:1 oleylamine to metal), we believe that our selenium precursor for Method I is the phosphine bound to two Se atoms; allowing for a more reactive Se reagent rather than the Se reactant in Method II and III. The chloride metal precursors are ligand exchanged to oleylamine capped metals; which have been known to increase reaction rates<sup>40,41</sup>. Phosphine selenide complexes bind to metal precursors to form activated intermediate complexes, shown in Figure 3.10.

Several other studies have also indicated that the binding of metal precursors to phosphine chalcogenide species creates an activated transition complex responsible for nanocrystal formation.<sup>42-45,45,46</sup> This formation of the metal-phosphine chalcogenide allows for the weakening of the phosphine chalcogenide bond, which instigates nucleophilic attack on the phosphorous by the present ligands, such as carboxylic acid or amines, and

promotes phosphine chalcogenide bond cleavage.<sup>47-50</sup> As a result of this bond cleavage, tetraphenylbiphosphine (TPBP) can be formed; as shown in figures 3.1 and 3.2, due to the nucleophilic attack of the excess phosphine or oleylamine.

In the literature, the formation of CuSe and In<sub>2</sub>Se<sub>3</sub> have been found as the active intermediates to CuInSe<sub>2</sub> nanoparticle growth; however, the NMR data did not show the formation of two selenium reactants, which does not support this phenomenon. This may be due to the fact that our <sup>31</sup>P-NMR experiments were observed at room temperature, which has been known to give an average chemical shift.<sup>34</sup>

### A. Method 1: DPP



## B. Method II: TBP

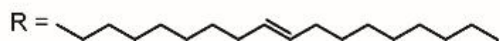
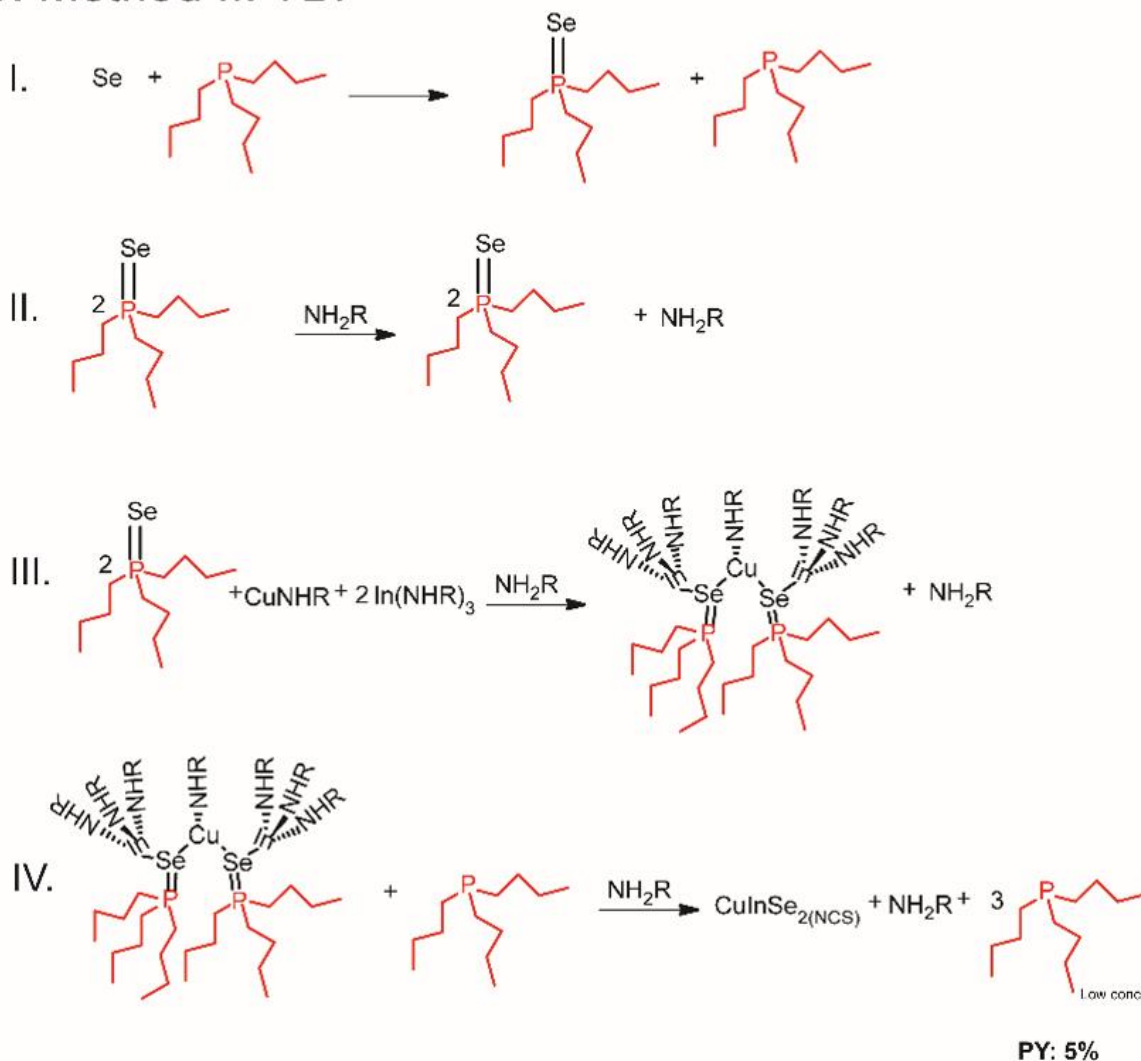
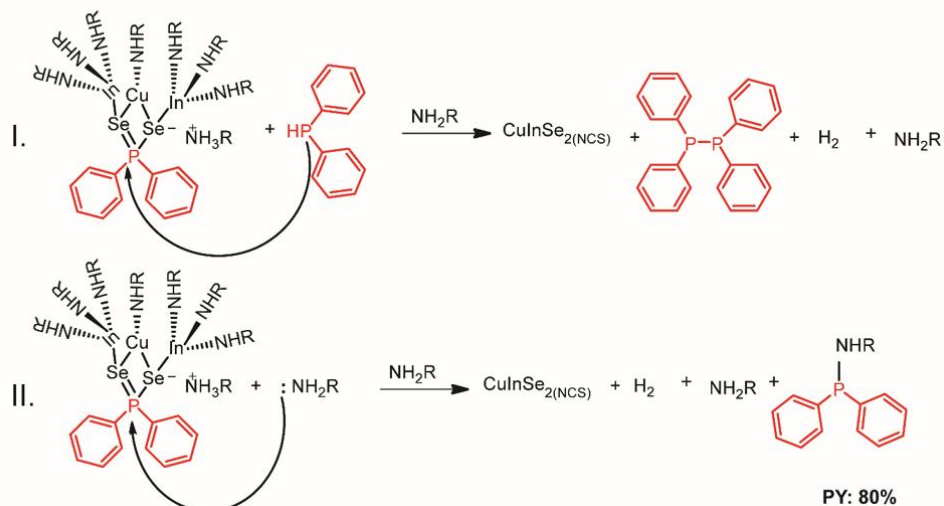


Figure 3.9: (**scheme 1**) Proposed mechanism for  $\text{CuInSe}_2$  nanocrystal formation using Method I (A) and Method II (B). (I) shows the formation of the phosphine chalcogenide molecule. (II) Depicts the injection of the phosphine chalcogenide molecule into OLA. (III) The formation of the intermediate complex. (IV) Bond cleavage between the phosphine and Se to form  $\text{CuInSe}_2$  nanocrystals.

## A. Method 1: DPP



## B. Method II: TBP

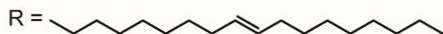
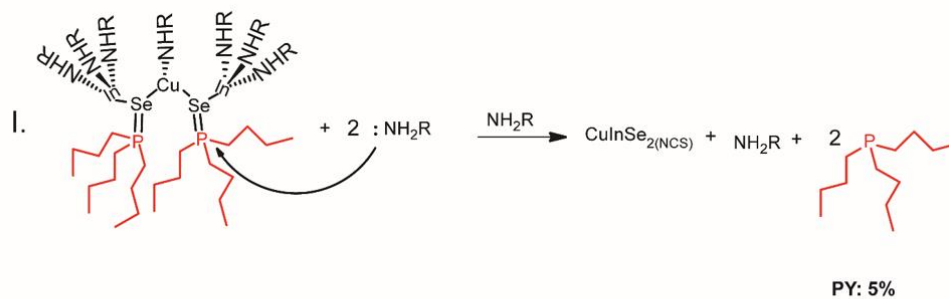


Figure 3.10: (**scheme 2**) Break down on step (IV) in figure 3.9 for Method I (A) and Method II (B). (A) I. A nucleophilic attack on the phosphorous atom with excess DPP on the intermediate complex yielding CuInSe<sub>2</sub> nanocrystals and tetraphenylbiphosphine TPBP (seen in Figure 3.2) II. Nucleophilic attack OLA on the intermediate complex yielding CuInSe<sub>2</sub> nanocrystals and DPP-OLA. (B) Nucleophilic attack on the intermediate complex with 2 OLA molecules yielding in CuInSe<sub>2</sub> and TBP as products. However, the production of TBP isn't shown in Figure 3.3 insinuating that the excess TBP are in low concentrations.

### 3.4: CONCLUSIONS

Three different approaches to the synthesis of CuInSe<sub>2</sub> nanocrystals were studied using <sup>31</sup>P-NMR and TGA Method I using DPP=Se as the selenium reagent, Method II TBP=Se and Method III TBP=Se with the addition of DPP. Nanocrystal synthesis proceeds by the same reaction mechanism in each case; however, the ease of P-H bond cleavage allows for a more reactive selenium reactant formation, therefore, providing higher conversion yields to be achieved in Methods I and III than Method II. Moreover, these differences in Se reactants not only affects the conversion yields, but also PV device performance. Even though Method I produces the highest conversion yield of ~86%, PV devices fabricated with these nanocrystals yield the lowest power conversion efficiencies. Conversely, the synthetic route with the lowest reaction yield of only of ~5% gave the best performing devices. Employing Method III significantly increases the conversion yield of Method II (~47%); but the amount of secondary phosphine, DPP in our case, will significantly alter the device performance. Devices made with nanocrystals synthesized with varying amounts of DPP exhibited the highest performance when 8.6 mmol of DPP was used to increase the reaction yield while exceeding the PV device efficiency of Method II.

### 3.5: REFERENCES

1. Kovalenko, M. V.; Manna, L.; Cabot, A.; Hens, Z.; Talapin, D. V.; Kagan, C. R.; Klimov, V. I.; Rogach, A. L.; Reiss, P.; Milliron, D. J.; *et.al.* Prospects of Nanoscience with Nanocrystals. *ACS Nano* **2015**, *9*, 1012–1057.

2. Thomas, S. R.; Chen, C.-W.; Date, M.; Wang, Y.-C.; Tsai, H.-W.; Wang, Z. M.; Chueh, Y.-L. Recent developments in the synthesis of nanostructured chalcopyrite materials and their applications: a review. *RSC Adv.* **2016**, *6*, 60643–60656.
3. Sargent, E. H. Colloidal quantum dot solar cells. *Nat. Photonics* **2012**, *6*, 133–135.
4. Akhavan, V. A.; Goodfellow, B. W.; Panthani, M. G.; Reid, D. K.; Hellebusch, D. J.; Adachi, T.; Korgel, B. A. Spray-deposited CuInSe<sub>2</sub> nanocrystal photovoltaics. *Energy Environ. Sci.* **2010**, *3*, 1600–1606.
5. Panthani, M. G.; Akhavan, V.; Goodfellow, B.; Schmidtke, J. P.; Dunn, L.; Dodabalapur, A.; Barbara, P. F.; Korgel, B. A. Synthesis of CuInS<sub>2</sub>, CuInSe<sub>2</sub>, and Cu(In<sub>x</sub>Ga<sub>1-x</sub>)Se<sub>2</sub> (CIGS) Nanocrystal ‘Inks’ for Printable Photovoltaics. *J. Am. Chem. Soc.* **2008**, *130*, 16770–16777.
6. Aldakov, D.; Lefrançois, A.; Reiss, P. Ternary and quaternary metal chalcogenide nanocrystals: synthesis, properties and applications. *J. Mater. Chem. C* **2013**, *1*, 3756–3776.
7. Chen, H.; Yu, S.-M.; Shin, D.-W.; Yoo, J.-B. Solvothermal Synthesis and Characterization of Chalcopyrite CuInSe<sub>2</sub> Nanoparticles. *Nanoscale Res. Lett.* **2009**, *5*, 217–223.
8. Huang, W.-C.; Tseng, C.-H.; Chang, S.-H.; Tuan, H.-Y.; Chiang, C.-C.; Lyu, L.-M.; Huang, M. H. Solvothermal Synthesis of Zincblende and Wurtzite CuInS<sub>2</sub> Nanocrystals and Their Photovoltaic Application. *Langmuir* **2012**, *28*, 8496–8501.

9. Grisaru, H.; Palchik, O.; Gedanken, A.; Palchik, V.; Slifkin, M. A.; Weiss, A. M. Microwave-Assisted Polyol Synthesis of CuInTe<sub>2</sub> and CuInSe<sub>2</sub> Nanoparticles. *Inorg. Chem.* **2003**, *42*, 7148–7155.
10. Mitzi, D. B.; Yuan, M.; Liu, W.; Kellock, A. J.; Chey, S. J.; Deline, V.; Schrott, A. G. A High-Efficiency Solution-Deposited Thin-Film Photovoltaic Device. *Adv. Mater.* **2008**, *20*, 3657–3662.
11. Norako, M. E.; Brutchey, R. L. Synthesis of Metastable Wurtzite CuInSe<sub>2</sub> Nanocrystals. *Chem. Mater.* **2010**, *22*, 1613–1615.
12. Akhavan, V. A.; Goodfellow, B. W.; Panthani, M. G.; Steinhagen, C.; Harvey, T. B.; Stolle, C. J.; Korgel, B. A. Colloidal CIGS and CZTS nanocrystals: A precursor route to printed photovoltaics. *J. Solid State Chem.* **2012**, *189*, 2–12.
13. Zhong, H.; Zhou, Y.; Ye, M.; He, Y.; Ye, J.; He, C.; Yang, C.; Li, Y. Controlled Synthesis and Optical Properties of Colloidal Ternary Chalcogenide CuInS<sub>2</sub> Nanocrystals. *Chem. Mater.* **2008**, *20*, 6434–6443.
14. Peng, S.; Liang, Y.; Cheng, F.; Liang, J. Size-controlled chalcopyrite CuInS<sub>2</sub> nanocrystals: One-pot synthesis and optical characterization. *Sci. China Chem.* **2011**, *55*, 1236–1241.
15. Steinhagen, C.; Panthani, M. G.; Akhavan, V.; Goodfellow, B.; Koo, B.; Korgel, B. A. Synthesis of Cu<sub>2</sub>ZnSnS<sub>4</sub> Nanocrystals for Use in Low-Cost Photovoltaics. *J. Am. Chem. Soc.* **2009**, *131*, 12554–12555.



16. Reifsnyder, D. C.; Ye, X.; Gordon, T. R.; Song, C.; Murray, C. B. Three-Dimensional Self-Assembly of Chalcopyrite Copper Indium Diselenide Nanocrystals into Oriented Films. *ACS Nano* **2013**, *7*, 4307–4315.
17. Guo, Q.; Kim, S. J.; Kar, M.; Safarman, W. N.; Birkmire, R. W.; Stach, E. A.; Agrawal, R.; Hillhouse, H. W. Development of CuInSe<sub>2</sub> Nanocrystal and Nanoring Inks for Low-Cost Solar Cells. *Nano Lett.* **2008**, *8*, 2982–2987.
18. Panthani, M. G.; Stolle, C. J.; Reid, D. K.; Rhee, D. J.; Harvey, T. B.; Akhavan, V. A.; Yu, Y.; Korgel, B. A. CuInSe<sub>2</sub> Quantum Dot Solar Cells with High Open-Circuit Voltage. *J. Phys. Chem. Lett.* **2013**, *4*, 2030–2034.
19. Guo, Q.; Ford, G. M.; Hillhouse, H. W.; Agrawal, R. Sulfide Nanocrystal Inks for Dense Cu(In<sub>1-x</sub>Ga<sub>x</sub>)(S<sub>1-y</sub>Se<sub>y</sub>)<sub>2</sub> Absorber Films and Their Photovoltaic Performance. *Nano Lett.* **2009**, *9*, 3060–3065.
20. Liu, Y.; Yao, D.; Shen, L.; Zhang, H.; Zhang, X.; Yang, B. Alkylthiol-Enabled Se Powder Dissolution in Oleylamine at Room Temperature for the Phosphine-Free Synthesis of Copper-Based Quaternary Selenide Nanocrystals. *J. Am. Chem. Soc.* **2012**, *134*, 7207–7210.
21. Wei, H.; Guo, W.; Sun, Y.; Yang, Z.; Zhang, Y. Hot-injection synthesis and characterization of quaternary Cu<sub>2</sub>ZnSnSe<sub>4</sub> nanocrystals. *Mater. Lett.* **2010**, *64*, 1424–1426.
22. Riha, S. C.; Parkinson, B. A.; Prieto, A. L. Solution-Based Synthesis and Characterization of Cu<sub>2</sub>ZnSnS<sub>4</sub> Nanocrystals. *J. Am. Chem. Soc.* **2009**, *131*, 12054–12055.

23. Tang, J.; Hinds, S.; Kelley, S. O.; Sargent, E. H. Synthesis of Colloidal CuGaSe<sub>2</sub>, CuInSe<sub>2</sub>, and Cu(InGa)Se<sub>2</sub> Nanoparticles. *Chem. Mater.* **2008**, *20*, 6906–6910.
24. Pan, D.; Wang, X.; Zhou, Z. H.; Chen, W.; Xu, X.; Lu, Y. Synthesis of Cu–In–S Ternary Nanocrystals with Tunable Structure and Composition. *J. Am. Chem. Soc.* **2008**, *130*, 5620–5621.
25. Nakamura, H.; Kato, W.; Uehara, M.; Nose, K.; Omata, T.; Otsuka-Yao-Matsuo, S.; Miyazaki, M.; Maeda, H. Tunable Photoluminescence Wavelength of Chalcopyrite CuInS<sub>2</sub>-Based Semiconductor Nanocrystals Synthesized in a Colloidal System. *Chem. Mater.* **2006**, *18*, 3330–3335.
26. Allen, P. M.; Bawendi, M. G. Ternary I–III–VI Quantum Dots Luminescent in the Red to Near-Infrared. *J. Am. Chem. Soc.* **2008**, *130*, 9240–9241.
27. Stolle, C. J.; Harvey, T. B.; Pernik, D. R.; Hibbert, J. I.; Du, J.; Rhee, D. J.; Akhavan, V. A.; Schaller, R. D.; Korgel, B. A. Multiexciton Solar Cells of CuInSe<sub>2</sub> Nanocrystals. *J. Phys. Chem. Lett.* **2014**, *5*, 304–309.
28. Ahmadi, M.; Pramana, S. S.; Xi, L.; Boothroyd, C.; Lam, Y. M.; Mhaisalkar, S. Evolution Pathway of CIGSe Nanocrystals for Solar Cell Applications. *J. Phys. Chem. C* **2012**, *116*, 8202–8209.
29. Kar, M.; Agrawal, R.; Hillhouse, H. W. Formation pathway of CuInSe<sub>2</sub> nanocrystals for solar cells. *J. Am. Chem. Soc.* **2011**, *133*, 17239–17247.
30. Zhong, H.; Wang, Z.; Bovero, E.; Lu, Z.; van Veggel, F. C. J.; Scholes, G. D. Colloidal CuInSe<sub>2</sub> Nanocrystals in the Quantum Confinement Regime: Synthesis, Optical Properties, and Electroluminescence. *J. Phys. Chem. C* **2011**, *115*, 12396–12402.

31. Zhong, H.; Li, Y.; Ye, M.; Zhu, Z.; Zhou, Y.; Yang, C.; Li, Y. A facile route to synthesize chalcopyrite CuInSe<sub>2</sub> nanocrystals in non-coordinating solvent. *Nanotechnology* **2007**, *18*, 25602-25607.
32. Akhavan, V. A.; Panthani, M. G.; Goodfellow, B. W.; Reid, D. K.; Korgel, B. A. Thickness-limited performance of CuInSe<sub>2</sub> nanocrystal photovoltaic devices. *Opt. Express* **2010**, *18*, A411-A420.
33. Evans, C. M.; Evans, M. E.; Krauss, T. D. Mysteries of TOPSe Revealed: Insights into Quantum Dot Nucleation. *J. Am. Chem. Soc.* **2010**, *132*, 10973–10975.
34. García-Rodríguez, R.; Liu, H. A Nuclear Magnetic Resonance Study of the Binding of Trimethylphosphine Selenide to Cadmium Oleate. *J. Phys. Chem. A* **2014**, *118*, 7314–7319.
35. Steckel, J. S.; Yen, B. K. H.; Oertel, D. C.; Bawendi, M. G. On the Mechanism of Lead Chalcogenide Nanocrystal Formation. *J. Am. Chem. Soc.* **2006**, *128*, 13032–13033.
36. Joo, J.; Pietryga, J. M.; McGuire, J. A.; Jeon, S.-H.; Williams, D. J.; Wang, H.-L.; Klimov, V. I. A Reduction Pathway in the Synthesis of PbSe Nanocrystal Quantum Dots. *J. Am. Chem. Soc.* **2009**, *131*, 10620–10628.
37. Wang, F.; Buhro, W. E. Morphology Control of Cadmium Selenide Nanocrystals: Insights into the Roles of Di-n-octylphosphine Oxide (DOPO) and Di-n-octylphosphinic Acid (DOPA). *J. Am. Chem. Soc.* **2012**, *134*, 5369–5380.
38. Cossairt, B. M.; Owen, J. S. CdSe Clusters: At the Interface of Small Molecules and Quantum Dots. *Chem. Mater.* **2011**, *23*, 3114–3119.

39. Guo, Y.; Marchuk, K.; Sampat, S.; Abraham, R.; Fang, N.; Malko, A. V.; Vela, J. Unique Challenges Accompany Thick-Shell CdSe/nCdS ( $n > 10$ ) Nanocrystal Synthesis. *J. Phys. Chem. C* **2012**, *116*, 2791–2800.
40. Li, L. S.; Pradhan, N.; Wang, Y.; Peng, X. High Quality ZnSe and ZnS Nanocrystals Formed by Activating Zinc Carboxylate Precursors. *Nano Lett.* **2004**, *4*, 2261–2264.
41. Liu, H.; Owen, J. S.; Alivisatos, A. P. Mechanistic Study of Precursor Evolution in Colloidal Group II–VI Semiconductor Nanocrystal Synthesis. *J. Am. Chem. Soc.* **2007**, *129*, 305–312.
42. Owen, J. S.; Chan, E. M.; Liu, H.; Alivisatos, A. P. Precursor Conversion Kinetics and the Nucleation of Cadmium Selenide Nanocrystals. *J. Am. Chem. Soc.* **2010**, *132*, 18206–18213.
43. Owen, J. S.; Park, J.; Trudeau, P.-E.; Alivisatos, A. P. Reaction Chemistry and Ligand Exchange at Cadmium–Selenide Nanocrystal Surfaces. *J. Am. Chem. Soc.* **2008**, *130*, 12279–12281.
44. García-Rodríguez, R.; Liu, H. Mechanistic Study of the Synthesis of CdSe Nanocrystals: Release of Selenium. *J. Am. Chem. Soc.* **2012**, *134*, 1400–1403.
45. García-Rodríguez, R.; Hendricks, M. P.; Cossairt, B. M.; Liu, H.; Owen, J. S. Conversion reactions of cadmium chalcogenide nanocrystal precursors. *Chem. Mater.* **2013**, *25*, 1233–1249.
46. Chen, C. H.; Brighty, K. E. A new phosphine-sulfides-to-phosphine-oxides exchange reaction. *Tetrahedron Lett.* **1980**, *21*, 4421–4424.

47. Heliński, J.; Skrzypeczyński, Z.; Wasiak, J.; Michalski, J. Efficient oxygenation of thiophosphoryl and selenophosphoryl groups using trifluoroacetic anhydride. *Tetrahedron Lett.* **1990**, *31*, 4081–4084.
48. Yu, K.; Liu, X.; Chen, Q. Y.; Yang, H.; Yang, M.; Wang, X.; Wang, X.; Cao, H.; Whitfield, D. W.; Hu, C.; Tao, Y. Mechanistic Study of the Role of Primary Amines in Precursor Conversions to Semiconductor Nanocrystals at Low Temperature. *Angew. Chem. Int. Ed.* **2014**, *53*, 6898–6904.
49. Yu, K.; Liu, X.; Zeng, Q.; Leek, D. M.; Ouyang, J.; Whitmore, K. M.; Ripmeester, J. A.; Tao, Y.; Yang, M. Effect of Tertiary and Secondary Phosphines on Low-Temperature Formation of Quantum Dots. *Angew. Chem. Int. Ed.* **2013**, *52*, 4823–4828.
50. Sun, Z. H.; Oyanagi, H.; Nakamura, H.; Jiang, Y.; Zhang, L.; Uehara, M.; Yamashita, K.; Fukano, A.; Maeda, H. Ligand Effects of Amine on the Initial Nucleation and Growth Processes of CdSe Nanocrystals. *J. Phys. Chem. C* **2010**, *114*, 10126–10131.

## Chapter 4: Synthesis and Characterization of Perovskite Nanocrystals

### 4.1: INTRODUCTION

Over the past decades, perovskite photovoltaic (PV) devices have been the fastest growing set of PV devices thus far. Single junction PV devices have risen from ~ 4% efficiencies to over 20% in under a decade<sup>1</sup>. Traditionally, perovskite PV devices are fabricated from spin coating solutions and annealing the perovskite layer to achieve the desired crystal structure. These process are air sensitive, time consuming, and energy intensive for the annealing of the layer. Nanocrystals can be used to increase the stability of the materials under ambient conditions by passivating (capping) the materials with ligands.<sup>2</sup> Furthermore, this will allow for more versatile deposition of the perovskite absorber layer. Nanocrystalline perovskite materials have been used for various applications such as light emitting diodes, lasers, photoelectrolysis, and photovoltaic devices.<sup>3</sup> In this chapter we focus on cesium and formamidinium based nanocrystal synthesis for PV devices.

Perovskite nanocrystals are very attractive materials to serve as the absorber layer for nanocrystal PV devices<sup>4</sup>. Due to their easiness of synthesis, nanocrystals can be formed under shorter times than traditional techniques of fabrications. The band gap can be tuned not only by size but also by the exchange or doping of halides (Br, I, and Cl) and/or cations such as methyl ammonium, bismuth, formamidinium, and antimony.<sup>5</sup> Furthermore, the nanocrystals exhibit high quantum yields and defect tolerant devices which allows for more electrons to be extracted from the nanocrystals. Currently, perovskite nanocrystalline devices hold the record efficiencies within this category at 13.4%.<sup>6</sup>

Perovskites are materials that have the same crystals structures as  $\text{CaTiO}_3$ . The materials receive their name from their crystal structure ( $\text{ABX}_3$ ) shown in Figure 4.1.<sup>7</sup> A

and B sites are cations of two different sizes where the A site cation is larger than the B site. The B site forms an octahedron with the X sites and the A sites form a cuboctahedral structure with the X sites. The X sites are anions that bind to both cations. In this dissertation the A sites will be either Cs, FA, MA, or a mix. The B site will be Pb and the X sites will be halogens specifically Br and I. Cesium lead halide nanocrystals were first reported in the late 1800s. Recently, CsPbX<sub>3</sub> nanocrystals were synthesized using the hot injection method founded by Kovalenko's group<sup>2,8,9</sup>. In short, octadecene and lead iodide are degassed at 110°C for one hour. Oleylamine and oleic acid are injected into the reaction flask at 170°C resulting in the formation of a lead complex. Lastly, Cs-oleate is injected into the flask and allowed to react for 5 seconds before quenching the reaction via ice water bath. There has been a lot of discrepancy over the crystal of the nanocrystals, which typically forms cubic and orthorhombic structures depending on the strain of the B site X site bond.

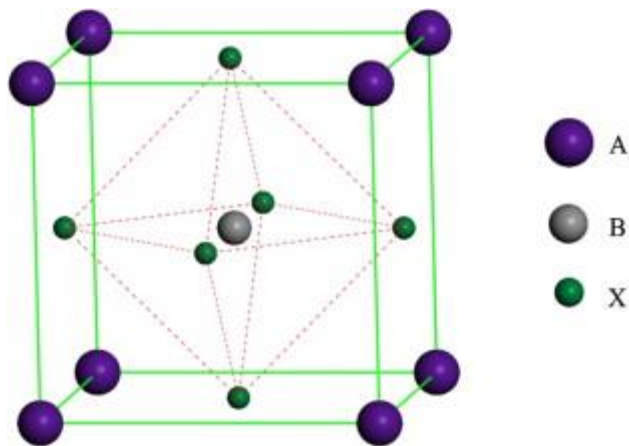


Figure 4.1: Perovskite crystal structure where the purple circles denotes the A sites, gray sphere denotes the B sites, and the green spheres denotes the X sites. Adapted from reference (7), copyrighted 2013 Elsevier B.V.

There are several methods used to synthesize perovskite nanocrystals such as hot injection, microwave, and robotic methods<sup>1-3,6,8,10-31</sup>. However, the nanocrystals are still

air sensitive and many morphologies exist after washing such as nanoplatelets, nanowires, and nanosheets. As a result, there has been many researchers are looking for capping ligands that will replace the liable oleyamine and oleic acid ligands. In literature, there are several ligands that are being explored such as zwitterionic, sulfonate, quaternary ammonium, and other ligands<sup>2,15,16,20,29</sup>. In this dissertation we will focus on the replacement of the oleic acid for phosphosphinic acid ligands which has been shown to increase air and moisture stability of the nanocrystals.

## **4.2: PEROVSKITE NANOCRYSTAL SYNTHESIS**

### **4.2.1: Materials**

. Lead Iodide (PbI<sub>2</sub>), lead bromide (PbBr<sub>2</sub>), Cesium Carbonate (Cs<sub>2</sub>CO<sub>3</sub>), 2.0M methylamine in THF, formamidinium acetate (FAac), octadecene (ODE, 90%), oleyamine (OLA, 70%), oleic acid (OA), diisooctylphosphinic acid (DOPA), anhydrous hexane (95%), anhydrous methyl acetate (99.5%) were obtained from Sigma-Aldrich company. All chemicals were used without further purification.

### **4.2.2: Formation of the Cs-oleate and FA-oleate Reactants**

Cs-oleate (0.59 M) was synthesized by loading a 3-neck 100 mL flask with ~2.5 mmols of C<sub>2</sub>CO<sub>3</sub> (0.814g), 40 mL of ODE, and 2.5 mL of OA. The OA is replaced with DOPA for phosphinic capped particles. The reaction flask was degassed at 120°C for 1hr at ~150 mTorr, then the flask temperature was raised to 150°C under a blanket of N<sub>2</sub> until all Cs<sub>2</sub>CO<sub>3</sub> reacted with OA or DOPA. Then the flask was allowed to cool to room temperature, and stored in the glovebox. As the temperature falls below 100°C, Cs-oleate will precipitate out of solution.



FA-oleate was synthesized by charging a 3-neck 100 mL flask with 0.521g of FAac, 16 mL of ODE, and 4 mL of OA. The reaction flask underwent a pump, freeze, thaw method prior to reacting to ensure that the water and oxygen was removed from the flask. The flask was reacted at 130°C until the all of the FAac was dissolved in the reaction solution. Then the heat is removed to a lower temperature of 50°C and placed under vacuum for 30 minutes. After the 30 minutes, the flask was re-filled with N<sub>2</sub> gas and stored in the glovebox.

#### **4.2.3: CsPbX<sub>3</sub> nanocrystal synthesis**

0.88 mmols of PbX<sub>2</sub> (lead bromide or iodide) and 20 mL of ODE was loaded into a 100 mL flask and degassed at 120°C for 1hr at ~150 mTorr. Under a blanket of N<sub>2</sub>, 2 mL of both OLA and OA (or DOPA) were injected into the reaction flask. The reaction flask was placed under vacuum and degassed for an additional 30 minutes at 120°C and ~150 mTorr. The reaction flask temperature was raised to the reaction temperature of 170°C (160°C for PbI<sub>2</sub>) under blanket of N<sub>2</sub> and 3.2 mL of the preheated 0.59 M Cs-oleate solution was injected into the reaction flask. After 5 seconds the reaction product was cooled to room temperature via an ice bath.

#### **4.2.4: CsFAPbX<sub>3</sub> (X = I or Br) nanocrystal synthesis**

0.88 mmols of PbX<sub>2</sub> (lead bromide or iodide) and 20 mL of ODE was loaded into a 100 mL flask and degassed at 120°C for 1hr at ~150 mTorr. Under a blanket of N<sub>2</sub>, 0.5 mL OLA and 1 mL of OA were injected into the reaction flask. The reaction flask was placed under vacuum and degassed for an additional 30 minutes at 120°C and ~150

mTorr. The reaction flask temperature was raised to the reaction temperature of 170°C (160°C for PbI<sub>2</sub>) under blanket of N<sub>2</sub> and 0.27 mL of the preheated 0.59 M Cs-oleate solution and 0.27 mL of FA-oleate were injected into the reaction flask. After 5 seconds the reaction product was cooled to room temperature via an ice bath.

#### **4.2.5: FAPbI<sub>3</sub> nanocrystal synthesis**

0.88 mmols of PbI<sub>2</sub> and 20 mL of ODE was loaded into a 100 mL flask and degassed at 120°C for 1hr at ~150 mTorr. Under a blanket of N<sub>2</sub>, 0.5 mL OLA and 1 mL of OA were injected into the reaction flask. The reaction flask was placed under vacuum and degassed for an additional 30 minutes at 120°C and ~150 mTorr. The reaction flask temperature was lowered to the reaction temperature of 80°C under blanket of N<sub>2</sub> and 2 mL of FA-oleate were injected into the reaction flask. After 30 seconds the reaction product was cooled to room temperature via an ice bath.

#### **4.2.6: CsFAMAPbX<sub>3</sub> (X = I or Br) Nanocrystal Synthesis**

0.187 mmol of PbI<sub>2</sub> or 0.187 mmol PbI<sub>2</sub> and 0.034 mmol PbBr<sub>2</sub> and 5 mL of ODE was loaded into a 25 mL flask and degassed at 120°C for 1hr at ~150 mTorr. Under a blanket of N<sub>2</sub>, 0.5 mL OLA and 1 mL of OA were injected into the reaction flask. The reaction flask was placed under vacuum and degassed for an additional 30 minutes at 120°C and ~150 mTorr. The reaction flask temperature was raised to the reaction temperature of 165°C under blanket of N<sub>2</sub> and 0.75 mL of the preheated 0.59 M Cs-oleate solution, 0.5 mL of FA-oleate, and 0.1 mL of methylamine were injected into the reaction

flask. After 60 seconds the reaction product was cooled to room temperature via an ice bath.

#### **4.2.7: Isolation of Nanocrystal**

After cooling the reaction product to room temperature, the reaction flask was brought into an Ar filled glovebox. The reaction product was equally divided into two separate centrifuge tubes and 15 mL of anhydrous methyl acetate was added to each tube. The perovskite nanocrystals were precipitated via centrifugation, 8000 rpm for 5 minutes, the supernatant was discarded and the precipitate was dispersed in 10 mL of anhydrous hexane. The nanocrystal dispersion was centrifuged again at 8500 rpm for 5 minutes. The supernatant was stored in a 20 mL vial in the refrigerator.

For perovskite nanocrystals synthesized using an organic A site, a slightly different washing procedure is employed. Inside an Ar filled glovebox, the reaction solution is decanted into one centrifuge tube. Centrifuge at 8000 RPM for 5 minutes. Most of the nanoparticles will precipitate out of solution. Pour the supernatant into the plastic tube Add 5 mL of anhydrous hexane into each tube. Add 10mL of anhydrous methyl acetate to the glass tube. Centrifuge at 8000 RPM for 5 minutes. The poorly capped particles will fall to the bottom. Add 15mL of anhydrous hexane to the glass centrifuge tube Centrifuge at 8500 RPM for 15 minutes. Pipette the solution into a 20 mL vial and store the sample in the freezer.

#### 4.2.8: Characterization of Perovskite Nanocrystals

Perovskite NCs were imaged by transmission electron microscopy (TEM) using a FEI Tecnai G2 Spirit BioTwin TEM or a JEOL 2010F TEM. The FEI Tecnai G2 TEM and JEOL 2010F TEM were operated at 80 kV and 200 kV, respectively. Samples were prepared for imaging by adding 240  $\mu\text{L}$  of anhydrous hexane and 20  $\mu\text{L}$  of isolated nanocrystals (40  $\mu\text{L}$  for iodide samples, due to lower reaction yields) into a 4.5 mL vial with a mesh nickel carbon-coated grid, supplied by Electron Microscopy Sciences (Cat#: CF150-Ni), placed at the bottom of vial. The vial is evaporated overnight in the glovebox, to prevent changes in morphology and crystal structure. For high resolution TEM imaging, nanocrystal solutions were drop casted on a copper coated lacy carbon film (Cat#: 50-268-70) supplied from Electron Microscopy Sciences.

UV-visible absorbance spectra were measured using a Varian Cary Bio (UV-vis) spectrophotometer using a quartz cuvette. Photoluminescence (PL) were performed on a Varian Cary Eclipse Fluorescence spectrometer. The quartz cuvettes were prepared in an Argon filled glovebox to protect the integrity of the nanocrystals.

A Rigaku R-axis Spider diffractometer was used to perform powder X-Ray diffraction (XRD). Samples were removed from the freezer and rotovap for 15 minutes under vacuum. Clean nylon loops, sample mounts, dipped into each sample. The diffractometer was operated at 40 kV and 40 mA under a Cu  $K\alpha$  radiation ( $\lambda = 1.5418 \text{ \AA}$ ) rotated at  $5^\circ \text{ sec}^{-1}$  for 10 min. 2DP and JADE were used to process the data and background subtraction.

## 4.3: RESULTS AND CONCLUSION

### 4.3.1: CsPbX<sub>3</sub> nanocrystals

Using the techniques described in section 4.2, CsPbX<sub>3</sub> nanocrystals were synthesized, isolated, and characterized. Figure 4.2 shows the TEM, high resolution TEM, and SEM images of CsPbBr<sub>3</sub>, CsPbI<sub>3</sub> synthesized using oleic acid, and CsPbI<sub>3</sub> synthesized using diioctylphosphinic acid, Figure 4.2 A-C. In order to avoid confusion will refer to CsPbBr<sub>3</sub> nanocrystals as CB, CsPbI<sub>3</sub> synthesized with oleic acid as OA, and CsPbI<sub>3</sub> synthesized with diioctylphosphinic acid as PA. The nanocrystals synthesized with Br exhibited cubic and rectangular morphologies with average nanocrystal lengths between 8 nm and 17 nm. When the OA ligand is replaced with a PA, larger nanocrystals are formed when using the exact reaction conditions. From high resolution TEM, the lattice fringes can be seen, and the lattice spacing can be determined. For the CB sample the lattice spacing was 5.9 Å indicating the (Figure 4.2 D). Furthermore, 3.1 Å for OA nanocrystals and 6.24 Å for PA nanocrystals lattice spacings were determined. Both lattice spacings were indicative of the (002) plane for the  $\alpha$ -cubic and  $\gamma$ -orthorhombic crystals structures. (Figure 4.2 E and 4.2 F). From the SEM images (Figure 4.2 G-I), it is clear that the nanocrystals form hundreds of nanometer lengths superlattices, also known as order arrays. It is to note that PA samples only form long range ordering when the concentration is increased to 10 times the concentration of the standard procedure discussed in section 4.2. The perovskite nanocrystal superlattice is further discussed in Chapter 5.

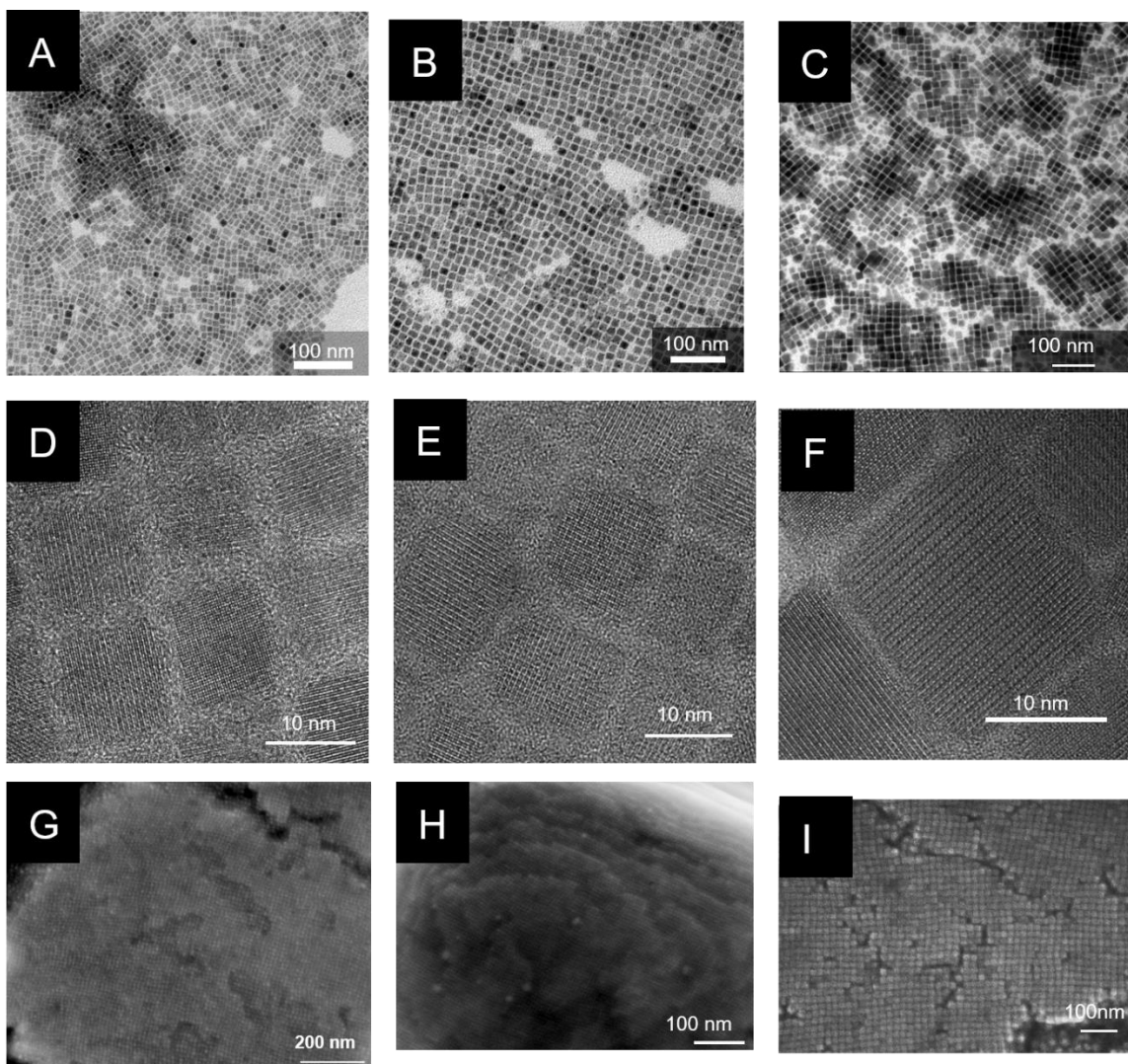


Figure 4.2.: TEM, high resolution TEM, and SEM images of CsPbBr<sub>3</sub>, CsPbI<sub>3</sub> synthesized with oleic acid (OA), and CsPbI<sub>3</sub> synthesized with diisooctylphosphinic acid (DOPA). (A) CsPbBr<sub>3</sub> nanocrystals with an average side length of (B) CsPbI<sub>3</sub> nanocrystals, synthesized with OA, with an average side length of  $8.6 \pm 1.5$  nm (OA). (C) CsPbI<sub>3</sub> nanocrystals, synthesized with DOPA, with an average side length of  $17.5 \pm 2.8$  nm (PA). (D-F) High resolution TEM images of CB, OA, and PA nanocrystals respectively. (G-I) SEM images of order arrays of CB, OA, and PA nanocrystals respectively.

The optical gap of the nanocrystals were determined from UV-vis absorbance and PL emission peak spectra shown in Figure 4.3. The PL emission peaks for CB, OA, and

PAB, were 2.36 eV, 1.89 eV, and 1.82 eV, when excited using a 400 nm wavelength respectively. The optical properties were shown to be dependent on the concentration of Cs-oleate that was used, Figure 4.4. The higher the concentration of Cs-oleate, the more the PL peak experienced a red shift. When using Cs-oleate with a concentration of 0.19M two peaks can be observed in figure 4.4 A, insinuating the fact that two distinct sizes may exist. Additionally, when a 0.1M solution of Cs-oleate is used in the OA synthesis, the nanocrystals cannot be successfully isolated from the crude solution and large white crystals form in solution; alluding to the precipitation of Cs-oleate.

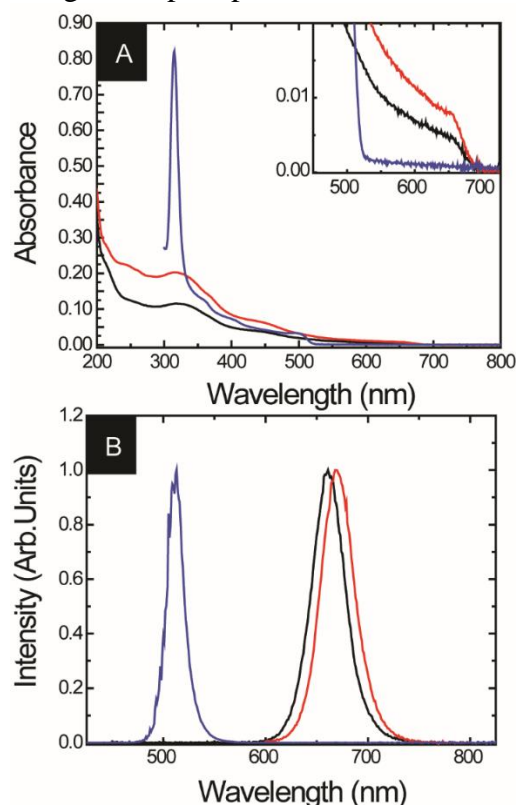


Figure 4.3: CsPbI<sub>3</sub> and CsPbBr<sub>3</sub> nanocrystals absorbance spectra (A) and PL spectra (B). The inset illustrates the magnified absorbance spectra between 600 nm and 800 nm. Room temperature absorbance and PL spectra of CsPbBr<sub>3</sub> and CsPbI<sub>3</sub> nanocrystals dispersed in hexane. OA (black curve), PAB (red curve), and CB (blue curve). The samples were observed using a 400 nm excitation wavelength.

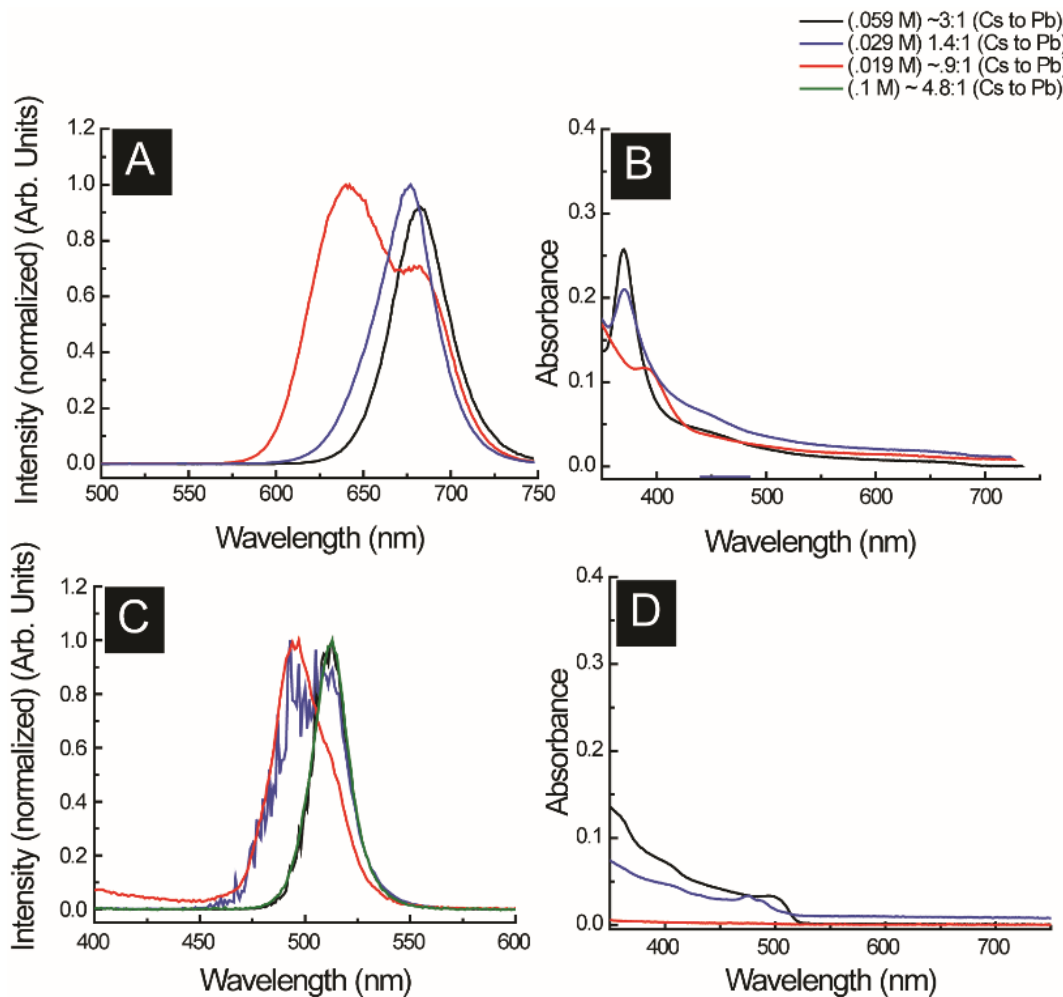


Figure 4.4: CsPbI<sub>3</sub> nanocrystals absorbance and PL spectra for varying concentration of Cs-oleate (A-B), 0.019M (red line), 0.029M (blue line), 0.059M (black line), and 0.1M (green line). CsPbBr<sub>3</sub> nanocrystals absorbance and PL spectra for varying concentration of Cs-oleate (C-D). The spectra were collected from nanocrystal dispersion in anhydrous hexane at room temperature. The samples were observed using a 400 nm excitation wavelength.

Not only are the energy gaps different, but the PL lifetimes are as well. Figure 4.5 shows the auger lifetimes for CB, OA, and PA nanocrystals in anhydrous hexane fitted to a 2-exponential fitting. The nanocrystals were excited using a 402 nm laser at room temperature. PA samples demonstrated the highest lifetimes of 160.3 ns which are a magnitude larger than the OA and CB samples. This may be due to the larger size of the



nanocrystals or better passivation of the nanocrystal surface or there maybe a shorter lifetime that is not detectable by our equipment. CB lifetimes are on par with literature values which ranges from 5 – 30 ns. However, OA lifetimes are slightly lower than literature values which ranges from 25 – 35 ns.

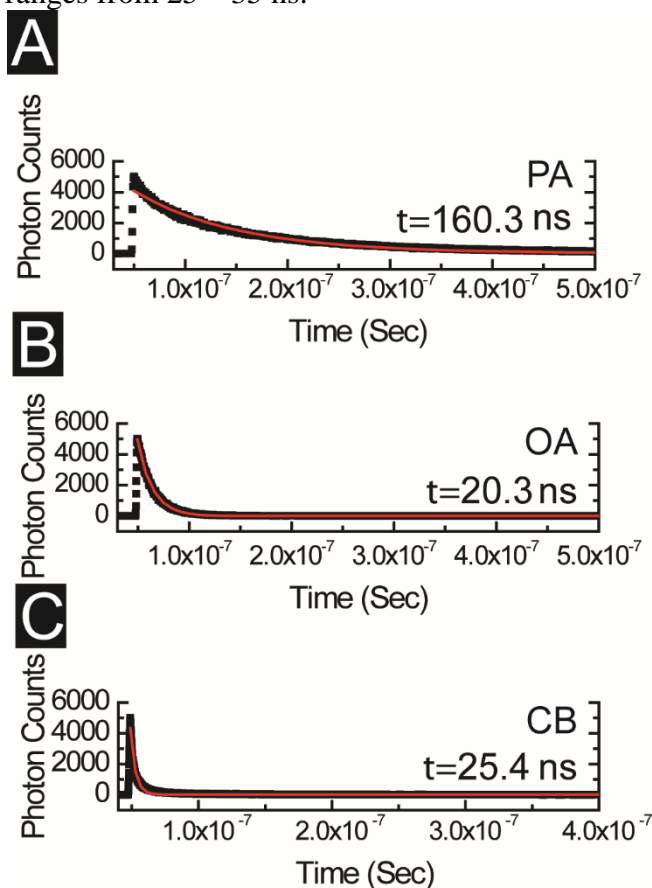


Figure 4.5: Room temperature solution based time-resolved PL of CsPbBr<sub>3</sub> and CsPbI<sub>3</sub> nanocrystals using a 402 nm laser. The spectra was fitted to a 2-exponential fitting (red curve).  $t$  denotes the average decay time ( $\tau$ ). (A) CsPbI<sub>3</sub> nanocrystals synthesized with DOPA (PA). (B) CsPbI<sub>3</sub> nanocrystals synthesized with oleic acid (OA). (C) CsPbBr<sub>3</sub> nanocrystals (CB).

Typically, CsPBX<sub>3</sub> nanocrystal crystal structure is either the desired cubic structure or the undesired and sometimes optically dead orthorhombic phase. In literature, there is a debate on the true crystal structures of the CsPbX<sub>3</sub> (X = Br or I). For the several years, it

was accepted that the crystal structure of the nanocrystals were cubic. However, over the past couple of years there have been evidence that the actual crystal is a black orthorhombic structure. Figures 4.6 and 4.7 shows the crystal structures for CB, OA, and PA structures respectively. CB nanocrystals showed the cubic crystal structures, whereas, the OA and PA nanocrystal showed the black orthorhombic crystal structure.

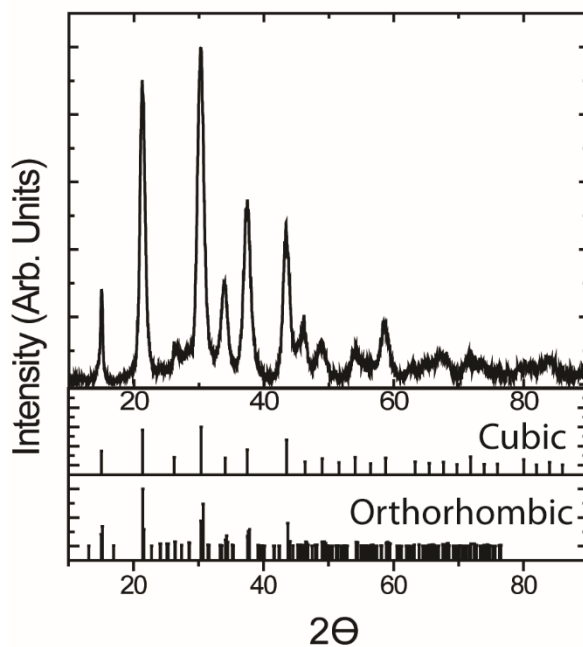


Figure 4.6: Room temperature XRD spectra of CsPbBr<sub>3</sub> nanocrystals. The reference pattern  $\alpha$ -Cubic (PDF#01-076-8588) and  $\gamma$ -orthorhombic (PDF)

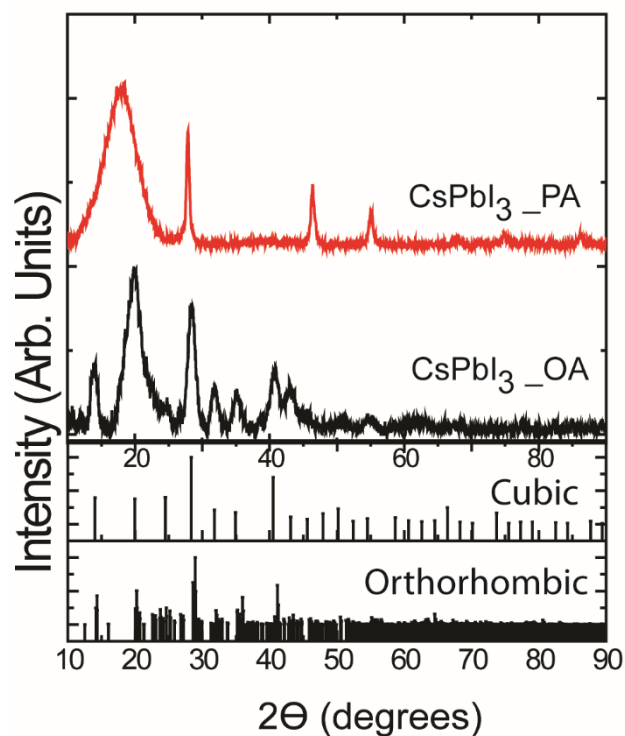


Figure 4.7: Room temperature XRD spectra of CsPbI<sub>3</sub> nanocrystals, OA (black curve) and PA (red curve). The reference pattern  $\alpha$ -Cubic (PDF#01-076-8588) and  $\gamma$ -orthorhombic (black orthorhombic crystal structure) (Henry Snaith's paper)

#### 4.3.2: Doping organic perovskite nanocrystals using Cs

Organic perovskite nanocrystals have the desirable energy with a range of 1.47 to 1.54 eV, however, these nanocrystal suffer from temperature and moisture instabilities. One method to alleviate this problem is to substitute some of the A sites with the inorganic Cs.<sup>11</sup> This has shown to substantially increase the stability of the nanocrystals. Figure 4.8 shows the TEM images for the organic and doped nanocrystals. It is to note that nanocrystals synthesized FAPbI<sub>3</sub> are unstable under the electron beam. When FAPbI<sub>3</sub> is doped with Cs atoms, the nanocrystals have an almost perfect cubic structure with even

spacing between the nanocrystals. The nanocrystals exhibit similar average lengths to the Cs only nanocrystals shown in Figure 4.2.

The optical gap of the nanocrystals were determined from UV-vis absorbance and PL emission peak spectra shown in Figure 4.9. The PL emission peaks for FAPbI<sub>3</sub>, CsFAMAPbI<sub>3</sub>, CsFAPbI<sub>3</sub>, and CsFAMAPb(BrI)<sub>3</sub> ranged from 1.59 eV to 1.94 eV, when excited using a 450 nm wavelength respectively. The XRD pattern shows the cubic crystal structures for FAPbI<sub>3</sub> nanocrystals. Furthermore, nanocrystals synthesized using both FA and MA reactants produced nanocrystals with a similar XRD pattern to the FAPbI<sub>3</sub> nanocrystals. On the other hand, CsFAPbI<sub>3</sub> nanocrystals demonstrated a mixture of crystal structures, the cubic FAPbI<sub>3</sub> and the black orthorhombic crystal structure phase.

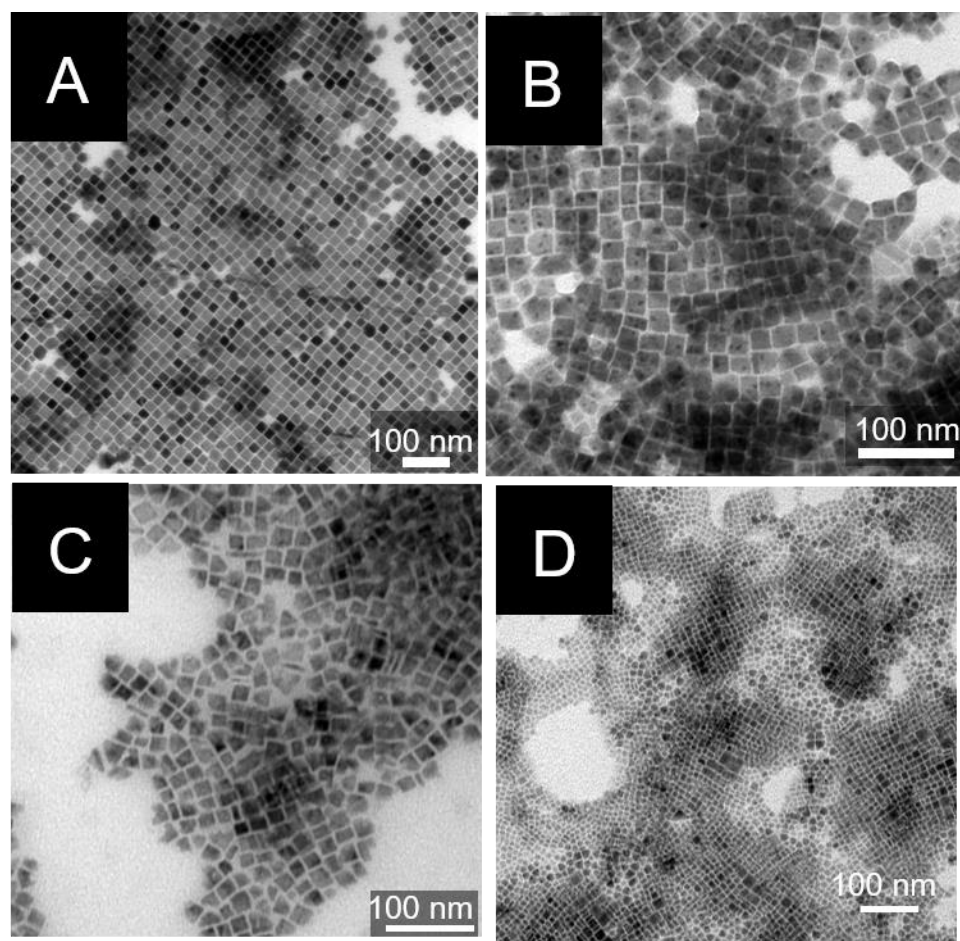


Figure 4.8.: TEM images of (A) CsFAPbI<sub>3</sub> nanocrystals (B) FAPbI<sub>3</sub> nanocrystals. (C) CsFAMAPbI<sub>3</sub> nanocrystals (D) CsFAMAPb(BrI)<sub>3</sub>

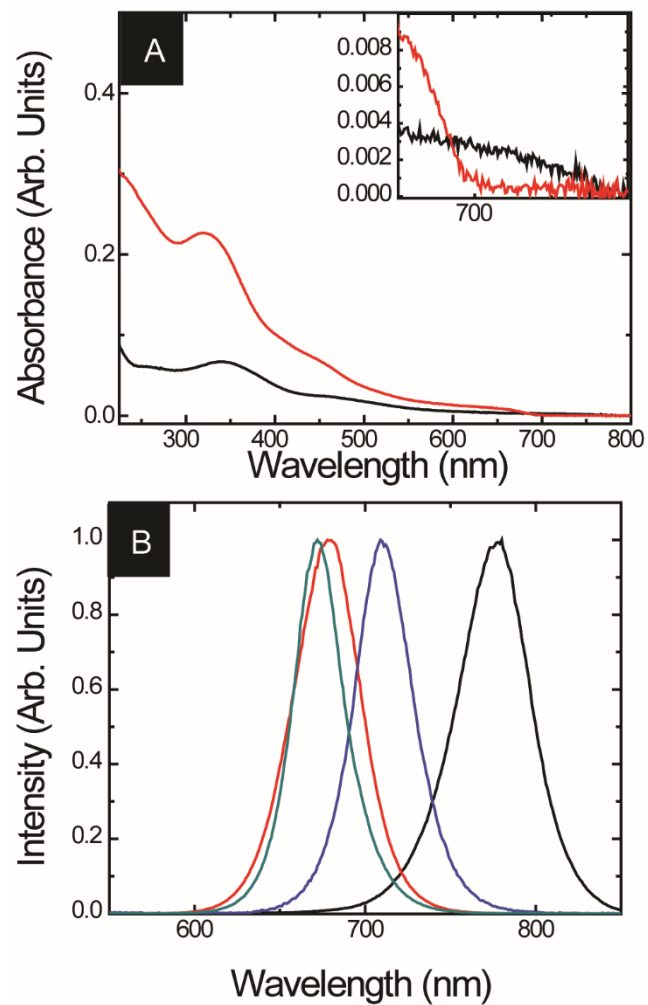


Figure 4.9: Room Temperature absorbance spectra (A) and PL spectra (B). The inset illustrates the magnified absorbance spectra between 650 nm and 800 nm. FAPbI<sub>3</sub> (black line), CsFAPbI<sub>3</sub> (red line), CsFAMAPbI<sub>3</sub> (blue line), and CsFAMAPb(BrI)<sub>3</sub> (green line) were dispersed in anhydrous hexane and excited using a 450 nm wavelength.

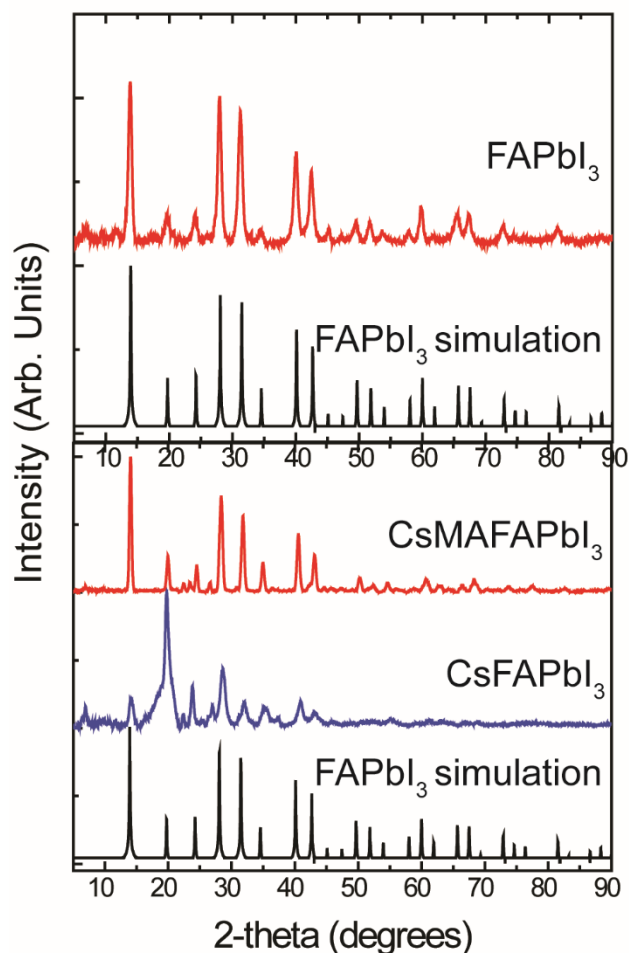


Figure 4.10: Room temperature XRD spectra of FAPbI<sub>3</sub>, CSMAFAPbI<sub>3</sub>, and CsFAPbI<sub>3</sub> nanocrystals. The black pattern is the FAPbI<sub>3</sub> simulation for the cubic ( $a = 6.3641 \text{ \AA}$ ) crystal structure. The CsFAPbI<sub>3</sub>

#### 4.4: CONCLUSIONS

Perovskite nanocrystals has the ability to be used in several applications to include LEDs, optoelectronics, and photovoltaics. The hot injection method has been employed to synthesize the nanocrystals. The nanocrystals were shown to have mostly cubic morphologies with average lengths that range from 8 nm to 17 nm. By replacing the labile oleic acid ligand for the nanocrystals were shown to increase in size and red shift

the energy gap. Along with Cs based perovskite nanocrystals, organic perovskite nanocrystals were also observed. It was shown that doping A sites of the organic FAPbI<sub>3</sub> nanocrystals with Cs atoms allowed for more stable nanocrystals under the electron beam in TEM. Additionally, the nanocrystals were almost perfectly cubic in morphologies. By increasing the stability of the nanocrystals we open new methods for photovoltaic device fabrication and possibly open the doors for a wider breath of applications.

#### **4.5: REFERENCES**

1. Ansari, M. I. H., Qurashi, A. & Nazeeruddin, M. K. Frontiers, opportunities, and challenges in perovskite solar cells: A critical review. *J. Photochem. Photobiol. C Photochem. Rev.* **35**, 1–24 (2018).
2. Akkerman, Q. A., Rainò, G., Kovalenko, M. V. & Manna, L. Genesis, challenges and opportunities for colloidal lead halide perovskite nanocrystals. *Nat. Mater.* **17**, 394–405 (2018).
3. Kovalenko, M. V., Protesescu, L. & Bodnarchuk, M. I. Properties and potential optoelectronic applications of lead halide perovskite nanocrystals. *Science* **358**, 745–750 (2017).
4. Zhang, W., Eperon, G. E. & Snaith, H. J. Metal halide perovskites for energy applications. *Nat. Energy* **1**, 16048 (2016).
5. Swarnkar, A., Ravi, V. K. & Nag, A. Beyond Colloidal Cesium Lead Halide Perovskite Nanocrystals: Analogous Metal Halides and Doping. *ACS Energy Lett.* **2**, 1089–1098 (2017).



6. Sanehira, E. M., Marshall, A. R., Christians, J. A., Harvey, S. P., Ciesielki, P. N., Wheeler, L. M., Schulz, P., Lin, L. Y., Beard, M. C., & Luther, J. M. Enhanced mobility CsPbI<sub>3</sub> quantum dot arrays for record-efficiency, high-voltage photovoltaic cells. *Sci. Adv.* **3**, eaao4204 (2017).
7. Lang, L., Yang, J.-H., Liu, H.-R., Xiang, H. J. & Gong, X. G. First-principles study on the electronic and optical properties of cubic ABX<sub>3</sub> halide perovskites. *Phys. Lett. A* **378**, 290–293 (2014).
8. Protesescu, L., Yakunin, S., Bodnarchuk, M. I., Krieg, F., Caputo, R., Hendon, C. H., Yang, R. X., Walsh, A., & Kovalenko, M. V. Nanocrystals of cesium lead halide perovskites (CsPbX<sub>3</sub>, X=Cl, Br, and I): novel optoelectronic materials showing bright emission with wide color gamut. *Nano Lett.* **15**, 3692–3696 (2015).
9. Kovalenko, M. V. & Bodnarchuk, M. I. Lead Halide Perovskite Nanocrystals: From Discovery to Self-assembly and Applications. *Chimia* **71**, 461–470 (2017).
10. Ananthakumar, S., Kumar, J. R. & Babu, S. M. Cesium lead halide (CsPbX<sub>3</sub>, X=Cl, Br, I) perovskite quantum dots-synthesis, properties, and applications: a review of their present status. *J. Photonics Energy* **6**, 042001 (2016).
11. Protesescu, L., Yakunin, S., Kumar, S., Bär, J., Bertolotti, F., Masciocchi, N., Guagliardi, A., Grotevent, M., Shorubalako, I., Bodnarchuk, M. I., Shih, C.-J., & Kovalenko, M. V. Dismantling the “Red Wall” of Colloidal Perovskites: Highly Luminescent Formamidinium and Formamidinium–Cesium Lead Iodide Nanocrystals. *ACS Nano* **11**, 3119–3134 (2017).

12. Su, Y., Chen, X., Ji, W., Zeng, Q., Ren, Z., Su, Z., & Liu, L. Highly Controllable and Efficient Synthesis of Mixed-Halide CsPbX<sub>3</sub> (X = Cl, Br, I) Perovskite QDs toward the Tunability of Entire Visible Light. *ACS Appl. Mater. Interfaces* **9**, 33020–33028 (2017).
13. Aneesh, J., Swarnkar, A., Ravi, V. K., Sharma, R., Nag, A., & Adarsh, K. V. Ultrafast Exciton Dynamics in Colloidal CsPbBr<sub>3</sub> Perovskite Nanocrystals: Biexciton Effect and Auger Recombination. *J. Phys. Chem. C* **121**, 4734–4739 (2017).
14. Bai, S., Yuan, Z. & Gao, F. Colloidal metal halide perovskite nanocrystals: synthesis, characterization, and applications. *J. Mater. Chem. C* **4**, 3898–3904 (2016).
15. Krieg, F., Ochsenbein, S. T., Yakunin, S., Brinck, S. t., Aellen, P., Süess, A., Clerc, B., Guggisberg, D., Nazarenko, O., Shynkarenko, Kumar, S., Shih, C.-J., Infante, I., & Kovalenko, M. V. Colloidal CsPbX<sub>3</sub> (X = Cl, Br, I) Nanocrystals 2.0: Zwitterionic Capping Ligands for Improved Durability and Stability. *ACS Energy Lett.* **3**, 641–646 (2018).
16. Wang, C., R. Chesman, A. S. & J. Jasieniak, J. Stabilizing the cubic perovskite phase of CsPbI<sub>3</sub> nanocrystals by using an alkyl phosphinic acid. *Chem. Commun.* **53**, 232–235 (2017).
17. De Roo, J., Ibáñez, M., Geiregat, P., Nedelcu, G., Walravens, W., Maes, J., Martins, J. C., Van Driessche, I., Kovalenko, M. V., & Hens, Z. Highly Dynamic Ligand Binding and Light Absorption Coefficient of Cesium Lead Bromide Perovskite Nanocrystals. *ACS Nano* **10**, 2071–2081 (2016).

18. Swarnkar, A., Marshall, A. R., Sanehira, E. M., Chernomordik, B. D., Moore, D. T., Christians, J. A., Chakrabarti, T., & Luther, J. M. Quantum dot-induced phase stabilization of  $\alpha$ -CsPbI<sub>3</sub> perovskite for high-efficiency photovoltaics. *Science* **354**, 92–95 (2016).
19. Sutton, R. J., Filip, M. R., Haghighirad, A. A., Sakai, N. Wenger, B., Giustino, F., & Snaith, H. J. Cubic or Orthorhombic? Revealing the Crystal Structure of Metastable Black-Phase CsPbI<sub>3</sub> by Theory and Experiment. *ACS Energy Lett.* **3**, 1787–1794 (2018).
20. Tan, Y., Zou, Y., Wu, L., Huang, Q., Yang, D., Chen, M., Ban, M., Wu, C., Wu, T., Bai, S., Song, T., Zhang, Q., & Sun, B. Highly Luminescent and Stable Perovskite Nanocrystals with Octylphosphonic Acid as a Ligand for Efficient Light-Emitting Diodes. *ACS Appl. Mater. Interfaces* **10**, 3784–3792 (2018).
21. Tong, Y., Blatt, E., Aygüler, M. F., Manzi, A., Milowska, K. Z., Hintermayr, V. A., Docampo, P., Bals, S., Urban, A. S., Polavarapu, L., & Feldmann, J. Highly Luminescent Cesium Lead Halide Perovskite Nanocrystals with Tunable Composition and Thickness by Ultrasonication. *Angew. Chem. Int. Ed.* **55**, 13887–13892 (2016).
22. Dutta, A., Dutta, S. K., Das Adhikari, S. & Pradhan, N. Phase-Stable CsPbI<sub>3</sub> Nanocrystals: The Reaction Temperature Matters. *Angew. Chem. Int. Ed.* **57**, 9083–9087 (2018).
23. Chen, Z., Li, H., Tang, Y., Huang, X., Ho, D., & Lee, C.-S. Shape-controlled synthesis of organolead halide perovskite nanocrystals and their tunable optical absorption. *Mater. Res. Express* **1**, 015034 (2014).

24. Jellicoe, T. C., Richter, J. M., Glass, H. F. J., Tabachnyk, M., Brady, R., Dutton, S. E., Rao, A., Friendk R. H., Credgington, D., Greenham, N. C., & Böhm, M. L. Synthesis and Optical Properties of Lead-Free Cesium Tin Halide Perovskite Nanocrystals. *J. Am. Chem. Soc.* **138**, 2941–2944 (2016).
25. Liu, H., Wu, Z., Gao, H., Shao, J., Zou, H., Yao, D., Liu, Y., Zhang, H., & Yang, B. One-Step Preparation of Cesium Lead Halide CsPbX<sub>3</sub> (X = Cl, Br, and I) Perovskite Nanocrystals by Microwave Irradiation. *ACS Appl. Mater. Interfaces* **9**, 42919–42927 (2017).
26. Long, Z., Ren, H., Sun, J., Ouyang, J. & Na, N. High-throughput and tunable synthesis of colloidal CsPbX<sub>3</sub> perovskite nanocrystals in a heterogeneous system by microwave irradiation. *Chem. Commun.* **53**, 9914–9917 (2017).
27. Pan, Q., Hu, H., Zou, Y., Chen, M., Wu, L., Yang, D., Yuan, X., Fan, J., Sun, B., & Zhang, Q. Microwave-assisted synthesis of high-quality “all-inorganic” CsPbX<sub>3</sub> (X = Cl, Br, I) perovskite nanocrystals and their application in light emitting diodes. *J. Mater. Chem. C* **5**, 10947–10954 (2017).
28. Luo, P., Xia, W., Zhou, S., Sun, L., Cheng, J., Xu, C., & Lu, Y. Solvent Engineering for Ambient-Air-Processed, Phase-Stable CsPbI<sub>3</sub> in Perovskite Solar Cells. *J. Phys. Chem. Lett.* **7**, 3603–3608 (2016).
29. Ruan, L., Shen, W., Wang, A., Zhou, Q., Zhang, H., & Deng, Z. Stable and conductive lead halide perovskites facilitated by X-type ligands. *Nanoscale* **9**, 7252–7259 (2017).

30. Marronnier, A., Roma, G., Boyer-Richard, S., Pedesseau, L., Jancu, J.-M., Bonnassieux, Y., Katan, C., Stoumpos, C. C., Kanatzidis, M. G., & Even, J. Anharmonicity and Disorder in the Black Phases of Cesium Lead Iodide Used for Stable Inorganic Perovskite Solar Cells. *ACS Nano* **12**, 3477–3486 (2018).
31. Song, W., Wu, X., Di, Q., Xue, T., Zhu, J., & Quan, Z. Morphologically controlled synthesis of ionic cesium iodide colloidal nanocrystals and electron beam-induced transformations. *RSC Adv.* **8**, 18519–18524 (2018).

## Chapter 5: Thermal stability of Perovskite nanocrystals\*

### 5.1: INTRODUCTION

Cesium lead halide perovskite nanocrystals has gained the attraction of researchers for various applications due to their optoelectronic and optical properties<sup>1-9</sup>. Currently, CsPbI<sub>3</sub> quantum dot photovoltaic devices holds the record at 13.4% percent conversion efficiency<sup>10</sup>. The efficiencies are still lower than perovskite thin film devices<sup>11</sup>. Some researcher's hypothesize that the efficiencies can be increased by forming superlattices or order assemblies. The formation of the order assemblies may allow for better charge transport due to equal spacing between each nanocrystal and coupling between the nanocrystals.<sup>12-15</sup> Better understanding of the quantum dots could increase quantum device efficiencies and the breadth of applications.

CsPbI<sub>3</sub> perovskite nanocrystals has been fabricated into different morphologies and sizes; which exhibit different optical properties and crystal structures.<sup>1,2,9,11,16-19</sup> Due to their uniform size and shape, researchers have gained interest in the formation of order assemblies. There has been several studies on understanding perovskite nanocrystals ordered arrays formation<sup>20,21</sup>. Tong, *et al.* discovered the self-assembly of CsPbBr<sub>3</sub> nanocrystals via one pot-synthesis into 3D supercrystals. A red shift in photoluminescence measurements was observed for the super crystals which was attributed to the coupling of

---

\*The work contained in this chapter is the subject of a scholarly article that is currently in preparation. Authors on this work include Cherrille J. Thomas, Yangning Zhang, Adrien Guillaussier, Detlef Smilgies, and Brian A. Korgel. Cherrille Thomas was responsible for planning the research, and synthesis of nanocrystals and order assembly formation with help from Yangning Zhang, analyzing the data, running the experiments at CHESS with help from Adrien and Yangning, researching and writing the completed document. Detlef setup the experiment stages and the beam line.

the nanocrystals when assembled. Nagaoka, *et al.* showed the effects of pressure on CsPbBr<sub>3</sub> nanocube superlattices. Through in-situ small and wide angle X-ray scattering, the crystal structure changed from a cubic orthorhombic mixture to solely the orthorhombic phase and finally to a pure cubic crystal structure with the formation of nanoplatelets. Moreover, understanding the thermal stability of these assemblies are of great interest<sup>22</sup>.

Here, we investigate the thermal stability of slow solvent evaporation of CsPbI<sub>3</sub> nanocrystal order assemblies. Two different capping ligands were explored. Oleic acid (OA), the traditional ligand used in the synthesis and diisooctylphosphinic acid (DOPA), which has been shown to increase the ambient stability of CsPbI<sub>3</sub> nanocrystals<sup>16</sup>. Using in-situ grazing incidence small and wide angle scattering (GISAXS and GIWAXS), we explored the changes in crystal structure for the ordered assemblies and within the nanocrystals itself. Ordered assemblies that used OA capped nanocrystals formed a simple cubic structure with the (001) planes parallel to the substrate. However, ordered assemblies formed with PA capped nanocrystals exhibited weak ordering that cannot be fully interpreted via in-situ GISAXS. Through in-situ GIWAXS we observed a transition from the  $\gamma$ -orthorhombic phase<sup>23,24</sup> to the  $\delta$ -orthorhombic phase as we heated the sample to 300°C. PA capped nanocrystals were shown to be more thermally stable than the traditionally capped CsPbI<sub>3</sub>.

## 5.2: EXPERIMENTAL DETAILS AND CHARACTERIZATION METHODS

### 5.2.1: Materials and Experimental Details

Lead Iodide ( $\text{PbI}_2$ ), Cesium Carbonate ( $\text{Cs}_2\text{CO}_3$ ), Octadecene (ODE, 90%), Oleylamine (OLA, 70%), oleic acid (OA), diisooctylphosphinic acid (DOPA), anhydrous hexane (95%), anhydrous chloroform (99%), anhydrous methyl acetate (99.5%) were obtained from Sigma-Aldrich company. All chemicals were used without further purification.

**Nanocrystal (NC) synthesis.** Our  $\text{CsPbX}_3$  NCs synthesis has been adopted from literature, but is briefly explained here. Cs-oleate (0.59 M) was synthesized by loading a 3-neck 100 mL flask with ~2.5 mmols of  $\text{C}_2\text{CO}_3$  (0.814g), 40 mL of ODE, and 2.5 mL of OA. The OA is replaced with DOPA for phosphinic capped particles. The reaction flask was degassed at 120°C for 1hr at ~150 mTorr, then the flask temperature was raised to 150°C under a blanket of  $\text{N}_2$  until all  $\text{Cs}_2\text{CO}_3$  reacted with OA or DOPA. Then the flask was allowed to cool to room temperature, and stored in the glovebox. As the temperature falls below 100°C, Cs-oleate will precipitate out of solution.

Moreover, 0.88 mmols of  $\text{PbX}_2$  and 20 mL of ODE was loaded into a 100 mL flask and degassed at 120°C for 1hr at ~150 mTorr. Under a blanket of  $\text{N}_2$ , 2 mL of both OLA and OA (or DOPA) were injected into the reaction flask. The reaction flask was placed under vacuum and degas for an additional 30 minutes at 120°C and ~150 mTorr. The reaction flask temperature was raised to the reaction temperature of 170°C (160°C for  $\text{PbI}_2$ ) under blanket of  $\text{N}_2$  and 3.2 mL of the preheated 0.59 M Cs-oleate solution was



injected into the reaction flask. After 5 seconds the reaction product was cooled to room temperature via an ice bath.

After cooling the reaction product to room temperature, the reaction flask was brought into an Ar filled glovebox. The reaction product was equally divided into two separate centrifuge tubes and 15 mL of methyl acetate was added to each tube. The perovskite nanocrystals were precipitated via centrifugation, 8000 rpm for 5 minutes, the supernatant was discarded and the precipitate was dispersed in 10 mL of anhydrous hexane. The nanocrystal dispersion was centrifuged again at 8500 rpm for 5 minutes. The supernatant was stored in a 20 mL vial in a glovebox.

**Ordered arrays procedure.** 40  $\mu\text{L}$  of  $\text{CsPbI}_3$  nanocrystals and 240  $\mu\text{L}$  of anhydrous hexane are charged into a 4.5 mL vial in the glovebox. A 650  $\mu\text{m}$  thick p-type Si wafer (supplied from University Wafer) or a mesh nickel carbon-coated transmission electron grid, supplied by Electron Microscopy Sciences, placed parallel with the bottom of vial. Samples are dried for 24-72 hours in an argon filled glovebox to preserve the integrity of the nanocrystals.

For chloroform samples, 40  $\mu\text{L}$  of  $\text{CsPbI}_3$  nanocrystals were added into a 4.5 mL vials and allowed to dry for 24 hours in an Ar-filled glovebox. Using 240  $\mu\text{L}$  of anhydrous chloroform, the dried nanocrystals were re-dispersed and a TEM grid or Si substrate was placed horizontally in the vial. The samples were dried for 24 hours in an argon filled glovebox.

### **5.2.1: Materials Characterization**

Perovskite NCs were imaged by transmission electron microscopy (TEM) using a FEI Tecnai G2 Spirit BioTwin TEM or a JEOL 2010F TEM. The FEI Tecnai G2 TEM and JEOL 2010F TEM were operated at 80 kV and 200 kV, respectively.

**Scanning electron microscopy (SEM)** images were taken using a Zeiss Supra 40 VP SEM at 4 keV accelerating voltage. The samples were grounded by a copper tape and images were collected through the in-lens detector.

**Grazing Incident Small and Wide Angle X-ray Scattering (GISAXS and GIWAXS)** were performed using the D1 beam line at the Cornell High Energy Synchrotron Source (CHESS). For heating experiments, Si substrates were heated on a temperature controllable stage under ambient conditions. GISAXS images were collected using a Pilatus 200k detector (487 x 407 pixels with a pixel size of 172  $\mu\text{m}$  x 172  $\mu\text{m}$ ) with a sample to detector distance of 1310 mm and the incident beam angle was 0.25 with a wavelength of 0.929 Å. GIWAXS was collected using a Pilatus V detector (487 x 195 pixels with a pixel size of 172  $\mu\text{m}$  x 172  $\mu\text{m}$ ) with a sample to detector distance of 105.75 mm and the incident beam angle was 0.25 and a wavelength of 0.929 Å. Images were integrated and analyzed using FIT2D and indexGIXS-2L softwares respectively.

### **5.3: RESULTS AND DISCUSSION**

CsPbI<sub>3</sub> NCs synthesis was adopted from literature and is explained in the section 5.2. Briefly, Cs-oleate is injected into the reaction solution of PbI<sub>2</sub>, ligands, and octadecene at 170°C. The nanocrystals are reacted for 5 secs, quenched, and isolated via centrifugation. Two different sets of ligands were used to passivate the nanocrystals

oleylamine and oleic acid and oleylamine and diisooctylphosphinic acid. To avoid any confusion, we will refer CsPbI<sub>3</sub> nanocrystals passivated with oleylamine and oleic acid as OA and those passivated with oleylamine and diisooctylphosphinic acid as PA. CsPbI<sub>3</sub> nanocrystals were shaped like cubes with an average side lengths of  $8.6 \pm 1.5$  nm (OA),  $17.5 \pm 2.8$  nm (PA) determined by transmission electron microscopy (TEM). The nanocrystals were dispersed in anhydrous hexane or chloroform and slowly evaporated onto silicon substrates or TEM grids under inert conditions (Figures 5.1a – 5.1d). (Please see the section 5.2 for details on sample preparation) Ordered assemblies in hundreds of nanometers lengths can be seen for the OA samples in both TEM and scanning electron microscopy (SEM); however, only short order assemblies can be seen for the PA samples. Furthermore, by increasing the nanocrystal concentration by a factor of ten, longer range assemblies were seen for the PA samples (Appendix B).

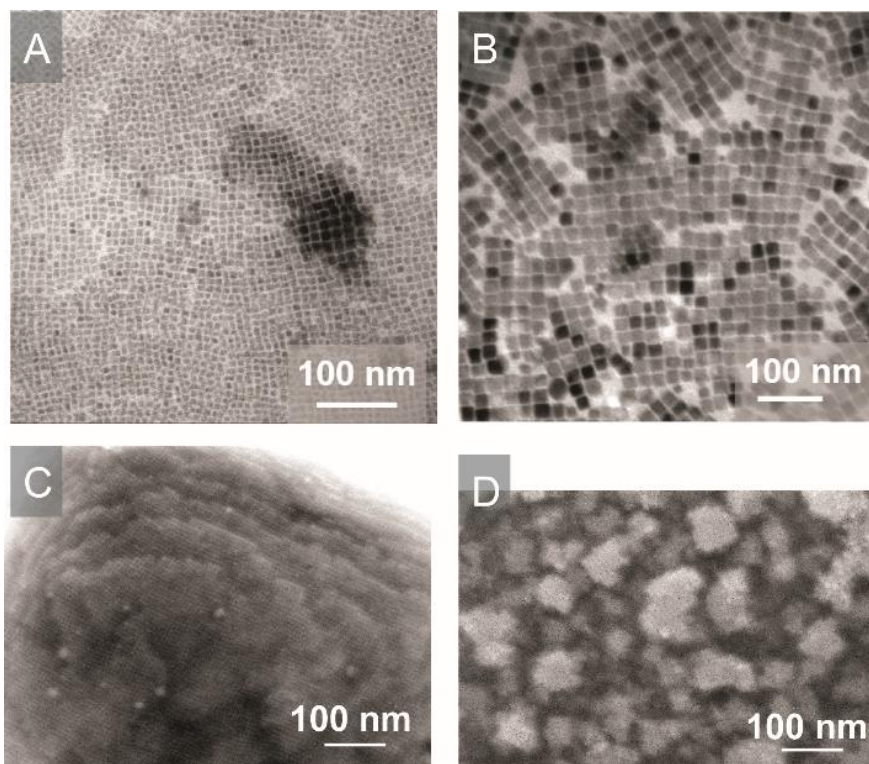


Figure 5.1: CsPbI<sub>3</sub> nanocrystals TEM images (A and B) along with ordered assemblies SEM images (C and D). (A) CsPbI<sub>3</sub> nanocrystals synthesized with oleic acid (OA) with an average side length of  $8.6 \pm 1.5$  nm. (B) CsPbI<sub>3</sub> nanocrystals synthesized with diisooctylphosphinic acid (PA) with an average side length of  $17.5 \pm 2.8$  nm. (C) Ordered assemblies of CsPbI<sub>3</sub> OA nanocrystals slow evaporated on Si wafer. (D) Ordered assemblies of CsPbI<sub>3</sub> PA nanocrystals evaporated on Si wafers.

These ordered assemblies were studied using GISAXS and GIWAXS for dried nanocrystal dispersions in anhydrous hexane and chloroform. Simple cubic structures can be seen for OA when dispersed in hexane with a lattice constant of  $a_{SL} = 12$  nm given rise to a nanocrystal separation of 3.4 nm. These values are slightly smaller than CsPbBr<sub>3</sub> nanocrystal ordered assemblies which were reported to be  $a_{SL} = 12.5$  nm with an interspacing of 2.3 nm. However, PA samples did not show strong ordering (Figures 5.2A and 5.2B) which order assembly dimension and structures couldn't be determined. Further,

neither OA or PA nanocrystals illustrated detectable ordered assemblies in GISAXS when dispersed in chloroform (Appendix B). In Figures 5.2C and 5.2D, both samples exhibited the black  $\gamma$ -orthorhombic crystal structure. The OA nanocrystal order arrays were oriented with the  $(002)_{\text{NC}}$  planes parallel to the substrates; were as, the PA order arrays exhibited mostly  $(110)_{\text{NC}}$  parallel planes oriented parallel to the substrate with a few spots agreeing with the  $(002)_{\text{NC}}$  orientation. This is due to the fact that at low temperatures both the  $(110)_{\text{NC}}$  and  $(002)_{\text{NC}}$  planes are both parallel to the substrate with the majority peaks being from the  $(110)_{\text{NC}}$  plane being parallel to the substrate<sup>22</sup>. These results differ from the  $\text{CsPbI}_3$  thin films, which was reported to immediately change to the  $\delta$ -orthorhombic (yellow phase) crystal structure upon exposure to ambient conditions<sup>22</sup>. This may be due to the protective ligand shell around the nanocrystals.

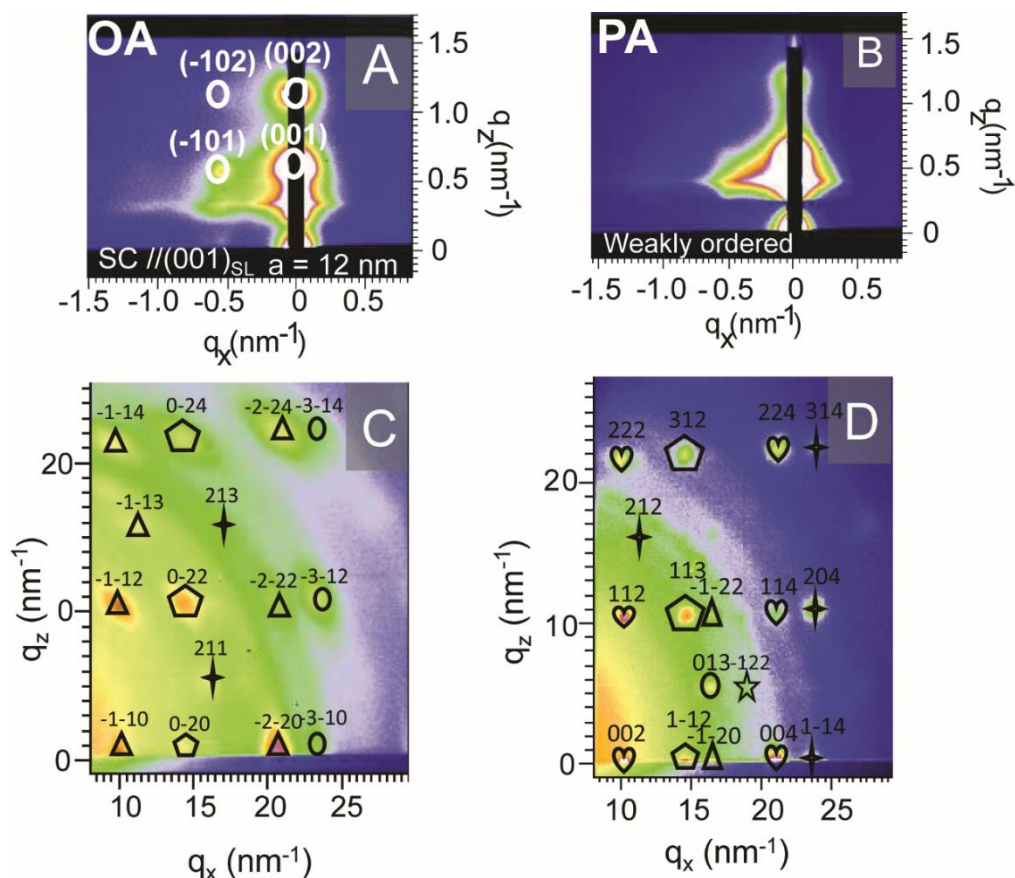


Figure 5.2: GISAXS (A and B) and GIWAXS (C and D) of order assemblies of CsPbI<sub>3</sub> nanocrystals. (A) GISAXS pattern of CsPbI<sub>3</sub> OA nanocrystals with a simple cubic structure  $a_{SL} = 12$  nm with the (001)<sub>SL</sub> planes parallel to the Si substrates. (B) GISAXS pattern of CsPbI<sub>3</sub> PA nanocrystals. (C) GIWAXS pattern of CsPbI<sub>3</sub> OA nanocrystals exhibiting  $\gamma$ -orthorhombic crystal structure with the (002)<sub>NC</sub> planes parallel to the Si substrate. The circle, triangle, pentagon, and four point star represents the  $[-130]_{BD}$ ,  $[-110]_{BD}$ ,  $[100]_{BD}$ , and  $[-120]_{BD}$  beam directions. (D) GIWAXS pattern of CsPbI<sub>3</sub> PA nanocrystals displaying  $\gamma$ -orthorhombic crystal structure with the (002)<sub>NC</sub> and (110)<sub>NC</sub> orientations parallel to the Si substrates. The heart, pentagon, four-point star, circle, and star represents the  $[-110]_{BD}$ ,  $[-111]_{BD}$ ,  $[-221]_{BD}$ ,  $[-33-1]_{BD}$ ,  $[-22-3]_{BD}$  beam directions for the (110)<sub>NC</sub> orientation parallel to the Si substrate. The triangle represents the  $[-210]_{BD}$  beam direction from the (002)<sub>NC</sub> parallel orientation.

In order to determine if the PA ligands increased the thermal stability of CsPbI<sub>3</sub> nanocrystals, In-situ GIWAXS and GISAXS was used to monitor the nanocrystal structure

and the structure of the order assemblies. The OA and PA nanocrystal assemblies were heated from room temperature 23°C to 300°C and then cooled back down to room temperature. In Figure 5.3A the (002)<sub>NC</sub> orientation parallel to the substrate was observed just like in Figure 5.2A. The (002)<sub>NC</sub> preferred orientation was stable up until 100°C where the (-1-13)<sub>NC</sub> and (213)<sub>NC</sub> plane peaks disappears. Once the temperature has reached 150°C the preferred orientation is lost and ultimately transitions to the non-perovskite yellow orthorhombic crystals structure at temperatures 200°C and above. Upon cooling OA order assemblies back down to room temperature, the non-perovskite phase remained (Appendix B). In Figure 5.4 the GISAXS exhibits the simple cubic structure with the parallel (001)<sub>SL</sub> plane until 100°C where the (-102)<sub>SL</sub> plane disappears and at 150°C the (002)<sub>SL</sub> plane disappears. At temperatures above 150°C, no peaks are shown in the GISAXS patterns indicating a loss of ordering; which is attributed to the formation of the δ-orthorhombic crystal structure (yellow phase) and the fusing of the nanocrystals.

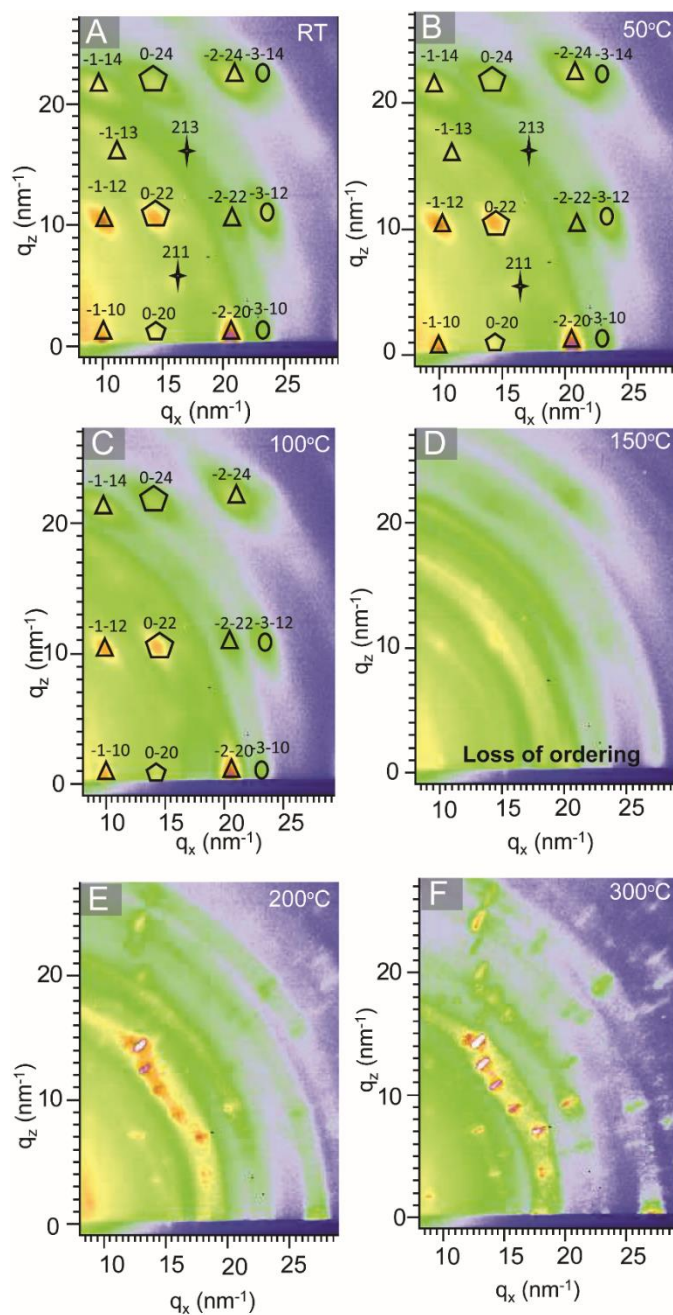


Figure 5.3: GIWAXS patterns of CsPbI<sub>3</sub> OA nanocrystals exhibiting  $\gamma$ -orthorhombic crystal structure with the (002)<sub>NC</sub> planes parallel to the Si substrate heated from room temperature (RT) to 300°C. The circle, triangle, pentagon, and four point star represents the  $[-130]_{BD}$ ,  $[-110]_{BD}$ ,  $[100]_{BD}$ , and  $[-120]_{BD}$  beam directions. (A) RT, (B) 50°C (C) 100°C (D) 150°C (E) 200°C and (F) 300°C



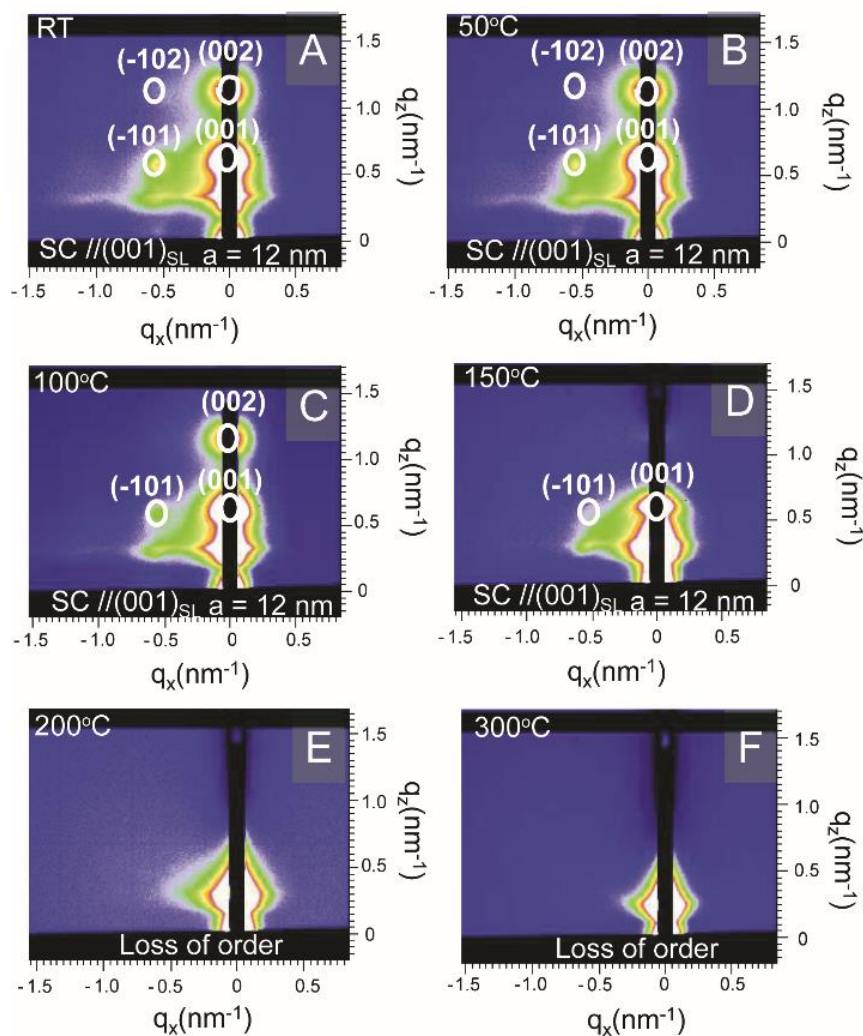


Figure 5.4: GISAXS patterns of CsPbI<sub>3</sub> OA nanocrystals with a simple cubic structure  $a_{SL} = 12$  nm with the (001)<sub>SL</sub> parallel orientation heated from room temperature (RT) to 300°C. (A) RT, (B) 50°C (C) 100°C (D) 150°C (E) 200°C and (F) 300°C

Figures 5.5 and 5.6 displays the GIWAXS and GISAXS patterns for the PA nanocrystal order assemblies. At room temperature, the (110)<sub>NC</sub> and the (002)<sub>NC</sub> preferred orientation is observed in Figure 5.5A, as in Figure 5.2D. The preferred orientation is stable

up until temperatures of 150°C -200°C where additional peaks from the  $\delta$ -orthorhombic phase are observable. After 200°C, the CsPbI<sub>3</sub> is transformed to the yellow phase, and upon cooling the crystals remain in the non-perovskite phase. One spot is seen in GISAXS, however, it is not enough to index the order structures. The spot remains stable up until temperatures of 100°C, at 150°C the PA samples lose ordering.

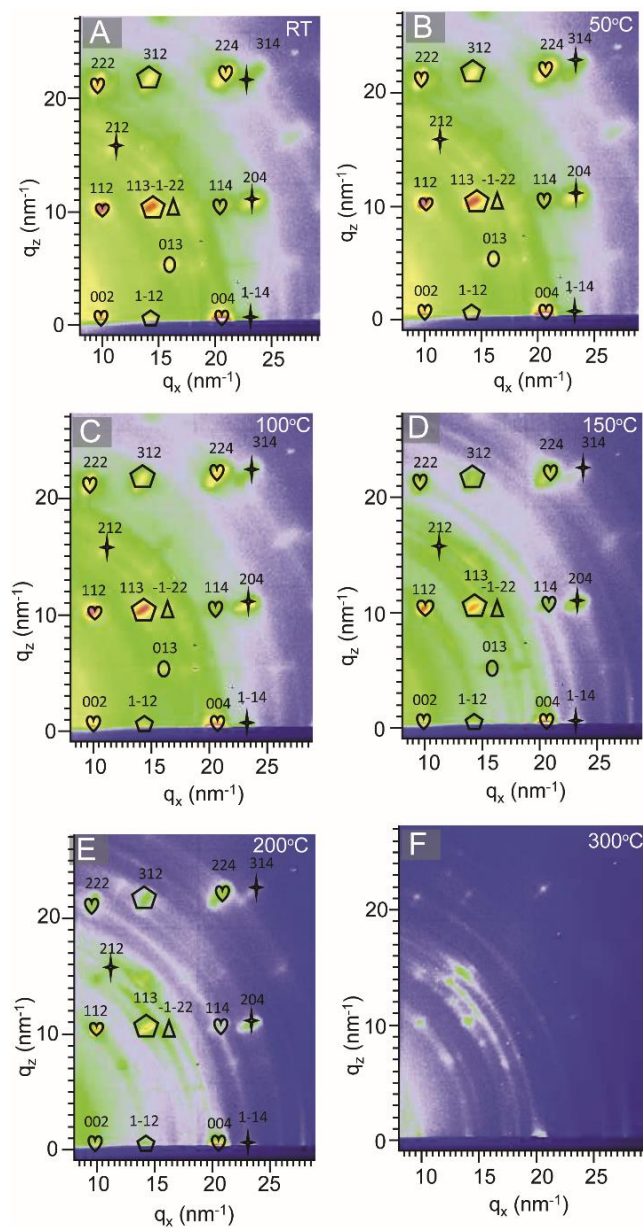


Figure 5.5: GIWAXS patterns of CsPbI<sub>3</sub> PA nanocrystals exhibiting  $\gamma$ -orthorhombic crystal structure with the (110)<sub>NC</sub> and the (002)<sub>NC</sub> planes parallel to the Si substrate heated from room temperature (RT) to 300°C. The heart, pentagon, four-point star, circle, and star represents the [-110]<sub>BD</sub>, [-111]<sub>BD</sub>, [-221]<sub>BD</sub>, [-33-1]<sub>BD</sub>, [-22-3]<sub>BD</sub> beam directions for the (110)<sub>NC</sub> orientation and the triangle represents the [-210]<sub>BD</sub> beam direction from the (002)<sub>NC</sub> orientation. (A) RT, (B) 50°C (C) 100°C (D) 150°C (E) 200°C and (F) 300°C

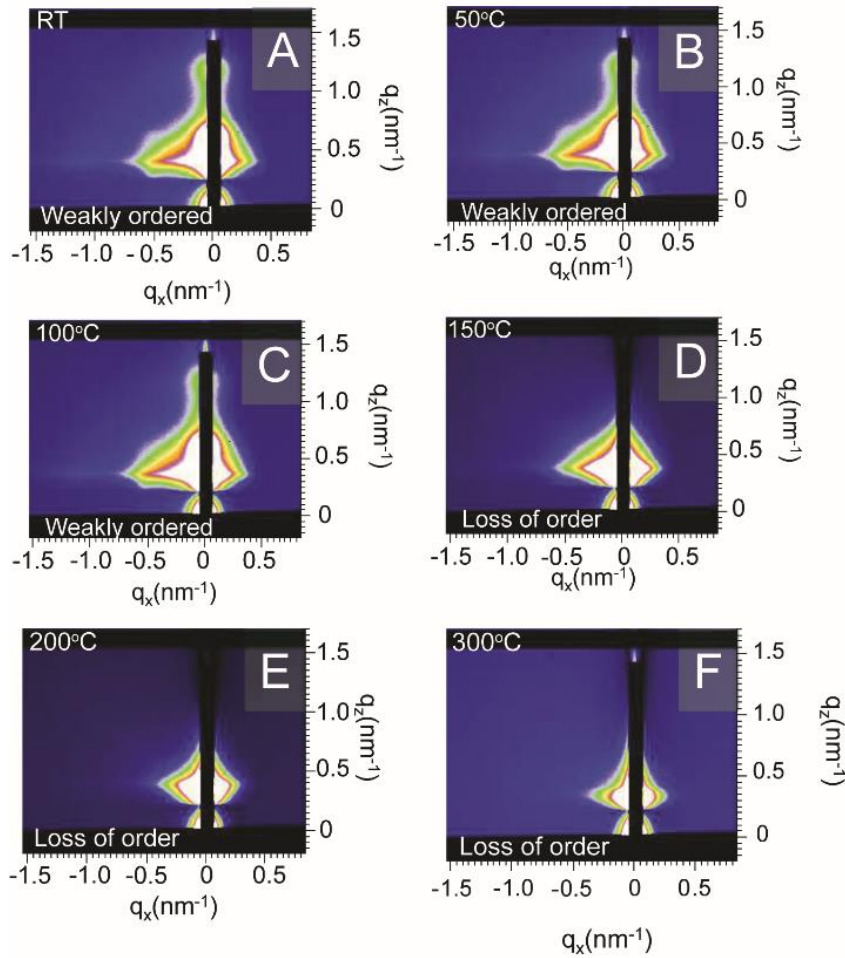


Figure 5.6: GISAXS patterns of CsPbI<sub>3</sub> PA nanocrystals with weak ordering heated from room temperature (RT) to 300°C. (A) RT, (B) 50°C (C) 100°C (D) 150°C (E) 200°C and (F) 300°C

#### 5.4: CONCLUSIONS

The thermal stability of CsPbI<sub>3</sub> nanocrystal order assemblies were investigated via in-situ GISAXS and GIWAXS. Both OA and PA nanocrystal motifs exhibited the  $\gamma$ -orthorhombic crystal structure. OA samples displayed long range ordering with assembly parallel orientation of (001)<sub>SL</sub>. Conversely, PA samples showed only one spot in GISAXS

patterns which is indicative of weak ordering. A (002)<sub>NC</sub> preferred orientation parallel to the silicon substrate was observed for OA samples; whereas, PA samples exhibited a mixed preferred orientations (110)<sub>NC</sub> and (002)<sub>NC</sub>. The mix preferred orientation may be a reason for weak ordering in the PA samples. Upon heating in air both samples transitioned from the black orthorhombic phase into the yellow orthorhombic phase which was observed using in-situ GISAXS and GIWAXS. PA samples maintained the  $\gamma$ -orthorhombic phase until temperatures of 150°C – 200°C were reached, and were proven to be more thermally stable than the nanocrystals stabilized with OA.

## 5.5: REFERENCES

1. Ananthakumar, S., Kumar, J. R. & Babu, S. M. Cesium lead halide (CsPbX<sub>3</sub>, X=Cl, Br, I) perovskite quantum dots-synthesis, properties, and applications: a review of their present status. *J. Photonics Energy* **6**, 042001 (2016).
2. Protesescu, L., Yakunin, S., Bodnarchuk, M. I., Krieg, F., Caputo, R., Hendon, C. H., Yang, R. X., Walsh, A., & Kovalenko, M. V. Nanocrystals of cesium lead halide perovskites (CsPbX<sub>3</sub>, X=Cl, Br, and I): novel optoelectronic materials showing bright emission with wide color gamut. *Nano Lett.* **15**, 3692–3696 (2015).
3. Wang, H.-C., Bao, Z., Tsai, H.-Y., Tang, A.-C. & Liu, R.-S. Perovskite Quantum Dots and Their Application in Light-Emitting Diodes. *Small* **14**, n/a-n/a (2018).
4. Ono, L. K., Juarez-Perez, E. J. & Qi, Y. Progress on Perovskite Materials and Solar Cells with Mixed Cations and Halide Anions. *ACS Appl. Mater. Interfaces* **9**, 30197–30246 (2017).

5. Li, X., Cao, F., Yu, D., Chen, J., Sun, Z., Shen, Y., Zhu, Y., Wang, L., Wei, Y., Wu, Y., & Zeng, H. All Inorganic Halide Perovskites Nanosystem: Synthesis, Structural Features, Optical Properties and Optoelectronic Applications. *Small* **13**, n/a-n/a (2017).
6. Su, Y., Chen, X., Ji, W., Zeng, Q., Ren, Z., Su, Z., & Liu, L. Highly Controllable and Efficient Synthesis of Mixed-Halide CsPbX<sub>3</sub> (X = Cl, Br, I) Perovskite QDs toward the Tunability of Entire Visible Light. *ACS Appl. Mater. Interfaces* **9**, 33020–33028 (2017).
7. Huang, H., Bodnarchuk, M. I., Kershaw, S. V., Kovalenko, M. V. & Rogach, A. L. Lead Halide Perovskite Nanocrystals in the Research Spotlight: Stability and Defect Tolerance. *ACS Energy Lett.* **2**, 2071–2083 (2017).
8. Swarnkar, A., Marshall, A. R., Sanhira, E. M., Chernomordik, B. D., Moore, D. T., Christians, J. A., Chakrabarti, T., & Luther, J. M. Quantum dot-induced phase stabilization of  $\alpha$ -CsPbI<sub>3</sub> perovskite for high-efficiency photovoltaics. *Science* **354**, 92–95 (2016).
9. Akkerman, Q. A., Rainò, G., Kovalenko, M. V. & Manna, L. Genesis, challenges and opportunities for colloidal lead halide perovskite nanocrystals. *Nat. Mater.* **17**, 394–405 (2018).
10. Sanhira, E. M., Marshall, A. R., Christians, J. A., Harvey, S. P., Ciesielki, P. N., Wheeler, L. M., Schulz, P., Lin, L. Y., Beard, M. C., & Luther, J. M. Enhanced mobility CsPbI<sub>3</sub> quantum dot arrays for record-efficiency, high-voltage photovoltaic cells. *Sci. Adv.* **3**, eaao4204 (2017).

11. Alpert, M. R., Niezgoda, J. S., Chen, A. Z., Foley, B. J., Cuthriell, S., Yoon, L. U., & Choi, J. J. Colloidal Nanocrystals as a Platform for Rapid Screening of Charge Trap Passivating Molecules for Metal Halide Perovskite Thin Films. *Chem. Mater.* **30**, 4515–4526 (2018).
12. Liljeroth, P., Overgaag, K., Urbieto, A., Grandidier, B., Hickey, S. G., & Vanmaekelbergh, D. Variable Orbital Coupling in a Two-Dimensional Quantum-Dot Solid Probed on a Local Scale. *Phys. Rev. Lett.* **97**, 096803 (2006).
13. Hanrath, T. Colloidal nanocrystal quantum dot assemblies as artificial solids. *J. Vac. Sci. Technol. A* **30**, 030802 (2012).
14. Whitham, K., Yang, J., Savitzky, B. H., Kourkoutis, L. F., Wise, F., & Hanrath, T. Charge transport and localization in atomically coherent quantum dot solids. *Nat. Mater. Lond.* **15**, 557–563 (2016).
15. Shabaev, A., Efros, A. L. & Efros, A. L. Dark and Photo-Conductivity in Ordered Array of Nanocrystals. *Nano Lett.* **13**, 5454–5461 (2013).
16. Wang, C., R. Chesman, A. S. & J. Jasieniak, J. Stabilizing the cubic perovskite phase of CsPbI<sub>3</sub> nanocrystals by using an alkyl phosphinic acid. *Chem. Commun.* **53**, 232–235 (2017).
17. Dutta, A., Dutta, S. K., Das Adhikari, S. & Pradhan, N. Phase-Stable CsPbI<sub>3</sub> Nanocrystals: The Reaction Temperature Matters. *Angew. Chem. Int. Ed.* **57**, 9083–9087 (2018).
18. Tan, Y., Zou, Y., Wu, L., Huang, Q., Yang, D., Chen, M., Ban, M., Wu, C., Wu, T., Bai, S., Song, T., Zhang, Q., & Sun, B. Highly Luminescent and Stable Perovskite

- Nanocrystals with Octylphosphonic Acid as a Ligand for Efficient Light-Emitting Diodes. *ACS Appl. Mater. Interfaces* **10**, 3784–3792 (2018).
19. Krieg, F., Ochsenbein, S. T., Yakunin, S., Brinck, S. t., Aellen, P., Süess, A., Clerc, B., Guggisberg, D., Nazarenko, O., Shynkarenko, Kumar, S., Shih, C.-J., Infante, I., & Kovalenko, M. V. Colloidal CsPbX<sub>3</sub> (X = Cl, Br, I) Nanocrystals 2.0: Zwitterionic Capping Ligands for Improved Durability and Stability. *ACS Energy Lett.* **3**, 641–646 (2018).
20. Tong, Y., Bladt, E., Aygüler, M. F., Manzi, A., Milowska, K. Z., Hintermayr, V. A., Docampo, P., Bals, S., Urban, A. S., Polavarapu, L., & Feldmann, J. Highly Luminescent Cesium Lead Halide Perovskite Nanocrystals with Tunable Composition and Thickness by Ultrasonication. *Angew. Chem. Int. Ed.* **55**, 13887–13892 (2016).
21. Nagaoka, Y. Hills-Kimball, K., Tan, R., Li, R., Wang, Z., & Chen, O. Nanocube Superlattices of Cesium Lead Bromide Perovskites and Pressure-Induced Phase Transformations at Atomic and Mesoscale Levels. *Adv. Mater.* **29**, n/a-n/a (2017).
22. Burwig, T., Fränzel, W. & Pistor, P. Crystal Phases and Thermal Stability of Co-evaporated CsPbX<sub>3</sub> (X = I, Br) Thin Films. *J. Phys. Chem. Lett.* **9**, 4808–4813 (2018).
23. Marronnier, A., Roma, G., Boyer-Richard, S., Pedesseau, L., Jancu, J.-M., Bonnassieux, Y., Katan, C., Stoumpos, C. C., Kanatzidis, M. G., & Even, J. Anharmonicity and Disorder in the Black Phases of Cesium Lead Iodide Used for Stable Inorganic Perovskite Solar Cells. *ACS Nano* **12**, 3477–3486 (2018).



24. Sutton, R. J., Filip, M. R., Haghighirad, A. A., Sakai, N. Wenger, B., Giustino, F., & Snaith, H. J. Cubic or Orthorhombic? Revealing the Crystal Structure of Metastable Black-Phase CsPbI<sub>3</sub> by Theory and Experiment. *ACS Energy Lett.* **3**, 1787–1794 (2018).

## Chapter 6: High-Energy Carrier Dynamics of CsPbI<sub>3</sub> Perovskite Nanocrystals\*

### 6.1: INTRODUCTION

Perovskite lead halide quantum dots, such as CsPbBr<sub>3</sub> and CsPbI<sub>3</sub>, are promising materials for various applications such as photovoltaics, light-emitting diodes (LEDs), and other optoelectronic devices.<sup>1-4</sup> Due to the ease of the synthesis, tunable energy gap, and high PL quantum yields, cesium lead halide nanocrystals have gained researchers attention as the active absorber layer for photovoltaic devices.<sup>5-8</sup> Currently, cesium lead iodide (CsPbI<sub>3</sub>) quantum dots holds the record for quantum dot photovoltaic devices at 13.4%.<sup>9</sup>

According to the Shockley-Queisser limit, the maximum percent conversion of a single junction photovoltaic device is 34%.<sup>10</sup> This limit can be exceeded by multiexciton generation (MEG) also known as carrier multiplication (CM).<sup>11-13</sup> CM occurs when a photon with energy at least twice the energy gap is absorbed by a quantum dot. Instead of losing the excess energy to heat, the excess energy is used to create multiple electron-hole pairs. This phenomenon was observed in several quantum dots systems, such as CuInSe<sub>2</sub><sup>14,15</sup>, PbSe<sup>16,17</sup>, Si<sup>18,19</sup>, and CdSe<sup>20,21</sup> to name a few.

To our knowledge, there have been a few studies on understanding exciton

---

\*The work contained in this chapter is the subject of a scholarly article that is currently in preparation. Authors on this work include Cherrelle J. Thomas, Yangning Zhang, Junjie Li, Leonard Francis, Richard Schaller, and Brian A. Korgel. Cherrelle Thomas was responsible for planning the research, and synthesis of nanocrystals with help from Yangning Zhang, analyzing the data, researching and writing the completed document. Junjie Li and Leonard Francis imaged the nanocrystals using high res TEM. Richard Schaller conducted the TAS measurements.

kinetics for cesium lead halide<sup>22-28</sup>. D. de Jong, et al.<sup>22</sup> discovered multiexciton complex formation in CsPbBr<sub>3</sub> nanocrystals of size 8.6 nm, when using a transient-induced absorption spectroscopy method. On the other hand, Makarov, et al.<sup>23</sup> observed biexciton Auger decay lifetimes that were shorter than the traditional scaling observed in the CdSe and PbSe systems. Moreover, they did not observe CM in the CsPbI<sub>3</sub> quantum dot system when they used a pump wavelength of 254 nm which was the shortest wavelength available to them. They attributed this to the fact that  $3 \cdot E_g$  is needed to produce CM in CsPbI<sub>3</sub> quantum dots. Although these studies provide insight into CM in cesium lead halide nanocrystals, to our knowledge only one study has been conducted on CsPbI<sub>3</sub> quantum dots. These studies are of great interest to researchers since the band energy gap of CsPbI<sub>3</sub> is in a range where CM can be observed; unlike CsPbBr<sub>3</sub> or CsPbCl<sub>3</sub> systems.

Here, we investigate CM in CsPbI<sub>3</sub> nanocrystals synthesized with two different ligand combinations: oleylamine (OLA) and oleic acid (OA) (LC1) and oleylamine (OLA) and diisooctylphosphinic acid (DOPA) (LC2). Using the LC1 ligand set, we found that it was difficult to isolate and stabilize various nanocrystal sizes. By using the LC2 ligand set, we were able to successfully stabilize and isolate various nanocrystal sizes. Wang, et al.<sup>29</sup> discovered that by replacing the oleic acid with an alkyl phosphinic acid, the stability of the CsPbI<sub>3</sub> nanocrystals were increased. Therefore, we synthesized three different sizes of nanocrystals: one using the LC1 ligand set (oleylamine and oleic acid) and the other two used the LC2 ligand set (oleylamine and diisooctylphosphinic acid). Using transient absorption spectroscopy (TAS), biexciton lifetimes were measured and

found to be similar for nanocrystals of similar size, regardless of the ligands. Moreover, CM was observed in all three samples under various pump wavelengths.

## **6.2: EXPERIMENTAL DETAILS AND CHARACTERIZATION METHODS**

### **6.2.1: Experimental Details**

**Materials.** Lead iodide ( $\text{PbI}_2$ ), cesium carbonate ( $\text{Cs}_2\text{CO}_3$ ), octadecene (ODE, 90%), oleylamine (OLA, 70%), oleic acid (OA), diisooctylphosphinic acid (DOPA), anhydrous hexane, anhydrous methyl acetate were obtained from Sigma-Aldrich company. All chemicals were used without further purification.

**Nanocrystal (NC) synthesis.** Cs-oleate (0.59 M) was synthesized by loading a 3-neck 100 mL flask with  $\sim 2.5$  mmol of  $\text{C}_2\text{CO}_3$  (0.814g), 40 mL of ODE, and 2.5 mL of OA. The OA is replaced with DOPA for phosphinic capped particles. The reaction flask was degassed at  $120^\circ\text{C}$  for 1hr at  $\sim 150$  mTorr, then the flask temperature was raised to  $150^\circ\text{C}$  under a blanket of  $\text{N}_2$  until all  $\text{Cs}_2\text{CO}_3$  reacted with OA or DOPA. Then the flask was allowed to cool to room temperature and stored in the glovebox. As the temperature falls below  $100^\circ\text{C}$ , Cs-oleate will precipitate out of solution.

Moreover, 0.88 mmols of  $\text{PbI}_2$  and 20 mL of ODE were loaded into a 100 mL flask and degassed at  $120^\circ\text{C}$  for 1hr at  $\sim 150$  mTorr. Under a blanket of  $\text{N}_2$ , 2 mL of both OLA and OA or DOPA were injected into the reaction flask. The reaction flask was placed under vacuum and degas for an additional 30 minutes at  $120^\circ\text{C}$  and  $\sim 150$  mTorr. The reaction flask temperature was raised to the reaction temperature of  $170^\circ\text{C}$  ( $120^\circ\text{C}$  for the PAQ sample) under blanket of  $\text{N}_2$  and 3.2 mL of the preheated 0.59 M Cs-oleate

solution (recipe above) was injected into the reaction flask. After 5 seconds, the reaction product was cooled to room temperature via an ice bath.

After cooling, the reaction product to room temperature, the reaction flask was brought into a glove box. The reaction product was equally divided into two separate centrifuge tubes and 15 mL of methyl acetate was added to each tube. The perovskite nanocrystals were precipitated via centrifugation (8000 rpm for 5 minutes) while the supernatant was discarded and the precipitate was dispersed in 10 mL of anhydrous hexane. The nanocrystal dispersion was centrifuged again at 8500 rpm for 5-15 minutes. The supernatant was stored in a 20 mL vial in a freezer.

### **6.2.2: Materials Characterization**

Perovskite NCs were imaged by transmission electron microscopy (TEM) using a FEI Tecnai G2 Spirit BioTwin TEM or a JEOL 2010F TEM. The FEI Tecnai G2 TEM and JEOL 2010F TEM were operated at 80 kV and 200 kV, respectively. Samples were prepared for imaging by adding 240  $\mu\text{L}$  of anhydrous hexane and 20  $\mu\text{L}$  of isolated nanocrystals (40  $\mu\text{L}$  for iodide samples, due to lower reaction yields) into a 4.5 mL vial with a mesh nickel carbon-coated grid, supplied by Electron Microscopy Sciences (Cat#: CF150-Ni), placed at the bottom of vial. The vial evaporated overnight in the glove box to prevent changes in morphology and crystal structure. For high resolution TEM imaging, nanocrystal solutions were drop casted on a copper coated lacy carbon film (Cat#: 50-268-70) supplied from Electron Microscopy Sciences.

UV-visible absorbance spectra were measured using a Varian Cary Bio (UV-vis) spectrophotometer using a quartz cuvette. Photoluminescence (PL) was performed on a Varian Cary Eclipse Fluorescence spectrometer. The quartz cuvettes were prepared in an argon filled glovebox to protect the integrity of the nanocrystals.

A Rigaku R-axis Spider diffractometer was used to perform powder X-Ray diffraction (XRD). Samples were removed from the freezer and rotovap for 15 minutes under vacuum. Clean nylon loops were dipped into each sample using sample mounts. The diffractometer was operated at 40 kV and 40 mA under a Cu K $\alpha$  radiation ( $\lambda = 1.5418 \text{ \AA}$ ) rotated at  $5^\circ \text{ sec}^{-1}$  for 10 min. 2DP and JADE were used to process the data and background subtraction.

Transient absorption spectroscopy (TAS) measurements were performed on CsPbI<sub>3</sub> nanocrystals dispersed in anhydrous hexane; using four pump pulses (400 nm, 310 nm, 290 nm, and 245 nm), 35 fs pulse width, and 2 kHz amplified Ti:sapphire laser (center for Nanoscale Materials at Argonne National Laboratories). All pump pulses were spatially overlapped with a mechanically delayed white light probe generated by focusing of the amplifier output into a 2-mm thick sapphire plate. All samples were loaded into a quartz cuvette in a N<sub>2</sub> filled glovebox. Furthermore, all samples were magnetically stirred during experiments.

### **6.3: RESULTS AND DISCUSSION**

CsPbI<sub>3</sub> nanocrystals were synthesized via hot injection using two different combinations of ligands, OLA & OA (LC1) and OLA & DOPA (LC2). (Details on the

synthesis is in the section 6.2) For these experiments, three sets of nanocrystals were studied: the first being CsPbI<sub>3</sub> capped with the first set of ligands which we will refer to as OA, the last two were both synthesized with the second ligand set, but one set had bulk like optical properties and the other exhibited quantum confined properties which we refer to as PAB and PAQ respectively. Figure 6.1 shows transmission electron microscopy (TEM) images, UV-vis absorbance spectra, and PL spectra of the nanocrystals. These nanocrystals were shaped like cubes with an average side lengths of  $8.6 \pm 1.5$  nm (OA),  $17.5 \pm 2.8$  nm (PAB), and  $10.5 \pm 2.6$  nm (PAQ), respectively determined by TEM. Using X-ray diffraction (XRD) the OA nanocrystals exhibited the  $\alpha$ -cubic crystal structure and the PAB and PAQ nanocrystals formed the  $\gamma$ -orthorhombic crystal structure. The black  $\gamma$ -orthorhombic structure has been shown to exist for this system (Figure 6.1F). The lattice spacings were determined using high resolution TEM, which were found to be 3.1 Å for OA nanocrystals and 6.24 Å for PAB nanocrystals. Both lattice spacing were indicative of the (002) plane for the respective crystal structure. (Figure 6.1D and 6.1E). The optical gap of the nanocrystals ( $E_g$ ) was determined from UV-Vis absorbance and PL emission peak spectra (Figure 6.2A and 6.2B). The PL emission peaks for OA, PAB, and PAQ nanocrystals were 1.89 eV, 1.82 eV, and 1.88 eV when excited using a 400 nm wavelength respectively. Using Rhodamine B dye as the referencthe quantum yield (PLQY) was determined to be 30%, 7%, and 20% for OA, PAB, and PAQ respectively.

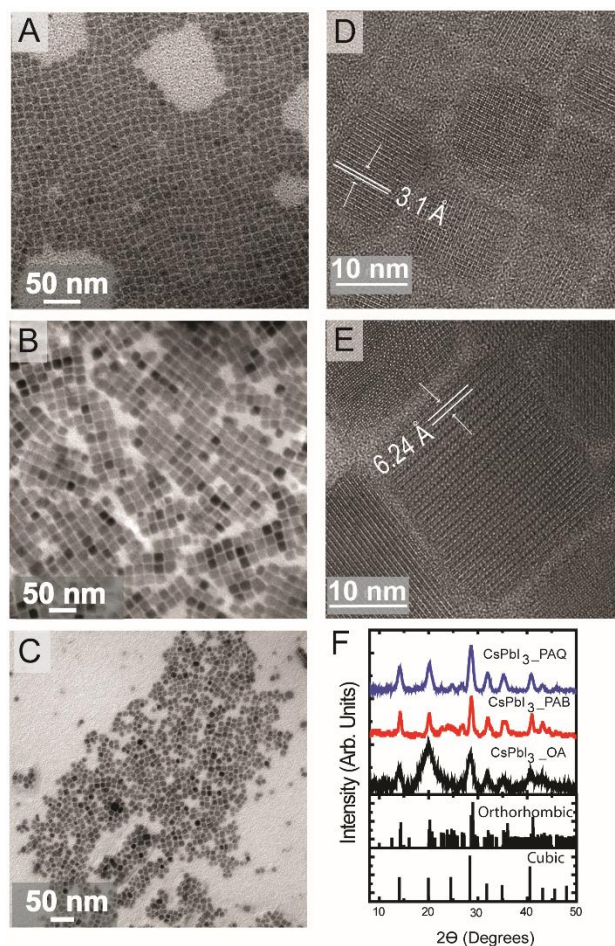


Figure 6.1: CsPbI<sub>3</sub> nanocrystals size histograms and TEM images (A-C) along with high resolution TEM images (D-E) and XRD spectra (E). (A) CsPbI<sub>3</sub> nanocrystals, synthesized with OA, with an average side length of  $8.6 \pm 1.5$  nm (OA). (B) CsPbI<sub>3</sub> nanocrystals, synthesized with DOPA, with an average side length of  $17.5 \pm 2.8$  nm (PAB). (C) CsPbI<sub>3</sub> nanocrystals, synthesized with DOPA, with an average side length of  $10.5 \pm 2.6$  nm (PAQ). (D-E) high resolution images of OA and PAB nanocrystals respectively. (F) Room temperature XRD spectra of CsPbI<sub>3</sub> nanocrystals, OA (black curve), PAB (red curve), and PAQ (blue curve). The reference pattern  $\alpha$ -Cubic (PDF#01-076-8588) and  $\gamma$ -orthorhombic (reference 31)



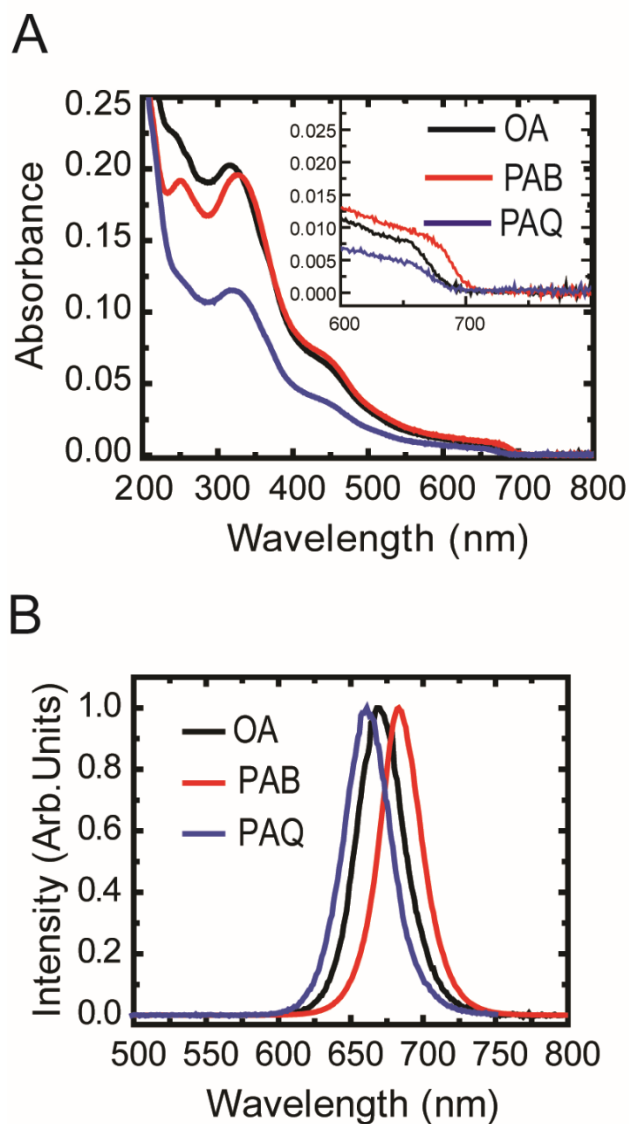


Figure 6.2: CsPbI<sub>3</sub> nanocrystals absorbance spectra (A) and PL spectra (B). The inset illustrates the magnified absorbance spectra between 600 nm and 800 nm. Room temperature absorbance and PL spectra of CsPbI<sub>3</sub> nanocrystals dispersed in hexane. OA (black curve), PAB (red curve), and PAQ (blue curve). The samples were observed using a 400 nm excitation wavelength. The samples exhibited PL quantum yields of 30%, 7%, and 20% respectively.

Transient absorption spectroscopy (TAS) measurements were performed on the OA, PAB, and PAQ nanocrystal dispersions in anhydrous hexane using four pump pulses, 400 nm, 310 nm, 290 nm, and 245 nm. All TAS measurements were performed under magnetic stirring to eliminate photo-induced effects on the detected signal. Figure 6.3 shows the TA bleach spectra for CsPbI<sub>3</sub> nanocrystal dispersions at a pump laser wavelength of 400 nm. TA bleach spectra for OA, PAB, and PAQ appeared at 656 nm (1.89 eV), 682 nm (1.82 eV), and 658 nm (1.88 eV) respectively. All TA kinetics were observed at the absorption bleach peak for each sample respectively.

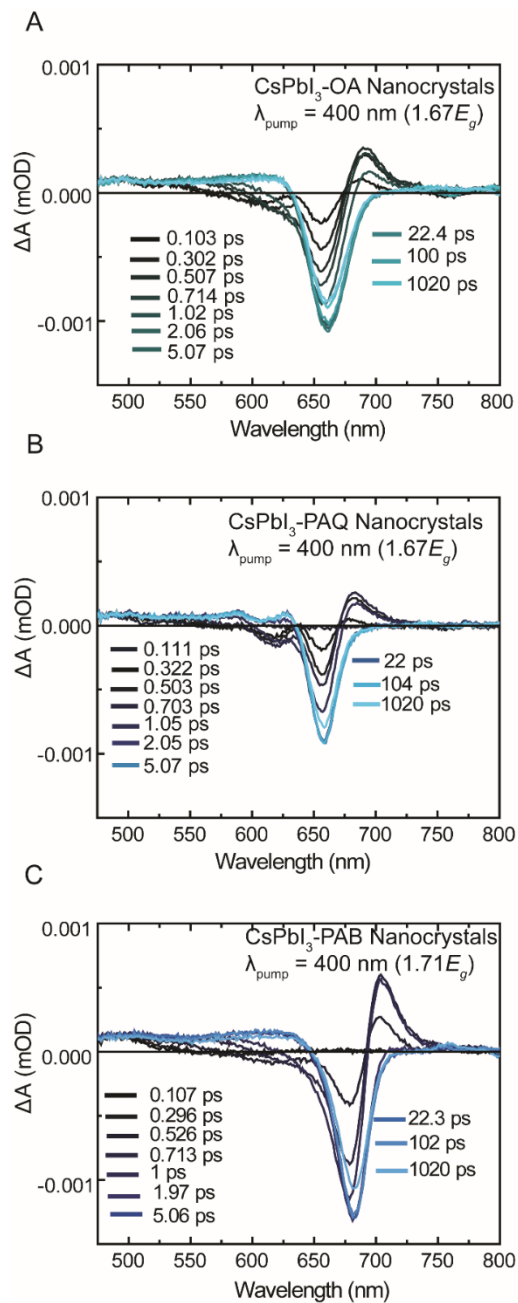


Figure 6.3: Delay time dependent transient absorption spectra of (A) OA ( $\langle N \rangle = 0.12$ ) nanocrystals (B) PAQ ( $\langle N \rangle = 0.11$ ) nanocrystals (C) PAB ( $\langle N \rangle = 0.40$ ) nanocrystals measured using a pump wavelength of 400 nm.

Figure 6.4 shows the TA kinetics of CsPbI<sub>3</sub> nanocrystals at a pump wavelength of 400 nm with various average number of photons absorbed by the nanocrystals  $\langle N \rangle$ .  $\langle N \rangle$  is calculated by the product of the absorption cross section  $\sigma$  (see figure 6.6) and pump fluence ( $J$ ),  $\langle N \rangle = \sigma J$ . Since the pump wavelength is less than twice the energy gap,  $h\nu < 2E_g$ , one 400 nm photon absorbed by the CsPbI<sub>3</sub> nanocrystals does not have enough energy to create more than one exciton. As a result, at low  $J$  the TA kinetics will exhibit the dynamics of single-excitons. However, as  $J$  is increased the TA kinetics will show the nonradiative Auger recombination dynamics of multiexcitons. Due to the fact that  $\langle N \rangle$  follows a Poisson distribution, it is not necessary for  $\langle N \rangle = 1$  for multiple excitons to appear in the dispersions. Furthermore,  $\langle N \rangle$  must be kept low to reduce the amount of multiexcitons produced via multiphoton absorption.

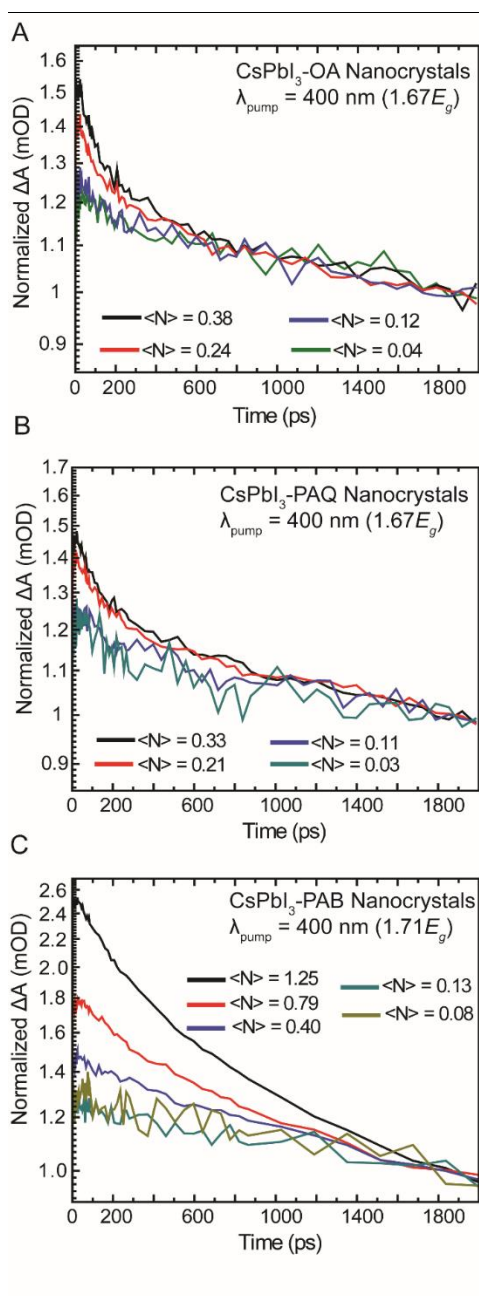


Figure 6.4: Fluent dependent transient absorption kinetics of (A) OA nanocrystals (B) PAB nanocrystals (c) PAQ nanocrystals measured using a pump wavelength of 400 nm. All kinetics are observed at the absorption bleach peak 656 nm, 682 nm, and 658 nm. All spectra are normalized to 1 at long delay times ( $\sim 2$  ns), where only single excitons are present.

From the TA kinetics, the biexciton Auger lifetimes can be found by subtracting the low pump flux single-exciton dynamics (that have been normalized at long delay times) from the high pump fluence dynamics, which have been normalized at long delay times. Figure 6.5 shows the biexciton Auger lifetimes for CsPbI<sub>3</sub> nanocrystals. The subtracted curves were fitted to a single exponential decay (Appendix C), which yields biexciton Auger lifetimes ranging from 150 ps to 753 ps depending on size or nanocrystal coupling. Conventionally, biexciton Auger lifetimes increase linearly with increasing nanocrystal volume. As shown in figure S4, the Auger lifetimes are plotted with respect to volume. The lifetimes and volumes are similar to those of CuInSe<sub>2</sub>, Si, PbSe, and CdSe reported in literature.<sup>12,18</sup>

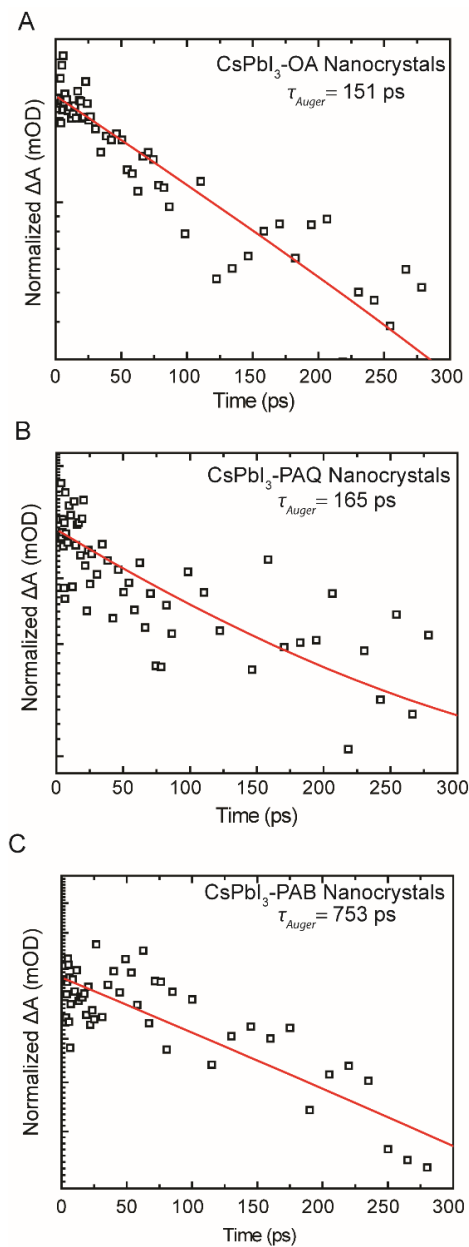


Figure 6.5: Biexciton Auger lifetime spectra at a pump wavelength of 400 nm (A) OA nanocrystals (from figure 4  $\langle N \rangle = 0.24$  -  $\langle N \rangle = 0.04$ ), (B) PAB nanocrystals (from figure 4  $\langle N \rangle = 0.79$  -  $\langle N \rangle = 0.13$ ), and (C) PAQ nanocrystals (from figure 4  $\langle N \rangle = 0.21$  -  $\langle N \rangle = 0.03$ ). The low fluence TA kinetics were subtracted from the high fluence TA kinetics. The kinetics are fitted to a single exponential decay (red lines).

Three additional pump wavelengths were used to investigate carrier multiplication (CM) in CsPbI<sub>3</sub> nanocrystals, 310 nm, 290 nm, and 245 nm. Since these pump wavelengths are more than twice the energy gap  $h\nu > 2E_g$ , one photon has enough energy to produce multiexcitons, even under low fluences. Please see Appendix C for the TA kinetics for the pump wavelengths at 310 nm, 290 nm, and 245 nm. Population ratios,  $R_{pop}$ , the ratios of short time TA signals over long time TA signals plotted as a function of pump fluence, is a technique used to determine whether CM is present in a system. The ratios are measured using various pump fluences at different pump wavelengths. The curves are fitted to a Poisson distribution eq 1

$$R_{pop} = \frac{\sigma J \times QY}{1 - e^{-\sigma J}} \quad (1)$$

Where QY is the CM quantum yield or the average number of excitons produced per absorbed photon and  $\sigma$  is the absorption cross section. The absorption cross section values are on the same order as the values reported in literature. The curves are fitted to eq 1 to determine QY and  $\sigma$  Figure 6.6 plots  $R_{pop}$  as a function of pump fluence under various pump wavelengths. The ratios were taken at 4 ps (where more than one exciton can occupy the nanocrystals) and at 1500 ps (where single excitons are solely present due to Auger recombination).



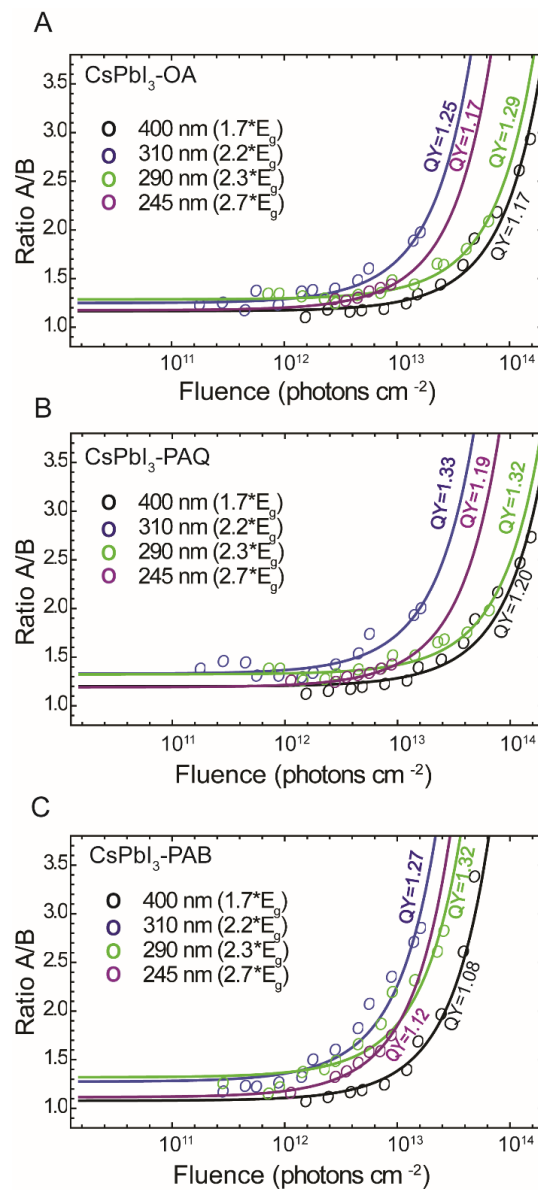


Figure 6.6: Rpop spectra, ratio of short and long time TA signals as a function of pump fluence (A) OA nanocrystals, (B) PAQ nanocrystals, and (C) PAB nanocrystals at 400 nm (black squares), 310 nm (red circles), 290 nm (blue triangles), and 245 nm (green upside down triangles) pump wavelengths. All data is fitted with a Poisson distribution (eq 1), where QY is the carrier multiplication quantum yield and  $\sigma_x$  is the absorption cross section at the respective pump wavelength ( $X = 400 \text{ nm}, 310 \text{ nm}, 290 \text{ nm}, \text{ or } 245 \text{ nm}$ ).

Typically, the QY should be 1 when using a pump wavelength that is less than twice the band gap, but here we observe QYs above one. This alludes to the fact that there may be traps or surface defects in the nanocrystals. Additionally, as the pump wavelength increases the Rpop ratios should increase as well. Here, we observe the opposite phenomenon, when the pump wavelength is increased to 2.3 times the energy gap, Rpop ratio begins to decrease. This can be due to the fact that the ligands start to absorb at bluer wavelengths. Figure 6.7 plots the absorbance data for the three ligands (OA, OLA, and DOPA) used in the synthesis. At a wavelength of 325 nm OA and OLA begins to weakly absorb; therefore, as the wavelength is changed to shorter wavelengths, 290 nm and 245 nm, the ligands absorb more strongly than the lower energy wavelengths. As a result, CM increased for the OA and PAB samples up until the pump wavelength of 290 nm and then decreases when the pump wavelength is 245 nm. However, in the PAQ samples the CM increases when the pump wavelength is decreased to 310 nm, the wavelength is decreased to 290 nm and 245 nm. The CM also decreases particularly in the 245 nm wavelength regime. This could be due to the absorption of the ligands, eluding to the fact that the PAQ nanocrystal dispersion may have a higher OLA concentration than PAB, and the PAQ and OA nanocrystals may have more ligands than the PAB systems.

The theoretic lowest energy, E, needed for CM can be estimated using eq 2

$$E = \left(2 + \frac{m_e}{m_h}\right) E_g \quad (2)$$

Where  $M_h$  and  $M_e$  are the effective masses of an electron or hole, which is 0.095 and 0.086 respectively.<sup>21</sup> From eq 2 the threshold for CM to occur in CsPbI<sub>3</sub> nanocrystals is 2.9\*E<sub>g</sub>,

however, we were able to observe weak CM in the CsPbI<sub>3</sub> nanocrystals below the threshold energy. This coincides with the discoveries found from Klimov and can be another reason for the low CM observed in our nanocrystals.

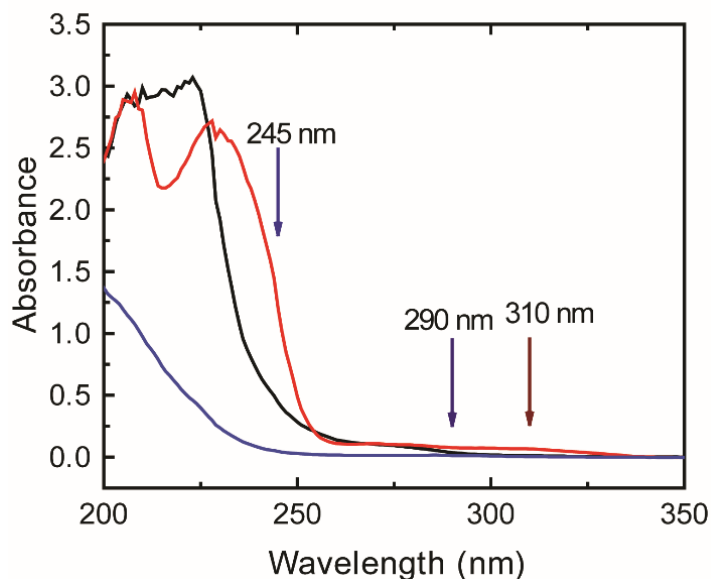


Figure 6.7: UV-vis absorbance spectra of the three capping ligands, OA (black squares), OLA (red circles), and DOPA (blue triangles), used in the CsPbI<sub>3</sub> nanocrystal synthesis. The vertical lines correspond to the pump wavelengths (400 nm, 310 nm, 290 nm, and 245 nm) used for TAS measurements

#### 6.4: CONCLUSIONS

CM was studied in three different CsPbI<sub>3</sub> nanocrystal dispersions, OA, PAB, and PAQ, via TAS measurements. TA kinetics were collected using a wide range of pump fluences and four different pump wavelengths 400 nm, 310 nm, 290 nm, and 245 nm. From

the TA kinetics, we were able to determine the biexcitation Auger lifetimes for the CsPbI<sub>3</sub> nanocrystals to be in the range of 150 ps to 753 ps depending on size. Despite the theoretical threshold for CM in CsPbI<sub>3</sub> nanocrystals being  $\sim 3^*E_g$ , we were able to observe weak CM in OA, PAB, and PAQ nanocrystal dispersions below  $3^*E_g$  via Rpop plots. This is where the PAB nanocrystals exhibited the higher CM efficiency of 22% when using a pump wavelength of 290 nm. The small CM QYs for the CsPbI<sub>3</sub> nanocrystals may be due to the absorption of the ligands in the regime of the high energy or the similar effective masses for the hole and electron in CsPbI<sub>3</sub> nanocrystals.

## 6.5: REFERENCES

1. Ananthakumar, S., Kumar, J. R. & Babu, S. M. Cesium lead halide (CsPbX<sub>3</sub>, X=Cl, Br, I) perovskite quantum dots-synthesis, properties, and applications: a review of their present status. *J. Photonics Energy* **6**, 42001 (2016).
2. Wang, H.-C., Bao, Z., Tsai, H.-Y., Tang, A.-C. & Liu, R.-S. Perovskite Quantum Dots and Their Application in Light-Emitting Diodes. *Small* **14**, 1702433 (2018).
3. Ono, L. K., Juarez-Perez, E. J. & Qi, Y. Progress on Perovskite Materials and Solar Cells with Mixed Cations and Halide Anions. *ACS Appl. Mater. Interfaces* **9**, 30197–30246 (2017).
4. Li, X., Cao, F., Yu, D., Chen, J., Sun, Z., Shen, Y., Zhu, Y., Wang, L., Wei, Y., Wu, Y. & Zeng, H. All Inorganic Halide Perovskites Nanosystem: Synthesis, Structural Features, Optical Properties and Optoelectronic Applications. *Small* **13**, 1603996 (2017).

5. Protesescu, L., Yakunin, S., Bodnarchuk, M., Krieg, F., Caputo, R., Hendon, C., Yang, R., Walsh, A. & Kovalenko, M. Nanocrystals of cesium lead halide perovskites (CsPbX<sub>3</sub>, X=Cl, Br, and I): novel optoelectronic materials showing bright emission with wide color gamut. *Nano Lett.* **15**, 3692–3696 (2015).
6. Su, Y., Chen, X., Ji, W., Zeng, Q., Ren, Z., Su, Z. & Liu, L. Highly Controllable and Efficient Synthesis of Mixed-Halide CsPbX<sub>3</sub> (X = Cl, Br, I) Perovskite QDs toward the Tunability of Entire Visible Light. *ACS Appl. Mater. Interfaces* **9**, 33020–33028 (2017).
7. Huang, H., Bodnarchuk, M. I., Kershaw, S. V., Kovalenko, M. V. & Rogach, A. L. Lead Halide Perovskite Nanocrystals in the Research Spotlight: Stability and Defect Tolerance. *ACS Energy Lett.* **2**, 2071–2083 (2017).
8. Swarnkar, A., Marshall, A. R., Sanhira, E. M., Chernomordik, B. D., Moore, D. T., Christians, J. A., Chakrabarti, T. & Luther, J. M. Quantum dot-induced phase stabilization of  $\alpha$ -CsPbI<sub>3</sub> perovskite for high-efficiency photovoltaics. *Science* **354**, 92–95 (2016).
9. Sanhira, E. M., Marshall, A. R., Christians, J. A., Harvey, S. P., Ciesielski, P. N., Wheeler, L. M., Schulz, P., Lin, L. Y., Beard, M. C. & Luther, J. M. Enhanced mobility CsPbI<sub>3</sub> quantum dot arrays for record-efficiency, high-voltage photovoltaic cells. *Sci. Adv.* **3**, eaao4204 (2017).
10. Shockley, W. & Queisser, H. J. Detailed Balance Limit of Efficiency of *p-n* Junction Solar Cells. *J. Appl. Phys.* **32**, 510–519 (1961).

11. Luo, J.-W., Franceschetti, A. & Zunger, A. Carrier Multiplication in Semiconductor Nanocrystals: Theoretical Screening of Candidate Materials Based on Band-Structure Effects. *Nano Lett.* **8**, 3174–3181 (2008).
12. Padilha, L. A., Stewart, J. T., Sandberg, R. L., Bae, W. K., Koh, W.-K., Pietryga, J. M. & Klimov, V. I. Carrier Multiplication in Semiconductor Nanocrystals: Influence of Size, Shape, and Composition. *Acc. Chem. Res.* **46**, 1261–1269 (2013).
13. Beard, M. C., Midgett, A. G., Hanna, M. C., Luther, J. M., Hughes, B. K. & Nozik, A. J. Comparing Multiple Exciton Generation in Quantum Dots To Impact Ionization in Bulk Semiconductors: Implications for Enhancement of Solar Energy Conversion. *Nano Lett.* **10**, 3019–3027 (2010).
14. Stolle, C. J., Harvey, T. B., Pernik, D. R., Hibbert, J. I., Du, J., Rhee, D. J., Akhavan, V. A., Schaller, R. D. & Korgel, B. A. Multiexciton Solar Cells of CuInSe<sub>2</sub> Nanocrystals. *J. Phys. Chem. Lett.* **5**, 304–309 (2014).
15. Stolle, C. J., Schaller, R. D. & Korgel, B. A. Efficient Carrier Multiplication in Colloidal CuInSe<sub>2</sub> Nanocrystals. *J. Phys. Chem. Lett.* **5**, 3169–3174 (2014).
16. Schaller, R. D. & Klimov, V. I. High Efficiency Carrier Multiplication in PbSe Nanocrystals: Implications for Solar Energy Conversion. *Phys. Rev. Lett.* **92**, 186601 (2004).
17. Trinh, M. T., Houtepen, A. J., Schins, J. M., Hanrath, T., Piris, J., Knulst, W., Goossens, A. P. L. M. & Siebbeles, L. D. A. In Spite of Recent Doubts Carrier Multiplication Does Occur in PbSe Nanocrystals. *Nano Lett.* **8**, 1713–1718 (2008).

18. Stolle, C. J., Lu, X., Yu, Y., Schaller, R. D. & Korgel, B. A. Efficient Carrier Multiplication in Colloidal Silicon Nanorods. *Nano Lett.* **17**, 5580–5586 (2017).
19. Beard, M. C., Knusten, K. P., Yu, P., Luther, J. M., Song, Q., Metzger, W. K., Ellingson, R. J. & Nozik, A. J. Multiple Exciton Generation in Colloidal Silicon Nanocrystals. *Nano Lett.* **7**, 2506–2512 (2007).
20. Nair, G. & Bawendi, M. G. Carrier multiplication yields of CdSe and CdTe nanocrystals by transient photoluminescence spectroscopy. *Phys. Rev. B* **76**, 81304 (2007).
21. Schaller, R. D., Petruska, M. A. & Klimov, V. I. Effect of electronic structure on carrier multiplication efficiency: Comparative study of PbSe and CdSe nanocrystals. *Appl. Phys. Lett.* (20051219). doi:10.1063/1.2142092
22. de Jong, E. M. L. D., Yamashita, G., Gomez, L., Ashida, M., Fujiwara, Y. & Gregorkiewicz, T. Multiexciton Lifetime in All-Inorganic CsPbBr<sub>3</sub> Perovskite Nanocrystals. *J. Phys. Chem. C* **121**, 1941–1947 (2017).
23. Makarov, N. S., Guo, S., Isaienko, O., Liu, W., Robel, I. & Klimov, V. I. Spectral and Dynamical Properties of Single Excitons, Biexcitons, and Trions in Cesium–Lead–Halide Perovskite Quantum Dots. *Nano Lett.* **16**, 2349–2362 (2016).
24. Yarita, N., Tahara, H., Ihara, T., Kawawaki, T., Sato, R., Saruyama, M., Teranishi, T. & Kanemitsu, Y. Multiexciton recombination dynamics in CsPbBr<sub>3</sub> perovskite nanocrystals revealed by femtosecond transient absorption and single dot spectroscopies. in *2017 Conference on Lasers and Electro-Optics Europe European*

*Quantum Electronics Conference (CLEO/Europe-EQEC) 1–1 (2017).*

doi:10.1109/CLEOE-EQEC.2017.8087818

25. Liu, Q., Wang, Y., Sui, N., Wang, Y., Chi, Z, Wang, Q, Chen, Y., Ji, W. & Zhang, H. Exciton Relaxation Dynamics in Photo-Excited CsPbI<sub>3</sub> Perovskite Nanocrystals. *Sci. Rep.* **6**, 29442 (2016).
26. Aneesh, J., Swarnkar, A., Ravi, V. K., Sharma, R., Nag, A. & Adarsh, K. V. Ultrafast Exciton Dynamics in Colloidal CsPbBr<sub>3</sub> Perovskite Nanocrystals: Biexciton Effect and Auger Recombination. *J. Phys. Chem. C* **121**, 4734–4739 (2017).
27. Eperon, G. E., Jedlicka, E. & Ginger, D. S. Biexciton Auger Recombination Differs in Hybrid and Inorganic Halide Perovskite Quantum Dots. *J. Phys. Chem. Lett.* **9**, 104–109 (2018).
28. Hu, F., Yin, C., Zhang, H., Sun, C., Yu, W. W., Zhang, C., Wang, X., Zhang, Y. & Xiao, M. Slow Auger Recombination of Charged Excitons in Nonblinking Perovskite Nanocrystals without Spectral Diffusion. *Nano Lett.* **16**, 6425–6430 (2016).
29. Wang, C., R. Chesman, A. S. & J. Jasieniak, J. Stabilizing the cubic perovskite phase of CsPbI<sub>3</sub> nanocrystals by using an alkyl phosphinic acid. *Chem. Commun.* **53**, 232–235 (2017).
30. Becker, M. A., Vaxenburg, R., Nedelcu, G., Serce, P. C., Shabaev, A., Mehel, M., Michopoulos, J. G., Lambrakos, S. G., Bernstein, N., Lyons, J. L., Stoferle, T., Mahrt, R. F., Kovalenko, M. V., Norris, D. J., Rainò, G. & Efros, A. L. Bright triplet excitons in caesium lead halide perovskites. *Nature* **553**, 189 (2018).



31. Sutton, R. J., Filip, M. R., Haghighirad, A. A., Sakai, N., Wenger, B., Giustino, F., & Sanith, H. J. Cubic or Orthorhombic? Revealing the Crystal Structure of Metastable Black-Phase CsPbI<sub>3</sub> by Theory and Experiment. *ACS Energy Lett.* **3**, 1787–1794 (2018).

## Chapter 7: Conclusions and Future Directions

### 7.1: CONCLUSIONS

The research in this dissertation is inspired by the question: *how can nanomaterials be used to alleviate the dependence on non-renewable resources?* Developing renewable technologies that can mitigate the need for non-renewable resources and reduce the carbon footprint on the environment.<sup>1,2</sup> The employment of nanocrystal solar cells is a viable technology to solve the problem. These solar cells can be manufactured on various substrates using several different methods, which makes them cost effective and possibly flexible expanding the array of applications.<sup>3,4</sup> However, nanocrystal solar cells suffer from low efficiencies, due to variable surface chemistry, surface traps in the nanocrystals, instability of the nanocrystals, poor charge transport in the films, and the synthesis of the nanocrystals. There have been many strides to improve these problems, such as ligand exchange, hot-injection synthesis techniques, and doping of the nanocrystals. These methods have been shown to improve the devices, however, efficiencies are still lower than the first and second generation solar devices.<sup>5-7</sup>

Here, focus is given to understanding the  $\text{CuIn}_{1-x}\text{Ga}_x\text{Se}_2$  (CIGS) and perovskite nanocrystals synthesis techniques and functionalization and how it effects nanocrystal morphology, reaction conversion yields, thermal stability, and exciton kinetics. CIGS thin film devices exhibit solar cell efficiencies of  $\sim 20\%$ <sup>8</sup> and  $13.4\%$ <sup>9</sup> for  $\text{CsPbI}_3$  nanocrystalline solar cells. By understanding how these intricate details effect the device performance. We will gain the ability to engineer nanocrystals for the manufacturing of solar cells that can produce device efficiencies on par with the first and second generation of solar cells, such as silicon.

### 7.1.1: CuIn<sub>1-x</sub>Ga<sub>x</sub>Se<sub>2</sub> nanocrystal Synthesis

One-pot and hot-injection synthetic methods of CuIn<sub>1-x</sub>Ga<sub>x</sub>Se<sub>2</sub> nanocrystals were investigated. It was found that the different synthetic methods produced nanocrystals of different morphologies and the hot injection methods allowed for shorter reaction times. Additionally, it was shown that once we exchanged oleylamine for other organic ligands, the nanocrystal morphology changed and in some instances the crystal structure was altered. When X = 0 or in other words no Ga is added into the nanocrystal, the crystal structure remained constant regardless of the synthetic method or reactants used.

### 7.1.2: CuInSe<sub>2</sub> <sup>31</sup>P Nuclear Magnetic Resonance

Diphenylphosphine selenide (DPP=Se) and tri-*n*-butylphosphine selenide (TBP=Se) were assessed as selenium (Se) sources for the synthesis of copper indium diselenide (CuInSe<sub>2</sub>) nanocrystals in oleylamine. Both Se reactants bind to Cu<sup>+</sup> and In<sup>3+</sup> ions to provide the well-defined molecular precursor species with similar Se=P bond cleavage energies. However, DPP=Se provides much higher conversion yields of CuInSe<sub>2</sub> nanocrystals because of the labile hydrogen on diphenylphosphine. Photovoltaic devices (PVs) fabricated with TBP=Se derived nanocrystals exhibit efficiencies nearly double those obtained using nanocrystals made with DPP=Se. Higher device efficiencies were obtained from nanocrystals with a reasonably high conversion yields by using TBP=Se as the Se source with the addition of DPP to the reaction. These results are elucidated *via* <sup>31</sup>P nuclear magnetic resonance (NMR) spectroscopy and thermogravimetric analysis (TGA). A mechanistic pathway for CuInSe<sub>2</sub> nanocrystal formation is proposed based on the spectroscopic findings.

### **7.1.3: Perovskite Nanocrystals**

Cesium, formamidinium, and mixed cation and anion perovskite nanocrystals were studied. Cesium based perovskite nanocrystals were shown to be orthorhombic and cubic in crystal structure. As well as, the energy gap was shown to vary depending on the concentration of Cs-oleate used. Furthermore, oleic acid was exchanged for diisooctylphosphinic acid (PA) to passivate the nanocrystals. Nanocrystals capped with PA were shown to have lifetimes that were a magnitude larger than those synthesized with oleic acid.

The organic perovskite system FAPbI<sub>3</sub> exhibits energy gaps in the NIR; however, the nanocrystals have shown to be unstable under the microscope beam. By doping FAPbI<sub>3</sub> nanocrystals with Cs atoms, allowed for the production of nearly cubic nanocrystals while increasing the stability of the organic nanocrystals under the TEM. The addition of the Cs atoms blue shifts the energy gap of the nanocrystals.

### **7.1.4: Thermal stability of Perovskite nanocrystals**

The thermal stability of  $\gamma$ -orthorhombic cesium lead iodide (CsPbI<sub>3</sub>) perovskite nanocrystal order assemblies were investigated via in-situ grazing-incidence small and wide angle scattering (GISAXS and GIWAXS). CsPbI<sub>3</sub> nanocrystals were capped with oleic acid (OA) or phosphinic acid (PA) and assembled onto silicon wafers via slow solvent evaporation. The formation of ordered arrays were supported by scanning and transmission electron microscopy. The capping ligand was determined to influence nanocrystal orientation on the substrate. CsPbI<sub>3</sub> nanocrystal capped with OA gave ordered arrays of (001)<sub>SL</sub> and (002)<sub>NC</sub> orientations. However, nanocrystals capped with

PA exhibited weakly ordered arrays with nanocrystal orientations of  $(110)_{\text{NC}}$  and  $(002)_{\text{NC}}$ . Upon heating the  $\text{CsPbI}_3$  nanocrystal assemblies to  $300^\circ\text{C}$  under ambient conditions, we observed the crystal structure transition from the  $\gamma$ -orthorhombic to the  $\delta$ -orthorhombic (yellow phase). Additionally, an increase in thermal stability was observed for PA capped nanocrystals which may be due to a stronger ligand bond.

### **7.1.5: High Energy Carrier Dynamics of CsPbI<sub>3</sub> Perovskite Nanocrystals**

Multiexciton generation (MEG) also known as carrier multiplication (CM) was studied in cesium lead iodide perovskite nanocrystals via transient absorption spectroscopy (TAS). Two different capping ligand combinations, oleylamine and oleic acid or oleylamine and diisooctylphosphinic acid with three different sizes, 8.6 nm, 10.5 nm, and 17.5 nm, were investigated in this study. Single-exciton and multiexciton states were explored using four pump wavelengths 400 nm, 310 nm, 290 nm, and 245 nm. Biexciton Auger decay lifetimes, absorption cross sections, and carrier multiplication quantum yields were found for each sample at the different wavelengths. Surprisingly, carrier multiplication was observed below the theoretical minimum energy needed for carrier multiplication to occur. A reduction in carrier multiplication quantum yields was observed for high energy pump wavelengths; which may be due to the absorption of the capping ligands at higher wavelengths.

## **7.2: FUTURE DIRECTIONS**

### **7.2.1: Understanding the $\text{CuIn}_{1-x}\text{Ga}_x\text{Se}_2$ Nanocrystals Surface Chemistry**

In Chapter two, various synthetic methods for the production of  $\text{CuIn}_{1-x}\text{Ga}_x\text{Se}_2$  nanocrystals were explored. Nanocrystals were found to exhibit multiple morphologies within the nanocrystals dispersions. The resulting nanocrystals are problematic for photovoltaic device performances. Along with the composition of the nanocrystals, the size and shape determines the optical and electronic properties of the materials.<sup>10-12</sup> As a result, nanocrystal films exhibit variations of optical and electrical properties throughout, resulting in poor charge transport in the films. By controlling the size and morphology of the nanocrystals, we will have the ability to maintain the desired optical and electrical properties in the films. Additionally, better electron and hole accepting layers may be chosen.

Not only should the size and morphology of the nanocrystals be controlled but also the surface chemistry. Currently, incomplete surface passivation and the use of electrical insulating ligands impede charge transport in the films due to the entrapment of electrons in mid gap states and long electron hopping distances respectively.<sup>13,14</sup> By understanding the surface chemistry, ligand cocktails can be used to improve surface passivation that will mitigate the production of mid gap states. Additionally, the longer ligands should be replaced for shorter ones decreasing the electron hopping within the films.

### 7.2.2: Lead – Free Perovskite Nanocrystals

The research conducted in this dissertation was focused on improving the thermal stability of Cs based perovskite nanocrystals. Specifically, enhancing the thermal stability of the nanocrystals will prevent lead contamination in the environment. This will prevent the release of Pb atoms upon decomposition. There are two popular methods that are used to combat this (1) exchanging labile capping ligands for more strongly bound ligands or (2) replacing the environmentally toxic Pb for environmentally benign elements, such as Ge or Sn<sup>15-21</sup>.

Ge serves as an attractive replacement due to the fact that Pb and Ge are in the same group and have similar electron configuration, and small band gap makes the materials advantageous for solar cells.<sup>18</sup> However, stabilizing Ge<sup>2+</sup> is very challenging. Bulk cesium germanium iodide (CsGeI<sub>3</sub>) crystals have been synthesized using a two phase method (organic/aqueous phase) which are stable under ambient conditions. Figures 7.1 and 7.2 shows the scanning electron microscopy (SEM) images of CsGeI<sub>3</sub> crystals and the X-ray diffraction pattern respectively. However, these crystals are not dispersible in solvents due to an incomplete functionalization on the surface. Attempts to functionalize the surface were tried using both oleylamine and oleic acid but produced CsI nanocrystals and flakes as shown in Figures 7.3 and 7.4. More research needs to be done on the successful passivation of the nanocrystals while stabilizing Ge<sup>2+</sup> nanocrystals. Completion of this work will allow the use of non-toxic perovskite nanocrystals for PV devices.

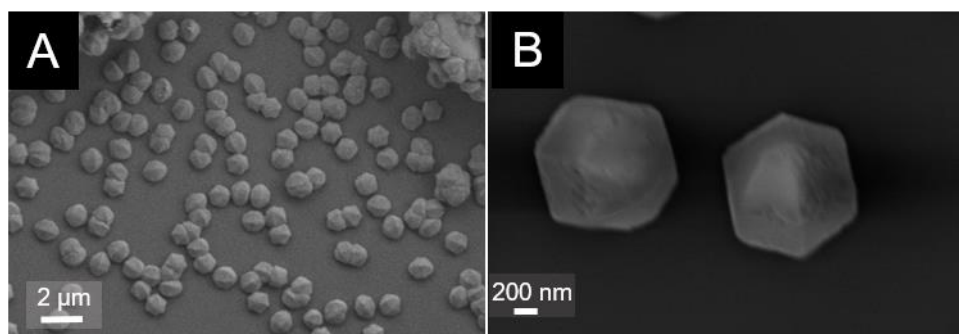


Figure 7.1: SEM images of bulk  $\text{CsGeI}_3$  crystals.

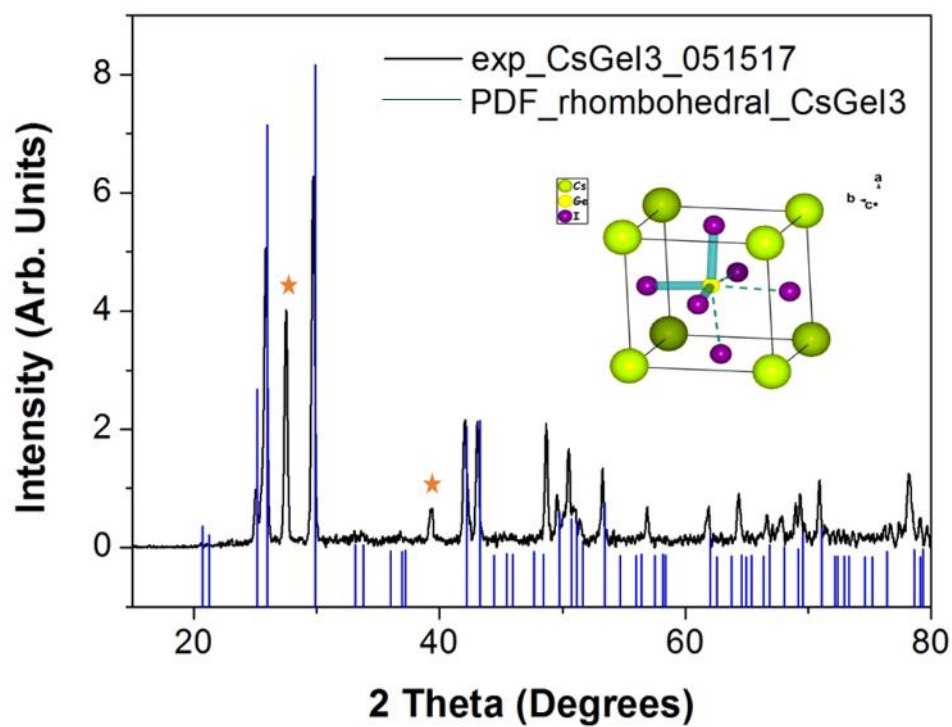


Figure 7.2: X-ray diffraction pattern for  $\text{CsGeI}_3$  bulk crystals. The bulk crystals show a rhombohedral crystal structure. The peaks labeled  $\star$  denotes the CsI peaks.



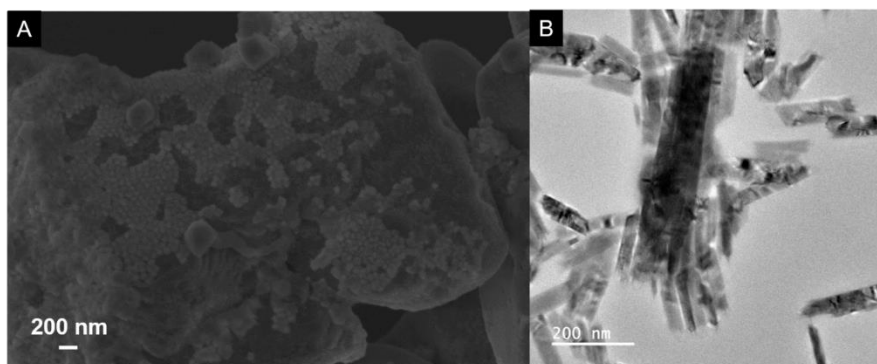


Figure 7.3: SEM (A) and TEM (B) images of  $\text{CsGeI}_3$  crystals after attempting to passivate with organic ligands. The cubic crystals shown in A were white and indicative of  $\text{CsI}$ .

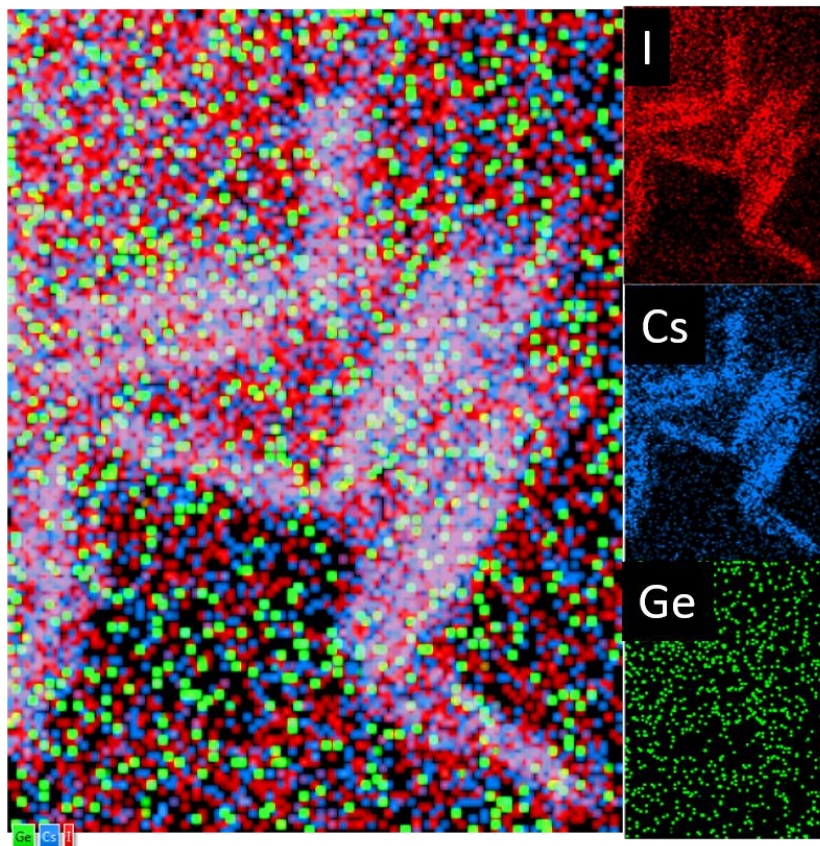


Figure 7.4: High resolution TEM EDS image of  $\text{CsGeI}_3$  crystals after attempts of passivation with organic ligands. The crystals are mainly composed of Cs and I.

### 7.2.2: Flexible Perovskite Nanocrystal Photovoltaic Devices

Even though perovskite nanocrystal solar cells hold the record for the highest nanocrystal photovoltaic device efficiencies, they are fabricated on rigid glass substrates shown in Figure 7.5<sup>9,22</sup>. This limits the applications and increases the weight of the photovoltaic devices. Replacing the rigid glass substrates with more flexible materials such as plastics or paper will dramatically reduce the fabrication, transportation, and installation cost of the photovoltaic devices. Before the fabrication of flexible devices, stabilizing lead based perovskite nanocrystals or improving the efficiencies of lead-free nanocrystals must occur.

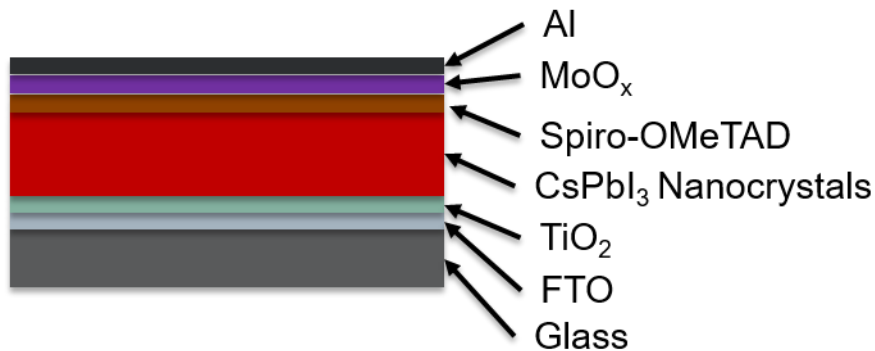


Figure 7.5: This is a typical setup for the perovskite CsPbI<sub>3</sub> nanocrystal photovoltaic devices. Photons are shone through the glass and are absorbed by the CsPbI<sub>3</sub> layer to make exciton pairs.

### 7.3: REFERENCES

1. Kabir, E., Kumar, P., Kumar, S., Adelodun, A. A. & Kim, K.-H. Solar energy: Potential and future prospects. *Renew. Sustain. Energy Rev.* **82**, 894–900 (2018).
2. Solar Energy vs Fossil Fuels: How Do They Compare? | EnergySage. *Solar News* (2017).

3. Kamat, P. V. Quantum Dot Solar Cells. Semiconductor Nanocrystals as Light Harvesters. *J. Phys. Chem. C* **112**, 18737–18753 (2008).
4. Hillhouse, H. W. & Beard, M. C. Solar cells from colloidal nanocrystals: Fundamentals, materials, devices, and economics. *Curr. Opin. Colloid Interface Sci.* **14**, 245–259 (2009).
5. Zvaigzne, M. A., Aleksandrov, A. E., Samokhvalov, P. S., Martynov, I. L., Lypenko, D. A., Tameev, A. R., Nikitenko, V. R., Chistyakov, A. A. Influence of the surface ligand molecules length on the optical properties and photoconductivity of PbS quantum dot condensates. *Tech. Phys. Lett.* **43**, 879–881 (2017).
6. Razgoniaeva, N., Yang, M., Garrett, P., Kholmicheva, N., Moroz, P., Eckard, H., Romero, L. R., Porotnikov, D., Khon, D., & Zamkov, M. Just Add Ligands: Self-Sustained Size Focusing of Colloidal Semiconductor Nanocrystals. *Chem. Mater.* **30**, 1391–1398 (2018).
7. Kwon, S. G. & Hyeon, T. Formation Mechanisms of Uniform Nanocrystals via Hot-Injection and Heat-Up Methods. *Small* **7**, 2685–2702 (2011).
8. Jackson, P., Hariskos, D., Lotter, E., Paetel, S., Wuerz, R., Menner, R., Wischmann, W., & Powalla, M. New world record efficiency for Cu(In,Ga)Se<sub>2</sub> thin-film solar cells beyond 20%. *Prog. Photovolt. Res. Appl.* **19**, 894–897 (2011).
9. Sanehira, E. M., Marshall, A. R., Christians, J. A., Harvey, S. P., Ciesielski, P. N., Wheeler, L. M., Schulz, P., Lin, L. Y., Beard, M. C. & Luther, J. M. Enhanced mobility CsPbI<sub>3</sub> quantum dot arrays for record-efficiency, high-voltage photovoltaic cells. *Sci. Adv.* **3**, eaao4204 (2017).

10. Alivisatos, A. P. Semiconductor clusters, nanocrystals, and quantum dots. *Science* **271**, 933 (1996).
11. Burda, C., Chen, X., Narayanan, R. & El-Sayed, M. A. Chemistry and Properties of Nanocrystals of Different Shapes. *Chem. Rev.* **105**, 1025–1102 (2005).
12. Boles, M. A., Engel, M. & Talapin, D. V. Self-Assembly of Colloidal Nanocrystals: From Intricate Structures to Functional Materials. *Chem. Rev.* **116**, 11220–11289 (2016).
13. Mourdikoudis, S. & Liz-Marzán, L. M. Oleylamine in Nanoparticle Synthesis. *Chem. Mater.* **25**, 1465–1476 (2013).
14. Stolle, C. J., Panthani, M. G., Harvey, T. B., Akhavan, V. A. & Korgel, B. A. Comparison of the Photovoltaic Response of Oleylamine and Inorganic Ligand-Capped CuInSe<sub>2</sub> Nanocrystals. *ACS Appl. Mater. Interfaces* **4**, 2757–2761 (2012).
15. Chen, L.-J. Synthesis and optical properties of lead-free cesium germanium halide perovskite quantum rods. *RSC Adv.* **8**, 18396–18399 (2018).
16. Huang, L.-Y. & Lambrecht, W. Phase stability, electronic structure and phonons in CsGeI<sub>3</sub>. in S8.007 (2016).
17. Tang, L.-C., Chang, C.-S., Tang, L.-C. & Huang, J. Y. Electronic structure and optical properties of rhombohedral CsGeI<sub>3</sub> crystal. *J. Phys. Condens. Matter* **12**, 9129 (2000).
18. Wu, X., Song, W., Li, Q., Zhao, X., He, D., & Quan, Z. Synthesis of Lead-free CsGeI<sub>3</sub> Perovskite Colloidal Nanocrystals and Electron Beam-induced Transformations. *Chem. – Asian J.* **13**, 1654–1659 (2018).

19. Chung, I., Song, J.-H., Im, J., Androulakis, J., Malliakas, C. D., Li, H., Freeman, A. J., Kenney, J. T., & Kanatzidis, M. G. CsSnI<sub>3</sub>: Semiconductor or Metal? High Electrical Conductivity and Strong Near-Infrared Photoluminescence from a Single Material. High Hole Mobility and Phase-Transitions. *J. Am. Chem. Soc.* **134**, 8579–8587 (2012).
20. Zhou, Y., Garces, H. F., Senturk, B. S., Ortiz, A. L. & Padture, N. P. Room temperature “one-pot” solution synthesis of nanoscale CsSnI<sub>3</sub> orthorhombic perovskite thin films and particles. *Mater. Lett.* **110**, 127–129 (2013).
21. da Silva, E. L., Skelton, J. M., Parker, S. C. & Walsh, A. Phase stability and transformations in the halide perovskite CsSnI<sub>3</sub>. *Phys. Rev. B* **91**, 144107 (2015).
22. Swarnkar, A., Marshall, A. R., Sanhira, E. M., Chernomordik, B. D., Moore, D. T., Christians, J. A., Chakrabarti, T. & Luther, J. M. Quantum dot-induced phase stabilization of  $\alpha$ -CsPbI<sub>3</sub> perovskite for high-efficiency photovoltaics. *Science* **354**, 92–95 (2016).

## APPENDIX (OR APPENDICES)

### Appendix A

#### A.1 SUPPORTING FIGURES

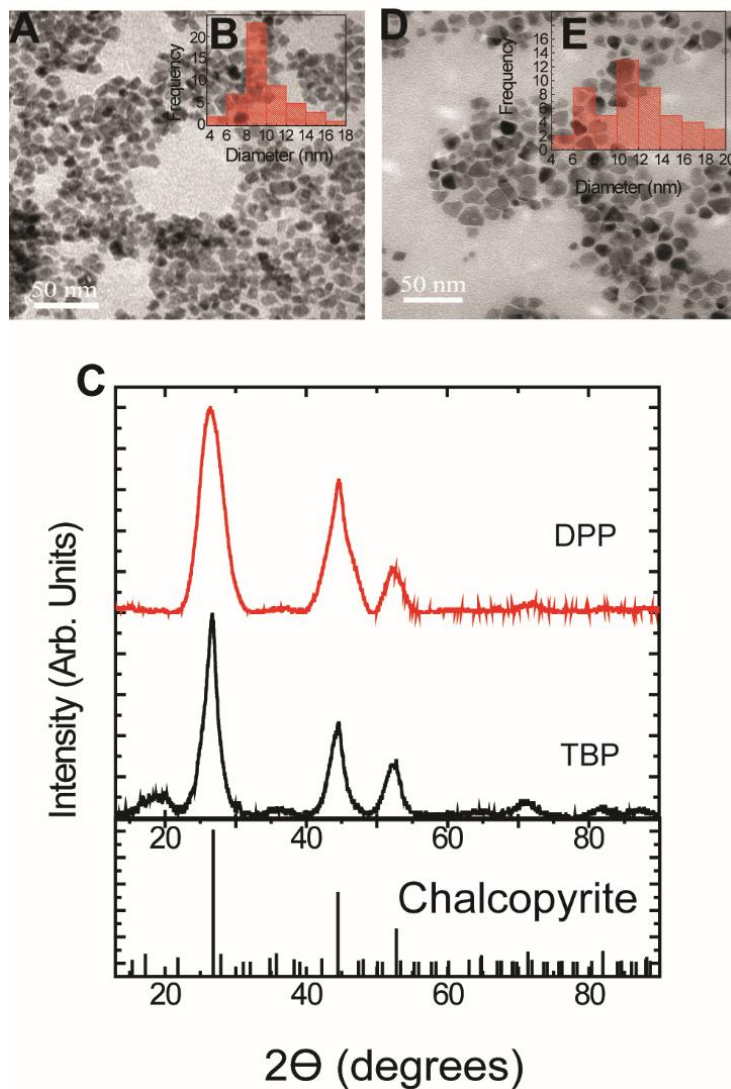


Figure A.1: A&D show TEM Images of the nanocrystal product after washing for the TBP and DPP respectively. B&E illustrates the size distributions between the two syntheses. C shows the XRD patterns for the TBP & DPP systems. Both systems exhibit the chalcopyrite crystal structure (PDF# 01-079-1809).

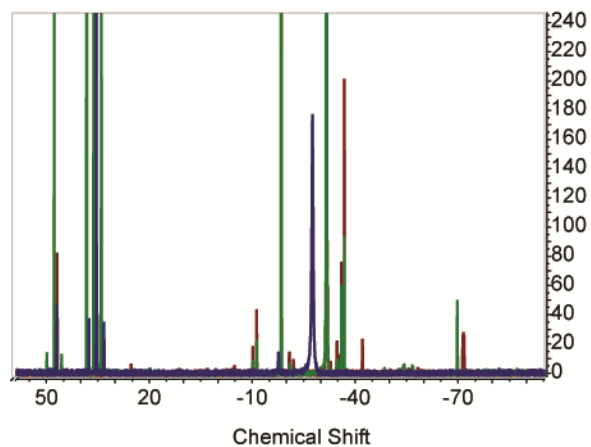


Figure A.2: Shows the secondary phosphines in Method II. The red spectra is TBP as received, the green spectra is TBP=Se, and the blue is 0 min.

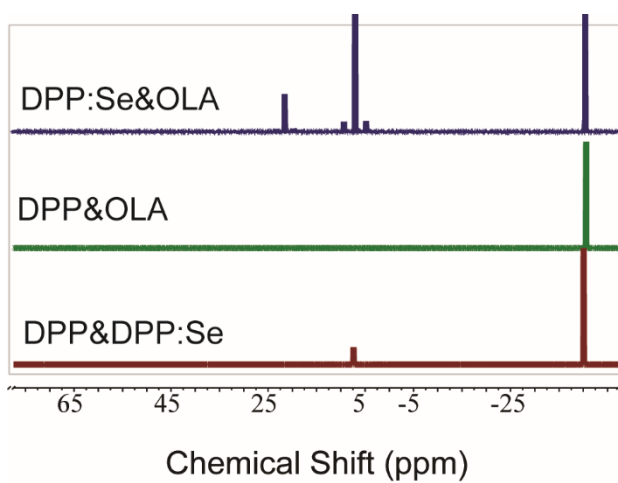


Figure A.3: DPP and OLA <sup>31</sup>P NMR study

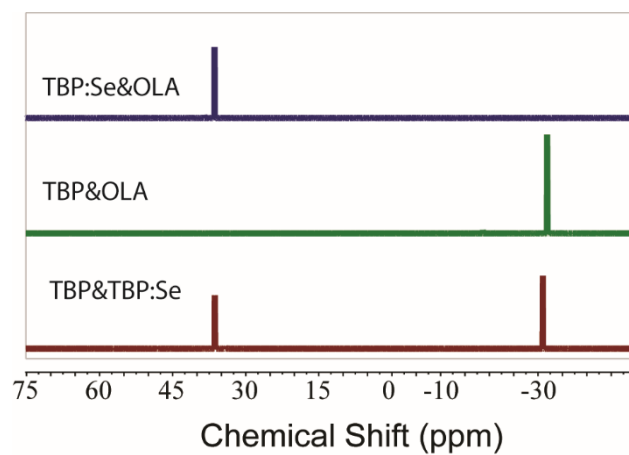


Figure A.4: TBP and OLA  $^{31}\text{P}$  NMR study

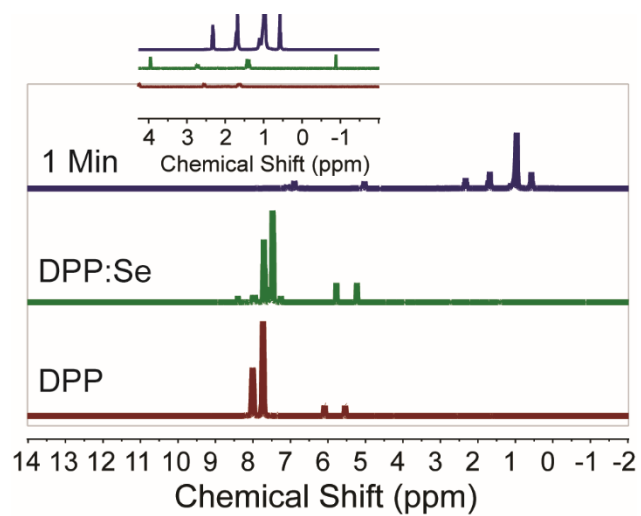


Figure A.5: DPP Selenium precursor study using  $^1\text{H}$  NMR



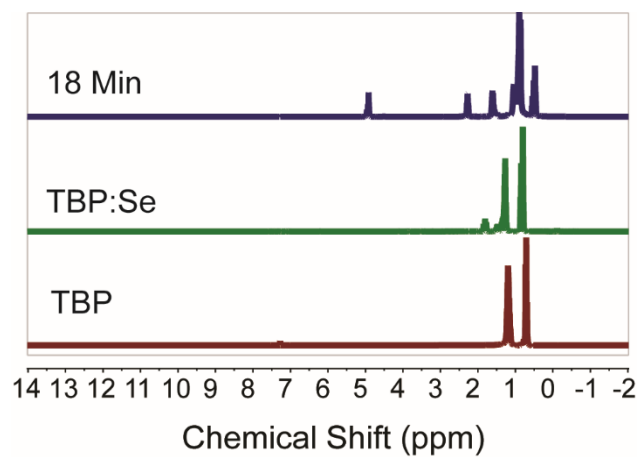


Figure A.6: TBP selenium complex and OLA study via  $^1\text{H}$  NMR

## Appendix B

### B.1: SUPPORTING DATA

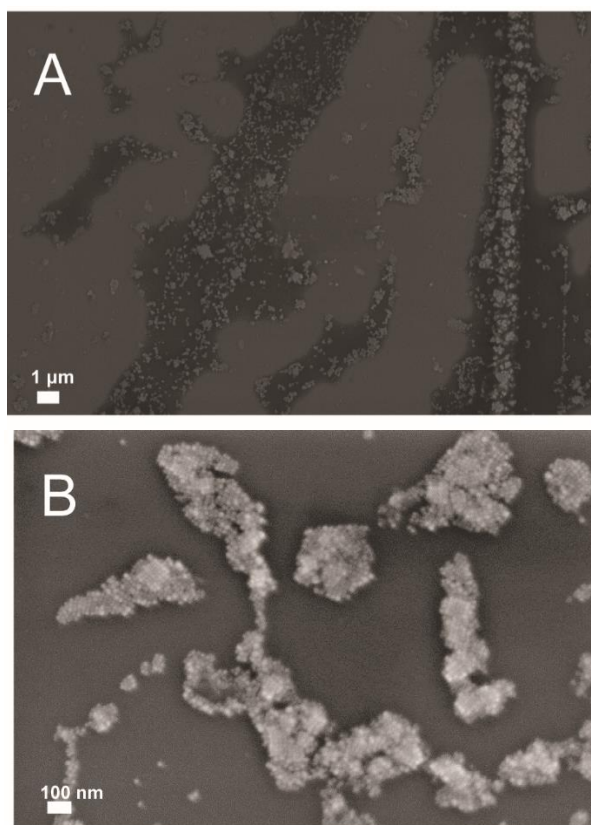


Figure B.1: A and B are SEM images of ordered assemblies of CsPbI<sub>3</sub> nanocrystals, synthesized with diisooctylphosphinic acid (PA) with an average side length of  $17.5 \pm 2.8$  nm, evaporated on a Si wafer.

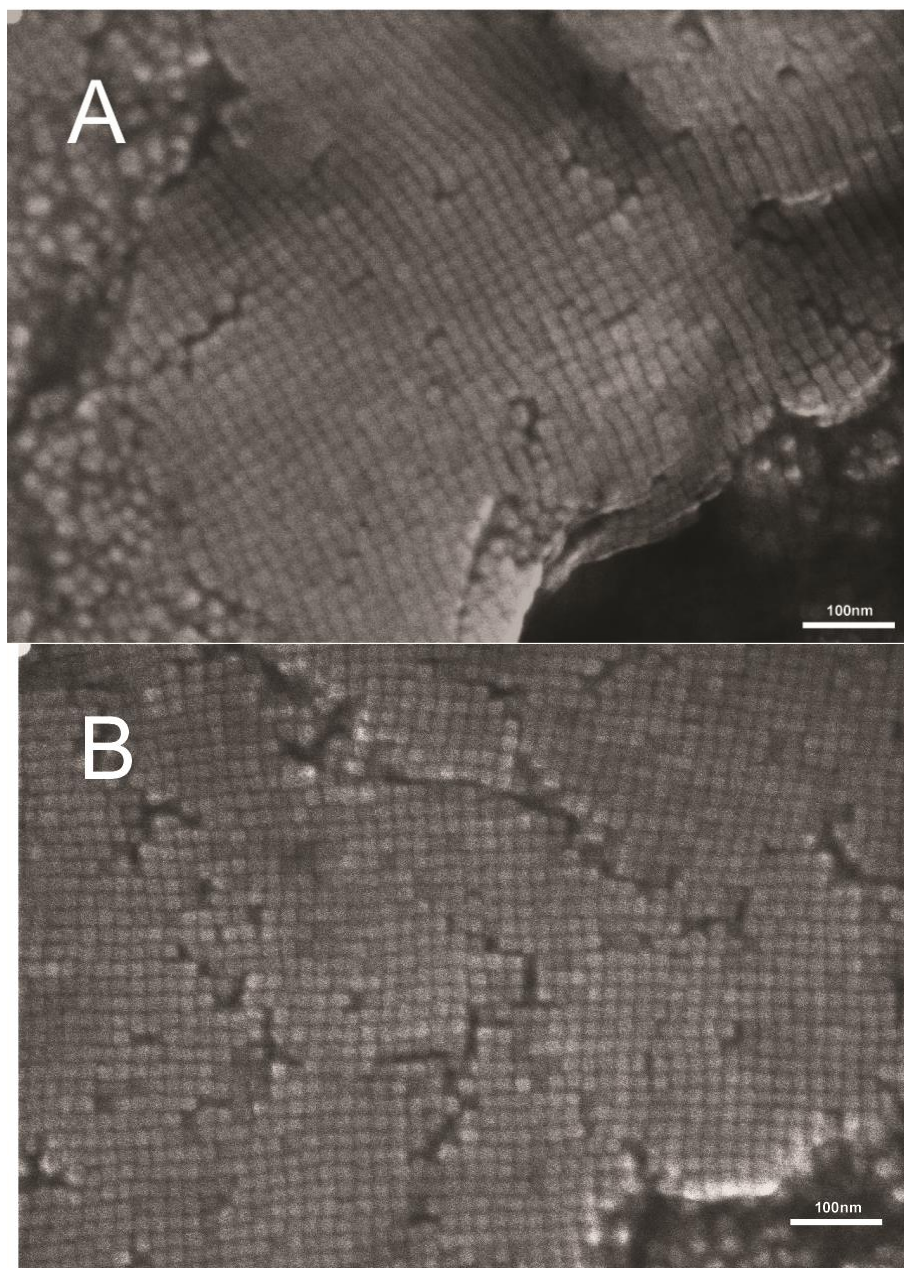


Figure B.2: A and B are SEM images of ordered assemblies of CsPbI<sub>3</sub> nanocrystals, synthesized with diisooctylphosphinic acid (PA) with an average side length of  $17.5 \pm 2.8$  nm, evaporated on a Si wafer. The nanocrystal concentration was increased 10x the original amount. The scale bar is 100 nm in length

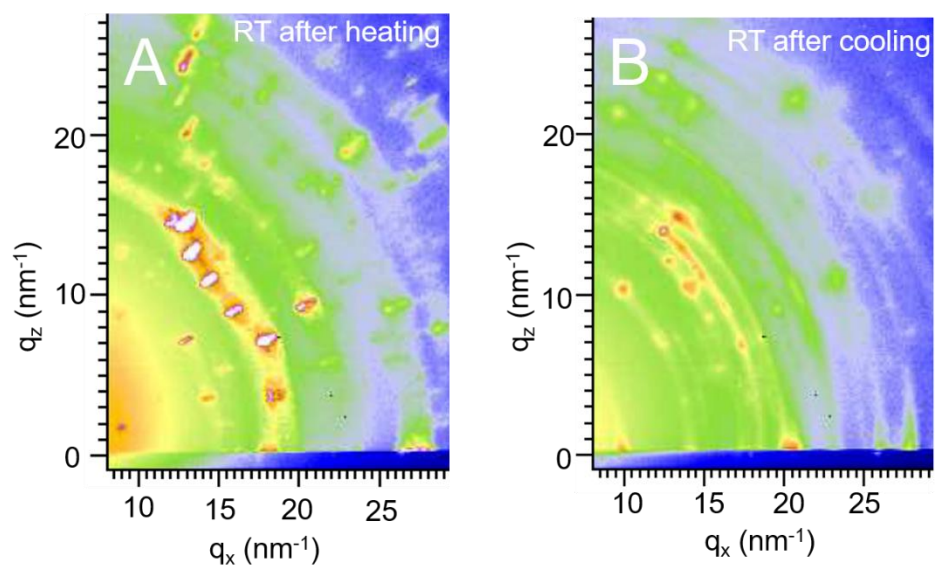


Figure B.3: After heating experiments GIWAXS images of (A) OA nanocrystals and (B) PA nanocrystals dispersed in anhydrous hexane and dried on a Si wafer.

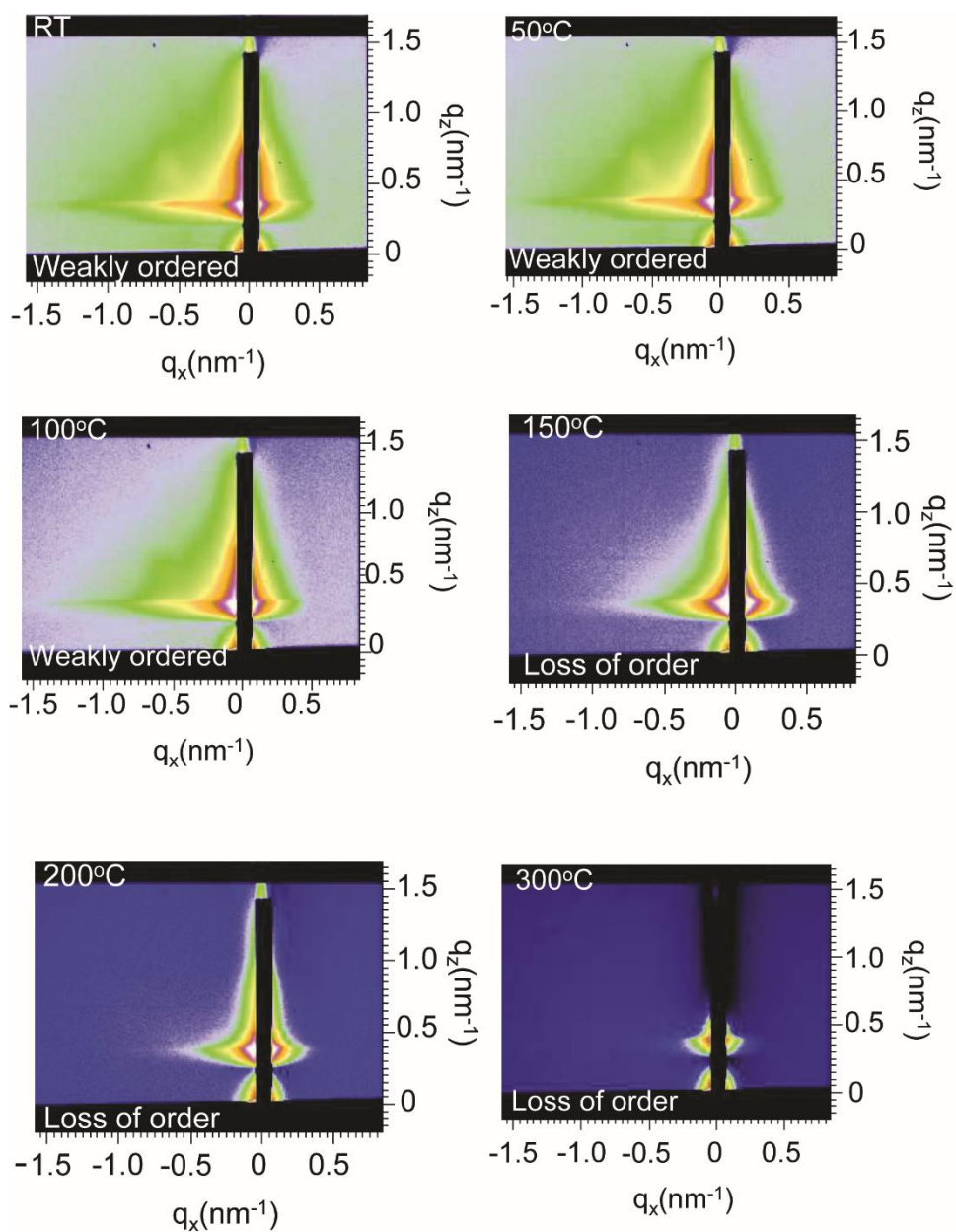


Figure B.4: GISAXS patterns of CsPbI<sub>3</sub> OA nanocrystals with weak ordering heated from room temperature (RT) to 300°C. (A) RT, (B) 50°C (C) 100°C (D) 150°C (E) 200°C and (F) 300°C Nanocrystals were dispersed in anhydrous chloroform before drying onto a Si wafer.



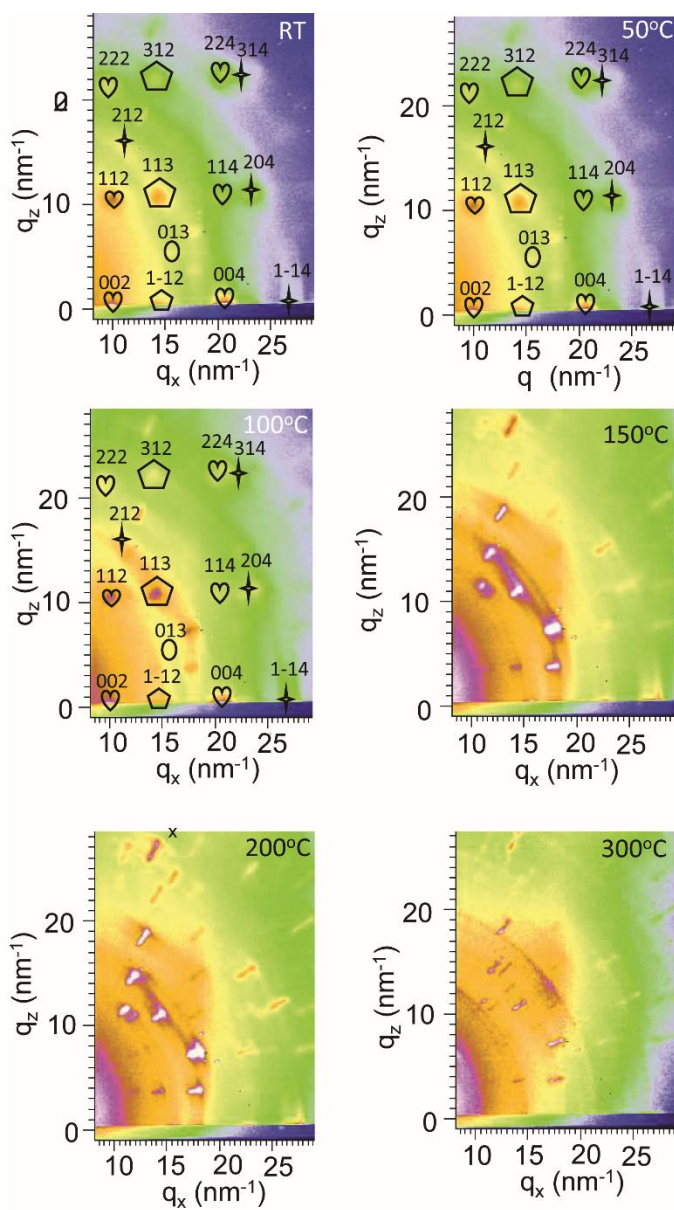


Figure B.5: GIWAXS patterns of CsPbI<sub>3</sub> OA nanocrystals exhibiting  $\gamma$ -orthorhombic crystal structure with the (110)<sub>NC</sub> and the (002)<sub>NC</sub> planes parallel to the Si substrate heated from room temperature (RT) to 300°C. The heart, pentagon, four-point star, circle, and star represents the [-110]<sub>BD</sub>, [-111]<sub>BD</sub>, [-221]<sub>BD</sub>, [-33-1]<sub>BD</sub>, [-22-3]<sub>BD</sub> beam directions for the (110)<sub>NC</sub> orientation and the triangle represents the [-210]<sub>BD</sub> beam direction from the (002)<sub>NC</sub> orientation. (A) RT, (B) 50°C (C) 100°C (D) 150°C (E) 200°C and (F) 300°C Nanocrystals were dispersed in anhydrous chloroform before drying onto a Si wafer.

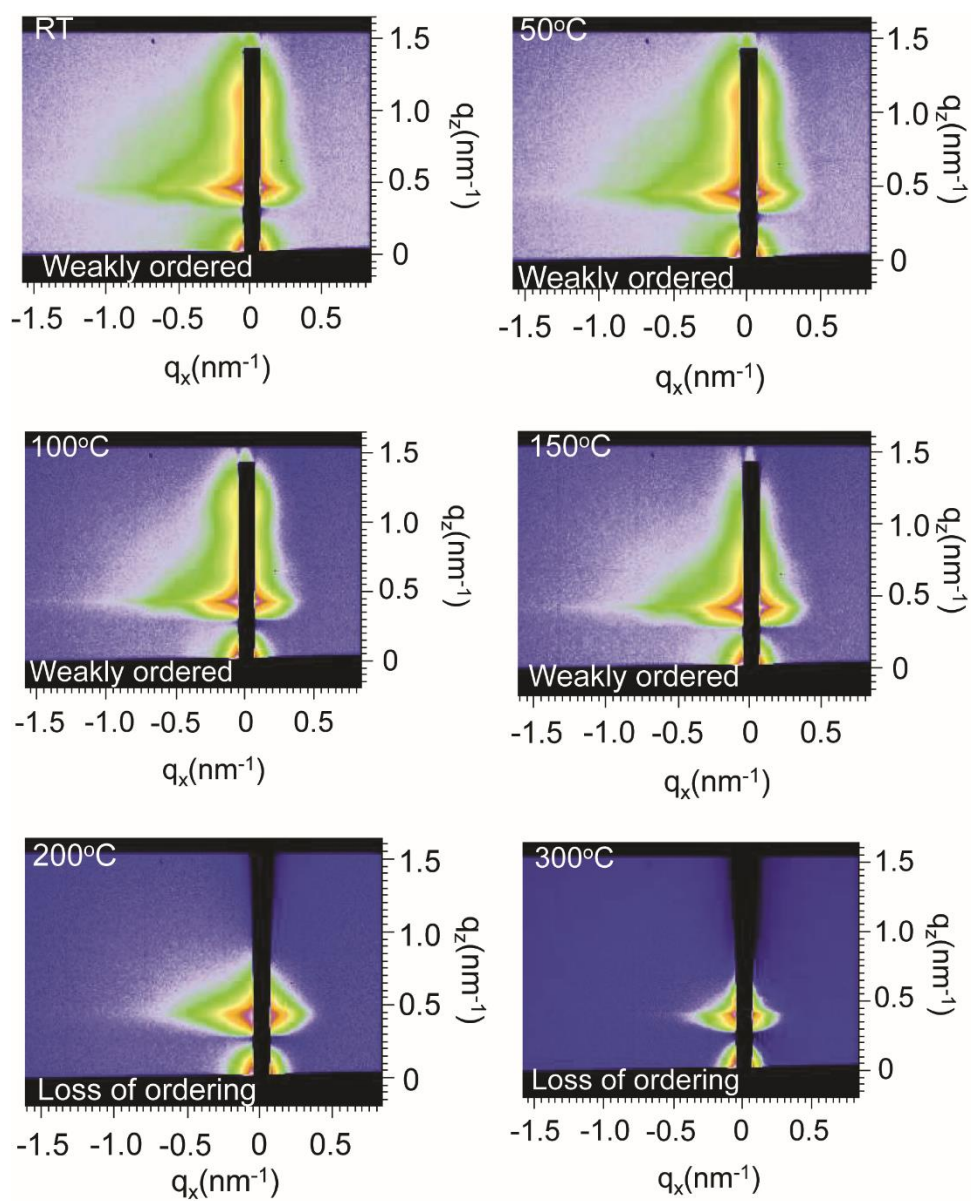


Figure B.6: GISAXS patterns of CsPbI<sub>3</sub> PA nanocrystals with weak ordering heated from room temperature (RT) to 300°C. (A) RT, (B) 50°C (C) 100°C (D) 150°C (E) 200°C and (F) 300°C Nanocrystals were dispersed in anhydrous chloroform before drying onto a Si wafer.

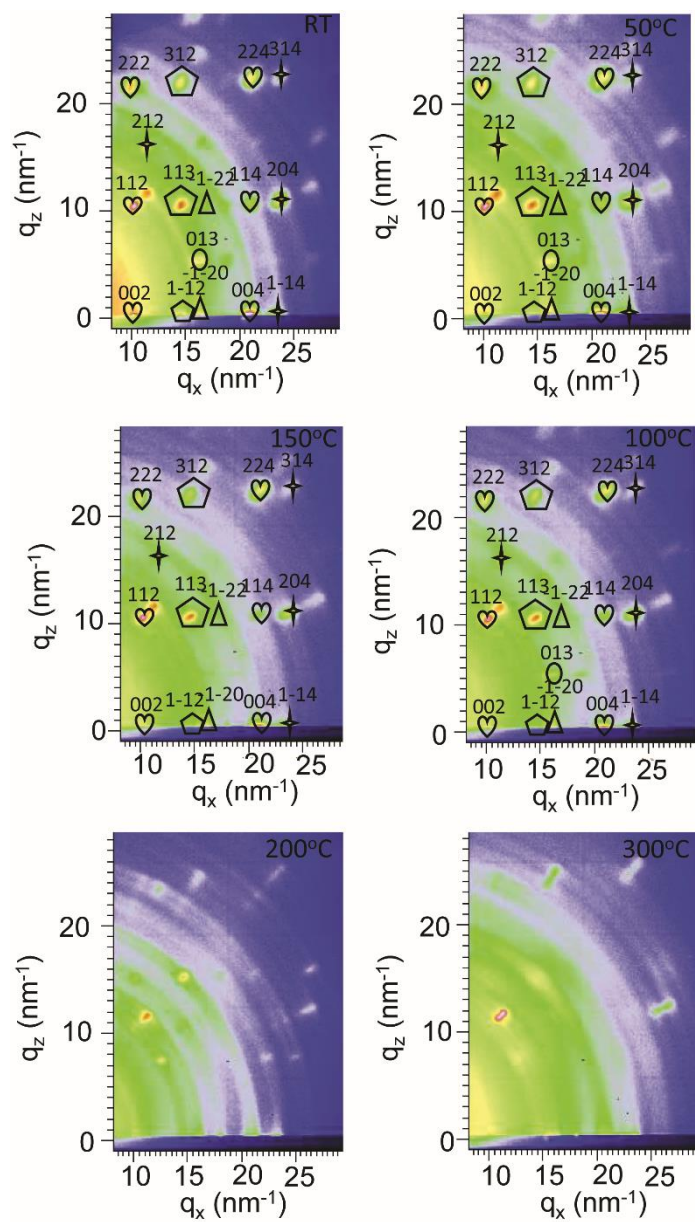


Figure B.7: GIWAXS patterns of CsPbI<sub>3</sub> PA nanocrystals exhibiting  $\gamma$ -orthorhombic crystal structure with the (110)<sub>NC</sub> and the (002)<sub>NC</sub> planes parallel to the Si substrate heated from room temperature (RT) to 300°C. The heart, pentagon, four-point star, circle, and star represents the  $[-110]_{BD}$ ,  $[-111]_{BD}$ ,  $[-221]_{BD}$ ,  $[-33-1]_{BD}$ ,  $[-22-3]_{BD}$  beam directions for the (110)<sub>NC</sub> orientation and the triangle represents the  $[-210]_{BD}$  beam direction from the (002)<sub>NC</sub> orientation. (A) RT, (B) 50°C (C) 100°C (D) 150°C (E) 200°C and (F) 300°C Nanocrystals were dispersed in anhydrous chloroform before drying onto a Si wafer.



## Appendix C

### C.1: SUPPORTING DATA

### Supporting Figures

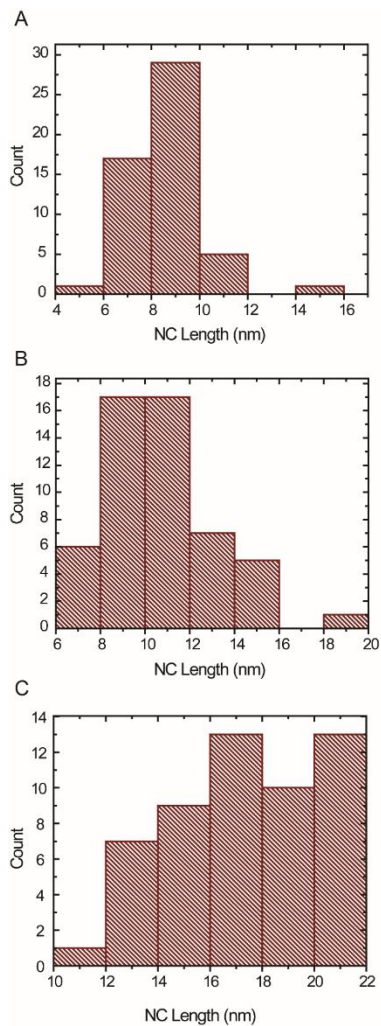


Figure C1: Histograms for CsPbI<sub>3</sub> nanocrystal dispersions for (A) OA, (B) PAQ, (C) PAB respectively.

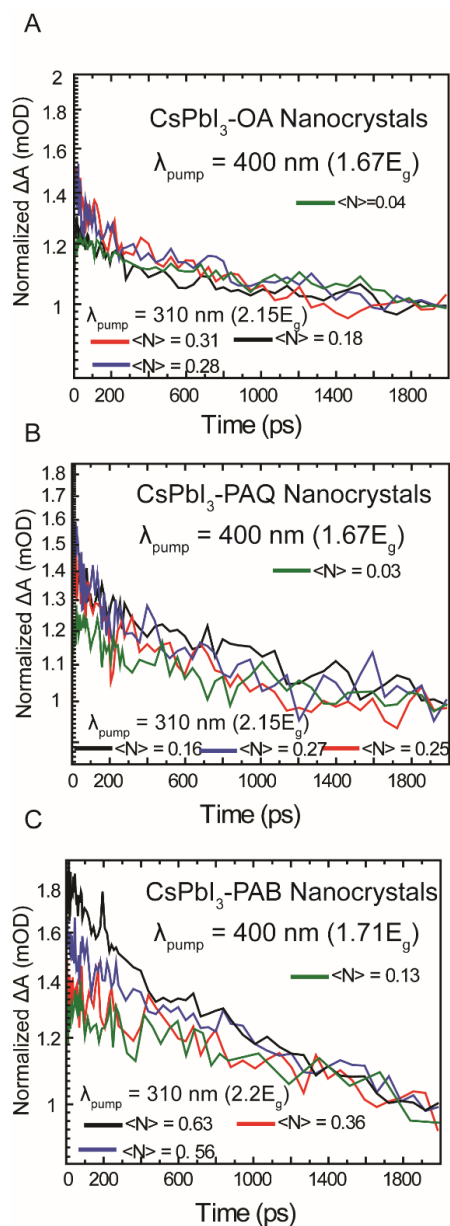


Figure C2: Fluent dependent transient absorption kinetics of (A) OA nanocrystals (B) PAQ nanocrystals (c) PAB nanocrystals measured using a pump wavelength of 310 nm. All kinetics are observed at the absorption bleach peak 656 nm, 658 nm, and 682 nm respectively. All spectra are normalized to 1 at long delay times ( $\sim 2$  ns), where only single excitons are present. The green spectra denotes the single-exciton curve found in figure 6.4.

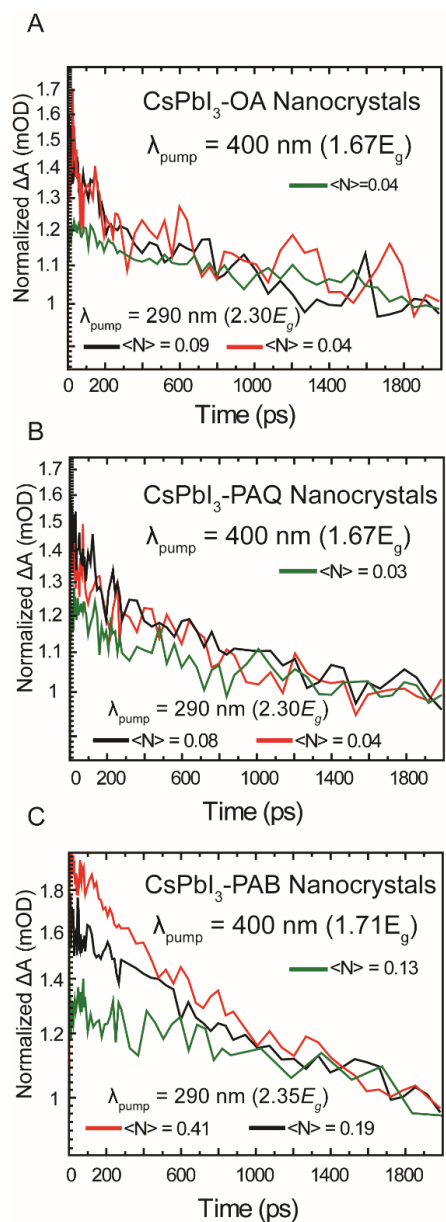


Figure C3: Fluent dependent transient absorption kinetics of (A) OA nanocrystals (B) PAQ nanocrystals (c) PAB nanocrystals measured using a pump wavelength of 290 nm. All kinetics are observed at the absorption bleach peak 656 nm, 658 nm, and 682 nm respectively. All spectra are normalized to 1 at long delay times ( $\sim 2$  ns), where only single excitons are present. The green spectra denotes the single-exciton curve found in figure 6.4.

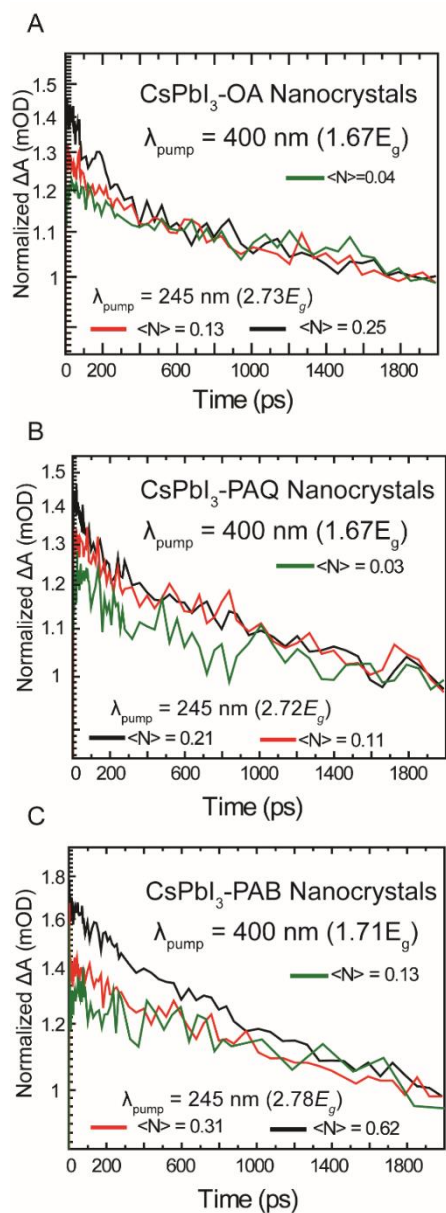


Figure C4: Fluorescence dependent transient absorption kinetics of (A) OA nanocrystals (B) PAQ nanocrystals (c) PAB nanocrystals measured using a pump wavelength of 245 nm. All kinetics are observed at the absorption bleach peak 656 nm, 658 nm, and 682 nm respectively. All spectra are normalized to 1 at long delay times ( $\sim 2$  ns), where only single excitons are present. The green spectra denotes the single-exciton curve found in figure 6.4.

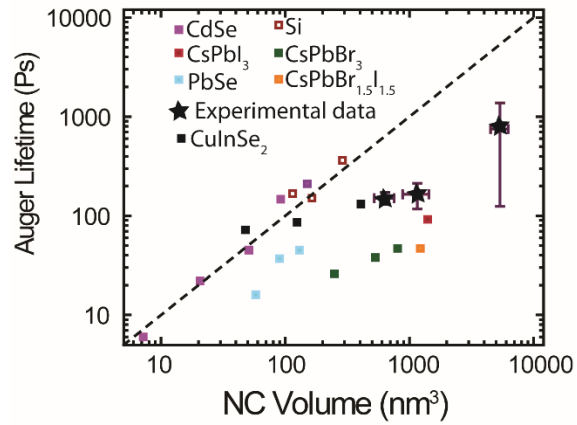


Figure C5: Auger lifetimes plotted with respect to nanocrystal volumes at a pump wavelength of 400 nm. The error bars corresponds to the standard deviations from the nanocrystal sizes and auger lifetimes for each sample.

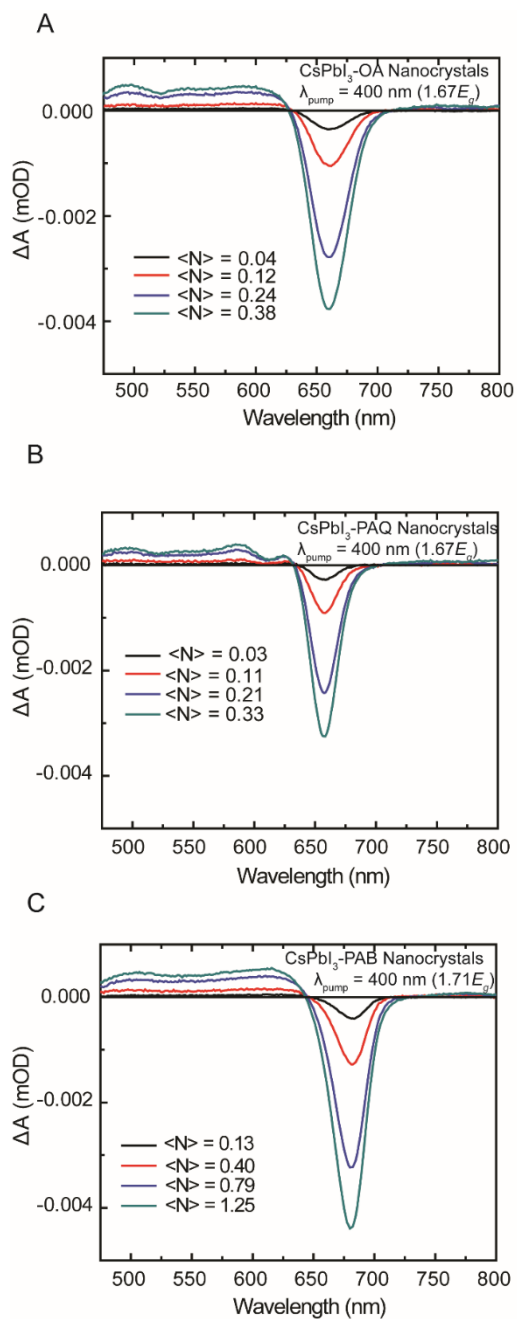


Figure C6: Transient absorption spectra of (A) OA nanocrystals (B) PAQ nanocrystals (C) PAB nanocrystals with varying  $\langle N \rangle$ , measured using a pump wavelength of 400 nm at a delay time of 2.5 ps

$\lambda_{pump}$	400 nm (cm <sup>2</sup> )	310 nm (cm <sup>2</sup> )	290 nm (cm <sup>2</sup> )	245 nm (cm <sup>2</sup> )
<i>OA</i>	1.6 x 10 <sup>-14</sup>	6.4 x 10 <sup>-14</sup>	1.7 x 10 <sup>-14</sup>	4.5 x 10 <sup>-14</sup>
<i>PAQ</i>	1.4 x 10 <sup>-14</sup>	5.6 x 10 <sup>-14</sup>	1.5 x 10 <sup>-14</sup>	3.8 x 10 <sup>-14</sup>
<i>PAB</i>	5.2 x 10 <sup>-14</sup>	1.3 x 10 <sup>-13</sup>	7.4 x 10 <sup>-14</sup>	1.1 x 10 <sup>-13</sup>

Table C1: Absorption cross section,  $\sigma$ , with respect to pump wavelength for each nanocrystal dispersion.  $\sigma$  was determined by fitting the data with a Poisson distribution (Chapter 6, eq 1), where QY is the carrier multiplication quantum yield and  $\sigma_x$  is the absorption cross section at the respective pump wavelength (X = 400 nm, 310 nm, 290 nm, or 245 nm).

$\lambda_{pump}$	310 nm (CM Efficiency %)	290 nm (CM Efficiency %)	245 nm (CM Efficiency %)
<i>OA</i>	6%	10%	0%
<i>PAQ</i>	11%	10%	0%
<i>PAB</i>	18%	22%	4%

Table C2: Carrier multiplication efficiency with respect to pump wavelength for each nanocrystal dispersion. CM efficiency was determined by dividing the higher energy pump QYs with the QY at 400 nm, subtract 1 from that value and multiply by 100 for each dispersion.

## References

- Acciarri, M., Le Donne, A., Marchionna, S., Meschia, M., Parravicini, J., Gasparotto, A., & Binetti, S. CIGS thin films grown by hybrid sputtering-evaporation method: Properties and PV performance. *Sol. Energy* (2018). doi:10.1016/j.solener.2018.02.024
- Ahmadi, M.; Pramana, S. S.; Xi, L.; Boothroyd, C.; Lam, Y. M.; Mhaisalkar, S. Evolution Pathway of CIGSe Nanocrystals for Solar Cell Applications. *J. Phys. Chem. C* 2012, 116, 8202-8209.
- Akhavan, V. A., Goodfellow, B. W., Panthani, M. G., Reid, D. K., Hellebusch, D. J., Adachi, T., & Korgel, B. A. Spray-deposited CuInSe<sub>2</sub> nanocrystal photovoltaics. *Energy Environ. Sci.* 3, 1600 (2010).
- Akhavan, V. A., Goodfellow, B. W., Panthani, M. G., Steinhagen, C., Harvey, T. B., Stolle, C. J., & Korgel, B. A. Colloidal CIGS and CZTS nanocrystals: A precursor route to printed photovoltaics. *J. Solid State Chem.* 189, 2–12 (2012).
- Akhavan, V. A., Harvey, T. B., Stolle, C. J., Ostrowski, D. P., Glaz, M. S., Goodfellow, B. W., Panthani, M. G., Reid, D. K., Vanden Bout, D. A., Korgel, B. A. Influence of Composition on the Performance of Sintered Cu(In,Ga)Se<sub>2</sub> Nanocrystal Thin-Film Photovoltaic Devices. *ChemSusChem* 6, 481–486 (2013).
- Akhavan, V. A., Panthani, M. G., Goodfellow, B. W., Reid, D. K. & Korgel, B. A. Thickness-limited performance of CuInSe<sub>2</sub> nanocrystal photovoltaic devices. *Opt. Express* 18, A411 (2010).
- Akhavan, V. A.; Goodfellow, B. W.; Panthani, M. G.; Steinhagen, C.; Harvey, T. B.; Stolle, C. J.; Korgel, B. A. Colloidal CIGS and CZTS nanocrystals: A precursor route to printed photovoltaics. *J. Solid State Chem.* 2012, 189, 2–12.
- Akhavan, V. A.; Panthani, M. G.; Goodfellow, B. W.; Reid, D. K.; Korgel, B. A. Thickness-limited performance of CuInSe<sub>2</sub> nanocrystal photovoltaic devices. *Opt. Express* 2010, 18, A411-A420.
- Akkerman, Q. A., Rainò, G., Kovalenko, M. V. & Manna, L. Genesis, challenges and opportunities for colloidal lead halide perovskite nanocrystals. *Nat. Mater.* 17, 394–405 (2018).
- Aldakov, D., Lefrançois, A. & Reiss, P. Ternary and quaternary metal chalcogenide nanocrystals: synthesis, properties and applications. *J. Mater. Chem. C* 1, 3756–3776 (2013).



Alivisatos, A. P. Semiconductor clusters, nanocrystals, and quantum dots. *Science* 271, 933 (1996).

Allen, P. M.; Bawendi, M. G. Ternary I–III–VI Quantum Dots Luminescent in the Red to Near-Infrared. *J. Am. Chem. Soc.* 2008, 130, 9240–9241.

Alpert, M. R., Niezgoda, J. S., Chen, A. Z., Foley, B. J., Cuthriell, S., Yoon, L. U., & Choi, J. J. Colloidal Nanocrystals as a Platform for Rapid Screening of Charge Trap Passivating Molecules for Metal Halide Perovskite Thin Films. *Chem. Mater.* 30, 4515–4526 (2018).

Alternative Energy - Wind, Solar, Hydro and other alt energy sources for home power. Available at: <http://www.altenergy.org/>. (Accessed: 11th August 2015)

Ananthakumar, S., Kumar, J. R. & Babu, S. M. Cesium lead halide (CsPbX<sub>3</sub>, X=Cl, Br, I) perovskite quantum dots-synthesis, properties, and applications: a review of their present status. *J. Photonics Energy* 6, 42001 (2016).

Aneesh, J., Swarnkar, A., Ravi, V. K., Sharma, R., Nag, A., & Adarsh, K. V. Ultrafast Exciton Dynamics in Colloidal CsPbBr<sub>3</sub> Perovskite Nanocrystals: Biexciton Effect and Auger Recombination. *J. Phys. Chem. C* 121, 4734–4739 (2017).

Ansari, M. I. H., Qurashi, A. & Nazeeruddin, M. K. Frontiers, opportunities, and challenges in perovskite solar cells: A critical review. *J. Photochem. Photobiol. C Photochem. Rev.* 35, 1–24 (2018).

Asghar, M. I., Zhang, J., Wang, H. & Lund, P. D. Device stability of perovskite solar cells – A review. *Renew. Sustain. Energy Rev.* 77, 131–146 (2017).

Bai, S., Yuan, Z. & Gao, F. Colloidal metal halide perovskite nanocrystals: synthesis, characterization, and applications. *J. Mater. Chem. C* 4, 3898–3904 (2016).

Bang, J. H. & Kamat, P. V. Quantum Dot Sensitized Solar Cells. A Tale of Two Semiconductor Nanocrystals: CdSe and CdTe. *ACS Nano* 3, 1467–1476 (2009).

Beard, M. C. & Ellingson, R. J. Multiple exciton generation in semiconductor nanocrystals: Toward efficient solar energy conversion. *Laser Photonics Rev.* 2, 377–399 (2008).

Beard, M. C., Knutsen, K. P., Yu, P., Luther, J. M., Song, Q., Metzger, W. K., Ellingson, R. J., & Nozik, A. J. Multiple Exciton Generation in Colloidal Silicon Nanocrystals. *Nano Lett.* 7, 2506–2512 (2007).

Beard, M. C., Midgett, A. G., Hanna, M. C., Luther, J. M., Hughes, B. K. & Nozik, A. J. Comparing Multiple Exciton Generation in Quantum Dots To Impact Ionization in Bulk

Semiconductors: Implications for Enhancement of Solar Energy Conversion. *Nano Lett.* 10, 3019–3027 (2010).

Beard, M. C., Midgett, A. G., Law, M., Semonin, O. E., Ellingson, R. J., & Nozik, A. J. Variations in the Quantum Efficiency of Multiple Exciton Generation for a Series of Chemically Treated PbSe Nanocrystal Films. *Nano Lett.* 9, 836–845 (2009).

Becker, M. A., Vaxenburg, R., Nedelcu, G., Sercel, P. C., Shabaev, A., Mehel, M., Michopoulos, J. G., Lambrakos, S. G., Bernstein, N., Lyons, J. L., Stoferle, T., Mahrt, R. F., Kovalenko, M. V., Norris, D. J., Rainò, G. & Efros, A. L. Bright triplet excitons in caesium lead halide perovskites. *Nature* 553, 189 (2018).

Besarati, S. M., Padilla, R. V., Goswami, D. Y. & Stefanakos, E. The potential of harnessing solar radiation in Iran: Generating solar maps and viability study of PV power plants. *Renew. Energy* 53, 193–199 (2013).

Boles, M. A., Engel, M. & Talapin, D. V. Self-Assembly of Colloidal Nanocrystals: From Intricate Structures to Functional Materials. *Chem. Rev.* 116, 11220–11289 (2016).  
Boundless. *World Energy Use. Boundless* (2015).

Brophy, V. & Lewis, J. O. *A Green Vitruvius: Principles and Practice of Sustainable Architectural Design.* (Routledge, 2012).

Bucherl, C. N., Oleson, K. R. & Hillhouse, H. W. Thin film solar cells from sintered nanocrystals. *Curr. Opin. Chem. Eng.* 2, 168–177 (2013).

Burda, C., Chen, X., Narayanan, R. & El-Sayed, M. A. Chemistry and Properties of Nanocrystals of Different Shapes. *Chem. Rev.* 105, 1025–1102 (2005).

Burwig, T., Fränzel, W. & Pistor, P. Crystal Phases and Thermal Stability of Co-evaporated CsPbX<sub>3</sub> (X = I, Br) Thin Films. *J. Phys. Chem. Lett.* 9, 4808–4813 (2018).

Castro, S. L., Bailey, S. G., Raffaele, R. P., Banger, K. K. & Hepp, A. F. Nanocrystalline Chalcopyrite Materials (CuInS<sub>2</sub> and CuInSe<sub>2</sub>) via Low-Temperature Pyrolysis of Molecular Single-Source Precursors. *Chem. Mater.* 15, 3142–3147 (2003).

Chamberlain, G. A. Organic solar cells: A review. *Sol. Cells* 8, 47–83 (1983).

Chapin, D. M., Fuller, C. S. & Pearson, G. L. A New Silicon p-n Junction Photocell for Converting Solar Radiation into Electrical Power. *J. Appl. Phys.* 25, 676–677 (1954).

Chen, C. H.; Brighty, K. E. A new phosphine-sulfides-to-phosphine-oxides exchange reaction. *Tetrahedron Lett.* 1980, 21, 4421–4424.

- Chen, H., Yu, S.-M., Shin, D.-W. & Yoo, J.-B. Solvothermal Synthesis and Characterization of Chalcopyrite CuInSe<sub>2</sub> Nanoparticles. *Nanoscale Res. Lett.* 5, 217–223 (2009).
- Chen, L.-J. Synthesis and optical properties of lead-free cesium germanium halide perovskite quantum rods. *RSC Adv.* 8, 18396–18399 (2018).
- Chen, Z., Li, H., Tang, Y., Huang, X., Ho, D., & Lee, C.-S. Shape-controlled synthesis of organolead halide perovskite nanocrystals and their tunable optical absorption. *Mater. Res. Express* 1, 015034 (2014).
- Chiang, M.-Y., Chang, S.-H., Chen, C.-Y., Yuan, F.-W. & Tuan, H.-Y. Quaternary CuIn(S<sub>1-x</sub>Se<sub>x</sub>)<sub>2</sub> Nanocrystals: Facile Heating-Up Synthesis, Band Gap Tuning, and Gram-Scale Production. *J. Phys. Chem. C* 115, 1592–1599 (2011).
- Chu, T. L. & Chu, S. S. Thin film II–VI photovoltaics. *Solid-State Electron.* 38, 533–549 (1995).
- Chun, Y.-G., Kim, K.-H. & Yoon, K.-H. Synthesis of CuInGaSe<sub>2</sub> nanoparticles by solvothermal route. *Thin Solid Films* 480–481, 46–49 (2005).
- Chung, I., Song, J.-H., Im, J., Androulakis, J., Malliakas, C. D., Li, H., Freeman, A. J., Kenney, J. T., & Kanatzidis, M. G. CsSnI<sub>3</sub>: Semiconductor or Metal? High Electrical Conductivity and Strong Near-Infrared Photoluminescence from a Single Material. High Hole Mobility and Phase-Transitions. *J. Am. Chem. Soc.* 134, 8579–8587 (2012).
- Cossairt, B. M.; Owen, J. S. CdSe Clusters: At the Interface of Small Molecules and Quantum Dots. *Chem. Mater.* 2011, 23, 3114–3119.
- Cotal, H., Fetzer, C., Boisvert, J., Kinsey, G., King, R., Herbert, P., Yoon, H., & Karam, N. III–V multijunction solar cells for concentrating photovoltaics - *Energy & Environmental Science* (RSC Publishing) Vol 2, 174 - 192 (2009).
- da Silva, E. L., Skelton, J. M., Parker, S. C. & Walsh, A. Phase stability and transformations in the halide perovskite CsSnI<sub>3</sub>. *Phys. Rev. B* 91, 144107 (2015).
- de Jong, E. M. L. D., Yamashita, G., Gomez, L., Ashida, M., Fujiwara, Y. & Gregorkiewicz, T. Multiexciton Lifetime in All-Inorganic CsPbBr<sub>3</sub> Perovskite Nanocrystals. *J. Phys. Chem. C* 121, 1941–1947 (2017).
- De Roo, J., Ibáñez, M., Geiregat, P., Nedelcu, G., Walravens, W., Maes, J., Martins, J. C., Van Driessche, I., Kovalenko, M. V., & Hens, Z. Highly Dynamic Ligand Binding and Light Absorption Coefficient of Cesium Lead Bromide Perovskite Nanocrystals. *ACS Nano* 10, 2071–2081 (2016).

- de Vries, B. J. M., van Vuuren, D. P. & Hoogwijk, M. M. Renewable energy sources: Their global potential for the first-half of the 21st century at a global level: An integrated approach. *Energy Policy* 35, 2590–2610 (2007).
- Dilena, E., Xie, Y., Vrescia, R., Prato, M., Maserati, L., Krahne, R., Paoletta, A., Bertoni, G., Povia, M., Moreels, I., & Manna, L.  $\text{CuIn}_x\text{Ga}_{1-x}\text{S}_2$  Nanocrystals with Tunable Composition and Band Gap Synthesized via a Phosphine-Free and Scalable Procedure. *Chem. Mater.* 25, 3180–3187 (2013).
- Dimroth, F. & Kurtz, S. High-Efficiency Multijunction Solar Cells. *MRS Bull.* 32, 230–235 (2007).
- Dutta, A., Dutta, S. K., Das Adhikari, S. & Pradhan, N. Phase-Stable  $\text{CsPbI}_3$  Nanocrystals: The Reaction Temperature Matters. *Angew. Chem. Int. Ed.* 57, 9083–9087 (2018).
- efficiency\_chart.jpg (4190x2456). Available at:  
[http://www.nrel.gov/ncpv/images/efficiency\\_chart.jpg](http://www.nrel.gov/ncpv/images/efficiency_chart.jpg). (Accessed: 12th August 2015)
- Efros, A. L., Kharchenko, V. A. & Rosen, M. Breaking the phonon bottleneck in nanometer quantum dots: Role of Auger-like processes. *Solid State Commun.* 93, 281–284 (1995).
- Eperon, G. E., Jedlicka, E. & Ginger, D. S. Biexciton Auger Recombination Differs in Hybrid and Inorganic Halide Perovskite Quantum Dots. *J. Phys. Chem. Lett.* 9, 104–109 (2018).
- Evans, C. M.; Evans, M. E.; Krauss, T. D. Mysteries of TOPSe Revealed: Insights into Quantum Dot Nucleation. *J. Am. Chem. Soc.* 2010, 132, 10973–10975.
- Extrom, C. L., Darveau, S. A., Martineq-Skinner, A. L., Ingersoll, M., Olejnicek, J., Mirasano, A., Haussler, A. T., Huguenin-Love, J., Kamler, C., Diaz, M., Ianno, N. J., & Soukup, R. J. Reaction pathway insights into the solvothermal preparation of  $\text{CuIn}_{1-x}\text{Ga}_x\text{Se}_2$  nanocrystalline materials. in 33rd IEEE Photovoltaic Specialists Conference, 2008. PVSC '08 1–6 (2008). doi:10.1109/PVSC.2008.4922729
- Freundlich, A., & Alemu, A. Multi quantum well multijunction solar cell for space applications. *physica status solidi (c)* - Wiley Online Library. Vol 2, 8, 2978 - 2981 (2005).
- García-Rodríguez, R.; Hendricks, M. P.; Cossairt, B. M.; Liu, H.; Owen, J. S. Conversion reactions of cadmium chalcogenide nanocrystal precursors. *Chem. Mater.* 2013, 25, 1233–1249.
- García-Rodríguez, R.; Liu, H. A Nuclear Magnetic Resonance Study of the Binding of Trimethylphosphine Selenide to Cadmium Oleate. *J. Phys. Chem. A* 2014, 118, 7314–7319.

- García-Rodríguez, R.; Liu, H. Mechanistic Study of the Synthesis of CdSe Nanocrystals: Release of Selenium. *J. Am. Chem. Soc.* 2012, 134, 1400–1403.
- Gong, J., Liang, J., & Sumathy, K. Review on dye-sensitized solar cells (DSSCs): Fundamental concepts and novel materials. *Renewable and Sustainable Energy Reviews* 16, 5848 - 5860 (2012).
- Graetzel, M., Janssen, R. A. J., Mitzi, D. B. & Sargent, E. H. Materials interface engineering for solution-processed photovoltaics. *Nature* 488, 304–312 (2012).
- Green, M. A. Crystalline and thin-film silicon solar cells: state of the art and future potential. *Sol. Energy* 74, 181–192 (2003).
- Green, M. A. Recent developments in photovoltaics. *Sol. Energy* 76, 3–8 (2004).
- Green, M. A. Thin-film solar cells: review of materials, technologies and commercial status. *J. Mater. Sci. Mater. Electron.* 18, 15–19 (2007).
- Grisaru, H.; Palchik, O.; Gedanken, A.; Palchik, V.; Slifkin, M. A.; Weiss, A. M. Microwave-Assisted Polyol Synthesis of CuInTe<sub>2</sub> and CuInSe<sub>2</sub> Nanoparticles. *Inorg. Chem.* 2003, 42, 7148–7155.
- Gu, S.-I., Shin, H.-S., Yeo, D.-H., Hong, Y.-W. & Nahm, S. Synthesis of the single phase CIGS particle by solvothermal method for solar cell application. *Curr. Appl. Phys.* 11, S99–S102 (2011).
- Günes, S., Abdel-Mottaleb, M. S. A., Hoppe, H. & Ayuk Mbi Egbe, D. Solar Cells: From Sunlight into Electricity. *Int. J. Photoenergy* 2015, e173963 (2015).
- Guo, Q., Ford, G. M., Hillhouse, H. W. & Agrawal, R. Sulfide Nanocrystal Inks for Dense Cu(In<sub>1-x</sub>Ga<sub>x</sub>)(S<sub>1-y</sub>Se<sub>y</sub>)<sub>2</sub> Absorber Films and Their Photovoltaic Performance. *Nano Lett.* 9, 3060–3065 (2009).
- Guo, Q., Kim, S. J., Kar, M., Shafarman, W. N., Birkmire, R. W., Stach, E. A., Agrawal, R., & Hillhouse, H. W. Development of CuInSe<sub>2</sub> Nanocrystal and Nanoring Inks for Low-Cost Solar Cells. *Nano Lett.* 8, 2982–2987 (2008).
- Guo, Q.; Ford, G. M.; Hillhouse, H. W.; Agrawal, R. Sulfide Nanocrystal Inks for Dense Cu(In<sub>1-x</sub>Ga<sub>x</sub>)(S<sub>1-y</sub>Se<sub>y</sub>)<sub>2</sub> Absorber Films and Their Photovoltaic Performance. *Nano Lett.* 2009, 9, 3060–3065.
- Guo, Q.; Kim, S. J.; Kar, M.; Safarman, W. N.; Birkmire, R. W.; Stach, E. A.; Agrawal, R.; Hillhouse, H. W. Development of CuInSe<sub>2</sub> Nanocrystal and Nanoring Inks for Low-Cost Solar Cells. *Nano Lett.* 2008, 8, 2982–2987.

Guo, Y.; Marchuk, K.; Sampat, S.; Abraham, R.; Fang, N.; Malko, A. V.; Vela, J. Unique Challenges Accompany Thick-Shell CdSe/nCdS ( $n > 10$ ) Nanocrystal Synthesis. *J. Phys. Chem. C* 2012, 116, 2791–2800.

Hagfeldt, A., Boschloo, G., Sun, L., Kloo, L. & Pettersson, H. Dye-Sensitized Solar Cells. *Chem. Rev.* 110, 6595–6663 (2010).

Hanrath, T. Colloidal nanocrystal quantum dot assemblies as artificial solids. *J. Vac. Sci. Technol. A* 30, 030802 (2012).

Harvey, T. B., Mori, I., Stolle, C. J., Bogart, T. D., Ostrowski, D., P., Glaz, M. S., Du, J., Pernik, D. R., Akhavan, V. A., Kesrounai, H., Vanden Bout, D. A., & Korgel, B. A. Copper Indium Gallium Selenide (CIGS) Photovoltaic Devices Made Using Multistep Selenization of Nanocrystal Films. *ACS Appl. Mater. Interfaces* 5, 9134–9140 (2013).

Heliński, J.; Skrzywczyński, Z.; Wasiak, J.; Michalski, J. Efficient oxygenation of thiophosphoryl and selenophosphoryl groups using trifluoroacetic anhydride. *Tetrahedron Lett.* 1990, 31, 4081–4084.

Hillhouse, H. W. & Beard, M. C. Solar cells from colloidal nanocrystals: Fundamentals, materials, devices, and economics. *Curr. Opin. Colloid Interface Sci.* 14, 245–259 (2009).

How Do Solar Panels Work? | Photovoltaic Cells. Available at: <https://www.livescience.com/41995-how-do-solar-panels-work.html>. (Accessed: 13th September 2018)

Hu, F., Yin, C., Zhang, H., Sun, C., Yu, W. W., Zhang, C., Wang, X., Zhang, Y. & Xiao, M. Slow Auger Recombination of Charged Excitons in Nonblinking Perovskite Nanocrystals without Spectral Diffusion. *Nano Lett.* 16, 6425–6430 (2016).

Huang, H., Bodnarchuk, M. I., Kershaw, S. V., Kovalenko, M. V. & Rogach, A. L. Lead Halide Perovskite Nanocrystals in the Research Spotlight: Stability and Defect Tolerance. *ACS Energy Lett.* 2, 2071–2083 (2017).

Huang, L.-Y. & Lambrecht, W. Phase stability, electronic structure and phonons in CsGeI<sub>3</sub>. in S8.007 (2016).

Huang, W.-C.; Tseng, C.-H.; Chang, S.-H.; Tuan, H.-Y.; Chiang, C.-C.; Lyu, L.-M.; Huang, M. H. Solvothermal Synthesis of Zincblende and Wurtzite CuInS<sub>2</sub> Nanocrystals and Their Photovoltaic Application. *Langmuir* 2012, 28, 8496–8501.

Iotti, R. C. & Rossi, F. Carrier thermalization versus phonon-assisted relaxation in quantum-cascade lasers: A Monte Carlo approach. *Appl. Phys. Lett.* 78, 2902–2904 (2001).

Jackson, P., Hariskos, D., Lotter, E., Paetel, S., Wuerz, R., Menner, R., Wischmann, W., & Powalla, M. New world record efficiency for Cu(In,Ga)Se<sub>2</sub> thin-film solar cells beyond 20%. *Prog. Photovolt. Res. Appl.* 19, 894–897 (2011).

Jellicoe, T. C., Richter, J. M., Glass, H. F. J., Tabachnyk, M., Brady, R., Dutton, S. E., Rao, A., Friendk R. H., Credgington, D., Greenham, N. C., & Böhm, M. L. Synthesis and Optical Properties of Lead-Free Cesium Tin Halide Perovskite Nanocrystals. *J. Am. Chem. Soc.* 138, 2941–2944 (2016).

Jiang, C., Lee, J.-S. & Talapin, D. V. Soluble Precursors for CuInSe<sub>2</sub>, CuIn<sub>1-x</sub>GaxSe<sub>2</sub>, and Cu<sub>2</sub>ZnSn(S,Se)<sub>4</sub> Based on Colloidal Nanocrystals and Molecular Metal Chalcogenide Surface Ligands. *J. Am. Chem. Soc.* 134, 5010–5013 (2012).

Joo, J.; Pietryga, J. M.; McGuire, J. A.; Jeon, S.-H.; Williams, D. J.; Wang, H.-L.; Klimov, V. I. A Reduction Pathway in the Synthesis of PbSe Nanocrystal Quantum Dots. *J. Am. Chem. Soc.* 2009, 131, 10620–10628.

Kabir, E., Kumar, P., Kumar, S., Adelodun, A. A. & Kim, K.-H. Solar energy: Potential and future prospects. *Renew. Sustain. Energy Rev.* 82, 894–900 (2018).

Kamat, P. V. Quantum Dot Solar Cells. Semiconductor Nanocrystals as Light Harvesters. *J. Phys. Chem. C* 112, 18737–18753 (2008).

Kar, M., Agrawal, R. & Hillhouse, H. W. Formation pathway of CuInSe<sub>2</sub> nanocrystals for solar cells. *J. Am. Chem. Soc.* 133, 17239–17247 (2011).

Kim, B.-S., Hong, J., Hou, B., Cho, Y., Sohn, J. In., Cha, SN. & Kim, J. M. Inorganic-ligand exchanging time effect in PbS quantum dot solar cell. *Appl. Phys. Lett.* 109, 063901 (2016).

King, R. R., Law, D. C., Edmondson, K. M., Fetzer, C. M., Kinsey, G. S., Yoon, H., Sherif, A., & Karam, N. H. 40% efficient metamorphic GaInP/GaInAs/Ge multijunction solar cells: Applied Physics Letters: Vol 90, No 18.183516 (2007).

Köberle, A. C., Gernaat, D. E. H. J. & van Vuuren, D. P. Assessing current and future techno-economic potential of concentrated solar power and photovoltaic electricity generation. *Energy* doi:10.1016/j.energy.2015.05.145

Kovalenko, M. V. & Bodnarchuk, M. I. Lead Halide Perovskite Nanocrystals: From Discovery to Self-assembly and Applications. *Chimia* 71, 461–470 (2017).

Kovalenko, M. V., Protesescu, L. & Bodnarchuk, M. I. Properties and potential optoelectronic applications of lead halide perovskite nanocrystals. *Science* 358, 745–750 (2017).

- Krieg, F., Ochsenein, S. T., Yakunin, S., Brinck, S. t., Aellen, P., Süess, A., Clerc, B., Guggisberg, D., Nazarenko, O., Shynkarenko, Y., Kumar, S., Shih, C.-J., Infante, I., & Kovalenko, M. V. Colloidal CsPbX<sub>3</sub> (X = Cl, Br, I) Nanocrystals 2.0: Zwitterionic Capping Ligands for Improved Durability and Stability. *ACS Energy Lett.* 3, 641–646 (2018).
- Kwon, S. G. & Hyeon, T. Formation Mechanisms of Uniform Nanocrystals via Hot-Injection and Heat-Up Methods. *Small* 7, 2685–2702 (2011).
- Lang, L., Yang, J.-H., Liu, H.-R., Xiang, H. J. & Gong, X. G. First-principles study on the electronic and optical properties of cubic ABX<sub>3</sub> halide perovskites. *Phys. Lett. A* 378, 290–293 (2014).
- Lee, H., Jeong, D.-s., Mun, T., Pejjai, B., Minnam Reddy, V. R., Anderson, T. J., & Park, C. Formation and characterization of CuInSe<sub>2</sub> thin films from binary CuSe and In<sub>2</sub>Se<sub>3</sub> nanocrystal-ink spray. *Korean J. Chem. Eng.* 33, 2486–2491 (2016).
- Lee, Y., Park, C., Balaji, N., Lee, Y.-J. & Dao, V. A. High-efficiency Silicon Solar Cells: A Review. *Isr. J. Chem.* 55, 1050–1063 (2015).
- Lewis, N. S. & Nocera, D. G. Powering the planet: Chemical challenges in solar energy utilization. *Proc. Natl. Acad. Sci.* 103, 15729–15735 (2006).
- Li, B., Xie, Y., Huang, J. & Qian, Y. Synthesis by a Solvothermal Route and Characterization of CuInSe<sub>2</sub> Nanowhiskers and Nanoparticles. *Adv. Mater.* 11, 1456–1459 (1999).
- Li, L. S.; Pradhan, N.; Wang, Y.; Peng, X. High Quality ZnSe and ZnS Nanocrystals Formed by Activating Zinc Carboxylate Precursors. *Nano Lett.* 2004, 4, 2261–2264.
- Li, X., Cao, F., Yu, D., Chen, J., Sun, Z., Shen, Y., Zhu, Y., Wang, L., Wei, Y., Wu, Y., & Zeng, H. All Inorganic Halide Perovskites Nanosystem: Synthesis, Structural Features, Optical Properties and Optoelectronic Applications. *Small* 13, n/a-n/a (2017).
- Liljeroth, P., Overgaag, K., Urbieto, A., Grandidier, B., Hickey, S. G., & Vanmaekelbergh, D. Variable Orbital Coupling in a Two-Dimensional Quantum-Dot Solid Probed on a Local Scale. *Phys. Rev. Lett.* 97, 096803 (2006).
- Lindahl, J., Zimmermann, U., Szaniawski, P., Törndahl, T., Hultqvist, A., Salomé, P., Platzer-Björkman, C., & Edoff, M. Inline Cu(In,Ga)Se<sub>2</sub> Co-evaporation for High-Efficiency Solar Cells and Modules. *IEEE J. Photovolt.* 3, 1100–1105 (2013).
- Liu, H., Wu, Z., Gao, H., Shao, J., Zou, H., Yao, D., Liu, Y., Zhang, H., & Yang, B. One-Step Preparation of Cesium Lead Halide CsPbX<sub>3</sub> (X = Cl, Br, and I) Perovskite Nanocrystals by Microwave Irradiation. *ACS Appl. Mater. Interfaces* 9, 42919–42927 (2017).



- Liu, H.; Owen, J. S.; Alivisatos, A. P. Mechanistic Study of Precursor Evolution in Colloidal Group II–VI Semiconductor Nanocrystal Synthesis. *J. Am. Chem. Soc.* 2007, 129, 305–312.
- Liu, Q., Wang, Y., Sui, N., Wang, Y., Chi, Z., Wang, Q., Chen, Y., Ji, W. & Zhang, H. Exciton Relaxation Dynamics in Photo-Excited CsPbI<sub>3</sub> Perovskite Nanocrystals. *Sci. Rep.* 6, 29442 (2016).
- Liu, Y.; Yao, D.; Shen, L.; Zhang, H.; Zhang, X.; Yang, B. Alkylthiol-Enabled Se Powder Dissolution in Oleylamine at Room Temperature for the Phosphine-Free Synthesis of Copper-Based Quaternary Selenide Nanocrystals. *J. Am. Chem. Soc.* 2012, 134, 7207–7210.
- Long, Z., Ren, H., Sun, J., Ouyang, J. & Na, N. High-throughput and tunable synthesis of colloidal CsPbX<sub>3</sub> perovskite nanocrystals in a heterogeneous system by microwave irradiation. *Chem. Commun.* 53, 9914–9917 (2017).
- Lu, W., Fang, J., Stokes, K. L. & Lin, J. Shape Evolution and Self Assembly of Monodisperse PbTe Nanocrystals. *J. Am. Chem. Soc.* 126, 11798–11799 (2004).
- Luo, J.-W., Franceschetti, A. & Zunger, A. Carrier Multiplication in Semiconductor Nanocrystals: Theoretical Screening of Candidate Materials Based on Band-Structure Effects. *Nano Lett.* 8, 3174–3181 (2008).
- Luo, P., Xia, W., Zhou, S., Sun, L., Cheng, J., Xu, C., & Lu, Y. Solvent Engineering for Ambient-Air-Processed, Phase-Stable CsPbI<sub>3</sub> in Perovskite Solar Cells. *J. Phys. Chem. Lett.* 7, 3603–3608 (2016).
- Luther, J. M., Law, M., Beard, M. C., Song, Q., Reese, M. O., Ellingson, R. J., & Nozik, A. J. Schottky Solar Cells Based on Colloidal Nanocrystal Films. *Nano Lett.* 8, 3488–3492 (2008).
- Makarov, N. S., Guo, S., Isaienko, O., Liu, W., Robel, I. & Klimov, V. I. Spectral and Dynamical Properties of Single Excitons, Biexcitons, and Trions in Cesium–Lead-Halide Perovskite Quantum Dots. *Nano Lett.* 16, 2349–2362 (2016).
- Mallory, S. A., Valeriani, C. & Cacciuto, A. An Active Approach to Colloidal Self-Assembly. *Annu. Rev. Phys. Chem.* 69, 59–79 (2018).
- Marronnier, A., Roma, G., Boyer-Richard, S., Pedesseau, L., Jancu, J.-M., Bonnassieux, Y., Katan, C., Stoumpos, C. C., Kanatzidis, M. G., & Even, J. Anharmonicity and Disorder in the Black Phases of Cesium Lead Iodide Used for Stable Inorganic Perovskite Solar Cells. *ACS Nano* 12, 3477–3486 (2018).
- Mashreki, T. I.A., & Afzaal, M. Nanocrystalline Materials for Hybrid Photovoltaic Devices. *Advanced Materials Research*, Vol. 1116, 45-50 (2015).

- Mattos, L. S., Scully, S. R., Syfu, M., Olson, E., Yang, L., Ling, C., Kayes, B. M., & He, G. New module efficiency record: 23.5% under 1-sun illumination using thin-film single-junction GaAs solar cells. in 2012 38th IEEE Photovoltaic Specialists Conference 003187–003190 (2012). doi:10.1109/PVSC.2012.6318255
- Miles, R. W., Zoppi, G. & Forbes, I. Inorganic photovoltaic cells. *Mater. Today* 10, 20–27 (2007).
- Mitzi, D. B.; Yuan, M.; Liu, W.; Kellock, A. J.; Chey, S. J.; Deline, V.; Schrott, A. G. A High-Efficiency Solution-Deposited Thin-Film Photovoltaic Device. *Adv. Mater.* 2008, 20, 3657–3662.
- Mourdikoudis, S. & Liz-Marzán, L. M. Oleylamine in Nanoparticle Synthesis. *Chem. Mater.* 25, 1465–1476 (2013).
- Nagaoka, Y. Hills-Kimball, K., Tan, R., Li, R., Wang, Z., & Chen, O. Nanocube Superlattices of Cesium Lead Bromide Perovskites and Pressure-Induced Phase Transformations at Atomic and Mesoscale Levels. *Adv. Mater.* 29, n/a-n/a (2017).
- Nair, G. & Bawendi, M. G. Carrier multiplication yields of CdSe and CdTe nanocrystals by transient photoluminescence spectroscopy. *Phys. Rev. B* 76, 81304 (2007).
- Nakamura, H.; Kato, W.; Uehara, M.; Nose, K.; Omata, T.; Otsuka-Yao-Matsuo, S.; Miyazaki, M.; Maeda, H. Tunable Photoluminescence Wavelength of Chalcopyrite CuInS<sub>2</sub>-Based Semiconductor Nanocrystals Synthesized in a Colloidal System. *Chem. Mater.* 2006, 18, 3330–3335.
- Nelson, J. *The Physics of Solar Cells*. (World Scientific Publishing Company, 2003).
- Nižetić, S., Giama, E. & Papadopoulos, A. M. Comprehensive analysis and general economic-environmental evaluation of cooling techniques for photovoltaic panels, Part II: Active cooling techniques. *Energy Convers. Manag.* 155, 301–323 (2018).
- Norako, M. E.; Brutchey, R. L. Synthesis of Metastable Wurtzite CuInSe<sub>2</sub> Nanocrystals. *Chem. Mater.* 2010, 22, 1613–1615.
- Nugent, D. & Sovacool, B. K. Assessing the lifecycle greenhouse gas emissions from solar PV and wind energy: A critical meta-survey. *Energy Policy* 65, 229–244 (2014).
- O'Regan, B. & Grätzel, M. A low-cost, high-efficiency solar cell based on dye-sensitized colloidal TiO<sub>2</sub> films. *Nature* 353, 737–740 (1991).
- Ono, L. K., Juarez-Perez, E. J. & Qi, Y. Progress on Perovskite Materials and Solar Cells with Mixed Cations and Halide Anions. *ACS Appl. Mater. Interfaces* 9, 30197–30246 (2017).

- Owen, J. S., Park, J., Trudeau, P.-E. & Alivisatos, A. P. Reaction Chemistry and Ligand Exchange at Cadmium–Selenide Nanocrystal Surfaces. *J. Am. Chem. Soc.* 130, 12279–12281 (2008).
- Owen, J. S.; Chan, E. M.; Liu, H.; Alivisatos, A. P. Precursor Conversion Kinetics and the Nucleation of Cadmium Selenide Nanocrystals. *J. Am. Chem. Soc.* 2010, 132, 18206–18213.
- Padilha, L. A., Stewart, J. T., Sandberg, R. L., Bae, W. K., Koh, W.-K., Pietryga, J. M. & Klimov, V. I. Carrier Multiplication in Semiconductor Nanocrystals: Influence of Size, Shape, and Composition. *Acc. Chem. Res.* 46, 1261–1269 (2013).
- Palm, J. Household installation of solar panels – Motives and barriers in a 10-year perspective. *Energy Policy* 113, 1–8 (2018).
- Pan, D.; Wang, X.; Zhou, Z. H.; Chen, W.; Xu, X.; Lu, Y. Synthesis of Cu–In–S Ternary Nanocrystals with Tunable Structure and Composition. *J. Am. Chem. Soc.* 2008, 130, 5620–5621.
- Pan, Q., Hu, H., Zou, Y., Chen, M., Wu, L., Yang, D., Yuan, X., Fan, J., Sun, B., & Zhang, Q. Microwave-assisted synthesis of high-quality “all-inorganic” CsPbX<sub>3</sub> (X = Cl, Br, I) perovskite nanocrystals and their application in light emitting diodes. *J. Mater. Chem. C* 5, 10947–10954 (2017).
- Panthani, M. G., Akhavan, V., Goodfellow, B., Schmidtke, J. P., Dunn, L., Dodabalapur, A., Barbara, P. F., & Korgel, B. A. Synthesis of CuInS<sub>2</sub>, CuInSe<sub>2</sub>, and Cu(In<sub>x</sub>Ga<sub>1-x</sub>)Se<sub>2</sub> (CIGS) Nanocrystal “Inks” for Printable Photovoltaics. *J. Am. Chem. Soc.* 130, 16770–16777 (2008).
- Panthani, M. G.; Stolle, C. J.; Reid, D. K.; Rhee, D. J.; Harvey, T. B.; Akhavan, V. A.; Yu, Y.; Korgel, B. A. CuInSe<sub>2</sub> Quantum Dot Solar Cells with High Open-Circuit Voltage. *J. Phys. Chem. Lett.* 2013, 4, 2030–2034.
- Parida, B., Iniyan, S. & Goic, R. A review of solar photovoltaic technologies. *Renew. Sustain. Energy Rev.* 15, 1625–1636 (2011).
- Peng, J., Lu, L. & Yang, H. Review on life cycle assessment of energy payback and greenhouse gas emission of solar photovoltaic systems. *Renew. Sustain. Energy Rev.* 19, 255–274 (2013).
- Peng, S.; Liang, Y.; Cheng, F.; Liang, J. Size-controlled chalcopyrite CuInS<sub>2</sub> nanocrystals: One-pot synthesis and optical characterization. *Sci. China Chem.* 2011, 55, 1236–1241.
- Pernik, D. R., Gutierrez, M., Thomas, C., Voggu, V. R., Yu, Y., Embden, J. v., Topping, A. J., Jasieniak, J. J., Vanden Bout, D. A., Lewandowski, R., & Korgel, B. A. Plastic Microgroove Solar Cells Using CuInSe<sub>2</sub> Nanocrystals. *ACS Energy Lett.* 1, 1021–1027 (2016).

Peterson, I. R. & Girling, I. R. Langmuir-Blodgett films. *Sci. Prog.* 1933- 69, 533–550 (1985).

Piliigo, C., Protesescu, L., Bisri, S. Z., Kovalenko, M. V. & Loi, M. A. 5.2% efficient PbS nanocrystal Schottky solar cells. *Energy Environ. Sci.* 6, 3054–3059 (2013).

Pivrikas, A., Sariciftci, N. S., Juška, G. & Österbacka, R. A review of charge transport and recombination in polymer/fullerene organic solar cells. *Prog. Photovolt. Res. Appl.* 15, 677–696 (2007).

Principles of Photovoltaics, Photovoltaic Materials | Solar Energy. Available at: [http://www.greenrhinoenergy.com/solar/technologies/pv\\_cells.php](http://www.greenrhinoenergy.com/solar/technologies/pv_cells.php). (Accessed: 11th August 2015)

Protesescu, L., Yakunin, S., Bodnarchuk, M. I., Krieg, F., Caputo, R., Hendon, C. H., Yang, R. X., Walsh, A., & Kovalenko, M. V. Nanocrystals of cesium lead halide perovskites (CsPbX<sub>3</sub>, X=Cl, Br, and I): novel optoelectronic materials showing bright emission with wide color gamut. *Nano Lett.* 15, 3692–3696 (2015).

Protesescu, L., Yakunin, S., Kumar, S., Bär, J., Bertolotti, F., Masciocchi, N., Guagliardi, A., Grotevent, M., Shorublalko, I., Bodnarchuk, M. I., Shih, C.-J., & Kovalenko, M. V. Dismantling the “Red Wall” of Colloidal Perovskites: Highly Luminescent Formamidinium and Formamidinium–Cesium Lead Iodide Nanocrystals. *ACS Nano* 11, 3119–3134 (2017).

Rappaport, P. The photovoltaic effect and its utilization. *Sol. Energy* 3, 8–18 (1959).

Razgoniaeva, N., Yang, M., Garrett, P., Kholmicheva, N., Moroz, P., Eckard, H., Romero, L. R., Porotnikov, D., Khon, D., & Zamkov, M. Just Add Ligands: Self-Sustained Size Focusing of Colloidal Semiconductor Nanocrystals. *Chem. Mater.* 30, 1391–1398 (2018).

Reifsnnyder, D. C.; Ye, X.; Gordon, T. R.; Song, C.; Murray, C. B. Three-Dimensional Self-Assembly of Chalcopyrite Copper Indium Diselenide Nanocrystals into Oriented Films. *ACS Nano* 2013, 7, 4307–4315.

Reinhard, P., Chirilă, A., Blösch, P., Pianezzi, F., Nishiwaki, S., Buecheler, S., & Tiwari, A. N. Review of Progress Toward 20% Efficiency Flexible CIGS Solar Cells and Manufacturing Issues of Solar Modules. *IEEE J. Photovolt.* 3, 572–580 (2013).

Research on heat transfer performance of passive solar collector-storage wall system with phase change materials - ScienceDirect. Available at: <https://www.sciencedirect.com/science/article/pii/S037877881630202X>. (Accessed: 13th September 2018)

Residential Solar Panels Cost Analysis: Full Breakdown. Solar Action Alliance

Riha, S. C.; Parkinson, B. A.; Prieto, A. L. Solution-Based Synthesis and Characterization of Cu<sub>2</sub>ZnSnS<sub>4</sub> Nanocrystals. *J. Am. Chem. Soc.* 2009, 131, 12054–12055.

Ruan, L., Shen, W., Wang, A., Zhou, Q., Zhang, H., & Deng, Z. Stable and conductive lead halide perovskites facilitated by X-type ligands. *Nanoscale* 9, 7252–7259 (2017).

Saga, T. Advances in crystalline silicon solar cell technology for industrial mass production. *NPG Asia Mater.* 2, 96–102 (2010).

Sanehira, E. M., Marshall, A. R., Christians, J. A., Harvey, S. P., Ciesielski, P. N., Wheeler, L. M., Schulz, P., Lin, L. Y., Beard, M. C., & Luther, J. M. Enhanced mobility CsPbI<sub>3</sub> quantum dot arrays for record-efficiency, high-voltage photovoltaic cells. *Sci. Adv.* 3, eaao4204 (2017).

Sargent, E. H. Colloidal quantum dot solar cells. *Nat. Photonics* 6, 133–135 (2012).

Schaller, R. D. & Klimov, V. I. High Efficiency Carrier Multiplication in PbSe Nanocrystals: Implications for Solar Energy Conversion. *Phys. Rev. Lett.* 92, 186601 (2004).

Schaller, R. D., Petruska, M. A. & Klimov, V. I. Effect of electronic structure on carrier multiplication efficiency: Comparative study of PbSe and CdSe nanocrystals. *Appl. Phys. Lett.* (20051219). doi:10.1063/1.2142092

Shabaev, A., Efros, A. L. & Efros, A. L. Dark and Photo-Conductivity in Ordered Array of Nanocrystals. *Nano Lett.* 13, 5454–5461 (2013).

Shalini, S., Balasundaraprabhu, R., Kumar, T. S., Prabavathy, N., Senthilarasu, S., & Prasanna, S. Status and outlook of sensitizers/dyes used in dye sensitized solar cells (DSSC): a review. *Int. J. Energy Res.* 40, 1303–1320 (2016).

Shockley, W. & Queisser, H. J. Detailed Balance Limit of Efficiency of p-n Junction Solar Cells. *J. Appl. Phys.* 32, 510–519 (1961).

Shockley–Queisser limit. Wikipedia, the free encyclopedia (2015).

Slide Show. Available at:

[http://education.mrsec.wisc.edu/SlideShow/slides/pn\\_junction/pn\\_junction\\_solar.html](http://education.mrsec.wisc.edu/SlideShow/slides/pn_junction/pn_junction_solar.html).

(Accessed: 11th August 2015)

Smith, M., Chen, G. D., Li, J. Z., Lin, J. Y., & Jiang, H. X. Excitonic recombination in GaN grown by molecular beam epitaxy: *Applied Physics Letters*: Vol 67, No 23, 3387 (1998).

Snoke, D. W., Braun, D., & Cardona, M. Carrier thermalization in Cu<sub>2</sub>O: Phonon emission by excitons. *Phys. Rev. B* 44, 2991 (1991)

Solar Energy | PVEducation. Available at:  
<http://www.pveducation.org/pvcdrom/introduction/solar-energy>. (Accessed: 11th August 2015)

Solar Energy Industries Association; NAICS: 813910. EC & M: Electrical Construction and Maintenance; Overland Park. Informa (2018)

Solar Energy vs Fossil Fuels: How Do They Compare? | EnergySage. Solar News (2017).

Solar Markets Around The World. Available at:  
[http://solarcellcentral.com/markets\\_page.html](http://solarcellcentral.com/markets_page.html). (Accessed: 12th August 2015)

Solar Spectrum. Available at:  
<http://www.greenrhinoenergy.com/solar/radiation/characteristics.php>. (Accessed: 13th September 2018)

Song, W., Wu, X., Di, Q., Xue, T., Zhu, J., & Quan, Z. Morphologically controlled synthesis of ionic cesium iodide colloidal nanocrystals and electron beam-induced transformations. *RSC Adv.* 8, 18519–18524 (2018).

Steckel, J. S.; Yen, B. K. H.; Oertel, D. C.; Bawendi, M. G. On the Mechanism of Lead Chalcogenide Nanocrystal Formation. *J. Am. Chem. Soc.* 2006, 128, 13032–13033.

Steinhagen, C.; Panthani, M. G.; Akhavan, V.; Goodfellow, B.; Koo, B.; Korgel, B. A. Synthesis of Cu<sub>2</sub>ZnSnS<sub>4</sub> Nanocrystals for Use in Low-Cost Photovoltaics. *J. Am. Chem. Soc.* 2009, 131, 12554–12555.

Stolle, C. J., Harvey, T. B. & Korgel, B. A. Photonic curing of ligand-capped CuInSe<sub>2</sub> nanocrystal films in 2014 IEEE 40th Photovoltaic Specialist Conference (PVSC) 0270–0274 (2014). doi:10.1109/PVSC.2014.6924897

Stolle, C. J., Harvey, T. B., Pernik, D. R., Hibbert, J. I., Du, J., Rhee, D. J., Akhavan, V. A., Schaller, R. D. & Korgel, B. A. Multiexciton Solar Cells of CuInSe<sub>2</sub> Nanocrystals. *J. Phys. Chem. Lett.* 5, 304–309 (2014).

Stolle, C. J., Lu, X., Yu, Y., Schaller, R. D. & Korgel, B. A. Efficient Carrier Multiplication in Colloidal Silicon Nanorods. *Nano Lett.* 17, 5580–5586 (2017).

Stolle, C. J., Panthani, M. G., Harvey, T. B., Akhavan, V. A. & Korgel, B. A. Comparison of the Photovoltaic Response of Oleylamine and Inorganic Ligand-Capped CuInSe<sub>2</sub> Nanocrystals. *ACS Appl. Mater. Interfaces* 4, 2757–2761 (2012).

Stolle, C. J., Schaller, R. D. & Korgel, B. A. Efficient Carrier Multiplication in Colloidal CuInSe<sub>2</sub> Nanocrystals. *J. Phys. Chem. Lett.* 5, 3169–3174 (2014).

Stolle, C. J.; Harvey, T. B.; Pernik, D. R.; Hibbert, J. I.; Du, J.; Rhee, D. J.; Akhavan, V. A.; Schaller, R. D.; Korgel, B. A. Multiexciton Solar Cells of CuInSe<sub>2</sub> Nanocrystals. *J. Phys. Chem. Lett.* 2014, 5, 304–309.

Su, Y., Chen, X., Ji, W., Zeng, Q., Ren, Z., Su, Z., & Liu, L. Highly Controllable and Efficient Synthesis of Mixed-Halide CsPbX<sub>3</sub> (X = Cl, Br, I) Perovskite QDs toward the Tunability of Entire Visible Light. *ACS Appl. Mater. Interfaces* 9, 33020–33028 (2017).

Sugathan, V., John, E. & Sudhakar, K. Recent improvements in dye sensitized solar cells: A review. *Renew. Sustain. Energy Rev.* 52, 54–64 (2015).

Sun, Z. H.; Oyanagi, H.; Nakamura, H.; Jiang, Y.; Zhang, L.; Uehara, M.; Yamashita, K.; Fukano, A.; Maeda, H. Ligand Effects of Amine on the Initial Nucleation and Growth Processes of CdSe Nanocrystals. *J. Phys. Chem. C* 2010, 114, 10126–10131.

Sutton, R. J., Filip, M. R., Haghighirad, A. A., Sakai, N., Wenger, B., Giustino, F., & Sanith, H. J. Cubic or Orthorhombic? Revealing the Crystal Structure of Metastable Black-Phase CsPbI<sub>3</sub> by Theory and Experiment. *ACS Energy Lett.* 3, 1787–1794 (2018).

Swarnkar, A., Marshall, A. R., Sanehira, E. M., Chernomordik, B. D., Moore, D. T., Christians, J. A., Chakrabarti, T., & Luther, J. M. Quantum dot-induced phase stabilization of  $\alpha$ -CsPbI<sub>3</sub> perovskite for high-efficiency photovoltaics. *Science* 354, 92–95 (2016).

Swarnkar, A., Ravi, V. K. & Nag, A. Beyond Colloidal Cesium Lead Halide Perovskite Nanocrystals: Analogous Metal Halides and Doping. *ACS Energy Lett.* 2, 1089–1098 (2017).  
Szendrei, K., Gomulya, W., Yarema, M., Heiss, W. & Loi, M. A. PbS nanocrystal solar cells with high efficiency and fill factor. *Appl. Phys. Lett.* 97, 203501 (2010).

Talapin, D. V., Lee, J.-S., Kovalenko, M. V. & Shevchenko, E. V. Prospects of Colloidal Nanocrystals for Electronic and Optoelectronic Applications. *Chem. Rev.* 110, 389–458 (2010).

Tan, Y., Zou, Y., Wu, L., Huang, Q., Yang, D., Chen, M., Ban, M., Wu, C., Wu, T., Bai, S., Song, T., Zhang, Q., & Sun, B. Highly Luminescent and Stable Perovskite Nanocrystals with Octylphosphonic Acid as a Ligand for Efficient Light-Emitting Diodes. *ACS Appl. Mater. Interfaces* 10, 3784–3792 (2018).

Tang, J.; Hinds, S.; Kelley, S. O.; Sargent, E. H. Synthesis of Colloidal CuGaSe<sub>2</sub>, CuInSe<sub>2</sub>, and Cu(InGa)Se<sub>2</sub> Nanoparticles. *Chem. Mater.* 2008, 20, 6906–6910.

Tang, L.-C., Chang, C.-S., Tang, L.-C. & Huang, J. Y. Electronic structure and optical properties of rhombohedral CsGeI<sub>3</sub> crystal. *J. Phys. Condens. Matter* 12, 9129 (2000).

- Tong, Y., Bladt, E., Aygüler, M. F., Manzi, A., Milowska, K. Z., Hintermayr, V. A., Docampo, P., Bals, S., Urban, A. S., Polavarapu, L., & Feldmann, J. Highly Luminescent Cesium Lead Halide Perovskite Nanocrystals with Tunable Composition and Thickness by Ultrasonication. *Angew. Chem. Int. Ed.* 55, 13887–13892 (2016).
- Trinh, M. T., Houtepen, A. J., Schins, J. M., Hanrath, T., Piris, J., Knulst, W., Goossens, A. P. L. M. & Siebbeles, L. D. A. In Spite of Recent Doubts Carrier Multiplication Does Occur in PbSe Nanocrystals. *Nano Lett.* 8, 1713–1718 (2008).
- Voggu, V. R., Sham, J., Pfeffer, S., Pate, J., Phillip, L., Harvey, T. B., Brown, R. M., & Korgel, B. A. Flexible CuInSe<sub>2</sub> Nanocrystal Solar Cells on Paper. *ACS Energy Lett.* 2, 574–581 (2017).
- Wang, C., R. Chesman, A. S. & J. Jasieniak, J. Stabilizing the cubic perovskite phase of CsPbI<sub>3</sub> nanocrystals by using an alkyl phosphinic acid. *Chem. Commun.* 53, 232–235 (2017).
- Wang, F.; Buhro, W. E. Morphology Control of Cadmium Selenide Nanocrystals: Insights into the Roles of Di-n-octylphosphine Oxide (DOPO) and Di-n-octylphosphinic Acid (DOPA). *J. Am. Chem. Soc.* 2012, 134, 5369–5380.
- Wang, H.-C., Bao, Z., Tsai, H.-Y., Tang, A.-C. & Liu, R.-S. Perovskite Quantum Dots and Their Application in Light-Emitting Diodes. *Small* 14, n/a-n/a (2018).
- Wei, H.; Guo, W.; Sun, Y.; Yang, Z.; Zhang, Y. Hot-injection synthesis and characterization of quaternary Cu<sub>2</sub>ZnSnSe<sub>4</sub> nanocrystals. *Mater. Lett.* 2010, 64, 1424–1426.
- WEO. Available at: <http://www.iea.org/weo/>. (Accessed: 13th September 2018)
- Whitham, K., Yang, J., Savitzky, B. H., Kourkoutis, L. F., Wise, F., & Hanrath, T. Charge transport and localization in atomically coherent quantum dot solids. *Nat. Mater. Lond.* 15, 557–563 (2016).
- Williams, R. Becquerel Photovoltaic Effect in Binary Compounds. *The Journal of Chemical Physics: Vol 32, No 5.* 1505 (2004)
- Wöhrlé, D. & Meissner, D. Organic Solar Cells. *Adv. Mater.* 3, 129–138 (1991).
- Wu, X., Song, W., Li, Q., Zhao, X., He, D., & Quan, Z. Synthesis of Lead-free CsGeI<sub>3</sub> Perovskite Colloidal Nanocrystals and Electron Beam-induced Transformations. *Chem. – Asian J.* 13, 1654–1659 (2018).
- Yarita, N., Tahara, H., Ihara, T., Kawawaki, T., Sato, R., Saruyama, M., Teranishi, T. & Kanemitsu, Y. Multiexciton recombination dynamics in CsPbBr<sub>3</sub> perovskite nanocrystals revealed by femtosecond transient absorption and single dot spectroscopies. in 2017



Conference on Lasers and Electro-Optics Europe European Quantum Electronics Conference (CLEO/Europe-EQEC) 1–1 (2017). doi:10.1109/CLEOE-EQEC.2017.8087818

Yin, Y. & Alivisatos, A. P. Colloidal nanocrystal synthesis and the organic-inorganic interface. *Nat. Lond.* 437, 664–70 (2005).

Yu, K.; Liu, X.; Chen, Q. Y.; Yang, H.; Yang, M.; Wang, X.; Wang, X.; Cao, H.; Whitfield, D. W., Hu, C.; Tao, Y. Mechanistic Study of the Role of Primary Amines in Precursor Conversions to Semiconductor Nanocrystals at Low Temperature. *Angew. Chem. Int. Ed.* 2014, 53, 6898–6904.

Yu, K.; Liu, X.; Zeng, Q.; Leek, D. M.; Ouyang, J.; Whitmore, K. M.; Ripmeester, J. A.; Tao, Y.; Yang, M. Effect of Tertiary and Secondary Phosphines on Low-Temperature Formation of Quantum Dots. *Angew. Chem. Int. Ed.* 2013, 52, 4823–4828.

Zasadzinski, J. A., Viswanathan, R., Madsen, L., Garnæs, J. & Schwartz, D. K. Langmuir-Blodgett films. *Science* 263, 1726–1733 (1994).

Zhang, W., Eperon, G. E. & Snaith, H. J. Metal halide perovskites for energy applications. *Nat. Energy* 1, 16048 (2016).

Zhong, H.; Li, Y.; Ye, M.; Zhu, Z.; Zhou, Y.; Yang, C.; Li, Y. A facile route to synthesize chalcopyrite CuInSe<sub>2</sub> nanocrystals in non-coordinating solvent. *Nanotechnology* 2007, 18, 25602-25607.

Zhong, H.; Wang, Z.; Bovero, E.; Lu, Z.; van Veggel, F. C. J.; Scholes, G. D. Colloidal CuInSe<sub>2</sub> Nanocrystals in the Quantum Confinement Regime: Synthesis, Optical Properties, and Electroluminescence. *J. Phys. Chem. C* 2011, 115, 12396–12402.

Zhong, H.; Zhou, Y.; Ye, M.; He, Y.; Ye, J.; He, C.; Yang, C.; Li, Y. Controlled Synthesis and Optical Properties of Colloidal Ternary Chalcogenide CuInS<sub>2</sub> Nanocrystals. *Chem. Mater.* 2008, 20, 6434–6443.

Zhou, Y., Garces, H. F., Senturk, B. S., Ortiz, A. L. & Padture, N. P. Room temperature “one-pot” solution synthesis of nanoscale CsSnI<sub>3</sub> orthorhombic perovskite thin films and particles. *Mater. Lett.* 110, 127–129 (2013).

Zvaigzne, M. A., Aleksandrov, A. E., Samokhvalov, P. S., Martynov, I. L., Lypenko, D. A., Tameev, A. R., Nikitenko, V. R., Chistyakov, A. A. Influence of the surface ligand molecules length on the optical properties and photoconductivity of PbS quantum dot condensates. *Tech. Phys. Lett.* 43, 879–881 (2017).

## **Vita**

Cherrelle Thomas was raised in Texas where she attended high school and obtained an associate's degree before her diploma. After graduating from high school she attended Howard University in Washington, DC. There she graduated magna cum laude with a bachelor of science in Chemical Engineering, before matriculating to the University of Texas at Austin. She researched copper indium selenide and perovskite nanocrystals for solar cells under the direction of Dr. Brian Korgel. Cherrelle earned a Master of Science in Engineering spring 2017, PhD. in Chemical Engineering Fall 2018, and two certificates nanoportfolio and Engineering Education.

The author can be reached at: [cherrelle.thomas@yahoo.com](mailto:cherrelle.thomas@yahoo.com)

This dissertation was typed by the author.